Development and Applications of a Low-Field Portable NMR System

A thesis presented in partial fulfillment of the
requirements for the degree of Doctor of Philosophy
in Physics at Massey University, Manawatu, New Zealand.

Robert L. Ward
October 2011

Abstract

Nuclear magnetic resonance (NMR) is a phenomenon similar to MRI in which radio frequency signals are used to excite and manipulate atomic nuclei within a static magnetic field. Following excitation, the nuclei return to equilibrium, all the while offering valuable molecular level information pertaining to the sample.

Within the last decade, the development of small and inexpensive NMR spectrometers and permanent magnet NMR sensors has been a significant focus within the NMR community. More recently, application scientists have sought practical applications for the new technologies.

In this thesis, a prototype NMR apparatus consisting of a spectrometer and 3.2MHz permanent magnet sensor was extended to enable scientific measurements. This involved developing radio frequency electronic circuitry for the spectrometer front-end, and electromagnetic noise shielding and temperature regulation for the magnetic sensor. Experimental results confirmed that repeatable measurements using the modified apparatus were indeed possible.

The NMR apparatus was thereafter successfully used to study flow, diffusion and kiwifruit using several different experimental techniques. A significantly larger effort was then expended upon the study of T_2 relaxation in pectin model systems using pH as the adjustable parameter. The fascinating experimental results were successfully interpreted and modeled across three pH zones in terms of a proton chemical exchange model and molecular conformational changes. In addition, it was found that pectin carboxyl de-protonation was significantly less than expected. Further experiments performed upon galacturonic acid monomers, dimers and trimers appeared to further illuminate the pectin results. Future experiments are planned.

Also while studying pectin solutions, an unexpected pH-dependent water transverse relaxation behavior was observed at both 3.2MHz and 400MHz. The only references found in the literature were from a small publication almost 50 years ago, and a 2011 publication.

Altogether, this thesis contributed to original knowledge in several ways: it showed how a low-field apparatus and single-sided sensor could be improved and utilized for a variety of scientific measurements; it showed both experimentally and theoretically how T_2 for pectin solutions change with pH; it revealed an unexpected de-protonation limit for pectin molecules; it revealed a T_2 pH dependence for water.

To my wife Liz
who has endured
much over the years.

Acknowledgements

Many people have contributed to this thesis in many different ways. First and foremost I would like to thank my wife who has stood beside me in relative poverty for too many years. It's almost over... and it's time we took a holiday together.

Second, I would like to thank my two daughters, Rebekah and Hannah, for putting up with my absence. Rebekah was born two months before we started my university adventure, and Hannah was born two years later. Again, it's almost over... and it's time we went on some adventures together.

Third, I would like to thank my supervisors, Dr. Bill Williams and Dr. Robin Dykstra. I have thoroughly enjoyed working with you guys. You have not only been supervisors during this project, but also friends. Bill – dude – your love of science is contagious and has inspired me greatly. Perhaps it is time for us to drink some beers, play some guitar, and talk some philosophy :-)

Many other people need to be thanked and acknowledged for their assistance during this project.

In no particular order, my thanks go to: Dr. Jason Hindmarsh for many chats about interesting things like kiwifruit, and occasional help on the "real" NMR systems. Dr. Pat Edwards for teaching me how to use the other "real" NMR systems, and for allowing me to pull apart expensive probe-heads. Dr. Aurelie Cucheval, whose French I could sometimes understand, for being a charming assistant during my pectin-making exploits. Mary-Helen Ward for being the only non-scientist with the skills and perseverance to suffer reading my thesis, and for pointing out a few typos that I'd missed. Michael Adams for encouraging me in black-magic, otherwise known as RF electronics. It was great, and I wish you could have stayed a lot longer. Keith Whitehead for arguing with me, and finally converting me to the Cult of MacHeads. Terry Southern for many interesting conversations about all sorts of things. Rinni Williamson (nee Singh) for arguing, laughing, crying, being fun, and for one joke I will never forget. Dr. Bob O'Driscoll for the interesting conversations that oscillated between Macs and electronics. Dr. Craig Eccles for his assistance with Prospa and the Mole. Steve Denby and Noel Foot in the mechanical workshop who usually said no, then did it. Dr. Mark Hunter and Ben Parkinson

for Mole assistance. Erich Schuster for the pectin images. Dr. Gavin Hedwig for the offer of a water bath. Dr. Lara Matia-Merino for the emulsions.

Table of contents

List of abbreviations

γ	The magnetogyric (or gyromagnetic) ratio
ω	Frequency in radians per second
ω_{eff}	Effective frequency in the rotating frame in radians per second
A	Amps
AFM	Atomic force microscopy
AC	Alternating current
ARRL	American Radio Relay League
B_0	Static magnetic field oriented along the z-axis
B_1	Oscillating magnetic field oriented along the x-axis
CE	capillary electrophoresis
CC	Counterion condensation
CLI	Command line interface
COOH	Carboxyl
CPL	Coupled
CP	Carr Purcell
CPMG	Carr Purcell Meiboom Gill
CSV	Comma separated values
CTR	Current transfer ratio
D-D	Dipole-dipole coupling
Da	Dalton: $1/12^{\text{th}}$ of the mass of a carbon atom at rest in its ground state
DC	Direct current
DE	Direct echo
DM	Degree of methyl-esterification
DP	Degree of polymerization
DSP	Digital signal processor
EMF	Electro motive force, or voltage
EMI	Electromagnetic interference
FID	Free induction decay
GalA	Galacturonic acid
GDL	Glucono delta-lactone
GUI	Graphical user interface

HCl	Hydrochloric acid
HDD	Hard disk drive
HM	High methoxyl
HPA	High-power amplifier
Hz	Frequency in Hertz
IC	Integrated circuit
$J(\omega)$	Spectral density as a function of frequency
kDa	Kilodalton
Kea	NMR spectrometer
kHz	Kilohertz
LED	Light emitting diode
LM	Low methoxyl
M	Molarity, measured in $\text{mol}\cdot\text{L}^{-1}$
M_r	Molecular weight
μA	Micro amps
μF	Micro Farads
μH	Micro Henries
mA	Milli amps
Mole	MObile Lateral Explorer or MObile Liquid Explorer
mole	$\sim 6.022 \times 10^{23}$ atoms of molecules
MRI	Magnetic resonance imaging
nF	Nano Farads
NaOH	Sodium hydroxide
NdFeB	Neodymium iron boron
NIB	Neodymium iron boron
NMR	Nuclear magnetic resonance
OH	Hydroxyl
pK_a	Acid dissociation constant
PAD	Pre-amplifier duplexer
PCB	Printed circuit board
(π)	180° RF pulse
$(\pi/2)$	90° RF pulse
pF	Pico Farads
PID	Proportional-integral-derivative
Prospa	NMR software
PSU	Power supply unit
Pt100	Platinum resistance thermometer (100Ω resistance at 0°C)
QST	Amateur radio enthusiasts magazine published by the ARRL
Q	Quality factor of a inductor, capacitor, or tuned circuit
R_1	Longitudinal (or spin-lattice) relaxation rate

R_2	Transverse (or spin-spin) relaxation rate
RX	Receive or receiver
RF	Radio frequency
RMS	Root mean square
R_{eff}	Concentration ratio of calcium ions to de-protonated carboxyls
RS	Radio Spares Components
RS-485	Serial differential hardware communications protocol
SAR	Specific absorption rate
SAXS	Small-angle X-ray scattering
SmCo	Samarium Cobalt
SMPSU	Switched mode power supply unit
SNR	Signal to noise ratio
SE	Stimulated echo
SMA	SubMiniature version A
SMB	SubMiniature version B
T	Magnetic flux density (Tesla)
T_1	Longitudinal (or spin-lattice) relaxation time
$T_{1\rho}$	Longitudinal (or spin-lattice) relaxation time in the rotating frame
T_2	Transverse (or spin-spin) relaxation time
t_E	Echo time
TX	Transmit or transmitter
USB	Universal serial bus
V	Volts
wt%	Weight percent

List of tables

List of figures

Introduction

Somebody once said that the greatest unexplored region in the universe is right under your hat. While this may in fact be true, other mysterious regions also exist all around us. Indeed, the fruit that we eat and water we drink are themselves micro worlds, teeming with large and small molecules performing elaborate movements. These molecules and movements are of significant interest in this thesis.

Individual molecules are incredibly small and can move very fast. Water molecules measure around one-hundred pico-metres across, and perform rotations every few pico-seconds at room temperature. Dissolved biopolymer molecules move slowly compared to their solvent, and often cast off their protons into the surroundings. None of these behaviors can be viewed directly by the human eye, but scientific tools such as those based upon nuclear magnetic resonance provide views into the intricate workings of these molecules.

Nuclear magnetic resonance has been around for many decades. Prior to the arrival of powerful computers and fast Fourier transforms, magnetic resonance experiments involved sweeping the magnetic field while applying continuous wave power at a fixed radio frequency (Becker et al. (2007) [17]). With the advent of the new tools, resonances could be excited quickly using pulse techniques. A sample could be irradiated like a bell being struck by a hammer, resulting in a response ringing forth to provide a rich collection of information about the sample.

Within the last decade, many changes have taken place in the world of nuclear magnetic resonance. Electronic circuits have become denser and faster, software applications have become larger and more powerful, and many NMR magnets have become smaller and less homogeneous. The convergence of hardware and software, and the emergence of permanent magnet sensors have enabled the creation of powerful magnetic resonance systems that are relatively inexpensive and compact enough to fit in a backpack. It is into this world that this PhD thesis was born.

Scientists and engineers in Palmerston North and Wellington New Zealand worked together to develop NMR tools, producing an advanced apparatus capable of stimulating and then measuring the evolution of tiny precessing magnets inside soft materials. Measuring the relaxation of these tiny magnets back to their pre-

stimulated states, and understanding the information contained in the relaxation, is the basis of much of the work in this thesis.

At the beginning of the project, a basic NMR system was supplied. This consisted of a newly developed NMR spectrometer, a small permanent-magnet NMR probe, a laptop computer, and a Microsoft Windows software application. The equipment was configured in a lab at Massey University and the first experiments performed. Alongside the experiments, a theoretical study of the amazing phenomenon of nuclear magnetic resonance was begun. Several years later, and near the completion of this thesis, the wonder of the qualities and properties of atomic nuclei and their interactions has not diminished. Indeed, the world now looks a different place, in the same spirit that Edward Purcell, in his 1952 Nobel Lecture, delighted as he caught a glimpse in his mind's eye of precessing protons in the snow on his doorstep (Purcell (1952) [120]).

In Chapter 1 of this thesis, the theory of nuclear magnetic resonance is introduced. The discussion is presented in a way that weaves together NMR theory with the experimental apparatus. The properties of nuclei are discussed. The emergence of a bulk magnetization vector, and its manipulation using external fields is described. Signal detection and relaxation are explained, thus providing a foundation for the succeeding chapters.

In Chapter 2 the NMR apparatus supplied for this project is examined, followed by the additional apparatus built during the project that enabled scientific measurements to be recorded. A variety of experiments were used to test the performance of the apparatus under different conditions; these are described, along with the numerous problems encountered.

In Chapter 3 the electronic design, development, and operation of two preamplifier duplexer modules, built for the Kea spectrometer, are discussed in detail.

In Chapter 4 the NMR apparatus is finally put to work measuring biopolymer solutions. These measurements revealed a rich assortment of results, and coupled with a mathematical model, provided profound insight into their molecular behavior.

In Chapter 5 water T_2 relaxation is examined. This fascinating chapter was unplanned and resulted from seemingly anomalous measurements observed in the previous chapter.

In Chapter 6 flow, diffusion, and relaxation are studied using out-of-the-ordinary pulse sequences and techniques.

In Chapter 7 conclusions are drawn from the previous chapters, and Chapter 8 suggests possibilities for future research.

CHAPTER 1

NMR theory

The aim of this chapter is to provide a theoretical foundation to undergird the following chapters in this thesis. It begins by examining the physical properties of atomic nuclei that make NMR possible and how these properties manifest themselves in the presence of a static magnetic field. Following this is an examination of how these nuclear properties are manipulated using experimental NMR apparatus and how the response to stimuli is detected. The NMR apparatus used to perform experiments is discussed in greater detail in a later chapter.

1.1 Overview

NMR is a substantial discipline, therefore it was necessary to begin by limiting the scope of this chapter. The first limitation arose from the approach taken to understanding NMR theory. There are many excellent books covering the theory of NMR (see Appendix D), however examining a reasonable selection showed that more than one model is used. One model is based upon quantum mechanics and provides a rigorous mathematical foundation for NMR. Another uses an intuitive vector model. A third weaves the quantum mechanical and vector models together, thus gaining the advantages of both systems. In this thesis, the vector model was generally used, however as one author points out, even with a vector model, the quantum mechanics are never far below the surface (Callaghan (1991) [26]). Because of this reality, the third approach was chosen for the following discussion.

The second limitation of this chapter arose from the type of nuclei being studied. Most chemical elements have at least one isotope that is NMR active. The majority of these were irrelevant to this thesis and were ignored. The major exception was the ^{1}H nucleus, often simply referred to as a proton. There were two reasons

for focussing exclusively on the proton. First, protons are abundant in many interesting samples such as water, fruit, oil, and rubber, and in all the samples studied in this thesis. The second reason is that protons provide the strongest readily accessible NMR signal of all atomic nuclei. This was especially important for the Mole probe (see Chapter 2) that was used throughout this project because it has a low polarizing field, and single-sided excitation and detection circuitry, resulting in extremely small NMR signals.

The third limitation of this chapter arose from the type of NMR measurements being pursued. The Mole probe is a pseudo-homogeneous probe thus it cannot perform spectroscopic measurements. It is well suited to measuring relaxation in soft materials and liquids, therefore this was the primary focus. With these considerations in mind, it is time to delve into the depths of the atom and understand how atomic nuclei and NMR provide a window into the sub-atomic world.

1.2 Nuclear properties

1.2.1 Nuclear spin angular momentum

In nature, angular momentum is manifest in several ways. The rotation of the earth around the sun is an example of orbital angular momentum. The rotation of the earth about its own axis is an example of spin angular momentum. Protons (and neutrons and electrons) exhibit an intrinsic spin angular momentum, often referred to simply as spin. Curiously, intrinsic spin angular momentum is not due spinning or rotation of the proton, but is rather an intrinsic property of the particle in the same sense as mass and charge (Griffiths (1995) [64], Levitt (2008) [93]). It is this form of angular momentum that will be referred to in the remainder of this thesis.

According to quantum mechanics, intrinsic spin angular momentum $\vec{S}$ possessed by a nuclide may take only discrete values; i.e. $\vec{S}$ is quantized. The magnitude of the angular momentum vector is determined by the nuclear spin quantum number I for the nuclide in units of $\hbar$ $(= h/2\pi)$ as follows:

$$|\,\vec{S}\,| = \sqrt{I(I+1)}\,\hbar \tag{1.1}$$

where h $(= 6.63 \times 10^{-34}\text{J}\cdot\text{s})$ is the Planck constant. The spin quantum number I varies depending upon the type of nuclide, however, I always takes a value from the following set:

$$I = \left\{0, \frac{1}{2}, 1, \frac{3}{2}, 2, \frac{5}{2}, ...\right\}. \tag{1.2}$$

Table 1.1: Properties of nuclides relevant to this thesis. Gamma (γ) is the magnetogyric ratio.

Spin quantum number I	Nuclide	Natural abundance (%)	γ ($\times 10^6$) (rad·s^{-1}·T^{-1})
0	^{12}C	98.9	
0	^{16}O	~100	
1/2	^{1}H	~100	267.522
1/2	^{19}F	100	251.81
1	^{2}H	0.015	41.066
3/2	^{23}Na	~100	70.808
3/2	^{35}Cl	75.77	10.610
3/2	^{37}Cl	24.23	8.832
5/2	^{17}O	0.04	–36.281

Values in this table taken from Levitt [93] and Nelson [112].

Some nuclides have spin quantum number $I = 0$ and therefore possess no intrinsic spin angular momentum. Examples of these nuclides are ^{12}C and ^{16}O. Protons are spin-1/2 and therefore $|\vec{S}| = \sqrt{3/4}\,\hbar$. The ^{2}H (deuterium) nuclide, which is hydrogen with an added neutron, has $I = 1$. The value of I for a particular nuclide may generally be determined from the composition of the nucleus using selection rules (Levitt (2008) [93]). A short list of nuclides and their spin quantum numbers relevant to this thesis are shown in Table 1.1.

1.2.2 Nuclear magnetism

Any nucleus that possesses intrinsic spin angular momentum also possesses a magnetic moment. These two vector quantities are mathematically related as follows:

$$\vec{\mu} = \gamma \vec{S} \tag{1.3}$$

where $\vec{\mu}$ is the nuclear magnetic moment and γ is the nuclide-dependent magnetogyric (or gyromagnetic) ratio. Several observations can be made directly from Eqn. 1.3. First, nuclides with $I = 0$ have no intrinsic spin angular momentum $\vec{S}$ and thus no magnetic moment. These nuclides are therefore invisible to NMR. Second, $\vec{\mu}$ and $\vec{S}$ are vectors and are therefore aligned either parallel or antiparallel to one another depending upon the sign of γ. Third, since $\vec{S}$ is quantized, the magnetic moment $\vec{\mu}$ is also quantized. Fourth, it is obvious from Table 1.1 that the

magnetic moment for the ^{1}H proton is significantly larger than most other nuclides shown.

1.2.3 Space quantization

The magnitudes of $\vec{S}$ and $\vec{\mu}$ are quantized; their directions in space are also quantized. For a nuclide with spin quantum number I, there are $2I+1$ experimentally observed orientations for the angular momentum vector. Each orientation is represented by a magnetic quantum number m from the following set:

$$m = \{-I, -I+1, \ ... \ I-1, I\} \tag{1.4}$$

where the m values are integral steps apart. The measured, or observable, magnitudes of the angular momentum are the projections of the angular momentum vector onto an arbitrary axis (for example, the z-axis). The experimental values for the z-component of $\vec{S}$ are:

$$S_z = m\hbar. \tag{1.5}$$

For a spin-1/2 proton, the magnetic quantum numbers are $m = \pm\frac{1}{2}$, therefore the observable magnitudes are:

$$S_z = \pm\frac{\hbar}{2}. \tag{1.6}$$

The $(2I+1)$ possible projections of a proton angular momentum vector onto the z-axis are shown in Fig. 1.1.

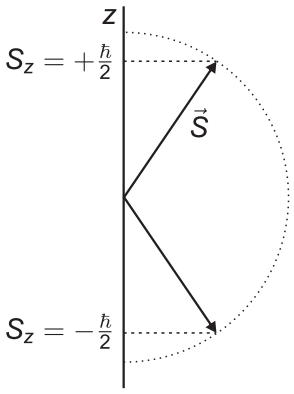

Figure 1.1: Space quantization of a proton angular momentum vector $\vec{S}$.

1.2.4 Magnetic moment precession

Placing a magnetic moment $\vec{\mu}$ within a static magnetic field $\vec{B}$ will cause the magnetic moment to experience a torque $\vec{\tau}$ that will attempt to align the magnetic moment with the field. This is analogous to a compass needle aligning with the Earth's magnetic field. The mathematical equation describing the interaction between a magnetic moment $\vec{\mu}$ and a static magnetic field $\vec{B}$ is:

$$\vec{\tau} = \vec{\mu} \times \vec{B} \tag{1.7}$$

where the torque $\vec{\tau}$ is perpendicular to both $\vec{\mu}$ and $\vec{B}$. Torque is the rate of change of angular momentum:

$$\vec{\tau} = \frac{d\vec{S}}{dt} \tag{1.8}$$

thus combining Eq. 1.7 and Eq. 1.8 gives:

$$\frac{d\vec{S}}{dt} = \vec{\mu} \times \vec{B}. \tag{1.9}$$

Eq. 1.9 shows that the angular momentum vector changes with time and the change is always perpendicular to both $\vec{\mu}$ and $\vec{B}$. Substituting Eq. 1.3 into Eq. 1.9 gives:

$$\frac{d\vec{\mu}}{dt} = \gamma\vec{\mu} \times \vec{B}. \tag{1.10}$$

This equation of motion can be expanded into its components:

$$\left.\begin{aligned} \frac{d\mu_x}{dt} &= \gamma(\mu_y B_z - \mu_z B_y) \\ \frac{d\mu_y}{dt} &= \gamma(\mu_z B_x - \mu_x B_z) \\ \frac{d\mu_z}{dt} &= \gamma(\mu_x B_y - \mu_y B_x) \end{aligned}\right\} \tag{1.11}$$

For NMR systems, the static magnetic field is termed $\vec{B}_0$ and is directed along the z-axis. Therefore, $B_x = B_y = 0$ and $B_z = B_0$. Eqs. 1.11 thus simplify to:

$$\left.\begin{aligned} \frac{d\mu_x}{dt} &= \gamma\mu_y B_0 \\ \frac{d\mu_y}{dt} &= -\gamma\mu_x B_0 \\ \frac{d\mu_z}{dt} &= 0 \end{aligned}\right\} \tag{1.12}$$

The solutions to Eqs. 1.12 are:

$$\left.\begin{aligned} \mu_x(t) &= \cos(\gamma B_0 t) \\ \mu_y(t) &= -\sin(\gamma B_0 t) \\ \mu_z(t) &= \mu_z \text{ (constant)} \end{aligned}\right\} \tag{1.13}$$

These equations show the z component of the magnetic moment remains fixed, while the x and y components precess around the z-axis with angular frequency:

$$\omega_0 = \gamma B_0 \tag{1.14}$$

as illustrated in Fig. 1.2. The precession frequency ω_0 ($= 2\pi f_0$ where f_0 is the frequency in Hz) is termed the Larmor frequency and depends upon the magnetogyric ratio of the nuclide and the magnetic flux density of the static field. The direction of the precession depends upon the nuclide: clockwise for $\gamma > 0$ and anti-clockwise for $\gamma < 0$. The precessional behavior is analogous to a spinning top or gyroscope in the Earth's gravitational field.

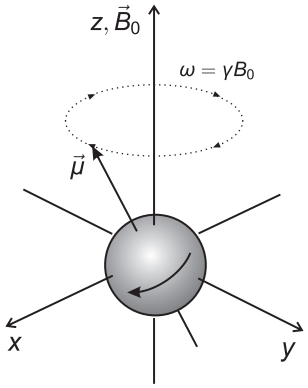

Figure 1.2: A proton with magnetic moment $\vec{\mu}$ precessing about the z-axis at angular frequency $\omega_0 = \gamma B_0$.

1.2.5 Energy quantization

The energy E of a magnetic moment $\vec{\mu}$ immersed in a magnetic field $\vec{B}$ is given by the dot product of the two vectors:

$$E = -\vec{\mu} \cdot \vec{B}. \tag{1.15}$$

The component of $\vec{\mu}$ that interacts with the external magnetic field $\vec{B}_0$ is the projection of $\vec{\mu}$ onto the z-axis. The interaction energy between μ_z and B_0 $(= B_z)$ is therefore:

$$E = -\mu_z B_0. \tag{1.16}$$

Given that $\mu_z = \gamma S_z$ from Eq. 1.3 and $S_z = m\hbar$ from Eq. 1.5 then:

$$E = -\gamma S_z B_0 = -\gamma m \hbar B_0. \tag{1.17}$$

For a proton the $(2I + 1)$ possible energy states have $m = \pm\frac{1}{2}$ thus:

$$E = \pm\frac{1}{2}\gamma\hbar B_0. \tag{1.18}$$

The lower energy $m = +\frac{1}{2}$ state has its magnetic component aligned with the B_0 field and is often denoted α. The higher energy $m = -\frac{1}{2}$ state has its magnetic component aligned against the B_0 field and is denoted β. The energy difference ΔE between the two states is:

$$\Delta E = E_\beta - E_\alpha = \frac{1}{2}\gamma\hbar B_0 - (-\frac{1}{2}\gamma\hbar B_0) = \gamma\hbar B_0. \tag{1.19}$$

Fig. 1.3 illustrates the energy difference between the two proton states with the magnetic field switched off and on. When the B_0 magnetic field is off, the two energy states are degenerate. When the magnetic field is switched on, the degeneracy is broken (Zeeman splitting) and the two distinct energy levels appear.

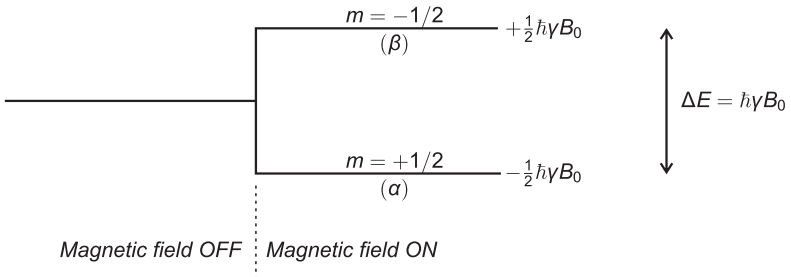

Figure 1.3: Switching the static magnetic field $\vec{B}_0$ from OFF to ON breaks the degeneracy, resulting in Zeeman splitting.

A spin-1/2 particle makes a single-quantum transition between the α and β states by absorption or emission of a photon with energy ΔE. Substituting photon energy $E = \hbar\omega$ into Eq. 1.19 gives:

$$E = \hbar\omega = \gamma\hbar B_0 \tag{1.20}$$

and therefore:

$$\omega = \gamma B_0 \tag{1.21}$$

where ω is the frequency in radians per second of the photon causing the transition. This results shows that the photon frequency required to cause an energy state transition is identical to the classically derived precession frequency of the magnetic moment. It is upon this basis that the NMR resonance condition occurs.

1.3 Ensemble properties

1.3.1 Boltzmann distribution

Fig. 1.4(a) represents an ensemble of isolated spin-1/2 protons in the absence of an external magnetic field $\vec{B}_0$. Their energy levels are degenerate and they are randomly orientated in space. Fig. 1.4(b) illustrates the same spins in the presence of an external magnetic field $\vec{B}_0$. The spins are shown to be precessing about the static field. Fig. 1.4(c) shows the equilibrium state in which vector addition of the microscopic magnetic moments has resulted in the formation of a bulk magnetization vector $\vec{M}_0$. The Boltzmann distribution describes the magnetic moments in terms of the populations of the two energy states:

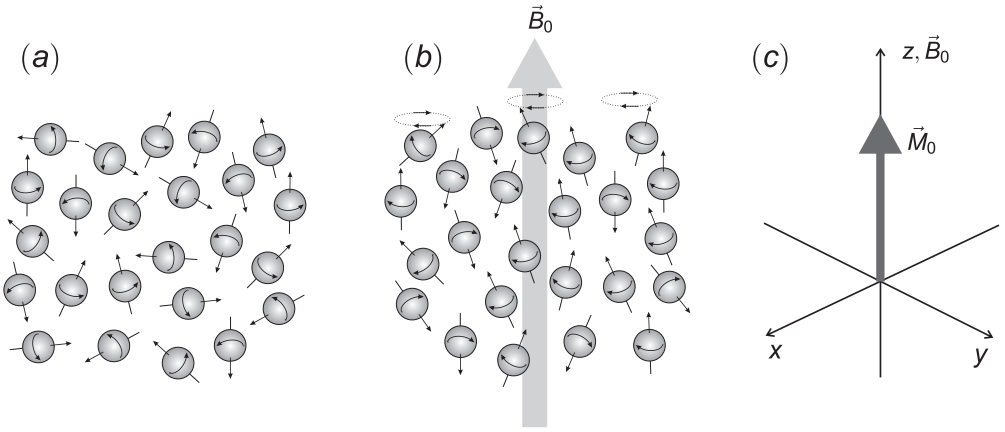

Figure 1.4: An ensemble of nuclear spins (a) randomly orientated and degenerate; (b) with degeneracy broken and spins aligning with or against the external B_0 field; (c) at equilibrium, with formation of bulk magnetization vector $\vec{M}_0$.

$$\frac{N_\alpha}{N_\beta} = e^{\Delta E/k_b T} \tag{1.22}$$

where N_α and N_β are the populations in the low and high energy states respectively, ΔE is the energy difference between the states, k_b is the Boltzmann constant ($= 1.38 \times 10^{23}\,\mathrm{J{\cdot}K^{-1}}$), and T is the absolute temperature in Kelvin. For the Mole probe, the B_0 field is around 75mT (see Chapter 2) therefore the energy difference between the spin states given by Eq. 1.19 is:

$$\Delta E = \gamma \hbar B_0 = 2.12 \times 10^{-27}\mathrm{J} \tag{1.23}$$

while at room temperature the thermal energy is (Atkins (1998) [16]):

$$k_b T = 4.11 \times 10^{-21}\mathrm{J}. \tag{1.24}$$

$k_b T$ is at least five orders of magnitude larger than ΔE thus the population difference between the α and β states is very small. The number of excess lower energy α-state spins per total spins is calculated using Eq. 1.22 and the exponential expansion $e^x \approx (1 + x)$:

$$\frac{\text{Excess spins}}{\text{Total spins}} = \frac{N_\alpha - N_\beta}{N_\alpha + N_\beta} \approx \frac{\Delta E}{2k_b T}. \tag{1.25}$$

Applying the results of Eqs. 1.23 and 1.24 to Eq. 1.25 shows approximately one excess lower energy α spin per 3.9×10^6 total spins. By comparison, the flux density of a modern superconducting magnet is about two hundred times greater than the Mole's flux density resulting in an excess population of one lower energy α spin per 20×10^3 total spins.

1.3.2 Curie's law

The equilibrium macroscopic magnetization $\vec{M}_0$ aligned along the z-axis is the net magnetic moment per unit volume and may be calculated using Curie's Law (Coates et al. (2000) [39]):

$$\vec{M}_0 = \frac{N\gamma^2\hbar^2 I(I+1)}{3k_b T}\vec{B}_0 \tag{1.26}$$

where N is the number of spins per unit volume. The important result from this expression is that $\vec{M}_0$ is proportional to the number of spins, the square of the magnetogyric ratio, and the strength of the applied $\vec{B}_0$ field.

For the Mole probe (see Chapter 2) it was important to maximize the signal-to-volume ratio in order to obtain the largest possible $\vec{M}_0$; this is discussed in §2.4.9 on page 52.

1.4 Spin manipulation and signal detection

Previous sections have shown that placing spin-1/2 nuclei within a magnetic field $\vec{B}_0$ results in the appearance of a bulk magnetization vector $\vec{M}_0$. The presence of the bulk magnetization vector is a necessary but insufficient pre-condition for extracting information from a sample. To key to unlocking nuclear information is to excite the $\vec{M}_0$ vector away from its equilibrium position along the z-axis and observe its behavior as it relaxes back to equilibrium. Both excitation and detection of $\vec{M}_0$ are mediated via magnetic fields that are generated and detected respectively by the B_1 coil which is shown in Fig 1.5.

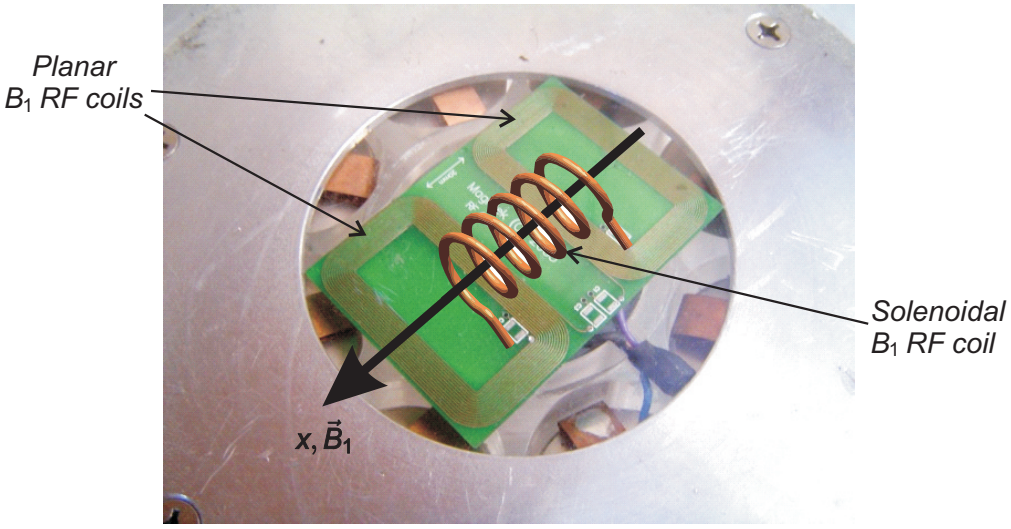

Figure 1.5: The PCB containing the planar $\vec{B}_1$ RF coils sits within the center hole of the Mole's aluminium top-plate. A solenoidal coil is superimposed on the photo to indicate the field direction equivalence between the two coil types.

To excite $\vec{M}_0$ away from its equilibrium position requires the application of a carefully tailored radio frequency (RF) pulse applied to the B_1 coil. At this point it is sufficient to say that the B_1 pulse will cause $\vec{M}_0$ to tip away from the z-axis whereupon it will precess about $\vec{B}_0$ at the Larmor frequency ω_0 as shown in Fig. 1.6. The bulk magnetization vector $\vec{M}_0$ and its precessional motion are of course a result of the individual precessing magnetic moments shown in Fig. 1.4.

The bulk magnetization vector $\vec{M}_0$ will not remain forever in the precessional state shown in Fig. 1.6. Instead, $\vec{M}_0$ is driven back to its equilibrium position along the z-axis by relaxation processes as discussed in §1.5.

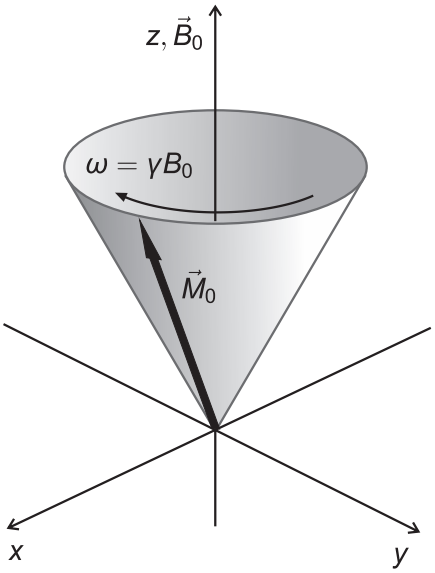

Figure 1.6: The bulk magnetization vector $\vec{M}_0$ is the vector sum of all the nuclear magnetic moments in the sample. Tipping the bulk magnetization vector away from the z-axis causes it to precess about the $\vec{B}_0$ magnetic field at angular frequency $\omega_0 = \gamma B_0$.

1.4.1 The B_1 field

The B_1 coil is the information conduit between the macroscopic NMR apparatus and the microscopic magnetic spins. To excite and manipulate the spins away from equilibrium as shown in Fig. 1.6, a carefully constructed B_1 field is required. Such fields are produced by driving oscillating RF current pulses, with carefully defined amplitudes and durations, through the B_1 coil windings. An oscillating current generates an oscillating magnetic field which in turn interacts with the $\vec{M}_0$ magnetic field vector. In reverse manner, the precessional magnetic flux from the $\vec{M}_0$ vector in Fig. 1.6 induces an oscillating current in the B_1 coil, which is measured by the NMR apparatus. A window is thus provided into the behavior of the spins.

A photograph of the Mole's planar B_1 RF coils was shown in Fig 1.5. Most NMR B_1 coils are solenoidal or saddle shaped and wrap around the sample in order to improve coupling between the B_1 coil and the spins. The Mole probe is a single-sided probe, or surface probe, so the B_1 coil is effectively two-dimensional. It is made from a printed circuit board (PCB) consisting of copper tracks on a fibre-glass substrate. Superimposed on the photograph is a three-dimensional solenoidal coil, located in a position that would provide a $\vec{B}_1$ field similar to the planar coil.

An arrow points along the x-direction, indicating the axis of the linearly oscillating $\vec{B}_1$ field. Unlike the $\vec{B}_0$ magnetic field which is relatively large and static, the B_1 magnetic field is small and oscillates close to the Larmor resonance frequency ω_0 of the magnetic spins. The design of the B_1 planar coil and associated circuitry is discussed further in §2.1.2 on page 29.

1.4.2 The rotating frame

The interaction between the precessing $\vec{M}_0$ magnetic field and the linearly oscillating $\vec{B}_1$ magnetic field is complicated, but is simplified by removing the time dependence. The usual technique for achieving this is to transform $\vec{M}_0$ and $\vec{B}_1$ from the stationary laboratory frame to a rotating frame which is rotating about the z-axis at the Larmor frequency. The first observation to be made within the rotating frame is the disappearance of the $\vec{B}_0$ field. This is understood from Eq. 1.21 where $\vec{B}_0$ is proportional to the precession frequency. The second observation is the behavior of the $\vec{M}_0$ vector. In the absence of the oscillating $\vec{B}_1$ field, $\vec{M}_0$ is stationary because it has no magnetic field about which to precess. This is also understood from Eq. 1.21.

1.4.2.1 The B_1 field

When the oscillating $\vec{B}_1$ magnetic field is switched on, an interaction occurs between the linearly oscillating $\vec{B}_1$ field and the $\vec{M}_0$ vector in the rotating frame. The presence of $\vec{B}_1$ provides a field for $\vec{M}_0$ to precess about, but in a complicated manner because $\vec{B}_1$ varies in time. This is simplified by treating the linearly polarized $\vec{B}_1$ field as two counter-rotating fields, one of which rotates in the same manner as the rotating frame, thereby appearing stationary in that frame. Separating the linearly polarized field into two counter rotating fields is described mathematically as:

$$\begin{aligned} 2B_1\cos(\omega_{\text{tx}}t)\vec{x} =& B_1[\cos(\omega_{\text{tx}}t)\vec{x} + \sin(\omega_{\text{tx}}t)\vec{y}] + \\ & B_1[\cos(\omega_{\text{tx}}t)\vec{x} - \sin(\omega_{\text{tx}}t)\vec{y}] \end{aligned} \tag{1.27}$$

where ω_{tx} is the frequency of the oscillations delivered to the B_1 coil by the RF transmitter (see Fig. 2.1 on page 28), $\vec{x}$ and $\vec{y}$ are cartesian basis vectors, and the two counter-rotating fields have strength B_1. When the angular frequencies $+\omega_{\text{tx}}$ and ω_0 are identical, B_1 in the rotating frame appears stationary, while the counter-rotating vector at angular frequency $-\omega_{\text{tx}}$ is distant from the Larmor resonance frequency and can be ignored.

1.4.2.2 The effects of magnet inhomogeneity

The description of the rotating frame given above implicitly assumes the $\vec{B}_0$ field is homogeneous. In reality however, all NMR magnets have some degree of inhomogeneity and shimming (adjusting DC currents in the shim coils) is often used to reduce inhomogeneities. The pseudo-homogeneous Mole probe however does not have this capability. In regions where the RF transmitter frequency is not identical to the rotating frame frequency ($\omega_{\text{tx}} \neq \omega_0$), a $\vec{B}_0$ component remains in the rotating frame, and in the absence of a $\vec{B}_1$ field, $\vec{M}_0$ will precess about it. When $\vec{B}_1$ is switched on, an effective field $\vec{B}_{\text{eff}}$ results from the vector sum of $\vec{B}_1$ and $\vec{B}_0$. $\vec{B}_{\text{eff}}$ is the field about which the bulk magnetization vector precesses while the $\vec{B}_1$ magnetic field is present. The effective field is calculated by first determining the difference between the Larmor and rotating frame angular frequencies:

$$\Delta\omega = \omega_0 - \omega_{\text{tx}} \tag{1.28}$$

then rearranging this equation and Eq. 1.14 to give:

$$\Delta B = \frac{\Delta\omega}{\gamma} \tag{1.29}$$

where ΔB is the reduced B_0 field in the rotating frame. Combining $\Delta\vec{B}$ along the z-axis and $\vec{B}_1$ along the x-axis results in an effective field $\vec{B}_{\text{eff}}$. This is the field that the bulk magnetization vector will precess about. The magnitude of $\vec{B}_{\text{eff}}$ is:

$$B_{\text{eff}} = \sqrt{(\Delta B)^2 + (B_1)^2} \tag{1.30}$$

giving a precession frequency about B_{eff} of:

$$\omega_{\text{eff}} = \gamma B_{\text{eff}} \tag{1.31}$$

and a tilt angle θ between the z-axis and B_{eff} of:

$$\theta = \tan^{-1}\left(\frac{B_1}{\Delta B}\right). \tag{1.32}$$

The effective field and the tilt angle are illustrated in Fig. 1.7.

1.4.2.3 Estimating the Mole's effective field

An estimation of the tilt angle and precession frequency over the Mole's active volume can be made by estimating (i) the $\vec{B}_1$ field strength and (ii) the B_0 field inhomogeneity. The Mole's $\vec{B}_0$ and $\vec{B}_1$ fields exhibit considerable spatial variation (Manz et al. (2006) [105]). According to Eq. 1.14 on page 8 the Mole's angular frequency ω_0 and therefore the effective field B_{eff} and precession frequency ω_{eff}

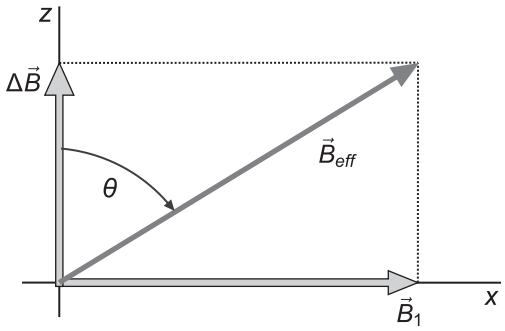

Figure 1.7: The effective field $\vec{B}_{\text{eff}}$ generated in the rotating frame from $\Delta\vec{B}$ along the z-axis and $\vec{B}_1$ along the x-axis. The tilt angle θ of $\vec{B}_{\text{eff}}$ depends upon the magnitudes of the two vectors.

must also vary spatially. Estimating the $\vec{B}_1$ field strength is possible using Prospa's Duration Sweep macro. Beginning with $\vec{M}_0$ at equilibrium along the z-axis, the pulse program turns on $\vec{B}_1$ for time τ, thereby tipping $\vec{M}_0$ away from the z-axis. The amplitude of the response is measured and the experiment is repeated using progressively longer τ values. Due to the orientation of the B_1 coil, the detected signal will be maximized when the transverse (or x-y) magnetization component is largest. This occurs when the magnetization $\vec{M}_0$ is tipped away from the z-axis by $\pi/2$ radians. $\vec{B}_1$ can then be calculated from:

$$\theta = \gamma B_1 \tau \tag{1.33}$$

using known values from the angle of rotation θ, magnetogyric ratio γ, and pulse time τ. Fig. 2.4 on page 32 shows typical settings for a CPMG experiment (refer to §1.6.2 for details) in which τ has been determined to be 40μs. Using this value for τ, the estimated B_1 field strength is:

$$B_1 = \frac{\theta}{\gamma\tau} = \frac{\pi/2}{(268 \times 10^6\,\text{rad}\cdot\text{s}^{-1}\cdot\text{T}^{-1}) \times (40 \times 10^{-6}\,\text{s})} = 147 \times 10^{-6}\,\text{T}. \tag{1.34}$$

The B_0 field spread over the Mole's sensitive volume due to inhomogeneity is around 50kHz ($\approx$ 1.17mT) (Manz et al. (2006) [105]). Assuming the inhomogeneity is spread equally either side of the Mole's Larmor frequency ($\omega_0 \pm$ 25kHz), the worst case frequency difference between the B_1 field ω_{tx} and the precession frequency of the most deviant spins is calculated using Eq. 1.28:

$$\Delta\omega = (2\pi \times 3.225\text{MHz}) - (2\pi \times 3.200\text{MHz}) = 2\pi \times 25\text{kHz}. \tag{1.35}$$

The reduced B_0 field in the rotating frame, ΔB, from Eq. 1.29 is thus:

$$\Delta B = \frac{2\pi \times 25\text{kHz}}{(268 \times 10^6\,\text{rad} \cdot \text{s}^{-1} \cdot \text{T}^{-1})} = 586 \times 10^{-6}\text{T} \tag{1.36}$$

therefore the effective field B_{eff} from Eq. 1.30 is:

$$B_{\text{eff}} = \sqrt{(586 \times 10^{-6})^2 + (147 \times 10^{-6})^2}\,\text{T} = 604 \times 10^{-6}\,\text{T} \tag{1.37}$$

giving a precession frequency from Eq. 1.31 about B_{eff} of:

$$\omega_{\text{eff}} = [(268 \times 10^6) \times (604 \times 10^{-6})]\,\text{rad} \cdot \text{s}^{-1} = 2\pi \times 25.8\text{kHz} \tag{1.38}$$

and a tilt angle θ between the z-axis and B_{eff} from Eq. 1.32 of:

$$\theta = \tan^{-1}\left(\frac{147 \times 10^{-6}\text{T}}{586 \times 10^{-6}\text{T}}\right) \approx 14^\circ. \tag{1.39}$$

These calculations provide useful insight into the behavior of $\vec{M}_0$ over the Mole's pseudo-homogeneous active volume. In spatial regions in which $\omega_{\text{tx}} = \omega_0$, it is seen that $\Delta B = 0$. In the presence of B_1, $\vec{B}_{\text{eff}}$ lies entirely along the x-axis and the bulk magnetization vector $\vec{M}_0$ precesses about the x-axis at frequency ω_{eff}. This frequency, calculated from Eq. 1.31, is around 6.3kHz. In regions where $\omega_{\text{tx}} \neq \omega_0$, precessional behavior is very different. In extreme regions where frequency deviation is ±25 kHz, switching B_1 on results in a $\vec{B}_{\text{eff}}$ vector tilted only 14 degrees away from the z-axis and $\vec{M}_0$ precessing around it at a frequency of around 26kHz. The contribution to the total NMR signal from different regions of the Mole's active volume is discussed in §2.4.9 on page 52.

1.4.3 Detecting the nuclear magnetization

Up to this point the bulk magnetization vector $\vec{M}_0$ has been shown to form in the presence of $\vec{B}_0$ and be manipulated by $\vec{B}_1$. Information on the microscopic content and dynamic behavior of the sample is contained within the precessing nuclear magnetization $\vec{M}_0$ vector and needs to be extracted.

Faraday's law of induction states that whenever a magnetic flux Φ through a loop varies in time, an EMF ξ is generated (Griffiths (1999) [65]):

$$\xi = -\frac{d\Phi}{dt}. \tag{1.40}$$

The precessing flux from the microscopic spins induces an EMF in the macroscopic B_1 coil due to the changing x component of the rotating magnetization. The induced EMF ξ is proportional to the rate of change of flux Φ, thus a larger signal requires a faster precession rate ω_0 that in turn requires a higher static field

strength. The detected signal from the Mole probe is therefore tiny in comparison to a high field NMR probe.

In addition to the tiny Faraday signal, the Mole's signal is further reduced due to the tiny bulk magnetization vector $\vec{M}_0$ discussed in Eq. 1.26 on page 11. Mathematically, the detected NMR signal is thus proportional to the square of the static field strength B_0, emphasizing the importance of field strength for purposes of detected signal strength.

Another factor that further reduces the detected signal from the Mole probe is the type of B_1 coil used for detecting the NMR signal. For maximum signal pickup the B_1 coil should be solenoidal and wrapped around the sample. The Mole's meander coil exchanges both of these requirements for the accessibility advantage of being a surface coil.

These are not the only problems encountered by probes such as the Mole. It will be explained in due course how the pseudo-homogeneous $\vec{B}_0$ field causes the tiny NMR signal to quickly decay away and how the nuclear magnetization needs to be regularly refocussed. This is not so problematic for high field NMR systems that have highly homogeneous $\vec{B}_0$ fields, however even these systems often require shimming in order for them to perform their desired functions.

The homogeneity of $\vec{B}_0$ also determines the kind of information that can be extracted from a sample. NMR signals detected from within a homogeneous field contain detailed spectroscopic information that cannot be obtained by pseudo-homogeneous probes such as the Mole. This is illustrated in Fig. 1.8 where (a) an exponentially-decaying sinusoidal FID signal from within a sample is detected in a B_1 coil then Fourier transformed revealing (b) spectroscopic information about the sample. The Mole probe cannot provide spectroscopic information from a sample, however it is well suited to obtaining relaxation information. This is the focus of the next section.

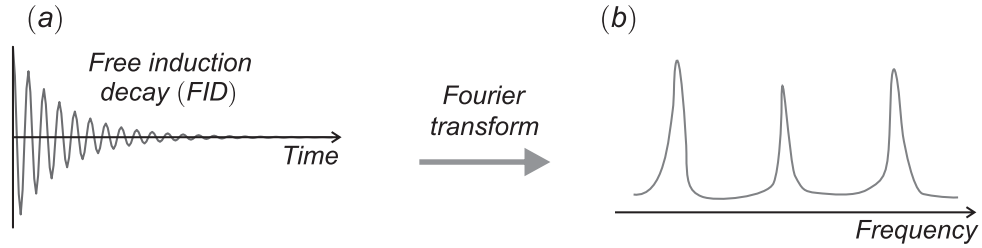

Figure 1.8: (a) A NMR FID signal resulting from a precessing magnetization being detected in the B_1 coil. (b) Spectral information about the sample contained in the FID signal and extracted by Fourier transformation. The pseudo-homogeneous Mole probe is unable to provide spectroscopic information.

1.5 Relaxation

Placing an NMR-active sample in a static magnetic field $\vec{B}_0$ results in the appearance of a bulk magnetization vector $\vec{M}_0$ as discussed in §1.3.1. The $\vec{M}_0$ vector does not appear instantaneously; rather it emerges gradually as the spins move from degeneracy toward a state of thermal equilibrium. Two important observations can be made regarding the equilibrium state: (i) the nuclear spin populations are described by the Boltzmann distribution as discussed in §1.3.1, and (ii) the transverse components of the magnetic moments precessing about $\vec{B}_0$ are randomly phased. In the equilibrium state, the bulk magnetization vector $\vec{M}_0$ is aligned along the $+z$-axis.

As explained previously, applying a B_1 RF pulse to the bulk magnetization vector $\vec{M}_0$ causes the vector to tip away from the z-axis whereupon it may be expected to precess indefinitely, however this is not observed experimentally. Indeed, given sufficient time, $\vec{M}_0$ returns back toward its thermal equilibrium state. The process causing the magnetic moments to return to thermal equilibrium is called relaxation and is a complex subject (Keeler (2005) [90]). As Callaghan notes: "Relaxation theory is complicated, requiring a deep understanding of quantum statistics" (Callaghan (1991) [26]). Relaxation will not be explained using quantum statistics; rather it will be explained in terms of the dipole-dipole coupling mechanism and T_1 and T_2 relaxation processes.

1.5.1 Dipole-dipole coupling

There are various mechanisms that cause nuclear spin relaxation. In the context of this thesis, the relevant mechanism is through-space dipole-dipole (D-D) coupling (Claridge (2004) [37], Levitt (2008) [93], Homans (2002) [78]). D-D coupling can be likened to two bar magnets, each with a north and south pole, interacting with each other through their localized fields. When far apart, their mutual influence is minimal, but when brought together, each affects the other, depending upon orientation and proximity. In real NMR samples, the magnetic dipole moments are moving about rapidly due to thermal motion. Each magnetic moment therefore experiences rapid field fluctuations from neighboring spins. It is the presence of fluctuating fields at the site of a nucleus that provides the relaxation mechanism.

Two relaxation processes emerge from the D-D interactions. The first process is T_1 relaxation, otherwise known as spin-lattice or longitudinal relaxation. The second relaxation process is T_2 relaxation, otherwise known as spin-spin or transverse relaxation. T_1 and T_2 refer to the time constants of the exponential relaxation functions, therefore they represent the efficiency of the relaxation mechanism. The reciprocal of the relaxation times are sometimes preferred; these are the relaxation rates and are defined as $R_1 = 1/T_1$ and $R_2 = 1/T_2$.

1.5.2 T_1 relaxation

Applying a Larmor frequency RF pulse to a spin system at equilibrium perturbs the magnetization $\vec{M}_0$. According to Eq. 1.15, this adds energy to the spin system. Returning the spin system to equilibrium requires that energy be removed. The T_1 relaxation process is responsible for removing energy from the spins and driving the z magnetization back to the Boltzmann populations. Energy transfer is between the spins and the surrounding lattice, which is the molecular motions, through mediating local magnetic fields (Keeler (2010) [90]). Spontaneous emission is not the mechanism of energy loss from the spins to the lattice since the probability of emission is proportional to the third power of the frequency ω. At low NMR frequencies, this probability is effectively zero (Griffiths (1995) [64], Fukushima (1981) [59], Levitt (2008) [93]). The energy transfer is non-radiative and in thermodynamic terms is an enthalpic (or nonadiabatic) process. This is in contrast to T_2 relaxation which will be seen in due course to be an entropic process (Homans (2002) [78], Cavanagh (2007) [32]).

T_1 relaxation occurs when two conditions are met: (i) the nuclear site of the relaxing spin experiences a fluctuating field at its Larmor frequency, and (ii) the fluctuating field has a transverse component capable of rotating the magnetic moment toward the z-axis. A fluctuating field at the Larmor frequency can therefore change the angle between the magnetic moment and the z-axis by moving the magnetic moment to a place of lower energy. According to Keeler, magnetic moments in mixed states can take any angle with respect to z (Keeler (2010) [91]).

1.5.3 T_2 relaxation

Applying a $(\pi/2)$ RF pulse to a spin system at equilibrium tips the bulk magnetization vector $\vec{M}_0$ into the transverse plane. It also causes the magnetic moments forming $\vec{M}_0$ to share a common phase in the transverse plane, often called a state of phase coherence. The task of the T_2 relaxation process is to drive the magnetic moments from coherently precessing about $\vec{B}_0$ to the maximum entropy state in which their phases are randomized.

There are two ways the D-D interaction can alter the phase of a precessing magnetic moment (Keeler (2010) [91]). The first is for the magnetic moment to experience a fluctuating field in the transverse plane at its Larmor frequency. In likeness to §1.4.2, a magnetic field with an x component can change a magnetic moment's y component and vice versa. Such an interaction also changes the z magnetization, therefore there will be an energy exchange between the magnetic moments. The second way a D-D interaction can alter a magnetic moment's phase is by changing the $\vec{B}_0$ field it experiences. This happens if the D-D interaction changes the z component of magnetization, thereby causing the magnetic moment

to experience a different $\vec{B}_0$ field strength. From Eq. 1.21, this changes the precession frequency of the magnetic moment. In this interaction, the z component of magnetization remains unaltered and no energy exchange occurs between the magnetic moments.

Both of these interactions, sometimes called non-secular and secular respectively, cause the precession frequencies of the magnetic moments to deviate randomly from ω_0, thus leading to loss of phase coherence.

The frequency of the fluctuating z fields is important in terms of the secular contribution to the T_2 relaxation time. If the local z fluctuations are rapid, variations are averaged over the magnetic moments and de-phasing is inefficient. This results in long T_2 relaxation times. If the z fluctuations are slow, the relaxation is much more efficient, resulting in short T_2 relaxation times. This means that T_2 relaxation is extremely sensitive to slow (secular) molecular motions (Callaghan (1991) [26]).

1.5.4 T_2^* relaxation

It was seen in §1.5.3 that slow z-direction field fluctuations reduce the T_2 relaxation time. The cause of this was random spatial variations in $\vec{B}_0$ which changed the precession frequency of the spins. Another factor causing changes in precession frequency is $\vec{B}_0$ magnetic field inhomogeneity. This results in the intrinsic relaxation time T_2 being shortened to an effective relaxation time T_2^*.

T_2^* is important because it is the experimentally observed T_2 relaxation time. T_2 cannot be directly measured in an inhomogeneous field, however T_2 information is contained in the measured T_2^* data, along with information about the homogeneity of the static $\vec{B}_0$ field. By removing the magnetic field inhomogeneity contribution, the original T_2 information may be extracted from T_2^*. This is possible because the static $\vec{B}_0$ field inhomogeneities do not vary randomly in time. Accumulated phase variations in the precessing magnetic moments can be removed by reversing the precession direction of the spins. The technique for achieving this is discussed in §1.6.

1.6 Spin-echoes

The final section of this chapter deviates from NMR theory to focus upon the necessity of spin-echo techniques. These are necessary when the NMR probe's B_0 field is inhomogeneous for the reasons discussed in §1.5.4.

Fig. 1.9(a) shows a spin-echo pulse sequence consisting of two RF pulses. The $(\pi/2)_x$ and $(\pi)_y$ labels show the angle in radians that the magnetization $\vec{M}_0$ is rotated through due to the RF pulses. The subscripts x and y are the axes about which the magnetization is rotated. Immediately following the first pulse is the

response FID generated from within the sample. This signal dies away quickly as the spins de-phase and cannot be easily detected using the Mole probe due to probe and pre-amplifier dead time. After a user-defined time period following the FID, a second RF pulse is applied. This pulse causes the magnetization of the spins to rotate though twice and angle of the first pulse. Some NMR systems achieve this by doubling the length of the (π) pulse; in the case of the Mole probe, Prospa doubles the amplitude of the (π) pulse to achieve the same ends. After a time period beyond the second pulse the re-phasing spins generate a echo response signal as shown.

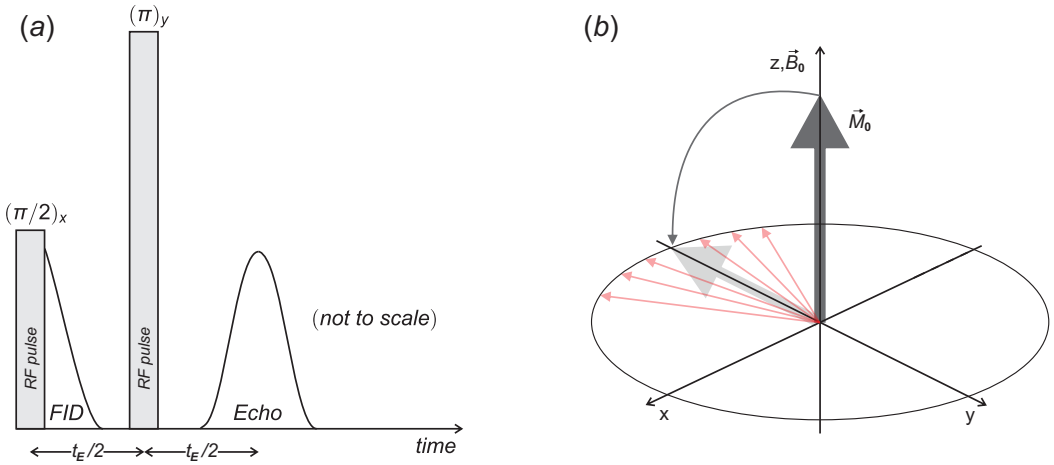

Figure 1.9: (a) The spin-echo pulse sequence consists of two RF pulses. The actual amplitudes of the FID and echo response signals would be several orders of magnitude smaller than the RF pulses. (b) The bulk magnetization vector $\vec{M}_0$ responding to the $(\pi/2)_x$ RF pulse in the rotating frame. The magnetic moments thereafter spread out in the transverse plane as they lose phase coherence.

The time between center of the ($\pi/2$) and (π) RF pulses is identical to the time between the center of the (π) pulse and the peak of the spin-echo. In Prospa, this time is defined using the Echotime parameter (t_E) as shown in Fig. 2.4 on page 32. The two time periods just mentioned each have length ($t_\mathrm{E}/2$) for reasons that will become obvious in §1.6.2. The preferred Echotime value in most experiments on the Mole is 500μs for reasons intrinsic to the design of the Mole probe and the sample being studied.

If the spin-echo experiment shown in Fig. 1.9 was to be repeated, a time period equalling five T_1 time constants should generally be observed between experiments in order to allow the spin system magnetization to return to equilibrium.

Fig. 1.9(b) shows how the bulk magnetization vector $\vec{M}_0$ responds to the $(\pi/2)_x$ RF pulse in the rotating frame. The B_1 pulse causes $\vec{M}_0$ to rotate about the x-axis, tipping away from the z-axis and onto the $-y$-axis in the transverse plane. After being tipped away from the z-axis the magnetic moments fan out as they lose phase synchronization. This is the cause of the FID signal decay shown in Fig. 1.9(a).

The effect of the second RF pulse is not shown in the figure. This pulse rotates the de-phased spins by π radians about the y-axis causing them to re-phase. By analogy this is like a room full of clocks. The $(\pi/2)$ pulse synchronizes all the clocks, but over a long time period some of the clocks run a little fast and others a little slow. The (π) pulse effectively leaves the hands wound in the opposite direction by twice the amount they had travelled in the first time period. The clocks then continue to run fast or slow so that after another identical time period they are temporarily synchronized once more.

1.6.1 Ring-down and recovery time

One of the benefits provided by the spin-echo technique is the ability to measure the NMR signal at a user-defined time beyond the RF refocussing pulse. There are two reasons why this is important.

First, the B_1 coil is used for both excitation of the sample and detection of the NMR signal. Immediately following an RF pulse, residual energy from the pulse remains in the B_1 tuned circuit. Before sampling of the tiny FID can begin, most of the energy in the tuned circuit needs to be dissipated. As a rule-of-thumb this ring-down time requires around twenty oscillation periods at the resonant frequency (Andrew and Jurga (1987) [15]). For a 500MHz NMR system this is around 40ns; for the Mole it is around 6.25μs.

The second related reason is that in addition to the probe ring-down time, the receiver pre-amplifier has a recovery time during which it is unable to amplify the minute NMR signal. The recovery time of the pre-amplifier used in the this project is around 25μs which is four times longer than the ring-down time. This is discussed further in §3.7 on page 81.

To put these times into perspective, it is necessary to know the temporal length of the FID. For the Mole, a FID typically lasts around 50μs before the signal reaches the level of the noise. Losing the first 25μs, or even 6.25μs, of the FID means the largest part of the decaying signal is gone before detection begins. The spin-echo technique alleviates this problem by enabling the spin-echo to appear beyond the dead-time of the probe and pre-amplifier. Of course, extending the echo timing between the RF pulses may introduce wanted or un-wanted diffusive effects as seen in §6.2 on page 192.

1.6.2 T_2 CPMG macro

Fig 1.10 shows a CPMG (Carr-Purcell-Meiboom-Gill) pulse sequence. This sequence is widely used for experiments involving grossly inhomogeneous and pseudo homogeneous fields due to its ability to extract otherwise unobtainable T_2 information from fast decaying FID signals. The CPMG sequence extends the spin-echo pulse sequence by adding a few or even many thousands of (π) refocussing pulses. Unlike its Carr-Purcell (CP) predecessor, the CPMG sequence changes the phase of the (π) pulses following the $(\pi/2)$ pulse from rotations about the x-axis to rotations about the y-axis on order to avoid cumulative errors resulting from a slight adjustment of the flip angle (Martin et al. [106]).

The FID response signal is shown with a time constant T_2^* that is considerably shorter than the T_2 time constant. Calculation of T_2 is achieved by fitting one or more superimposed decaying exponentials to the echo peaks, or in some cases to echo integrals. (The Terranova-MRI system measures the integral under the spectral peak in order to eliminate wide-band noise (Magritek [99]).) The intrinsic T_2 relaxation time of the spin system is thus obtained from echoes containing effective T_2^* relaxation time information.

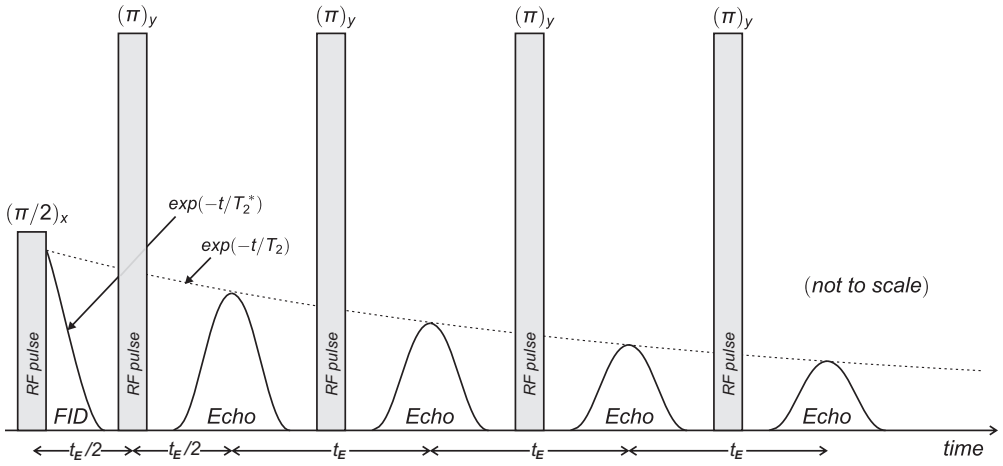

Figure 1.10: The CPMG pulse sequence consists of a $(\pi/2)_x$ RF pulse followed by a train of $(\pi)_y$ refocussing pulses. The actual amplitudes of the FID and echo response signals would be several orders of magnitude smaller than the RF pulses. The intrinsic transverse relaxation time T_2 is measured by fitting one or more decaying exponentials to the chain of spin-echo signals.

The timing of the RF pulses used in the CPMG pulse sequence is similar to the spin-echo sequence. Samples such as oil or rubber in which the T_2 times are very

short require only a small number (perhaps tens or hundreds) of refocussing pulses. By contrast, water has a long intrinsic T_2 time and requires many thousands of refocussing pulses to measure T_2. One practical problem caused by large numbers of refocussing pulses is discussed in §2.4.10 on page 56.

CHAPTER 2

Experimental apparatus

The aim of this chapter is to examine the NMR apparatus used during this project. The first part of the chapter introduces the basic NMR apparatus. This is followed by an examination of the difficulties encountered in getting the apparatus to operate satisfactorily, and solutions to the difficulties. A series of experiments used to understand the behavior of the apparatus are described. A few of the many problems encountered are explained, followed by suggestions for future research and development.

2.1 The basic apparatus

The NMR apparatus used in this project is shown in schematic form in Fig. 2.1. The Kea spectrometer, Mole probe, Prospa software, and laptop computer were supplied at the beginning of the project. The remaining apparatus was built during the project. The supplied apparatus provided the basic NMR tools necessary to perform experiments. The additional apparatus was necessary to ensure experimental data was attainable and repeatable. The basic apparatus will now be described; the additional apparatus will be examined in due course.

2.1.1 Kea spectrometer

The Kea spectrometer was designed primarily by Robin Dykstra for his PhD thesis (Dykstra (2006) [52]). In Dykstra's thesis the spectrometer was named ModSpec, and changed to Kea during subsequent commercialization. The Kea spectrometer is at the center of the NMR apparatus, inter-connecting the laptop computer, Prospa software, Mole probe, and high-power RF amplifier (HPA) as shown in

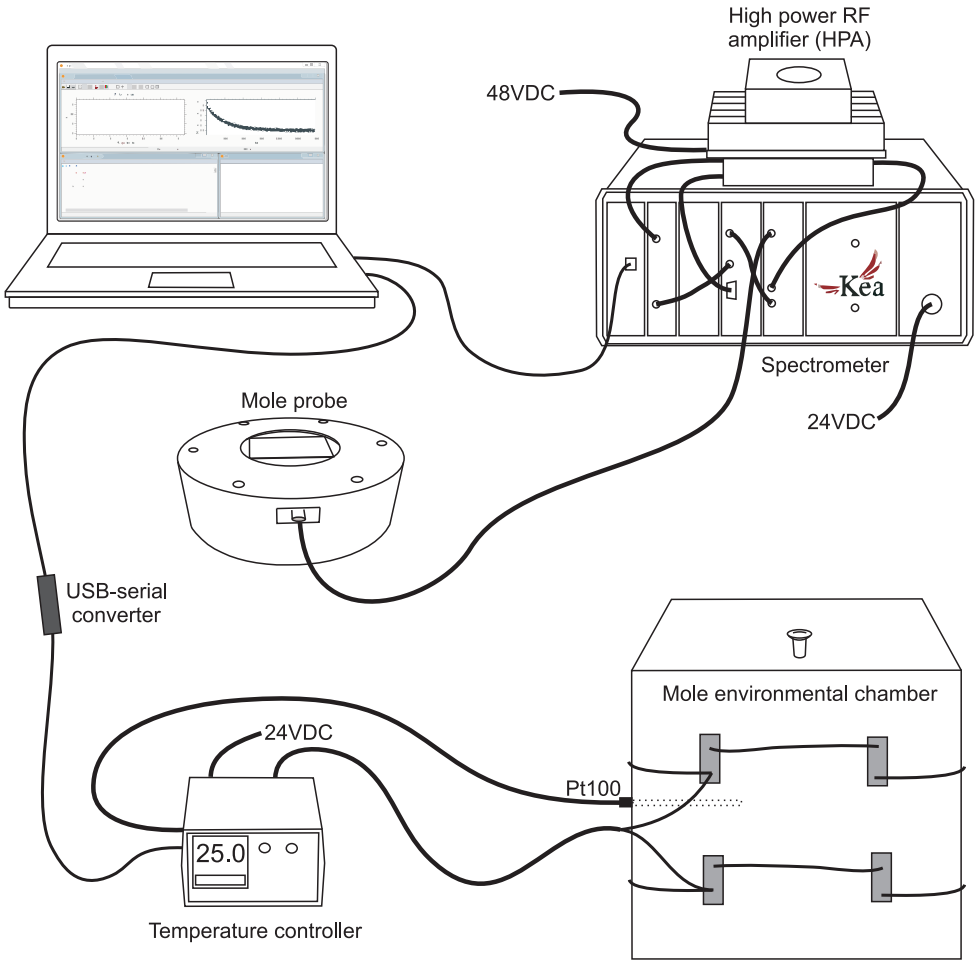

Figure 2.1: The NMR apparatus showing the various modules and their interconnections. The computer and Prospa software, spectrometer, high power RF amplifier and Mole probe were supplied for this project. The temperature controller and environmental chamber were built during the project. The spectrometer modules from left to right are: digital signal processor, digital transceiver, empty slot, digital receiver, pre-amplifier duplexer, high power RF amplifier (internal, not fitted), power supply.

Fig. 2.1. The Kea spectrometer was designed to accommodate an internal HPA but no suitable module was available at the beginning of the project, thus an external commercial HPA was used instead as shown (Tomco [148]). The spectrometer modules are discussed in detail in Dykstra's thesis.

The external HPA was connected to the Kea spectrometer by two 50Ω RG-316 coaxial cables. One cable carried low power signals from the spectrometer to the HPA. The other carried the amplified signals from the HPA back to the pre-amp duplexer (PAD) module within the Kea spectrometer. A third signaling cable carried a logic level gate signal from the Kea front panel DB-9 connector to the HPA in order to control the output on/off state of the HPA output stage. A large fan was mounted on top of the HPA's heat-sink to reduce the possibility of amplifier overheating.

During the course of this project, a number of spectrometer upgrades were performed. For example, the DSP module was upgraded from version 2.1 to version 3.0 and finally to version 4.0. The newer DSP modules extended the onboard memory for storing in-phase and quadrature NMR data from 32k×24bits to 256k×24bits, thus enabling significantly more data to be recorded during an experiment. The spectrometer USB communications port was also upgraded from USB 1.1 to USB 2.0, thereby dramatically increasing the data transfer rate between the spectrometer and laptop. These upgrades made some NMR experiments significantly faster and the extra memory meant that valuable data never needed to be discarded. Experiments that were formerly not possible due to fast repetition time requirements now found a new speed bottleneck in Prospa rather than the USB communications port.

Various other upgrades were performed during this project in order to improve various aspects of the apparatus. The pre-amp duplexer module underwent significant development which is discussed in detail in Chapter 3.

2.1.2 The Mole probe

The Mole probe (MObile Lateral Explorer or MObile Liquid Explorer) is a compact integrated NMR sensor (Manz et al. (2006) [105]). Due to its design the Mole is ideally suited to measuring relaxation and diffusion within soft materials. The Mole's static B_0 magnetic field is normal to the center of the top surface of the probe. The residual induction causing B_0 is due to seventeen rare earth neodymium-iron-boron (NdFeB, or NIB) magnets. The magnets are arranged as eight pairs in a ring within the Mole's Perspex block and tilted inwards toward the seventeenth magnet which resides in the center of the Mole near the top surface. Some of the magnets can be seen within the Perspex former is Fig. 2.2. The Mole's oscillating B_1 magnetic field is generated by RF pulses from the HPA and the B_1 electronic circuitry shown in Fig. 2.2 and schematically in Fig. 2.3.

Figure 2.2: The Mole probe and tune/match circuitry used for most of this project. This is not the original Mole probe supplied for this project as will be discussed in the text. Sample vials and Perspex vial holders are discussed in §2.4.9 on page 52. Some of the NIB magnets can be seen located in pairs inside the Mole's Perspex former. The lone central magnet is located beneath the sample vial and B_1 coil.

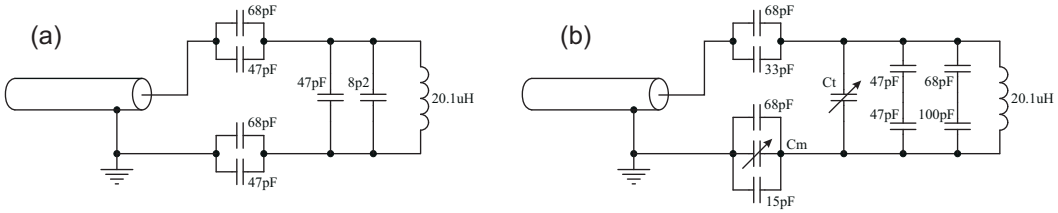

Figure 2.3: (a) The original Perspex Mole probe B_1 circuit. (b) The modified B_1 circuit with tune/match capacitors C_t and C_m added. The DC resistance of the inductor was 2.0Ω at 25°C.

The precession frequency for protons on the Mole probe is around 3.2MHz at room temperature. From Table 1.1 on page 5 the magnetogyric ratio γ for a proton is around 268×10^6 rad·s^{-1}·T^{-1} (or 42.6 MHz·T^{-1}) therefore the flux density of the Mole's B_0 magnetic field is approximately 75mT.

The Mole probe originally supplied for this project did not function properly so was replaced with the prototype Perspex-bodied Mole shown in Fig. 2.2. This probe was developed by Mark Hunter and Bertram Manz between 2000 and 2005 (Manz et al. (2006) [105]). Hunter engineered the electromagnetic design and modeling of the Mole's magnet array; Manz put the Mole together and developed the B_1 RF circuitry.

Other variations of this Mole probe were also developed with operating frequencies ranging from 400kHz to 3.3MHz and with homogeneous-regions from 15mm to 50mm above the probe's surface. Subsequent developments have resulted in a new 2008 design operating at 5.1MHz with homogeneous-region 5mm beyond the probe's surface [3]. The behavior of the Mole probe used in this project will be examined further in due course.

2.1.3 Prospa software

Prospa is a Microsoft Windows software application written by Craig Eccles (Magritek [98]). During the course of this project Prospa was run extensively atop Windows XP Professional, Windows Vista and Windows 7. Prospa's graphical user interface (GUI) was generally used to configure and execute NMR experiments using built-in and custom designed macros. The GUI window for a CPMG macro is shown in Fig. 2.4 with typical setting used during this project.

Prospa provides a built-in text editor and comprehensive scripting language that enables the experimenter to write custom macros and pulse programs. Several macros were written and used during this project; an example is given in Appendix C. Prospa macros generally send a pulse program from the computer

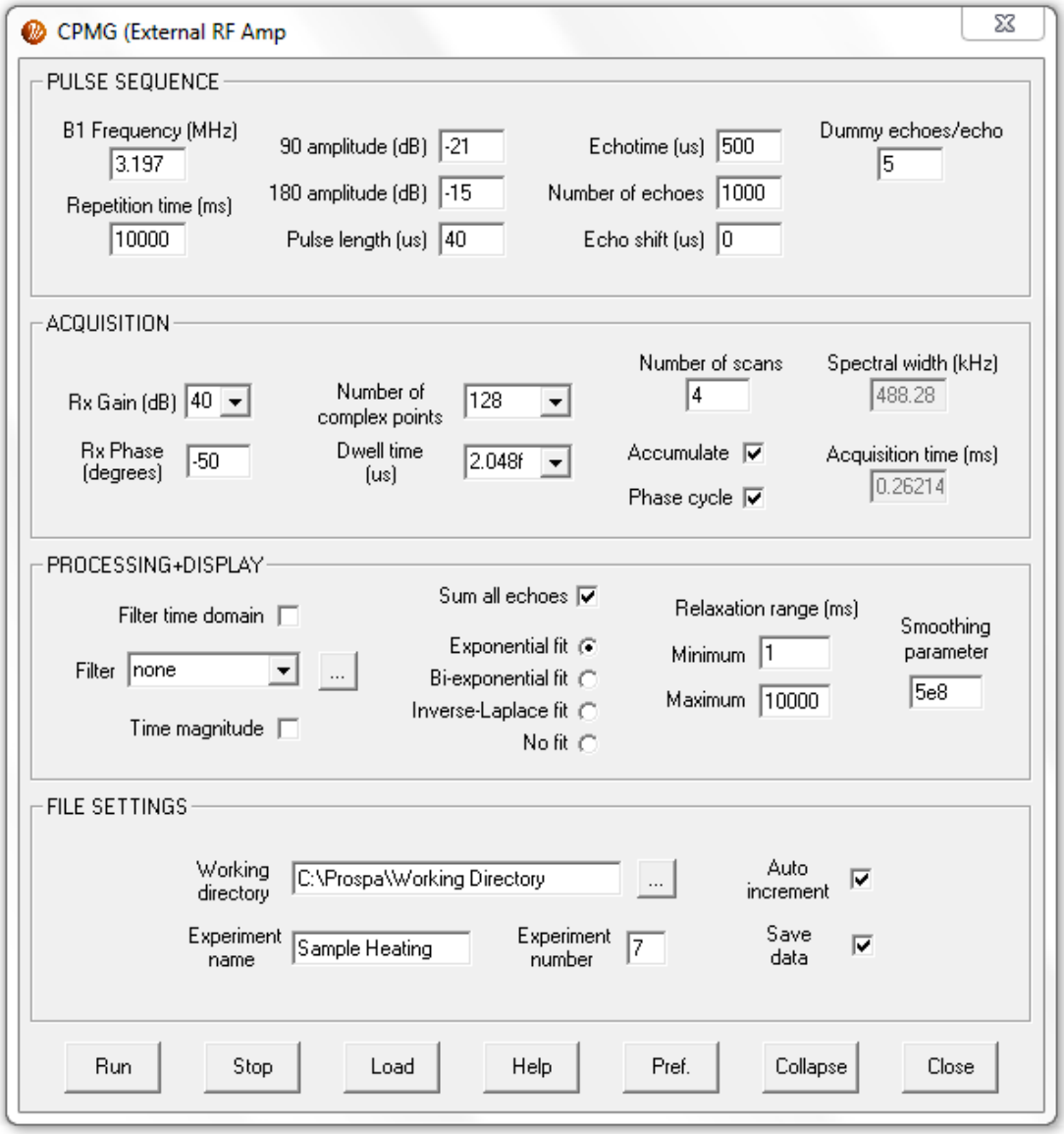

Figure 2.4: CPMG macro GUI showing typical settings used during this project. The –15dB setting equates to around 29.7V_{RMS} across 50Ω.

to the spectrometer for execution. Following pulse program execution the Prospa macro collects the experimental data from the DSP module. The data may then be saved to the computer hard drive, plotted, curve fitted and/or analyzed within the Prospa environment. Prospa macros generally save experimental data in comma separated value (CSV) format for importing into other software packages. Microsoft Excel and OriginLab were used extensively during this project to analyze and display CSV data. Prospa macros also generally save the experimental parameters accompanying each experiment.

Prospa was regularly updated during the course of this project. Of particular benefit was the addition of backdoor macros which provided the functionality required to automate the execution of other macros in sequential order without user intervention. This proved essential for many repetitive experiments that could previously not be executed at specified times using different experimental parameter sets.

2.2 Preliminary use of the apparatus

The supplied NMR apparatus was initially assembled on a lab desk located in Massey University Science Tower C1.03. Linear power supplies were used to power the HPA and spectrometer. The Mole probe was situated on a solid cardboard box around 200mm above a lab bench, away from the bench's metal framing. A 200MHz Oxford horizontal bore magnet was located about 6m away, and three Bruker magnets (400MHz, 500MHz and 700MHz) were located between 6m and 10m away. The magnetic field from the horizontal bore magnet could be observed near the Mole with a Magnaprobe (3D compass); the measured field strength was about three orders of magnitude less than the Mole's B_0 field. The two closest Bruker magnets were magnetically shielded and were oriented with the main field running vertically thus reducing the stray field.

Initial testing of the NMR apparatus using a spin-echo experiment showed a very poor signal-to-noise ratio (SNR) however it was unknown at the time whether this was due to a good signal buried in noise, or a poor signal, or both. It was assumed the supplied Mole probe was working so elimination of noise seemed a more reasonable starting point than looking for tiny NMR signals from the probe. In addition the pre-amp duplexer module was under heavy development and was a potential source of signal and noise problems.

2.2.1 Improving the signal-to-noise

Improving the signal-to-noise began with attempts to minimize electrical noise entering the apparatus. This was achieved by ensuring that various parts of the

apparatus were connected to a common ground potential. To minimize coupling between modules in the spectrometer, aluminium plates of similar size to the spectrometer modules had previously been cut and mounted onto rails between each pair of modules. Each plate was grounded to an aluminium chassis rail at the rear of the spectrometer. The spectrometer's aluminium front panel faceplates were powder coated during manufacture. The powder coating provided an insulating layer between the plates and the spectrometer's aluminium chassis rails, and between the plates and printed circuit board mounts. The powder coat insulation was removed from various places with a grinder to ensure the aforementioned parts were all grounded. To minimize pickup through the coaxial cable connecting the spectrometer and Mole probe, an additional braided conductor was removed from another coax cable and fitted over the existing cable and grounded at one end.

2.2.2 The defective Mole probe

The grounding and shielding of the NMR apparatus described above may have improved the shielding, but it did not improve the signal-to-noise of the system. Moving the apparatus to the 5th floor electronics lab away from the other NMR systems also made no obvious difference to the signal-to-noise. Eventually the primary source of the poor signal-to-noise ratio was found to be a defective magnet within the Mole probe which was presumably distorting the pseudo-homogeneous B_0 field. This was initially confirmed by connecting a working Mole probe to the spectrometer and observing good quality signals from a sample. The B_0 field from the damaged probe was then mapped leading to the conclusion that at least one magnet within the array was sub-optimal. The faulty probe had a signal-to-noise ratio of slightly less than three; this was five to six times less than the prototype Mole used for the remainder of this project. In hindsight the signal-to-noise diagnosis could have been much more efficiently undertaken by systematically exchanging the various components in the system with known working components.

2.2.3 Switching regulator problems

After the defective Mole probe had been replaced with the prototype Perspex-bodied Mole, a visible single shot spin-echo signal was attainable in the Massey lab. However spectrum measurements using Prospa indicated that large transients were still present, separated by around 150kHz in the frequency spectrum, therefore a 150kHz source was sought. The only switching regulator present in the NMR system at that time was a National Semiconductor LM2599, located on the power supply module, with a switching frequency of 150kHz (National Semiconductor [133]).

To test whether this indeed was the source of interference it was necessary to temporarily replace the LM2599 switching regulator with a linear regulator. A

spare spectrometer backplane printed circuit board was laid flat on the lab bench and the modules plugged vertically into it. This allowed easy access to the power supply module. With all modules plugged in however the switching noise was no longer present in the Prospa spectrum even with the LM2599 still operating. Fitting the modules back into the spectrometer chassis made the switching noise re-appear.

The 150kHz interference was only present when the modules were plugged into the spectrometer box, so the box and chassis were slowly disassembled to determine the cause. The metal plates between the modules were removed. Insulating tape was used to insulate the metal front panels from the chassis. The cooling fans on the base of the chassis were disconnected. The aluminium chassis was then slowly dismembered, until removal of a screw broke a conductive loop within the chassis resulting in disappearance of the switching noise. Evidently an oscillating magnetic flux generated by the LM2599 circuitry was generating a current in the chassis which was in turn generating a magnetic field that was coupling to the pre-amp duplexer module. The pre-amp duplexer module used at this time was a prototype based around a commercial pre-amplifier (Advanced Receiver Research [126]). In hindsight the design of the module was far from optimum and especially susceptible to noise pickup. Soldering a tin enclosure over and under the switching regulator components attenuated the switching transients sufficiently at their source that they were no longer visible in Prospa's frequency spectrum.

Significant electromagnetic interference (EMI) was still present in the Massey lab. The results from a single shot spin-echo experiment were compared with a measurement using similar apparatus at Magritek's premises in Wellington. Evidently the Massey lab environment was very electrically noisy compared to the Magritek environment. The noise being detected in the Mole's sensitive B_1 tuned circuit was not surprising given the close proximity of electrical power and signal cabling that circled the lab, and other nearby noise sources such as several large NMR systems, several air-conditioning units, a lift, a mechanical workshop, and a radio station.

2.2.4 Temperature instability

In addition to EMI, temperature was also a problem for the NMR apparatus. Variations in lab temperature were expected to cause the Mole's B_0 field to vary with time due to the non-zero temperature coefficient of the Mole's permanent magnets. The lab air-conditioner was old and struggled to maintain a constant temperature, and was often adjusted by the lab occupants. In addition, air circulation within the lab was poor and there was often localized heating from sunlight streaming through the lab windows.

The extent to which the temperature variations would affect experimental results was unknown at this stage, so the first step was to quantify the variation in temperature around the Mole. To achieve this, a EL-USB-1 temperature logger was placed around 300mm above the Mole and left to record data for four days between the 28th August and 1st September 2008 (Lascar [53]). The results showed the temperature was cycling every 24 hours, reaching a minimum of 15.5°C and maximum of 22.5°C. It was unknown whether the air-conditioner's set temperature was adjusted during the measurement period, and it was a moot question in any case because the experiment needed to measure realistic temperatures that the Mole would experience.

While temperature variations were being observed, B_0 variations were also measured using Prospa's CPMGFreqSweep macro. The results indicated that the lab temperature was indeed altering the residual induction of the Mole's magnets and causing the proton Larmor frequency to drift. There was not an immediate correlation between temperature and B_0 however due to the thermal lag of the Mole's magnets.

Calculations revealed the effect a 7°C temperature change would cause in terms of proton Larmor frequency. The temperature coefficient of the magnets was specified by the manufacturer as $-0.11\%/°C$ thus the proton Larmor frequency change would be around 25kHz (Macmill Magnets [97]). This is discussed further in §2.4.6 on page 49.

2.3 Solving the EMI and temperature drift problems

At this stage in the project EMI had proven to be a formidable challenge. Electrical noise appeared to have multiple entry points into the apparatus and was proving difficult to eliminate. The Mole probe was placed inside an old grounded copper hot water cylinder inner but this had made no difference to noise pickup. The power rails for the various modules were still powered from linear power supplies to minimize power supply noise. The cabling between the Mole probe and pre-amplifier duplexer module had been dual shielded. The noise must have been entering through the Mole probe, or through the pre-amplifier duplexer, or both. A solution involving shielding the Mole probe and stabilizing the temperature is now discussed.

2.3.1 Investigating Mole EMI shielding

Shielding the Mole probe against EMI required placing the probe within a grounded conductive casing. A technique that had previously been observed at Victoria

University to significantly reduce noise pickup in the Earth's Field NMR probe was to place the probe inside an open ended rectangular tunnel made from thick copper plates.

A quotation from a local company for 12mm copper plate was around \$2000/m^2 (Mike Christie Sheetmetals Ltd [2]). Constructing a similar but larger copper box for the Mole probe was not an option due to expense, so aluminium plate was considered instead. 5083 grade aluminium with 0.4% iron content was available so a sample was obtained and tested for magnetic properties using a 1T magnet but none was evident. A quote from the same company for six pieces of 5083 aluminium plate 500mm×500mm×12mm was \$490 with cold-cutting to a resolution of 0.1mm an additional \$240.

While the cost of aluminium was significantly less than copper, the conductivity of copper was higher (6.45×10^7 S·m^{-1} compared to 4.00×10^7 S·m^{-1}) thus providing greater attenuation against incident electromagnetic radiation. The attenuation is measured in terms of skin depth δ (Ludwig and Bretchko (2000) [96]):

$$\delta = \frac{1}{\sqrt{\pi f \mu \sigma_{\text{cond}}}} \tag{2.1}$$

where f is the frequency of the incident electromagnetic wave in Hz, μ is the permeability of the metal in H·m^{-1}, and σ_{cond} is the conductivity of the metal in S·m^{-1}. The value of μ is $4\pi\times10^{-7}$ H·m^{-1} since the dimensionless μ_r is close to unity for both paramagnetic aluminium and diamagnetic copper (Young (1979) [161]). At the Mole's operating frequency, $\delta = 0.035$mm for copper and $\delta = 0.044$mm for aluminium.

While copper would have provided better shielding than aluminium, the difference was not important given the ratio of δ to the thickness of the plate. Also important was the density of copper which is significantly greater than aluminium making it less suitable for portable equipment. Aluminium has a density of 2.7×10^3 kg·m^{-3} compared to 8.9×10^3 kg·m^{-3} for copper (Young (1992) [162]). The Mole box dimensions above would require around 17.5kg of aluminium compared to 57.5kg of copper. 12mm aluminium plate was readily available and suitable for making a sturdy box, although thinner aluminium plate would have sufficed for shielding purposes.

2.3.2 Investigating temperature control options

Assuming a Mole box built from the materials described above, the next problem to solve was how to maintain a lock between the proton Larmor frequency and the B_1 tuned circuit frequency. One method for achieving this was to lock the temperature of the Mole probe magnets by maintaining a constant temperature inside the aluminium box. An alternative method could have been to allow the magnet

temperature to drift and automatically adjust the B_1 tuned circuit frequency to track the B_0 frequency. This could possibly have been achieved by designing a tuning capacitor with temperature coefficient to match the magnet drift. This was an interesting option but better suited to a future research project.

To lock the temperature of the Mole's magnets, the first technique considered was locating the Mole box in a water bath. A water bath was available from the chemistry department with a milli-Kelvin temperature control system. While this may have provided excellent temperature control the apparatus would have become non-portable and uncomfortably close to water. An alternative technique was to use a console-style air-bath unit. Water would not be problematic but the available unit was large and the electrical power components and pumps were located near the location of the noise-sensitive Mole. The air bath was also non-portable.

Heating the aluminium Mole box using copper tubing and a small commercial water bath was considered. The tubing would have been attached to the outside of the Mole box using 3M DP190 Grey Epoxy Adhesive or 3M 9713 Electrically Conductive Tape. Copper piping was readily available and could be bent to the required shape. Water would then be passed through the pipes and the Mole could be heated and cooled over a wide the temperature range. The water bath could be located in another room resulting in minimal electrical or audible interference. The downsides of this technique were introduction of water and piping, maintenance of the water bath, and loss of portability.

An alternative to the previous solutions was to use electrical components to control the temperature. Electronic temperature controllers were widely available from manufacturers such as Omron [113] and Cal [40] and came with many options. For example, they could be powered from 12V, 24V or 240V. Output controls for switching heating and cooling elements on and off included relay contacts, solid state relays (SSR), and voltage and current outputs. Temperature sense inputs were available for Pt100 platinum resistance thermometers and thermocouple sensors. An RS-485 serial communication port was available on some controllers thereby allowing the controller to be configured and data logged using a computer. Temperature regulation in these controllers is typically performed using built-in proportional-integral-derivative (PID) software algorithms, and built-in auto-tuning could be used to determine the optimal PID coefficients for a given environment. These controllers could be purchased locally at a cost of several hundred dollars.

Various heating and cooling components that could be controlled by the temperature controller were also available. The first electrical heating component to be considered was an incandescent lightbulb mounted inside the Mole box. This would have provided a heat source, but wiring entering the Mole box was observed in other situations to behave as an antenna to the sensitive Mole B_1 coil. A better alternative would have been to heat the Mole box from the outside using large

adhesive heating mats attached to the sides of the aluminium enclosure. The heater mats would cover a large part of the surface area of the Mole box causing relatively even heating and would be low-profile and non-obtrusive. Unfortunately the price for 200mm×150mm 12V 30W heater mats was around $100 each (RS 731-366) with at least four mats required.

An alternative to heating mats was power resistors. These devices were relatively inexpensive, available in many power ratings, and designed specifically to dissipate heat. They had a significantly smaller footprint than the heater mats mentioned above, therefore heating of the box would be more localized. Several power resistors attached to each side of the box would be required to spread the heating. The resistors would need to be wired together around the outside of the Mole box.

Peltier devices were considered for cooling functionality. They could be attached to the Mole box in a similar manner to power resistors and would have required only minor changes to the control electronics. At this stage however a simpler solution was to ignore cooling and simply heat the Mole to several degrees above the maximum ambient using heating elements.

2.3.3 Designing and building the environmental chamber

Drawings for an aluminium box were drafted and sent to a local manufacturing company. The water-cut metal plates were subsequently delivered to the mechanical workshop at Massey University for construction. Holes were drilled and tapped in the four side plates and base, and non-ferromagnetic (brass) screws were used to fasten the pieces together. The plate edges around the top of the environmental chamber were milled to half the plate thickness and to a depth of 12mm to flush fit the top plate. Non-magnetic hinges and a knob were added to the top plate forming a door into the environmental chamber.

The Mole was positioned centrally in the environmental chamber 50mm above the base. This provided thermal separation between the Mole and the base plate, while still allowing a large sample to be placed on the Mole's top surface with the lid closed. A BNC coaxial socket-socket connector suitable for press-fitting through the side of the aluminium box was sourced from RS Components (Telegartner, RS 112-1798) and fitted as shown in Fig. 2.7(a). This ensured no opening was created for EMI to enter the environmental chamber.

A 2.2Ω 50W resistor was purchased (RS 225-3026) and attached to the center of the outer wall of the completed box. The aluminium surface was first cleaned with acetone. A thin layer of heat-sink paste (RS 554-311) was applied to the thermally conductive area on the resistor. The two resistor side tabs had a drop of superglue applied and were then pressed against the aluminium wall for a few seconds until the glue adhered.

To test the ability of the resistor to transfer heat to the inside of the environmental chamber, a temperature logger was placed inside the chamber and the lid closed. A 6A power supply was used to deliver about 78W into the power resistor. The air temperature inside the Mole chamber increased above the ambient temperature at an initial rate in excess of 7.5°C/hour.

Noting the ability of a solitary power resistor to significantly raise the temperature inside the environmental chamber, sixteen 1Ω power resistors were purchased and attached to the aluminium surface using the method described. Four resistors were located on each side wall of the environmental chamber to spread the heating. The resistor values and wiring configuration were calculated considering the previous 78W experiment and the availability of a 24VDC 150W switched mode power supply (SMPSU). To transfer maximum power from the power supply required a 4Ω load. A suitable configuration was two parallel banks of eight resistors in series (Farnell 114-1517). In this configuration the resistors would consume 144W of the available 150W.

To determine the best temperature controller to use required a survey of the requirements. The temperature controller would require a power supply, the ability to switch the 144W heater load on and off, and the ability to accurately measure the Mole temperature. Since the heater load was to be powered from 24VDC it was sensible to share the same power supply. 240V controllers were available but this would have added additional wiring and complexity due to the high voltage. There was around 6W spare on the 150W SMPSU which was easily sufficient to power the temperature controller.

Switching the resistive load on and off could be achieved in several ways. Some controllers had an integrated solid state relay for switching high voltage AC loads well in excess of 144W but use of high voltages had already been dismissed. Other controllers had voltage and current outputs but these outputs required additional power switching circuitry.

For switching 144W to the resistive load, a relay or solid state switch such as a silicon transistor or a field effect transistor (FET) could be used. A relay would prove annoying due to clicking contacts and relays have limited contact switching lifetimes, so solid state devices were instead researched. Using a transistor as a low-side switch would mean 24VDC would always be present around the load circuit. This could lead to a short circuit between the +24V wiring and the grounded metal box. A better alternative would be to use an intelligent high-side FET switch to control the +24V feed. Intelligent high-side switches are used to control high current automotive loads and often have built-in short circuit and thermal protection. An IR6220 (International Rectifier [125]) intelligent high-side device capable of switching +24V at up to 10A and with $R_{DS(on)}$ of 100mΩ was chosen (RS 287-9836). For a 6A load the power dissipation in the device would be around

0.6W although the data sheet only specified $R_{DS(on)}$ for a 1A load. The device could be directly controlled from the temperature controller's SSR voltage output.

The chosen temperature controller was an Omron E5CN Q2MT-500 at a cost of around $320 (RS 481-9296). This was considerably less expensive than from Farnell or Omron. The controller would be powered from the same 24VDC power supply supplying the heater load. The controller's +12VDC/21mA output was suitable for directly driving the IR6220. Connections for a 3-wire Pt100 probe and a serial communications port were both available. A schematic diagram showing the components and their interconnections is shown in Fig. 2.5. The completed temperature controller unit is shown in Fig. 2.6.

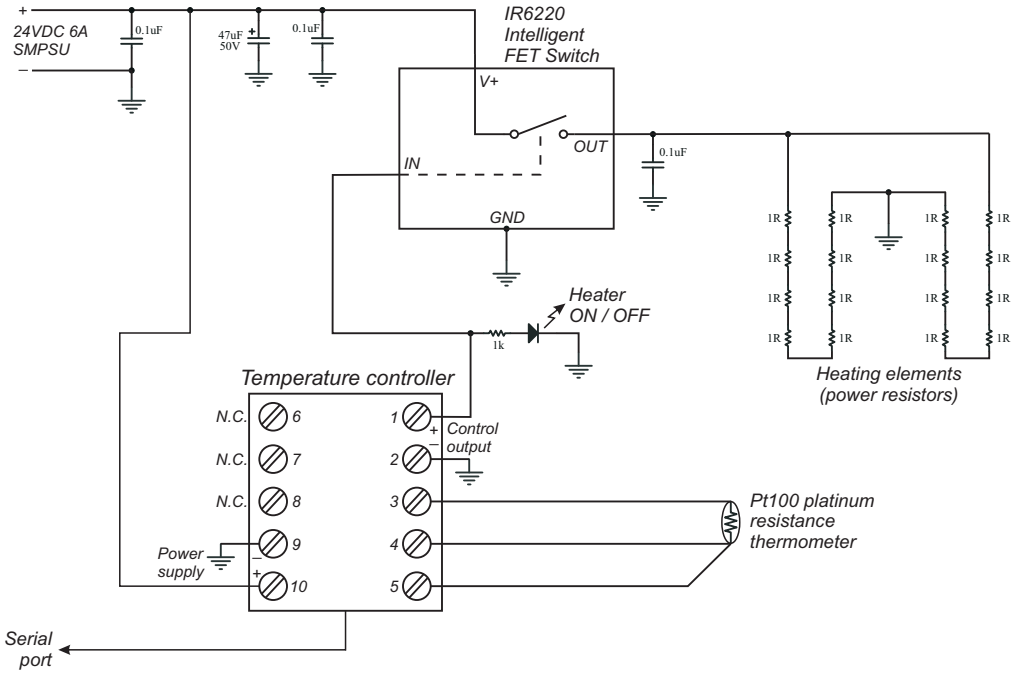

Figure 2.5: Temperature control circuit showing all electrical connections between the Omron controller, Pt100 sensor, FET switch, power resistors, and 24VDC 6A power supply. The LED indicates heating operation. The 0.1μF bypass capacitors were used to reduce electrical transients.

A Pt100 sensor suitable for measuring the Mole probe temperature was required. Since the Mole was located inside the environmental chamber the Pt100 probe had to pass through the chamber wall. To reach the Mole probe a 150mm long Pt100 probe was sourced (Omron [113]). The probe was made from hollow stainless steel tube with the Pt100 sensor located at the tip. This style of sensor is widely used in hostile and sterile environments and is capable of providing excellent

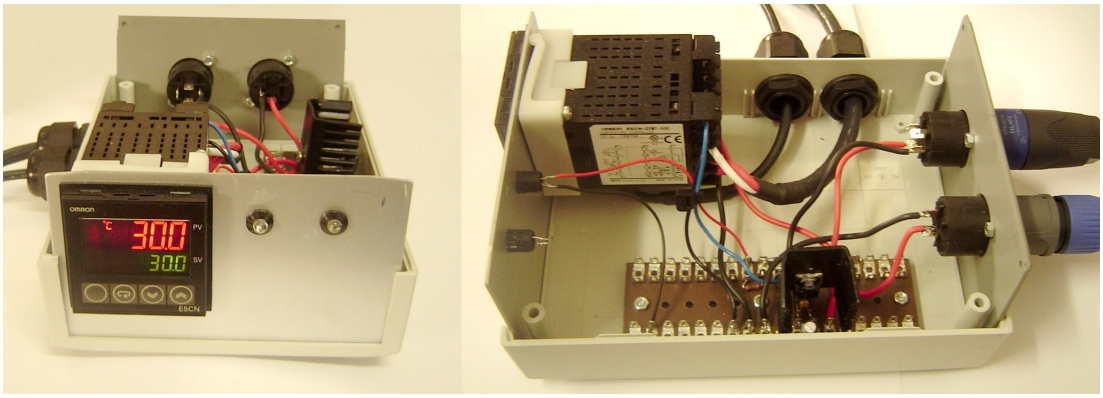

Figure 2.6: The completed temperature controller with top cover removed. The Pt100 and RS-485 serial port cables exit through the side of the box. The power supply and power resistor cabling exits through the rear of the box. A small heat-sink is attached to the IR6220 FET switch.

accuracy within the control system. A hole was drilled through the environmental chamber wall to loosely fit the 6mm temperature probe as shown in Fig. 2.7(a). Copper shimming was used to ensure a tight fit and to allow future removal of the Pt100 probe if necessary. The probe was custom made in Auckland, New Zealand using Omron parts and Pt100NZ sensor, and cost around $127 (Sensortech Technology [4]). To provide a thermal connection between the Pt100 sensor tip and the Mole probe an aluminium block 40mm×25mm×12mm was cut and attached to the top surface of the Mole as shown in Fig. 2.7(b). A 6mm hole was drilled through the block for attaching to the Mole probe and a 5.5mm diameter hole was drilled about half way into the aluminium block for accepting the 4.8mm diameter tip of the temperature probe. Heat-sink paste was applied at the interfaces.

The Omron temperature controller had a built-in RS-485 communications port. Building a circuit to convert RS-485 to USB for connecting to the computer was a possibility, but in light of time constraints the standard Omron E58 CIF Q1 accessory was purchased. Pricing from Omron was around $240 which was considerably less expensive than from Farnell or RS. Windows software was provided by Omron to enable configuration and temperature logging. An attempt was made to program Prospa to communicate directly with the temperature controller using protocols specified by Omron, however this was unsuccessful due to limitations in Prospa's serial communications software interface. This would have been useful as Prospa macros could have been modified to measure and control the temperature.

After completing assembly of the temperature controller apparatus, the controller was placed in auto-tune mode to calculate the PID coefficients. After

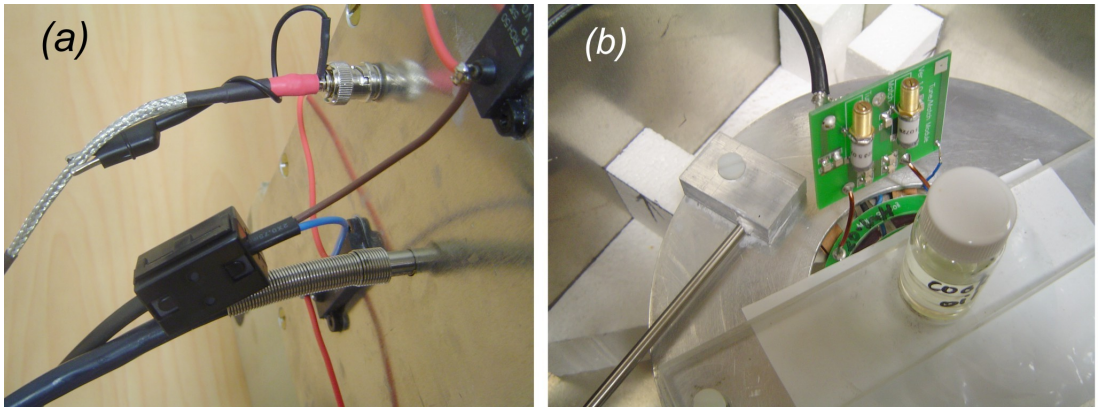

Figure 2.7: (a) Power resistors, Pt100 temperature probe, and coaxial cable outside the environmental chamber. (b) The Pt100 tip inserted into the aluminium block to sense the temperature of the Mole probe.

auto-configuring, the Mole temperature did not stray more than ±0.1°C so long as the room temperature was 2-3°C below the set temperature. If the environmental chamber lid was left open for more than a few tens of seconds, and depending upon the room temperature, the Pt100 probe temperature was observed to deviate increasingly from the set temperature.

Under worst case full load conditions the power dissipated in the high-side FET device made it too hot to touch, so a small 9.9°C/W heat-sink was attached to the FET's tab (Farnell 170-074). This unexpected heating was probably due to the increased resistance of the FET as it heated. A newer replacement part data sheet shows $R_{DS(on)}$ increasing with junction temperature, and a reduced $R_{DS(on)}$ specification of 80mΩ (International Rectifier IPS521 [124]).

One concern was whether a 6A DC current moving through the power resistors around the outside of the environmental chamber would effect B_0 magnetic field homogeneity. The Biot-Savart equation was used to calculate the magnetic field (assuming a long straight wire) as follows (Halliday et al. (1997) [67]):

$$B = \frac{\mu_0 I}{2\pi R} \tag{2.2}$$

where I is the current and R is the distance perpendicular to the wire. A realistic distance between the wiring and the Mole's sensitive region was $R = 0.15$m, therefore $B \approx 8\mu$T. This value is less than the Earth's magnetic field thus could be safely ignored. Another concern was whether temperature cycling would cause the super glue bond between the power resistors and aluminium box to break, however has not happened during at least two years of use.

2.4 Testing the apparatus

The Mole probe environmental chamber and temperature control system were now in the form shown in Fig. 2.1, and were reducing EMI and maintaining the Mole probe at a constant temperature. It was now possible to begin learning how to use the apparatus and to discover its pitfalls and complexities.

2.4.1 Environmental chamber EMI shielding

The first experiments focussed upon measuring the environmental chamber's effectiveness as an electromagnetic shield. This involved recording data with the Mole probe in the same physical location both inside and outside the environmental chamber. Large transients significantly exceeding the base noise were often detected outside the environmental chamber so data was only recorded in their absence to avoid introducing an additional measurement parameter. Noise measurements were recorded using Prospa's MonitorNoise macro and displayed in both time and frequency domains. The RMS noise was repeatedly found to be at least 30% lower with the Mole located inside the closed environmental chamber.

2.4.2 Switching power supplies and other noise sources

It was decided to replace the large linear power supplies used to power the spectrometer, temperature controller and RF amplifier with small SMPS bricks. Experiments were required to determine whether introducing additional switching power supplies would increase the electrical noise.

To begin these experiments only linear power supplies were used. The internal spectrometer 24V-7VDC SMPS module was replaced with a linear power supply. The first experiment compared noise levels while using the 7V linear and then 7V switching power supply using Prospa's MonitorNoise macro. The result indicated no difference in the noise level. The next experiment replaced the large HPA 48VDC linear power supply used to power the RF amplifier with a 48VDC 2.7A SMPSU (Phihong model PSA150U-480) but again no difference was found. Two additional mains powered 24VDC SMPSUs were added, one for powering the spectrometer and the other for powering the temperature controller. Again no additional noise was observed, even when moving the power supplies close to the apparatus' cabling. Opening the environmental chamber lid and locating one of the two SMPSUs within 250mm of the magnet generated frequency domain spikes but with the environmental chamber lid closed the spikes disappeared.

Two other observations were made in connection with the 24V SMPS units. First, placing a unit near the Mole, even outside the metal box, caused a dramatic decrease to its cooling fan speed. Presumably this was due to Mole's magnetic field

affecting the fan motor. Second, with the Mole outside the environmental chamber, placing the two 24V SMPSUs on top of each other generated severe transients in the MonitorNoise macro around 50kHz apart, presumably caused by a strong cross-coupling between the power supply electronics.

Further observations were made relating to grounding of system components during the noise measurements. The first concerned grounding of the stainless steel Pt100 temperature probe casing. Without copper shimming to provide a firm electrical ground between the sensor and the environmental chamber, large noise spikes were observed in the MonitorNoise macro. The second grounding issue related to the new pre-amplifier duplexer module that is discussed in Chapter 3. A part of the pre-amplifier duplexer circuitry was mounted inside a milled aluminium box consisting of a base and a lid. The lid was screwed to the base, however the screws were not sufficiently tight and lock washers were omitted. This also resulted in large noise spikes being detected by the MonitorNoise macro. Fixing the lid firmly to the base eliminated the problem.

The Omron RS-485 to USB conversion cable could also have introduced noise into the system due to its connection between the computer, powered USB hub (not shown in Fig. 2.1), spectrometer, and temperature controller. However increased noise was not observed.

2.4.3 Intermittent noise

A final experiment was performed to determine whether intermittent transients were entering the apparatus. Such transients had been observed previously but it was unknown whether they could enter the newly optimized system. Before this experiment was performed, the pre-amplifier duplexer module designed by Michael Adams was changed for a new design with lower noise and additional shielding as discussed in Chapter 3. The new PAD module was used hereafter in this project.

The MonitorNoise macro was modified to repeatedly scan for transients but only to record the scan if an amplitude exceeding around 10 times the noise floor was detected. Around 5,000 scans were acquired before a transient was detected. The transient amplitude was in excess of 20 times the RMS noise, indicating that noise was still capable of entering the apparatus albeit infrequently.

2.4.4 T_2 bi-exponential stability

The next experiments focussed on testing the repeatability of T_2 CPMG measurements by evaluating them over an extended time period. T_2 measurements were chosen as they would probably also be used in future experiments. The 2008/9 summer break provided a good opportunity to perform long term experiments since the university was closed.

A Prospa backdoor macro T2DriftTest was written (see Appendix C.1 on page 221) to perform the measurements. The Mole environmental chamber temperature was set to 25°C and the NMR lab air conditioner set to cool the room to around 18°C. A canola oil sample was placed on the Mole and the backdoor macro started. Each T_2 dataset consisted of 128 scans repeated at 30s intervals; a new set of 128 scans was started every 7 hours. This ensured the measurements happened at different times each day. Over 22 days, 71 identical sets of experiments were performed. The environmental chamber and lab temperatures were also logged during the 22 day period. The T_2 relaxation results are shown in Fig. 2.8. The temperature results (not shown) showed the Mole temperature remaining steady at (25.0 ± 0.1)°C while the lab temperature oscillated daily around (20 ± 2)°C.

Data from each experimental dataset was fitted using Prospa's in-built bi-exponential fitting algorithm. Fitting two exponentials to a bi-exponential decay offers no unique solution and the resultant fits are very susceptible to signal and noise variations. If fitting times and amplitudes were stable, this would be indicative of both excellent signal-to-noise and excellent T_2 signal repeatability.

The mean ($\bar{x}$) and standard deviation (σ) of the four datasets were calculated. The long time constant T_2 relaxation time had $\bar{x} = 205.7$ms and $\sigma = 1.7$ms and corresponding amplitude $\bar{x} = 0.373$ and $\sigma = 0.004$. The shorter time constant T_2 relaxation time had $\bar{x} = 54.4$ms and $\sigma = 0.4$ms and corresponding amplitude $\bar{x} = 0.627$ and $\sigma = 0.004$. These values will be compared to the mono-exponential result in the following section.

Amplitude and time constant outliers were evident in experiments 59 and 63 in Fig. 2.8. The raw relaxation data for these two datasets was compared by plotting them on top of one another on a common graph, but this revealed no obvious visual differences between the bi-exponential decays.

The dispersion of T_2 measurements shown in Fig. 2.8 may have been greater if the measurements had been completed during the university semester when nearby electrical equipment was in use. The usefulness of the results however was in showing that the NMR apparatus was capable of remaining stable over an extended time period in the presence of varying laboratory temperature.

2.4.5 T_2 mono-exponential stability

Previously multi-exponential time and amplitude data was extracted from an oil sample and the stability and repeatability of measurements inferred from the results. Many samples such as pectin solutions in Chapter 4 exhibit mono-exponential relaxation, therefore it was sensible to repeat the T_2 stability measurements on a sample with similar relaxation behavior and T_2 time constant – such as water doped with $CuSO_4$. A backdoor macro was written to measure the sample over several days. The results are shown in Fig. 2.9.

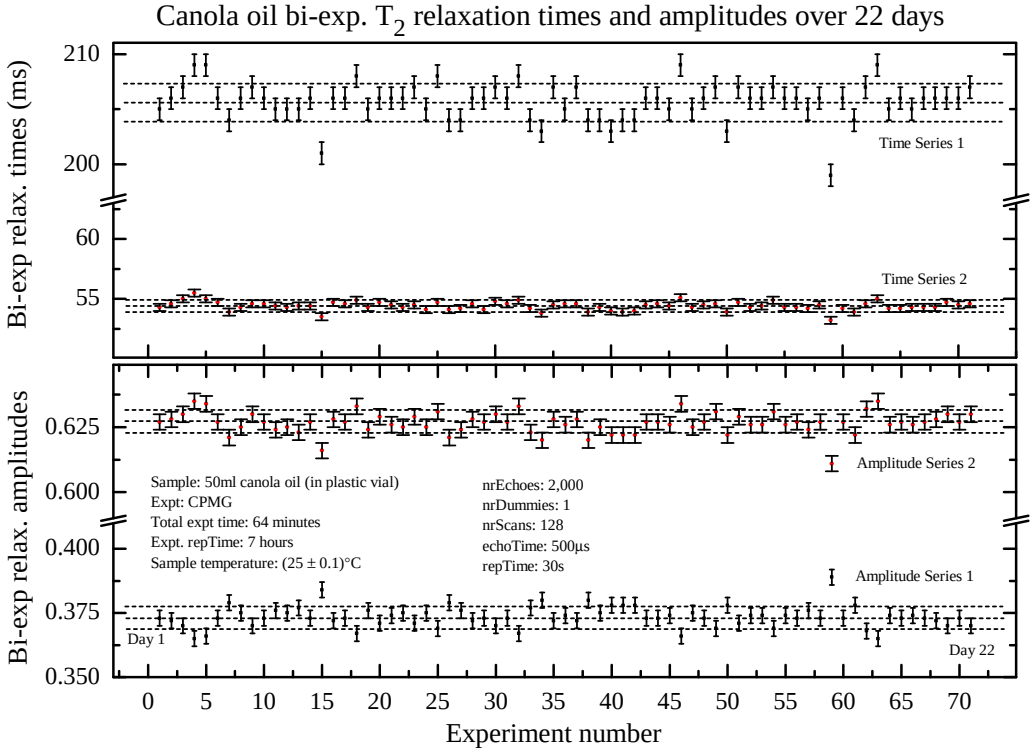

Figure 2.8: Bi-exponential T_2 relaxation data from canola oil sample measured over a 22 day period. Each measurement provided two time constants and two amplitudes as shown. The dashed lines show the mean, and one standard deviation either side of the mean. The uncertainties were provided by Prospa's fitting algorithm.

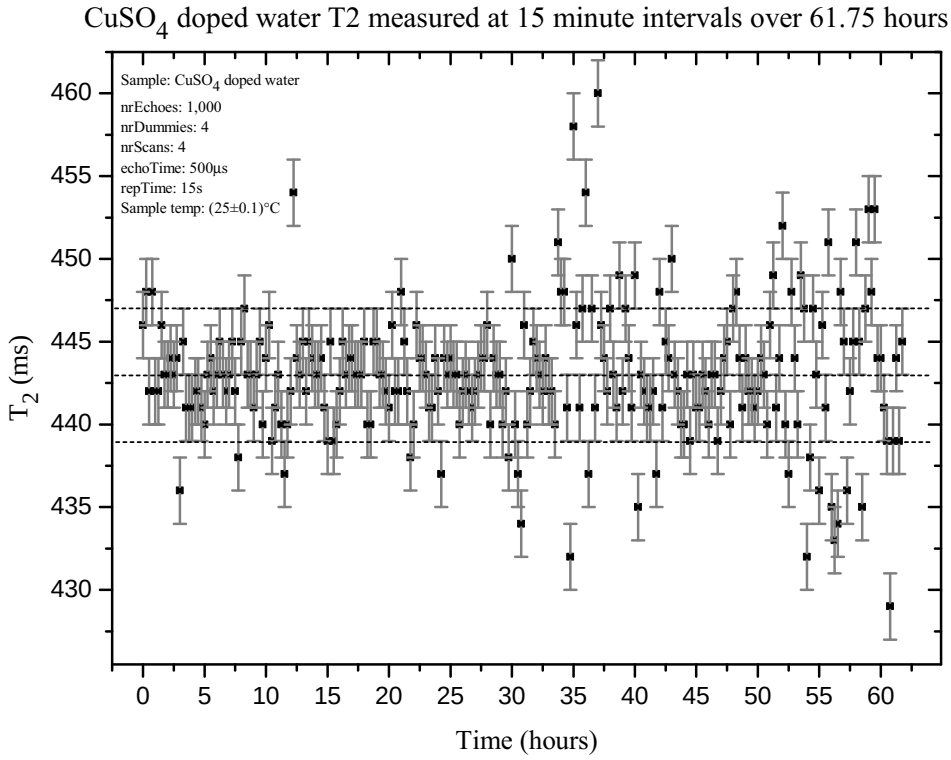

Figure 2.9: Mono-exponential T_2 relaxation data from $CuSO_4$ doped water over a 62 hour period. The dashed lines show the mean, and one standard deviation either side of the mean. The uncertainties were provided by Prospa's fitting algorithm.

The mean and standard deviation of the T_2 times were calculated to be $\bar{x} =$ 443ms and $\sigma = 4$ms respectively as indicated on the graph. The largest groups of deviations happened at around 10 hours, 35 hours and 58 hours. These were close to one day apart suggesting environmental interference.

The dimensionless coefficient of variation c_v $(= \sigma/\mu)$, defined as the ratio of the standard deviation to the mean, shows that the bi-exponential c_v values calculated in the previous section were very similar to the mono-exponential c_v result. The bi-exponential results were: 8.3×10^{-3} (time series 1), 1.1×10^{-2} (amplitude series 1), 7.4×10^{-3} (time series 2), and 6.4×10^{-3} (amplitude series 2). The mono-exponential result from the T_2 times was 9.0×10^{-3}. The important point to take from this data is that 128 scans were used in acquiring each bi-exponential data point while only 4 scans were used in acquiring each mono-exponential data

point.

The difference between the shortest and longest measured T_2 times was approximately 30ms which is considerable in the context of a T_2 time with 443ms mean. Evidently a sample measured using 4 scans should not be taken on its own but instead needs to be placed in the context of other similar measurements. There is the possibility of spurious fitting of T_2 relaxation decays due to noise superimposed on the signal. This is especially problematic when there are only a few echoes, and is the reason why valuable relaxation data should not be discarded. In the context of the pectin measurements in Chapter 4, four scans were sufficient because each measurement was not taken in isolation, but rather as part of a series of measurements.

2.4.6 Mole proton frequency versus temperature

It was previously estimated from the magnet specifications how B_0 should change with temperature. To test this empirically, the Mole temperature was varied over an easily accessible experimental temperature range of between 20°C and 30°C while measuring the proton Larmor frequency at which the maximum signal amplitude was obtained.

The temperature time constant for the Mole was around four hours so a minimum of twenty hours was required following each temperature change to ensure the magnets reached thermal equilibrium (Personal correspondence [3]).

The apparatus was configured to begin at 20°C. A water sample was placed on the Mole and a frequency sweep was performed between 3.165MHz and 3.225MHz in 40 steps, and repeated for each integral temperature. This provided the NMR signal peak integral (in the frequency domain) at each frequency, indicating where the NMR signal was largest. Each dataset was fitted with a continuous function and differentiated in OriginLab to accurately determine the frequency at maximum amplitude. The results are shown in Fig. 2.10.

A linear fit to the data in Fig. 2.3 reveals a Mole temperature coefficient at 25°C of:

$$\frac{-0.00364\text{MHz}/^\circ\text{C}}{3.19700\text{MHz}} \times 100\% = -0.114\%/^\circ\text{C}. \tag{2.3}$$

This value is identical (to 2 d.p.) to the manufacturer's specified temperature coefficient of induction for the Mole's N-42 NdFeB magnets (Macmill Magnets [97]).

2.4.7 Effects of frequency mismatch

Changing the NMR sample requires the environmental chamber lid to be opened which in turn allows heat energy to escape from within the chamber. This was

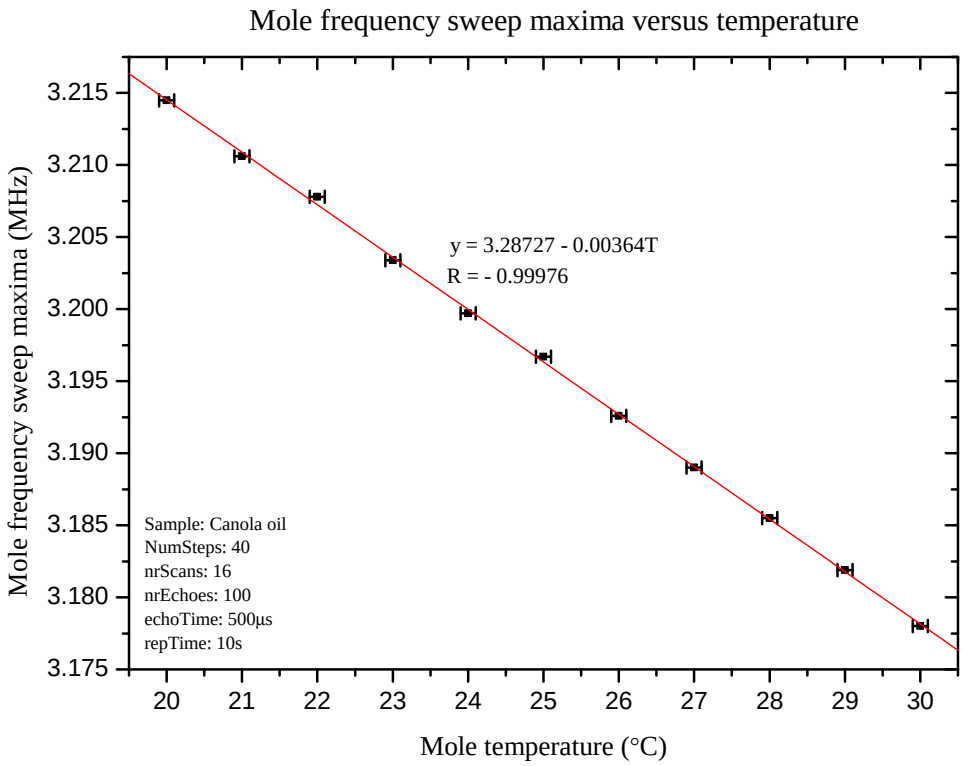

Figure 2.10: Mole proton Larmor frequency versus temperature. Uncertainties in temperature are ±1 least significant digit from the Omron temperature controller display.

observed to cause the temperature controller to overshoot slightly as it tried to compensate for the change in Pt100 temperature. It was useful therefore to quantify what effect a change in temperature would have upon T_2 measurements if B_0 happened to drift away from the B_1 excitation and B_1 tuned circuit frequencies.

To test this experimentally B_0 was set at the 25°C operating frequency, then the B_1 excitation and tuned circuit frequencies were systematically adjusted together from 3.15MHz to 3.25MHz. The amplitudes of the resulting signals are shown in Fig. 2.11. Each experiment was correctly phased to the in-phase (not quadrature) signal to comply with the CPMG macro phasing requirements.

The center vertical dashed line in Fig. 2.11 shows the 25°C proton Larmor frequency. The outer dashed lines indicate the Larmor frequencies at ±3°C deviation as determined from Eqn. 2.3. The amplitude coefficient of the signals was

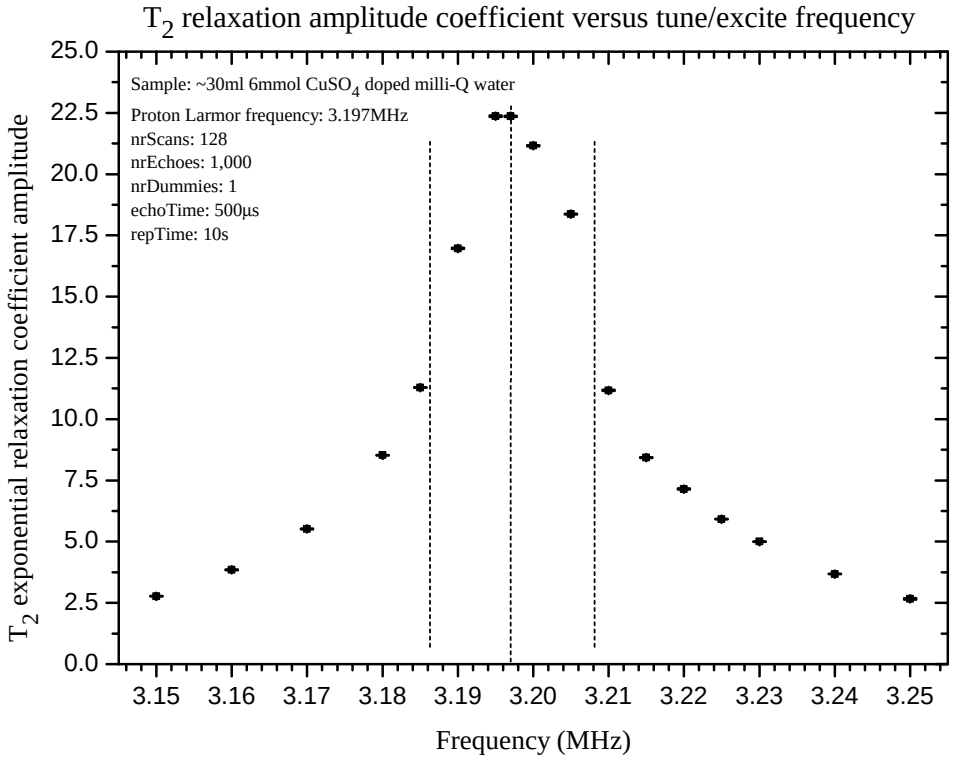

Figure 2.11: Amplitude of T_2 as the excitation and tuned circuit B_1 frequencies deviate together either side of the proton Larmor frequency.

determined by fitting the raw T_2 relaxation data in OriginLab since relaxation data displayed in Prospa is normalized. The amplitude of the NMR signal evidently reduced by around 50% at (25±3)°C. The loss of signal amplitude was presumably due to sub-optimal spin manipulation.

In addition to determining the T_2 amplitudes, the T_2 relaxation times were also fitted in OriginLab for each frequency dataset. The T_2 times were found to increase linearly from 82ms to 89ms between 3.15MHz and 3.25MHz. Uncertainties in the T_2 relaxation times increased from ±0.2ms around the center frequency to ±0.5ms at the lowest frequency and ±1.2ms at the highest frequency. The large increase in uncertainties was due to decreased signal-to-noise as a result of the reduced signal amplitude. The increase in T_2 was possibly due to sample heating which will be discussed in due course but was not investigated further at this time.

The conclusion from these experiments was that optimal signal-to-noise and repeatable T_2 measurements required B_0 to remain closely locked to the B_1 frequencies during experiments. This was important for the numerous pectin and kiwifruit experiments that are discussed in future chapters.

2.4.8 Water T_2 versus temperature

Many NMR measurements in this project involved samples containing significant quantities of water. The samples were generally prepared and/or modified at the laboratory temperature before being placed in the environmental chamber. Since T_2 is a function of temperature, it was useful to understand how sample temperature variations would effect experimental T_2 data.

To measure water T_2 as a function of temperature using the Mole, a polystyrene cup was two-thirds filled with 84°C water. A mylar sheet was placed on the Mole probe surface and six business cards were placed on the mylar sheet above the central magnet. The cup of water was placed on top of the business card stack. A CPMG experiment was performed to measure T_2. The result of this experiment was noise and no signal. Evidently the cup of hot water had damaged the probe's central magnet. This is discussed further in §2.5.4 on page 60.

After repairing the probe a less destructive technique was determined to measure T_2 versus temperature. A 10mL Milli-Q water sample was placed in a clean glass vial and sealed. A block of polystyrene 90mm×46mm×36mm was drilled with a 27.5mm diameter hole to fit the vial snuggly. This was to enable the vial to be floated in the water bath and to provide thermal insulation for the sample as it was transported between a temperature controlled water bath and the environmental chamber. The water bath temperature was initially set to 5°C and monitored using an alcohol thermometer. The polystyrene block and vial were floated in the water bath ensuring the sample and vial reached the set temperature.

After 2 ½ hours the sample was removed from the water bath and quickly placed in the Mole's Perspex vial holder and T_2 was rapidly measured. The sample was then returned to the water bath for adjustment to the next temperature and repeated. The results are shown in Fig. 2.12.

From these results it was evident that water samples between 5°C and 45°C experience T_2 relaxation time changes of around 1.5%/°C. This showed that controlling the sample temperature is vital for achieving satisfactory results.

2.4.9 Optimal sample location and volume

The Mole probe has a small volume above its top surface in which the B_0 and B_1 magnetic fields are pseudo-homogeneous and spatially overlapping. To maximize the NMR signal, the sample should fill the overlapping volumes. The simplest way

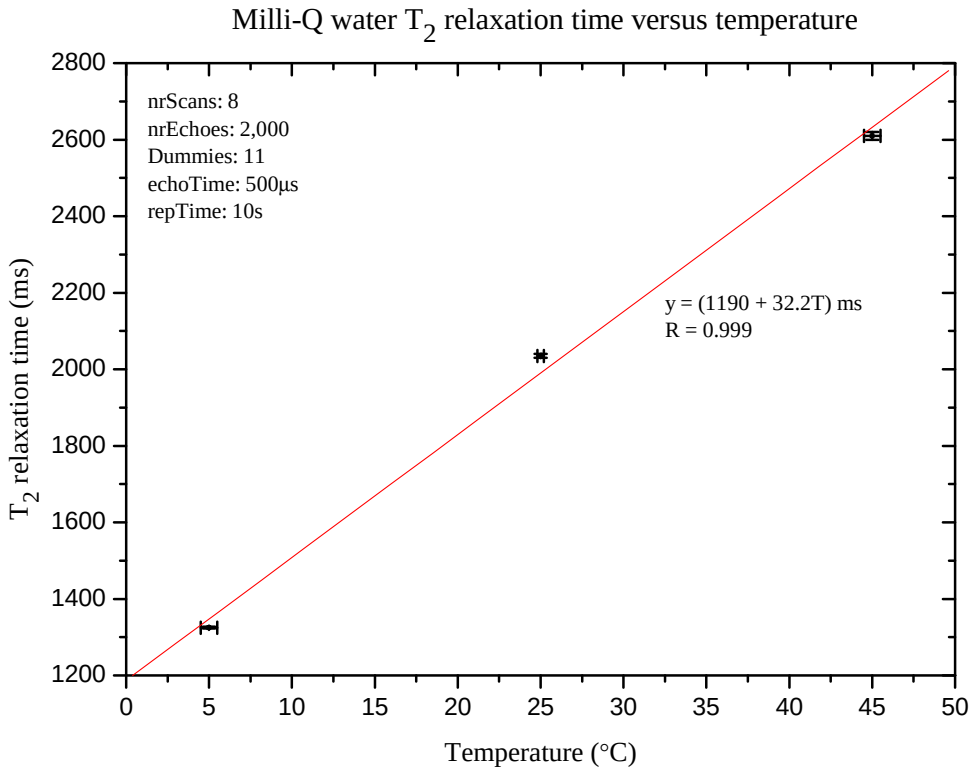

Figure 2.12: Milli-Q water T_2 relaxation time versus temperature. A linear fit showed T_2 increasing by (32 ± 2)ms/°C. Uncertainties in T_2 are from Prospa's mono-exponential fitting algorithm. Uncertainties in temperature are estimates from the thermometer reading and relocation of the sample from the water bath to the environmental chamber.

to accomplish this is to use a large sample, however in many instances the sample needs to be made as small as possible while maintaining a maximum NMR signal. This was the case for the pectin solutions discussed in Chapter 4.

To determine the optimal signal-to-volume ratio and the spatial location from which the NMR signal originates, a large 150mL sample container that easily encompassed the entire homogeneous volume was placed centrally on the Mole probe. The container was around 65mm in diameter and 80mm tall. To determine where the signal was coming from, the sample container was gradually filled with canola oil while measuring the quantity of NMR signal. The signal was insignificant up to a height of 5mm above the probe surface. Between 5mm and 15mm the signal amplitude grew rapidly. Between 15mm and 20mm there was again little increase in signal amplitude, and no observable increase above 20mm. This experiment provided both the maximum attainable NMR signal and a signal height profile.

The large sample container was now exchanged for two vials. The first was plastic with 31mm inside diameter and was available in bulk within New Zealand (Wainhouse Distribution Limited [95]). The second was glass with 25.3mm inside diameter and was available in bulk from the Massey University chemical stores (Massey Chemical Stores [1]). Both vials were suitable for containing small liquid and soft solid samples. The vials were filled with oil and in-turn located in the center of the probe surface. In each case the oil column height extended from ∼1mm to beyond 20mm above the probe's surface. The plastic and glass vials were found to have respectively 92.5% and 77.4% of the maximum signal attained previously. The glass vial had 84% of the plastic vial's signal.

To measure signal-to-volume ratio, each vial was in-turn gradually filled with canola oil and the NMR signal amplitude measured. The results are shown in Fig. 2.13. Evidently the signal from the sample within the glass vial did not increase even when the volume was increased beyond 8.75mL.

Evidently the signal from the sample in the plastic vial was slightly greater than the signal from the sample in the glass vial, irrespective of sample volume. This showed that a small amount of NMR signal originates just outside the boundaries of the glass vial.

The glass vials however were preferred for many experiments, and especially for the pectin experiments discussed in Chapter 4, in spite of providing less signal. There were three reasons they were preferred: first, they provided easy viewing of the sample during the chemical mixing and dissolving stages, and easy viewing of color changes and lumpiness during experiments. Second, they provided better mixing conditions for pectin powders due to the creation of a deep vortex within a rapidly stirring solvent. Third, they were readily available from the chemical store.

Due to the results in Fig. 2.13, two Perspex vial holders were constructed for fitting the vials; the vial holder for the glass vial is shown in Fig. 2.14. The

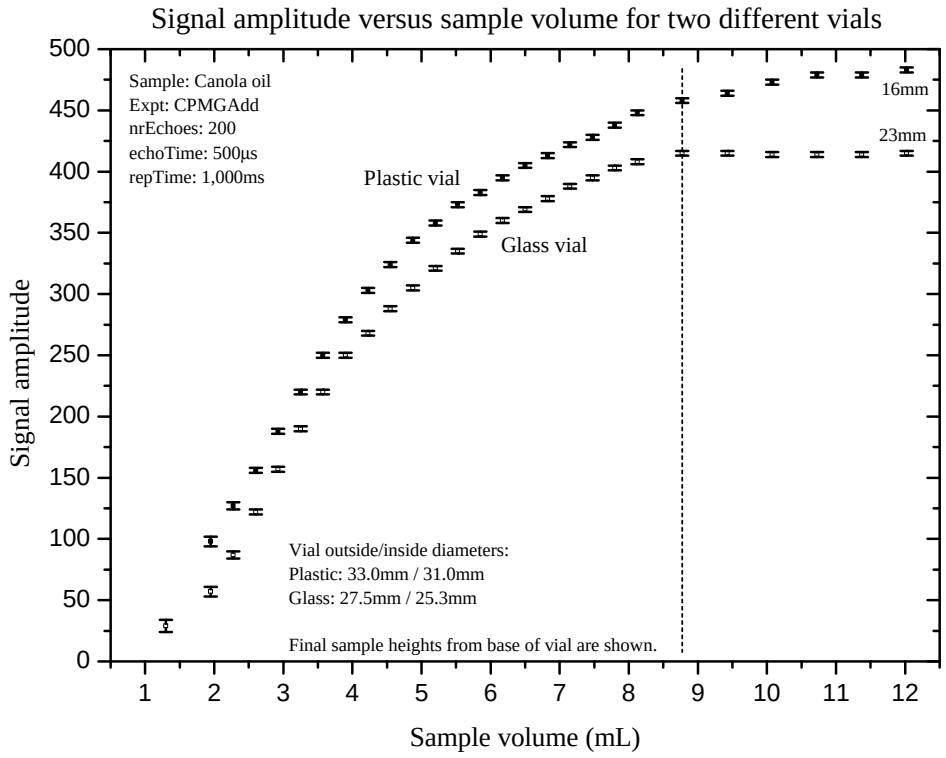

Figure 2.13: Comparative signal amplitudes versus sample volume for two different sized vials. The larger diameter plastic vial provided slightly larger NMR signal for the same volume of sample. Spin-echo amplitudes were indeterminate at very low volume, presumably due to the curvature in the vial bases forcing the sample away from the homogeneous volume. The vertical dashed line indicates the optimal volume of around 8.75mL for the glass vial.

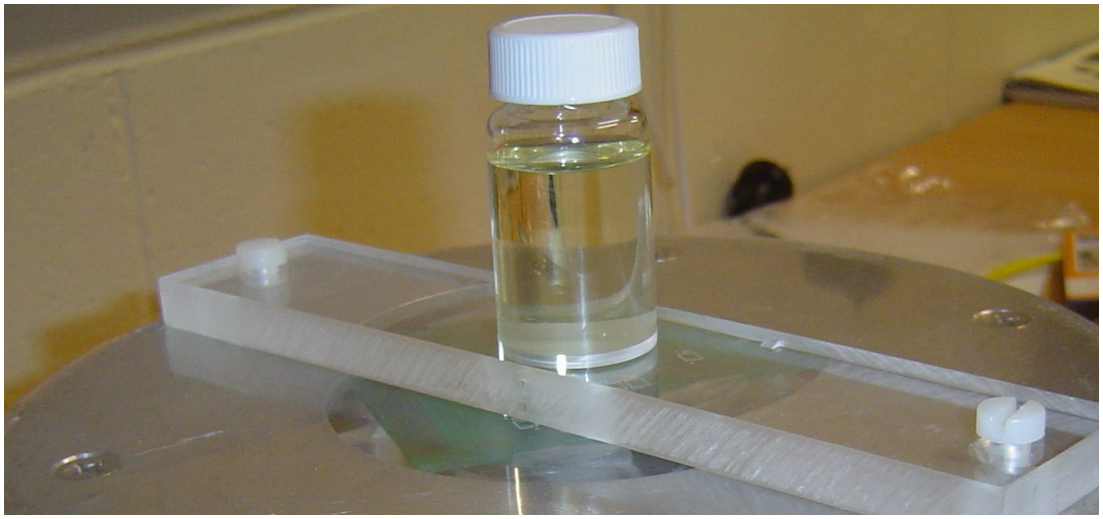

Figure 2.14: Perspex vial holder and glass vial. The vial holder is attached to the Mole probe with nylon screws.

holders were milled to a diameter that provided a firm fit, and to a depth that ensured the sample volume was located at the optimal position within the B_0 field. This ensured experimental repeatability. No NMR signal was detectable from the Perspex holders or vials.

2.4.10 Sample heating

Experiments in §2.4.8 showed how T_2 for water varied with temperature. A concern with using small samples was the possibility of the sample being heated by the B_1 coil leading to inaccurate T_2 measurements. This was especially of concern with water-based samples, since the required number of RF refocussing pulses is often significant due to long T_2 times and the requirement for short pulse spacing to minimize diffusive effects. A water sample at 25°C on the Mole probe requires about 10.5s for the T_2 signal to decay away to noise levels. For 500μs pulse spacing, about 21,000 (π) refocussing pulses are required in order to sample the full decay.

The power delivered to the B_1 coil can be calculated if a good impedance match between the HPA and B_1 circuit is assumed. In this case all incident power from the HPA is dissipated as heat in the B_1 coil resistance. For the following experimental parameters: 500μs echo time, 26μs RF pulse duration, -10dB (π) refocussing pulse amplitude (equating to 51.6V_{RMS} into 50Ω), 32,000 echoes, and 30s repetition time,

the average RF power dissipated in the B_1 coil is:

$$\frac{(51.6\text{V})^2}{50\Omega} \times \frac{32,000 \times 26\mu\text{s}}{30\text{s}} \approx 1.5\text{W}. \tag{2.4}$$

The number of echoes in this calculation is around 50% above that required for measuring water at 25°C, thus it provides a worst case scenario. If all of this power was delivered into 10mL of water with heat capacity 4.186 J/(g·K) the number of seconds required to raise the sample temperature by 1°C would be:

$$\frac{4.186\,\text{J}/(\text{g}\cdot\text{K}) \times 10\text{g} \times 1^\circ\text{C}}{1.5\text{W}} \approx 30\text{s}. \tag{2.5}$$

An experiment was run over several hours using the parameters described above to test the effects of long RF pulse sequences upon a 10mL water sample. A Pt100 sensor was located just below the surface of the water and attached to a digital multimeter. The Mole environmental chamber lid was sealed and the Mole and ambient temperatures were recorded. The results are shown in Fig. 2.15.

The temperature of the sample increased immediately after RF power was applied (around 25 minutes in Fig. 2.15) at an initial rate of about 0.13°C/minute. At this rate, after 8 minutes the temperature would have increased by approximately 1°C and the water T_2 would have increased by around 32ms. Evidently about one-sixteenth of the RF power delivered to the probe ended up as heat in the water sample. The environmental chamber heater elements stayed off during the sustained RF heating period as more heat was being added to the inside of the environmental chamber than was being lost to the outside, while the ambient temperature hovered around 20°C.

Initially it was suspected that sample heating was due to the water absorbing RF energy from the oscillating fields. Some mobile phones and MRI systems transfer radio frequency energy from their antennas to the human body causing localized heating. The quantity of power absorbed is measured in terms of the specific absorption rate (Jin (1998) [88]):

$$\text{SAR (Watts/kg)} = \frac{\text{total RF energy dissipated in the sample (Joules)}}{\text{exposure time (s)} \cdot \text{Sample weight (kg)}}. \tag{2.6}$$

At the low operating frequency of the Mole probe, it was unlikely that RF absorption was the heating mechanism. Jin argues that for a B_0 below 0.5T, the interaction between the B_1 field and the human body can be neglected. It seemed more likely therefore that sample heating was via conduction from the B_1 circuit board copper traces through the Perspex vial holder and glass vial to the sample. This could be tested by removing the conductive heat pathway between the RF coil and sample, and repeating the experiment.

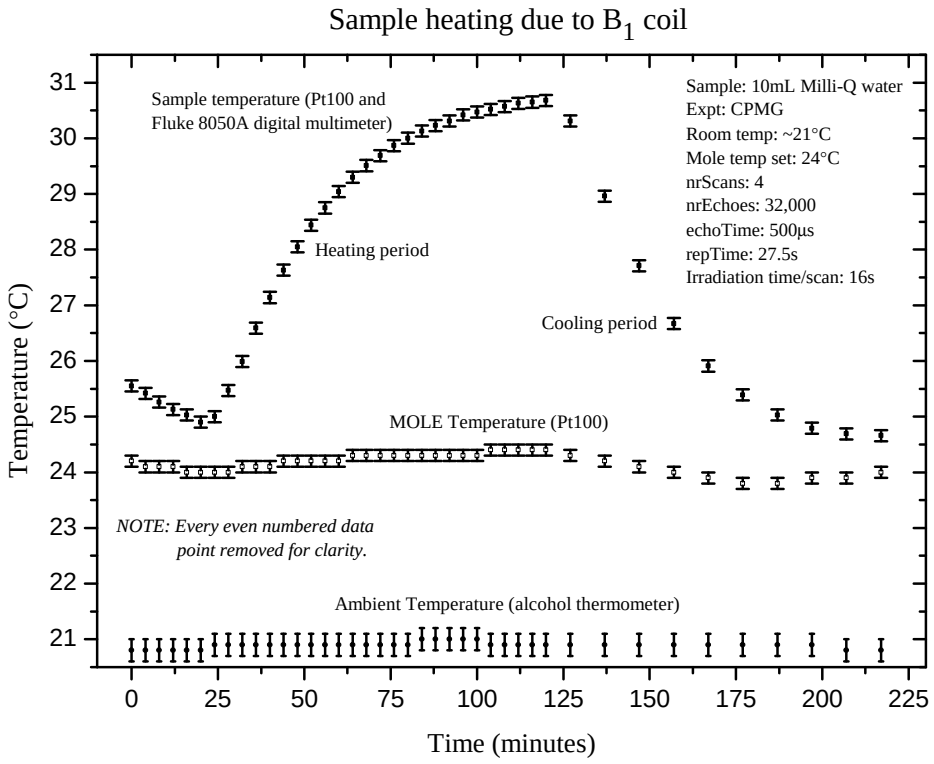

Figure 2.15: Temperature versus time for 10mL water sample. The first 25 minutes show the water temperature approaching the environmental chamber temperature. Upon application of RF pulses the water and Mole temperatures increase before falling again at the cessation of the RF pulses. The repTime parameter was set to 27.5s in the backdoor macro to provide scan beginning every 30s on average while also providing time for recording the three temperatures; $(4 \times 27.5\text{s}) + 10\text{s} = 120\text{s}$, thus an average of 30s per scan. The estimated uncertainty in sample and Mole temperature measurements was ± 0.1°C and the room temperature uncertainty was ± 1°C.

In all experiments following these results, sample heating was minimized either by using a fewer refocussing pulses, by increasing temporal separation between scans, or by increasing the sample size.

It is worth noting that water has a very high heat capacity. Samples with lower heat capacity would increase in temperature at a greater rate. On the other hand, most samples would experience less heating due to their requirement for fewer RF pulses.

2.5 Problems encountered

Numerous problems were encountered during the development and testing of the NMR apparatus for this project. Many stemmed from the intrinsic nature of the apparatus while others were engineering problems that required further development. Some of the problems and difficulties are now briefly discussed.

2.5.1 Electrical noise sources

Electrical noise pickup was considered earlier, however the significant difficulties involved in tracking down the sources of noise were not emphasized. For example, upon eliminating most of the transient noise as discussed previously, another noise source appeared. The source was unknown and could not be eliminated using techniques discussed previously. Eventually the source was tracked down to a mains powered external hard disk drive attached to the host computer. Removing its USB connection eliminated the noise. Previously the HDD had caused no problems and it is unknown why it suddenly started generating noise.

The reason noise presents significant difficulties in low-field NMR is in large part due to sensitivity of the NMR probe. Electrical noise may be too weak to be detected using an oscilloscope, but is easily detected and amplified within the NMR front-end and high-gain receiver amplification circuitry. Electrical noise is also often intermittent and very difficult to track to a source.

2.5.2 Damaged tuning capacitor

Another problem was repeated failures of the Mole probe's tuning capacitor. The B_1 circuitry shown in Fig. 2.3 on page 31 contains two identical high voltage multi-turn trimmer capacitors (Voltronics, AT20-5, 0.8-20pF [44]). The matching capacitor C_m is in series with the signal line and does not experience the high voltage of the tuning capacitor C_t that is connected directly across the B_1 coil. The tuning capacitor voltage is enhanced by order of the loaded Q of the tuned

circuit. The exact Q of the new B_1 circuit is unknown but is expected to be similar to the original B_1 circuit value of around 65 (Manz et al. (2006) [105]).

The tuning capacitor failed three times during the course of this project and had to be replaced each time. The failure mechanism manifested itself in unusual intermittent measurements. For example, one capacitor failure led to apparent water T_2 relaxation times of between 200ms and 2,000ms. Another failure was detected during a frequency sweep experiment in which the frequency sweep peak became a trough, resulting in two frequency peaks rather than one. At least one of the capacitor failures happened when the B_1 pulse duration was set to 25μs. Shortening the B_1 pulse duration required compensation in the form of increased amplitude thereby increasing the voltage across the tuning capacitor. As a result of this failure the B_1 duration was increased to 40μs and the amplitude reduced correspondingly for the remainder of the project.

Testing for component failure required removal of the B_1 circuitry from the Mole probe, desoldering the tuning capacitor from the B_1 circuit board, and using a 500VDC Megger to confirm high voltage breakdown. Rotating the capacitor screw indicated the breakdown was localized but the exact location of the breakdown was not obvious from an examination of the disassembled capacitor. Replacement cost for the capacitors was around $55USD each with a minimum order quantity of five pieces, and delivery from the USA.

2.5.3 Prospa and DSP problems

The stability of the NMR hardware and software was generally satisfactory during this project. Prospa had a few instability issues in earlier versions but v2.2.23 proved to be stable over a long term. One recurring problem was the re-establishment of the USB software connection between Prospa and the spectrometer after an experiment had been forced to stop.

The DSP modules were generally stable, however one module crashed several times during overnight experiments and was eventually replaced. The problem was apparently caused by an integrated circuit (IC) with a slightly different timing specification. The substituted part had been sourced from an alternative manufacturer.

2.5.4 Damaged Central Magnet

It was suspected the cup of hot water mentioned in §2.4.8 that caused loss of signal from the Mole probe had damaged the central magnet. To test this hypothesis a Perspex jig, built earlier to test the original Mole probe B_0 field homogeneity, was attached to the Mole using stainless steel screws as shown in Fig. 2.16. The B_0 field profile along the z-axis was measured using a Gaussmeter and Hall effect

probe (Lakeshore [92]) with care being taken not to rotate the probe between measurements. The pseudo-homogeneous region between around 5mm and 15mm above the probe surface revealed the profile shown in Fig. 2.17.

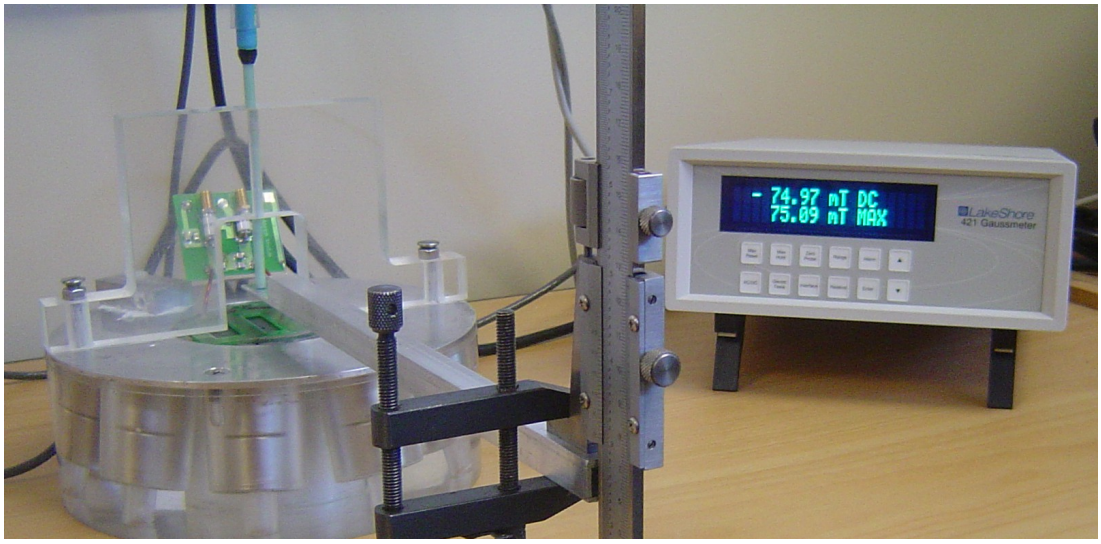

Figure 2.16: Measuring the B_0 field profile using a Hall effect probe. The probe was positioned vertically with the aid of a Perspex jig. A Vernier height gauge used for the height measurements had an aluminium arm clamped onto it to keep the metal gauge at a distance from the magnet.

The damaged Mole probe was taken to Wellington and re-mapped along the z-axis using an automated 3D mapper. The central magnet was then removed and replaced. The damaged magnet was 4.47mm thick and measured (115±2)mT at the center of the face. The replacement magnet measured 4.49mm and (129±2)mT.

The z-axis B_0 profile was then re-measured at different central magnet heights until the z-axis B_0 field remained constant. Interestingly, by raising or lowering the central magnet the B_0 profile exhibited an almost linear gradient along the z-axis irrespective of the height of the central magnet. Thirteen profiles were measured at quarter-turn rotation intervals of the central magnet holder using the automated mapper. The results are shown in Fig. 2.18. The B_0 field strength between 5mm and 15mm varied from 88mT down to 82.7mT at one extreme and from 73.3mT up to 75mT at the other extreme. The profile of B_0 off the z-axis was not investigated.

2.5.5 Acoustic ringing

After replacing the central magnet the Mole was returned to Palmerston North and re-tested. A single spin-echo with 500μs echo time had previously returned a time

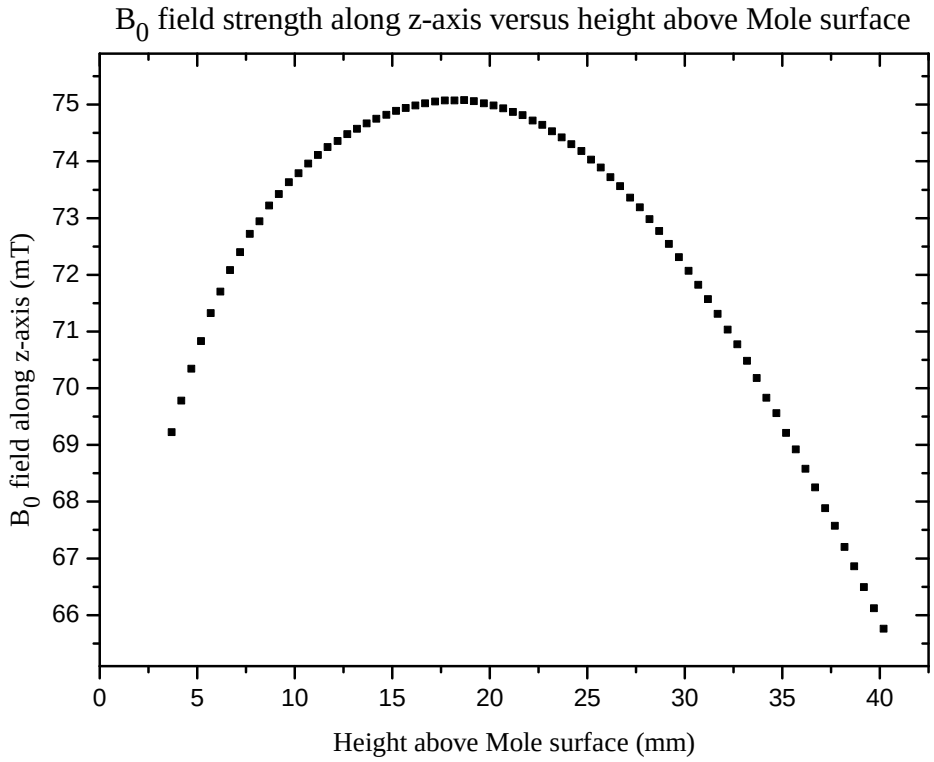

Figure 2.17: Damaged Mole B_0 profile measured along the z-axis.

domain echo, but now returned an echo heavily modulated with ∼40kHz oscillation. Extending the echo time to 1,500μs largely eliminated the oscillation. The cause of the oscillation was unknown at this time and further damage to the Mole was suspected, however this did not explain the absence of the 40kHz oscillation at the longer echo time. After researching ringing in NMR magnets it was discovered that coil disease/acoustic ringing was possibly the cause of the oscillation (Buess and Petersen (1978) [25], Fukushima and Roeder (1978) [58]).

Acoustic ringing in the context of NMR probes describes an event in which a voltage is induced in the B_1 coil by an ultrasonic wave in a nearby metal object. In this instance the object was the Mole's central magnet. The ultrasonic wave was believed to originate from the B_1 coil's linearly oscillating magnetic field generating eddy currents within the skin depth of the central magnet. According to Buess and Petersen, circulating electrons experience a Lorentz force due to the B_0 field

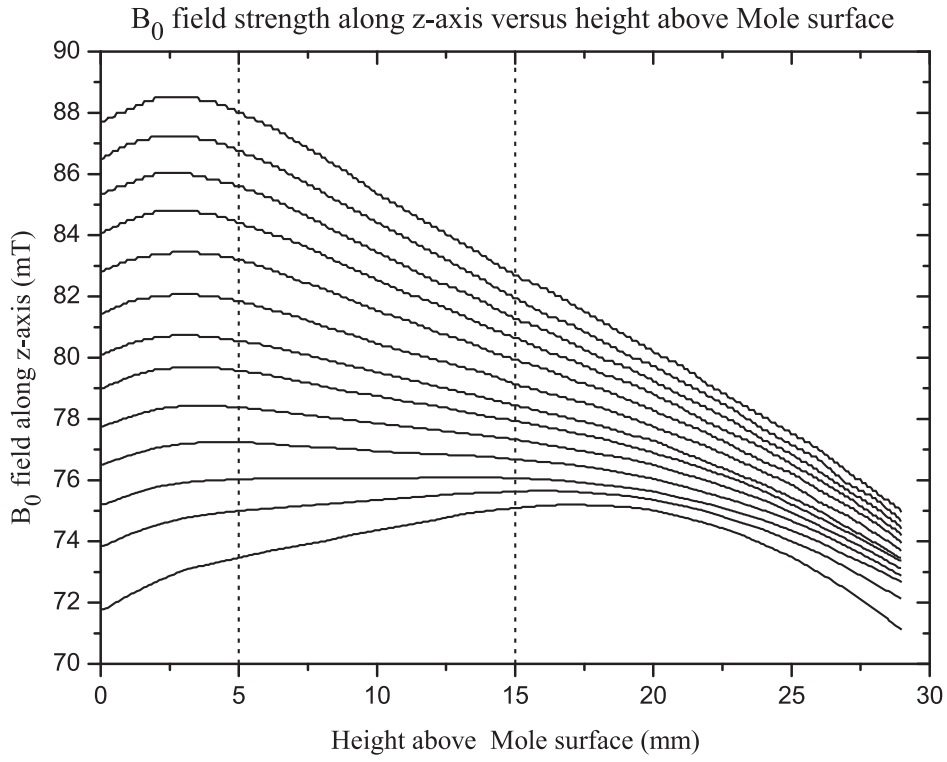

Figure 2.18: Mole B_0 profile along the z-axis for differing central magnet heights. The central magnet height was adjusted by a quarter-turn rotation at each step. The change in B_0 was approximately linear between 5mm and 15mm above the probe surface.

which is perpendicular to the B_1 field. This produces a transverse wave in the magnet that propagates along the direction of the B_0 axis before being reflected back toward the B_1 coil. Upon returning to the surface from which it began, the wave generates an electric field which is detected in the B_1 coil.

It should be noted that Buess and Petersen considered acoustic ringing in aluminium (and brass, but minimal acoustic ringing occurred at their <10kG fields), and Fukushima and Roeder investigated a range of metals. Neither of their papers referred to acoustic ringing in rare earth magnets.

To confirm the presence of acoustic ringing in the Mole probe central magnet, the magnet was removed and placed directly on the B_1 coil on the lab bench and a spin-echo experiment was performed again. Measurements were difficult due to EMI from the surroundings so the B_1 coil was mounted in the base of a small aluminium box using three adhesive rubber blocks. Earthing the box using the B_1

cable shield significantly reduced the EMI pickup and sitting the box lid on top of the box reduced it further. Oscillations were present with the central magnet sitting directly above and below the B_1 coil and absent with the magnet removed suggesting that oscillations were not coming from the aluminium box. Increasing the distance between the magnet and B_1 coil by 3.3mm reduced the amplitude of the oscillations by around 80%. Phase cycling also mostly cancelled the ringing.

Buess and Petersen observed ringing in 1.0mm thick aluminium at six regularly spaced frequencies below 10MHz. They also observed acoustic resonances 90kHz apart in the same 1mm thick sample. The Mole probe central magnet was scanned over a range of excitation frequencies between 3.570MHz and 3.650MHz. The wide variation in tuning required soldering additional capacitors to the B_1 circuit to obtain the required tuning and matching conditions at each excitation frequency. It was found that at the lowest and highest frequencies the ringing was around $10\mu V_{p\text{-}p}$ and increased to around $35\mu V_{p\text{-}p}$ at the center frequency. The oscillation frequency was also markedly higher at the outer frequencies in similar fashion to Buess and Petersen's observations.

Inserting a piece of 50mm×50mm copper foil between the B_1 coil and magnet shifted the tuning of the B_1 circuit thus again requiring additional capacitors to obtain the correct tuning and matching. Upon re-testing, the copper foil was found to have significantly reduced the oscillations, irrespective of whether or not it was grounded. Wrapping the central magnet in copper foil eliminated the oscillations.

The central magnet holder originally had silver foil on the inside base and around the walls as shown in Fig. 2.19(a), however this was no longer functioning to stop acoustic ringing. This may have been due to damage to the electrical continuity of the foil during magnet removal, or perhaps to a slightly different sized central magnet leading to different electrical connections. To shield the entire magnet using 0.05mm copper foil required removing a thin layer of material from the inside of the holder in order to fit the foil and magnet. This was achieved using a lathe, then copper foil was cut and placed in the base and around the perimeter of the holder and carefully soldered as shown in Fig. 2.19(b) without melting the magnet holder. Acetone was used to remove the adhesive backing from the foil. Another copper disc was cut slightly larger than the magnet diameter to make a top cap with a 1.5mm lip and was fitted over the new magnet. This eliminated the acoustic ringing problem.

Buess and Petersen note other methods used to solve acoustic ringing. These include coating the metal surface with an acoustically lossy substance such as RTV (silicon) or using brass rather than aluminium as it is a much poorer transmitter of ultrasonic waves due to scattering by metal grains.

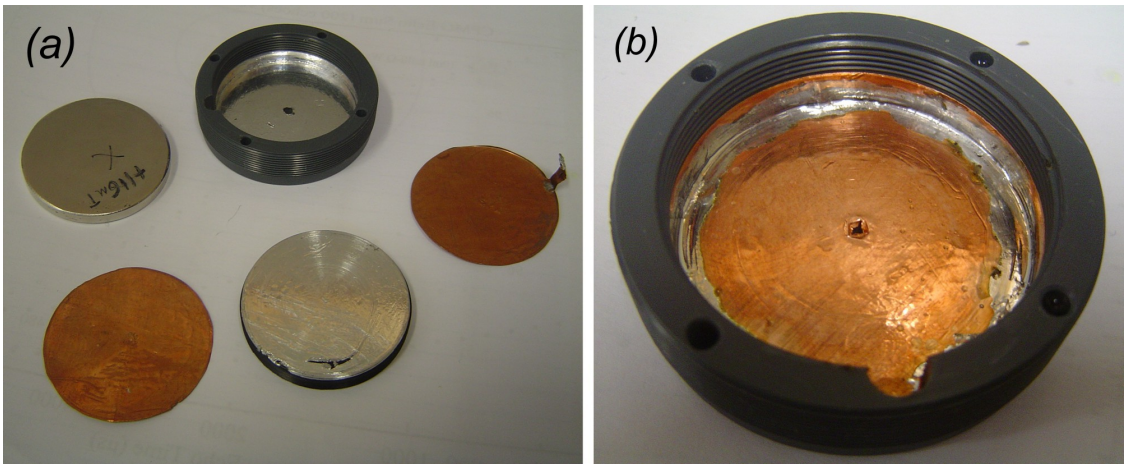

Figure 2.19: (a) The original central magnet, holder, cap, and copper shields. (b) The modified holder with copper shielding for the base and sides. The two were joined with low temperature non-lead-free solder.

2.6 Summary and future improvements

This chapter has illustrated some of the significant problems and difficulties encountered while using the NMR apparatus. The major problems were the temperature instability of the Mole probe and electrical noise pickup by the receiver circuitry. The support apparatus reduced these problems but in the process made the system more complicated and expensive, and less portable.

The experience gained by performing and analyzing the experiments in this chapter was invaluable in light of the remainder of the thesis. Experimental measurements are only as good as the equipment upon which they are made, and knowledge of how to optimally use the equipment was essential.

The Mole's temperature behavior could be improved if the temperature coefficient of the magnets was closer to zero. Macmill Magnets specify the temperature coefficient of samarium-cobalt (SmCo) magnets at between -0.05 and $-0.03\%/°C$. This is a two- to four-fold improvement over NdFeB magnets. In addition, Macmill's SmCo magnets have a maximum operating temperature of $250 - 300°C$ compared to around 80°C for the N-42 NdFeB magnets. This is important in light of the damage done to the central magnet and the many possible practical applications in which the Mole may be required to operate at elevated temperatures. The downside of SmCo magnets is they are brittle and their magnetic field strength is around twenty-five percent lower that NdFeB magnets. A good development for future magnets and probe designs would be to eliminate the temperature problem

altogether, or at least reduce temperature dependence to within bounds that can be experimentally ignored.

The Mole's signal-to-noise problems could be improved by beginning with a larger NMR signal. One path to achieving this is to increase the B_0 field strength; the new 5MHz Mole design achieves this but at the sacrifice of penetration depth. This would not be a problem in many instances, including most of the work completed in this project.

The version 3.0 DSP module greatly increased the memory available for sampling relaxation data. Valuable relaxation data no longer had to be discarded. Transferring data from the new DSP to the host computer using USB 2.0 provided a useful speed increase with the possibility of another with USB 3.0 now becoming available. Still faster optical connections are on the horizon and would provide useful electrical isolation between computer and spectrometer. Rapid transfer speed is important for experiments where the scan rates need to be very fast.

The tuning capacitors used during this project were a point of weakness. This needs to be investigated and a more robust B_1 circuit developed.

Frequency locking the proton Larmor and B_1 tuned circuit frequencies together with a temperature controlled capacitor may be possible. The ideal capacitor would sample the temperature of the Mole, adjust its plate separation accordingly, and hence its capacitance. Such a capacitor coupled with lower temperature coefficient magnets may for all practical purposes make probe tuning generally unnecessary. The B_1 excitation frequency could then be determined without user intervention by using an occasional automated wobble sequence.

Overall, many possible improvements lie on the horizon and we look forward to continued innovation.

CHAPTER 3

Pre-amplifier duplexer

The aim of this chapter is to provide a detailed description of two pre-amplifier duplexer modules that were designed and developed for the Kea spectrometer during this project. Existing designs are briefly discussed, then the new designs are introduced in terms of their design requirements and functionality, followed by full electronic circuit implementations. Due to the complexity of the designs and the advanced electronics, each design is presented schematically and with accompanying diagrams and text. The various blocks within the electronic circuits are then described in turn. The chapter concludes with a comparison of the two completed modules.

3.1 Overview

The pre-amplifier duplexer (PAD) is one of six core hardware modules comprising the Kea spectrometer. The PAD provides the RF front-end for the spectrometer, interconnecting the high power transmitter amplifier (HPA), low power receiver amplifier, and NMR probe.

In its most rudimentary form the PAD has two roles to fulfill: routing of RF signals between the three front-end components, and amplification of response signals originating within the NMR sample. A PAD module satisfying these requirements was built for the LapSpec spectrometer, which is a variant of the Kea spectrometer, as part of Robin Dykstra's PhD thesis (Dykstra (2006) [52]).

While the LapSpec PAD module provided the spectrometer with a basic RF front end, it lacked wobble (tuning and matching) functionality. Without this functionality it was necessary to connect the NMR probe to a spectrum analyzer and directional coupler each time it required tuning and matching.

Around this time Michael Adams, a RF engineer from Germany, visited the Massey University NMR lab and worked on a new PAD design to fit the LapSpec and Kea spectrometers. The goal of this design was two-fold: to produce a new PAD module without using an expensive commercial pre-amplifier, and to add wobble functionality.

Achieving these goals required a significant set of skills. A knowledge of RF circuit design was a basic necessity, along with computer aided design (CAD) skills for making schematic diagrams and printed circuit boards. RF circuit design is far more challenging than basic electronic design, and integrating directional coupler, duplexer, and pre-amplifier circuitry onto a common circuit board is especially difficult. This is due in part to the presence of highly sensitive detection circuits, high amplifier gains, and enormous signal amplitude variations.

At the conclusion of Adams' work, a new working PAD was available. Shortly thereafter, Adams returned to Germany. His PAD module was used for a short time thereafter, before becoming unavailable, so a replacement module was required. Due to the complexity of the pre-amplifier circuitry, it was decided to use a commercial pre-amp block as the beginning of a new design.

Two new designs were conceived. The first used radio frequency relays to route signals between ports. The second design was closer to Adams' original PAD.

3.2 Design requirements and functionality

There were three requirements the new PAD designs had to satisfy: signal routing, signal amplification, and wobble functionality. These are discussed below, along with descriptions of the functionality.

3.2.1 Signal routing

The first design requirement was signal routing, which involves the careful delivery of radio frequency signals between sources and destinations. Routing of RF signals is required in both normal NMR experiments (normal mode) and in wobble experiments (wobble mode). In normal mode, radio frequency pulses such as $(\pi/2)$ or (π) pulses are routed from the TX amplifier to the probe. Soon afterward the FID or spin-echo response signal from the sample is routed from the probe to the receiver amplifier. In this mode, routing is sequential and fast switching between transmit and receive modes is essential. In wobble mode, low power RF pulses are routed to the probe and the reflected power decoupled by the directional coupler is routed to the receiver at the same time, bypassing the low-noise pre-amplifier. In this mode, transmitting and receiving occurs simultaneously. Signal routing will be discussed further when the two PAD designs are examined.

3.2.2 Signal amplification

The second design requirement was signal amplification. The NMR sample induces a tiny FID or spin-echo signal in the B_1 coil as discussed in §1.4.3 on page 17, and needs significant amplification before it can be digitally sampled. First stage amplification takes place in the pre-amplifier on the PAD module and second and third stage amplification take place on the RX amplifier module. It was vitally important that extraneous noise was not added to the NMR signal, especially prior to first stage amplification. Methods for reducing noise pickup will be discussed in due course. Signal pre-amplification was not required in wobble mode because wobble signal levels already have sufficient amplitude.

3.2.3 Wobble functionality

The third design requirement was wobble functionality, which involves measurement of reflected power. Wobble functionality provides the experimenter with a simple means of tuning and matching the NMR probe to the TX and RX amplifiers. In this mode the TX amplifier delivers relatively low-level RF pulses with swept carrier frequency to the probe while measuring the reflected power. In the case of a perfect match, no power reflection from the probe back to the RF power amplifier will be observed and during receive mode the signal-to-noise ratio of the NMR signal is at maximum. In the general case, impedance matching is imperfect and some incident power is reflected back toward the source.

3.3 PAD relay version design implementation

Fig. 3.1 shows a photograph of the completed PAD relay version. The schematic diagram and printed circuit board layout is shown in Appendix A on page 213. The photo shows the DIN 41612 connector that attaches the PAD to the backplane and the SMA (SubMiniature Version A) and SMB RF connectors that attach to the RF front-end components. A tin wall surrounds the quarter-wave line and parallel crossed diode circuit, and extends behind the pre-amp module. The tin strip walls are mounted through holes in the PCB and attached to the PCB and to each other with solder. The lid for the box is not shown in the photograph. The pre-amp module was attached to the tin strip with screws and mating SMA connectors. The input to the pre-amp is connected to the circuits inside the tin box. The output of the pre-amp connects to a right-angle SMA-to-RG-316 connector and carries signals via 50Ω cable to the tiny RF switch IC located at the crossroads of three 50Ω PCB traces. The black 15V voltage regulator and white optocouplers are located near the backplane connector, spatially separated from the other components. The two RF relays, directional coupler and series crossed diodes are located near to the

front-end RF connectors and interconnected with top layer 50Ω traces. Eight shiny PCB pads indicate the future mounting position of a low-pass filter.

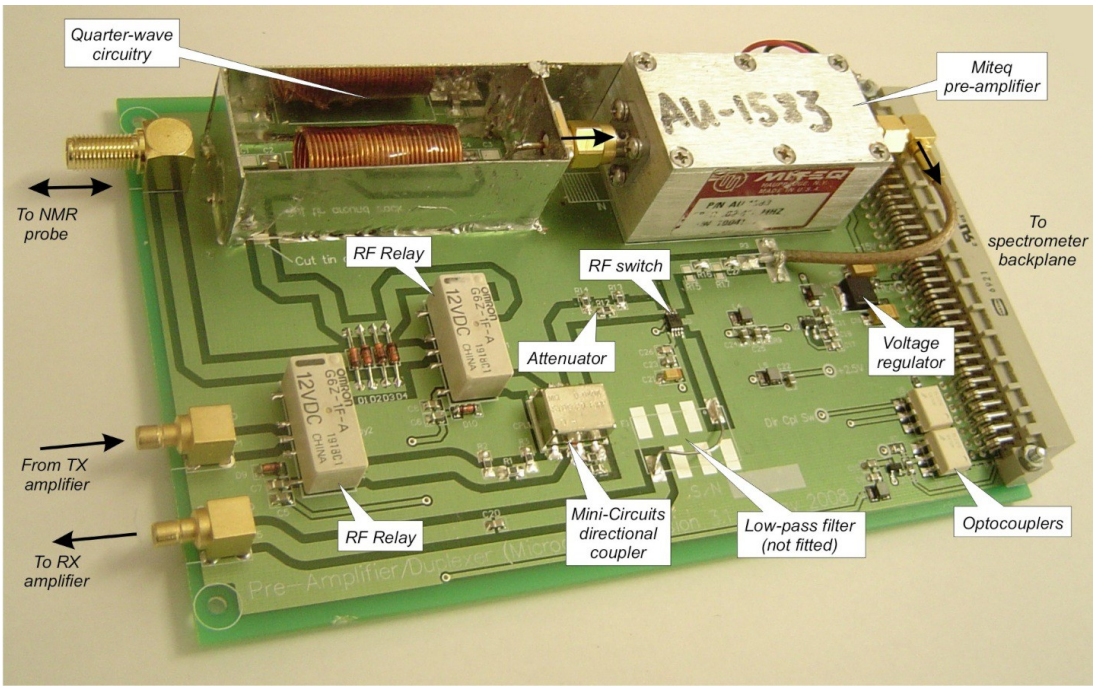

Figure 3.1: PAD relay version 3.1. The shielding box around the $\lambda/4$ circuitry is shown without the tin lid fitted. Earlier PAD versions were not part of this thesis.

Fig. 3.2 illustrates the functional behavior and routing of signals within the PAD relay version. The TX amplifier transmits a RF pulse toward the PAD module. In normal mode the two relays have their contacts set to the TX/RX position and the duplexer routes the signal to the NMR probe. The duplexer then switches to RX mode and routes the sample's response signal from the NMR probe to the pre-amp, RF switch, and low power RX amplifier, which is on the Kea receiver amplifier module. During normal mode operation the directional coupler is not part of the signal path.

In wobble mode the TX amplifier transmits a series of RF pulses toward the NMR probe. The two sets of relay contacts are in the wobble position so the pulses pass through the directional coupler en route. In the absence of a perfect match, power is reflected from the NMR probe B_1 circuit back toward the TX amplifier. A small sample of the reflected power is tapped off by the directional coupler and routed through the RF switch to the RX amplifier.

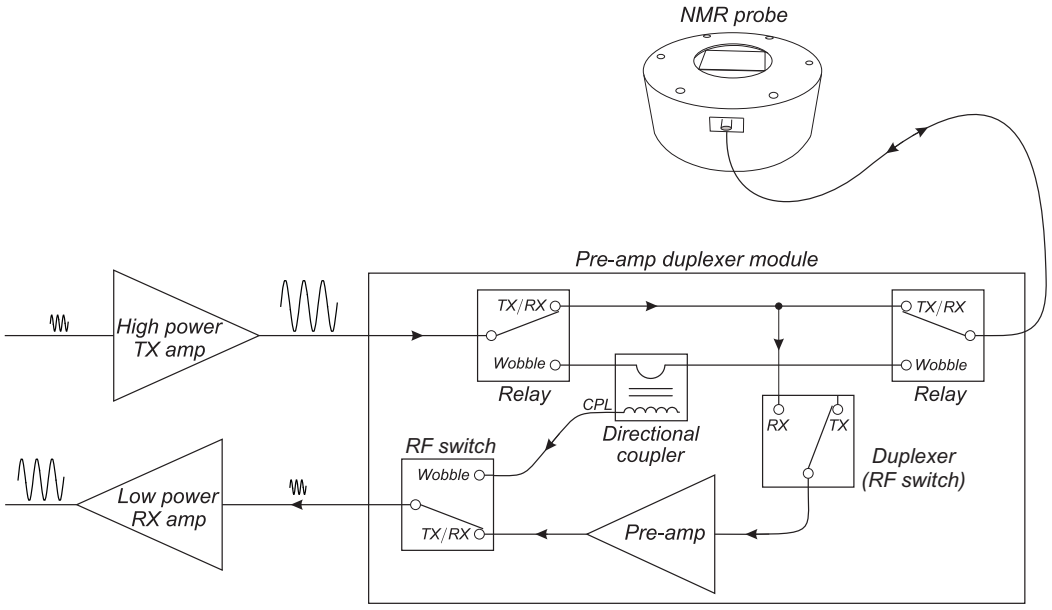

Figure 3.2: The PAD relay version shown in normal mode, ready to route RF pulses to the NMR probe. The duplexer changes from TX to RX to receive the sample's response signal. In wobble mode the duplexer remains in the TX state, the relays and RF switch change from TX/RX to wobble, and reflected signals are routed through the directional coupler CPL port.

3.3.1 Relay considerations

The PAD relay version uses the two single-pole double-throw (SPDT) mechanical RF relays to switch between normal mode and wobble mode. Relays were chosen for switching between modes for several reasons. First, they provide excellent electrical isolation through their mechanical contacts. This allows either the normal mode or wobble mode electronic circuitry to be cleanly switched into the circuit while the other is cleanly switched out of the circuit. The relay coils are de-energized in normal mode rather than wobble mode to reduce power consumption and to reduce the possibility of coupling between the relay coils and low-level FID or spin-echo signals that are passing through the relay contacts. A second benefit provided by relays is isolation of the directional coupler from the mainline when in normal mode. This means the directional coupler cannot introduce any mainline insertion loss or impedance changes and is unable to interfere with the minute FID or spin-echo signals. A third benefit is that the directional coupler is only required to carry the low power wobble mode signals and not the high power RF pulses that are part of

normal experiments. The directional coupler can therefore be a small low power device.

The two-relay design provides an elegant solution for changing between normal and wobble modes. Unfortunately the relays also provided a design dilemma because relay manufacturers offer few small RF relays rated to handle several tens of watts of RF power as required for the Mole probe. RF relays form a small subset of the total relay market and options were found to be very limited. A higher power RF relay that could be sourced was the 250 watt PCB mountable TOHTSU CX-120P but it was physically large and expensive. An alternative was the Omron G6Z RF relay, which was small and reasonably priced. This relay, however, illustrated the second design dilemma, which is interpreting the manufacturer's continuous power rating specifications for pulsed operation. For example, the relay specifications state a maximum carry and switching power of 10W. For $(\pi/2)$ and (π) RF pulse amplitudes shown in Fig. 2.4, the Mole requires about 18W for a duration of 40μs at a duty cycle of around ten percent. The average power delivered to the Mole during a long CPMG sequence is therefore about 18W $\times$ 10% duty cycle = 1.8W. A second example is that the maximum switching voltage is specified as 30VAC RMS and DC while the Mole's (π) pulse requires a peak voltage of about 42.3V. But maximum relay contact voltage is rated under switching conditions while the PAD relays are never switched when voltages are present. A third example is that the carry and switching current ratings are also less than required by the Mole. But again these ratings are for continuous power transfer rather than pulsed operation.

In addition to these ratings, the G6Z relay contacts are designed to operate up to several gigahertz. At higher frequencies skin effects lead to increased resistance, which would reduce the power handling capability of the relay contacts. This fact is probably implicit in the data sheet's insertion loss specification, which shows increased insertion loss with frequency but is irrelevant at the low operating frequency of the Mole probe. Finally, the electrical and mechanical endurance ratings for the switching contacts are rated as hundreds of thousands and one million respectively. The number of switching operations the PAD relays would experience during their lifetime is likely to be a tiny fraction of these numbers. Given the lack of applicability of the relay specifications to the PAD requirements, it is not possible to know whether or not the relays would be reliable for Mole operation over a long time period. Omron Relay and Devices Corporation was contacted regarding rating the contacts for pulsed operation but no specifications were available. The PAD relay version received limited testing during the course of this project for reasons to be discussed in §3.14 and showed no evidence of failure.

Of course the relays may experience significantly worse conditions if the source and load are mismatched. Under fault conditions the Tomco RF amplifier can deliver significantly more than 18W of pulsed power. Power through the relay

contacts could be limited in future designs by using a lower power RF amplifier and by monitoring forward power via the currently unused forward coupled (CPL FWD) port on the directional coupler shown in Fig. 3.6 on page 78. Further protection could be added by having a short automatic wobble test at the beginning of every experiment.

3.4 PAD standard version design implementation

Fig. 3.3 shows two photographs of the completed PAD standard version. The schematic diagrams and printed circuit board layouts are shown in Appendix A on page 213. This PAD shares sections of its design with Adams' PAD discussed previously. The upper photo shows the DIN 41612 connector that attaches the PAD to the backplane and the SMA and SMB RF connectors that attach to the RF front-end components. A milled aluminium box encloses the quarter-wave and directional coupler circuits. The milled box is screwed to the PCB from beneath. A photograph of the milled box with lid is shown in Fig. 3.13 on page 92. The pre-amp module is attached to the PCB via a short piece of tin strip and screws, and also to the milled box through the threaded mating RF connectors. The input to the pre-amp is connected to the circuits inside the milled box. The output of the pre-amp connects to a right-angle SMA-to-RG-316 connector that carries signals via 50Ω cable to the tiny RF switch IC on the circuit board. The black 15V voltage regulator and white optocoupler are located near the backplane connector, spatially separated from the other components. The pre-amplifier RX signal (or wobble signal) passes through the unfitted low-pass filter PCB traces before arriving at the SMB output port. The TX amplifier SMB connector attaches to a short piece of RG-316 cable that carries TX signals into the milled box. The SMA probe connector mounted within the milled box can be seen in Fig. 3.3, and in Fig. 3.13 on page 92. The directional coupler's reflected power signals exit the second hole in the side of the milled box via RG-316 cable, thereafter passing through a π attenuator before reaching the RF switch.

The completed module shown in the photos was modified after it was built, due to complexities arising around the RF switch biasing and pre-amp levels. The modifications are shown in Fig. 3.12 on page 89 and are discussed in due course.

Fig. 3.4 illustrates the functional behavior and routing of signals within the PAD standard version. There are no relay contacts so TX amplifier RF pulses go directly to the duplexer, through the directional coupler and on to the NMR probe. The duplexer then switches to RX mode to route the response signal to the pre-amp and on to the RX amplifier. The directional coupler is always part of the

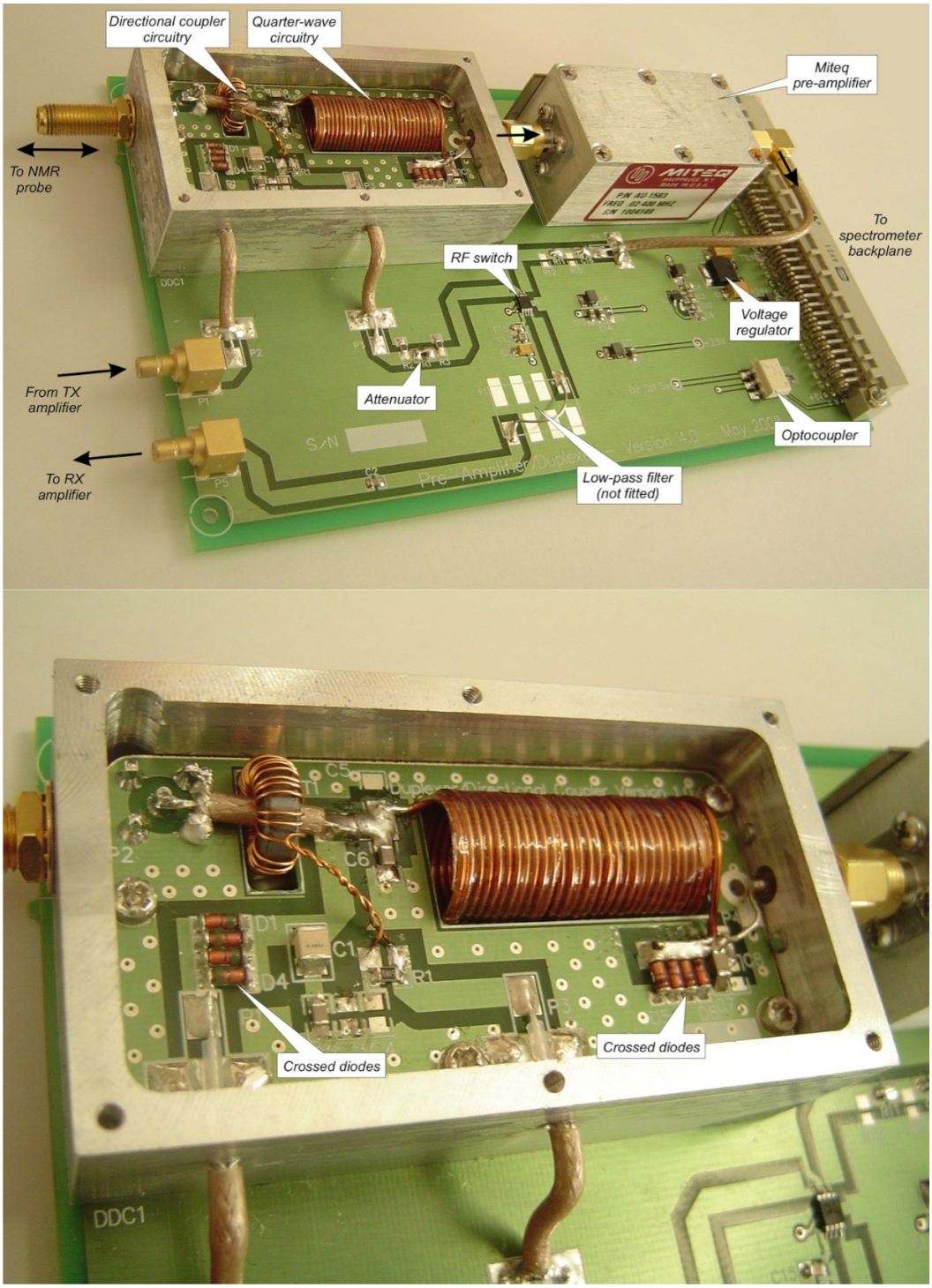

Figure 3.3: PAD standard version 4.0 and enlarged milled box containing the duplexer and directional coupler circuitry. Earlier PAD versions were not part of this thesis.

electronic circuit. Wobble mode behavior is similar to the PAD relay version.

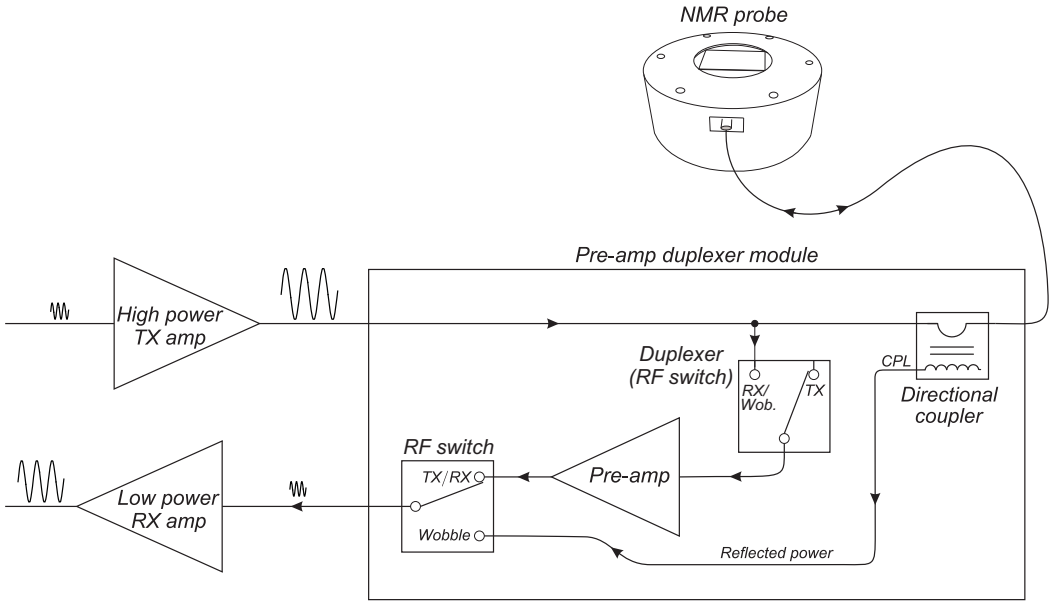

Figure 3.4: The PAD standard version shown in normal mode, ready to route RF pulses to the NMR probe. The duplexer changes from TX to RX to receive the sample's response signal. In wobble mode the duplexer remains in the TX state, the RF switch changes from TX/RX to wobble, and reflected signals are routed through the directional coupler CPL port.

Following the FID or spin-echo signal, the duplexer switches from RX mode back to TX mode in readiness for the next RF pulse. The PAD must be capable of routing these signals quickly, and to their correct destination. The electronic circuitry used to implement the duplexer will be discussed in the next section.

3.5 The duplexer

The duplexer is a radio frequency switch that routes signals depending upon their amplitude. The duplexer used in the PAD designs is constructed from diodes and a lumped element quarter-wave line. These will now be discussed in turn.

3.5.1 Diode switches

Diodes are used to route RF signals because of their ability to behave as electrical switches. When reverse biased, diodes switch off and do not conduct. When

forward biased, diodes increasingly conduct as forward voltage V_F increases. The diodes used in the PAD design have forward current $I_F \approx 1\mu A$ when $V_F \approx 250\mu V$ and increase to around $I_F \approx 1,000mA$ when $V_F \approx 700mV$.

Two sets of crossed diodes are used on each PAD module as shown in Fig. 3.5. Each set consists of four diodes arranged as anti-parallel pairs. The BAV21 (Fairchild [42]) and BAV103 (Fairchild [41]) diodes appear from the data sheets to be identical except the former is a leaded device and the latter a surface mount device. Leaded devices were used on the PAD relay version to simplify PCB trace routing.

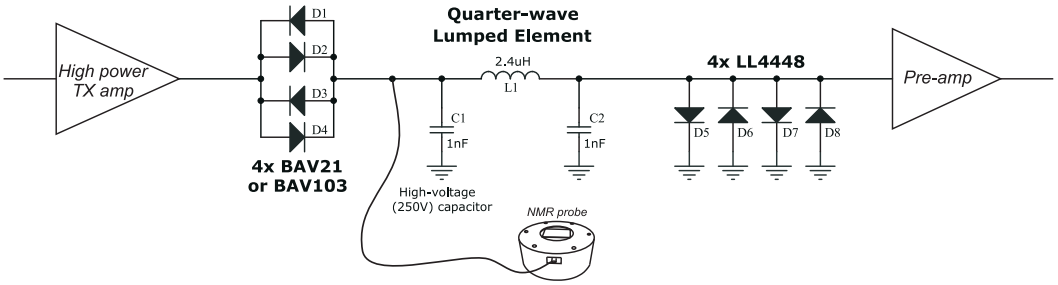

Figure 3.5: A section of circuitry from both PADs showing the crossed diodes and quarter-wave line arrangement with respect to the amplifiers and NMR probe.

The main function of the BAV crossed diodes D1-4 in series with the TX amplifier output is to isolate the probe and pre-amplifier input from the noisy TX amplifier during receiving the NMR signal. In normal mode the TX pulses are large, enabling two of the crossed diodes to conduct during each half cycle of the RF pulses. The BAV diodes are considerably slower at switching than the LL4448 diodes (50ns compared to 4ns) but have higher peak current handling capability (3.7A per device compared to 1.6A per device). Following a TX pulse the only voltage present on the probe side of the diodes is from the tiny FID or spin-echo response signal (ignoring probe ring-down), which is insufficient to cause the BAV diodes to conduct, therefore the TX amplifier is isolated from the probe.

The LL4448 diodes (Philips [118]) also conduct during the large TX pulses. During each TX pulse they work alongside the quarter-wave line to block the large amplitude TX amplifier pulses from reaching the sensitive pre-amp. At the conclusion of the TX pulse all diodes are switched off. Unlike the BAV diodes the LL4448 diodes do not block the tiny response signal's path. The response signal has insufficient amplitude to bring the LL4448 diodes into forward conduction and is therefore routed into the pre-amplifier.

In wobble mode the PAD relay version uses its relays to remove both sets of diodes from the circuit. By contrast, both sets of crossed diodes on the PAD

standard version remain in circuit in wobble mode, and are driven into conduction during wobble pulses.

3.5.2 Quarter-wave line

A quarter-wave ($\lambda/4$) line is a transmission line one-quarter wavelength in length. A $\lambda/4$ line with characteristic impedance Z_0 has the mathematical property:

$$Z_S Z_L = (Z_0)^2 \tag{3.1}$$

where Z_S is the source impedance looking to the transmission line and Z_L is the load impedance terminating the transmission line (Horowitz and Hill (1990) [79]). The value of Z_0 is a fixed property of the transmission line, therefore the $\lambda/4$ line behaves as an impedance transformer for Z_S and Z_L.

A $\lambda/4$ line is constructed from lumped elements C1, C2 and L1 as shown in Fig. 3.5. The capacitors have identical values; at the frequency corresponding to $\lambda/4$ the capacitor and inductor impedances are conjugates, leading to two potential resonant circuits. The first resonant circuit appears if the load impedance Z_L is open circuited. In this instance L1 and C2 form a series resonant circuit, which appears to the source as a short circuit. The second resonant circuit appears if the load impedance Z_L is short circuited. In this instance C2 is short circuited, leaving C1 and L1 to form a parallel resonant circuit that appears to the source as an open circuit.

These properties of the $\lambda/4$ line are very useful when coupled with crossed diodes arranged as shown in Fig. 3.5. When the TX amplifier delivers high power pulses to the probe, the BAV diodes and the LL4448 diodes conduct. The LL4448 diodes short circuit the $\lambda/4$ line making it appear open circuit to the high power RF pulses. Almost all of the energy from the TX amplifier is therefore reflected to the NMR probe. When the tiny response signal appears from the probe, it is blocked by the BAV diodes and is instead routed through the quarter-wave line to the pre-amp input. The $\lambda/4$ line and 50Ω pre-amp input appear together as a 50Ω load.

It should be noted that capacitor C1 experiences the full TX amplifier voltage and is rated accordingly. Capacitor C2 is protected from the high TX amplifier voltages by the LL4448 crossed diodes.

3.6 Directional couplers

Directional couplers are 3-port devices useful for measuring power flow in a single direction. Bi-directional couplers have an additional port, enabling simultaneous measurement of power flow in forward and reverse directions. The majority of

power transferred through a directional coupler occurs between the mainline in and out ports. The ancillary coupled (forward) and coupled (reverse) ports tap off a small sample of the mainline power depending upon the direction of power flow. Directional couplers have an essential role in protecting RF power amplifiers from load mismatch (Norman and Dye (2001) [51]) and in tuning and matching NMR probe circuits. The directional couplers implemented on the two PAD modules are now discussed in turn.

3.6.1 PAD relay version directional coupler

A schematic drawing of the directional coupler used in the PAD relay version is shown in Fig. 3.6. The only commercial Mini-Circuits part suitable for operation at the Mole frequency and having 50Ω impedance was the SYDC-20-61HP+ bi-directional coupler (Mini-Circuits [108]). Since only reflected power was of interest, the coupled (forward) port (CPL FWD) was terminated with 50Ω as shown in Fig. 3.6. The Mini-circuits coupler has a specified coupling coefficient of 20dB, thus the ratio of mainline to coupled power is 100:1 when all ports are ideally terminated. The power rating of the directional coupler is 15W maximum. This should never be exceeded on the PAD module because the directional coupler is switched out of the circuit by the relays during high power NMR experiments, and only switched into the circuit during low power wobble experiments.

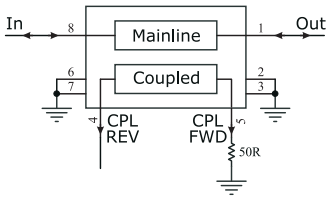

Figure 3.6: A schematic representation of the commercial Mini-Circuits SYDC-20-61HP+ bi-directional coupler with CPL FWD port terminated with 50Ω. According to the manufacturer's specifications, optimal performance requires pins 2, 3, 6, and 7 to be connected to ground as shown (Mini-Circuits App Note [109]).

3.6.2 PAD standard version directional coupler

A schematic drawing of the PAD standard version directional coupler is shown in Fig. 3.7. This directional coupler was not a commercial off-the-shelf component. It was instead built from capacitors C1 and C2, resistor R1, and hand-constructed transformer T1. The design for the directional coupler is not original; Adams used

a similar design in his PAD module and similar designs can be found in Radio Frequency Transistors (Norman and Dye (2001) [51]), Radio-Frequency Electronics (Hagen (1996) [66]) and a QST paper from 1959, which appears to be the original published design (Bruene (1959) [23]).

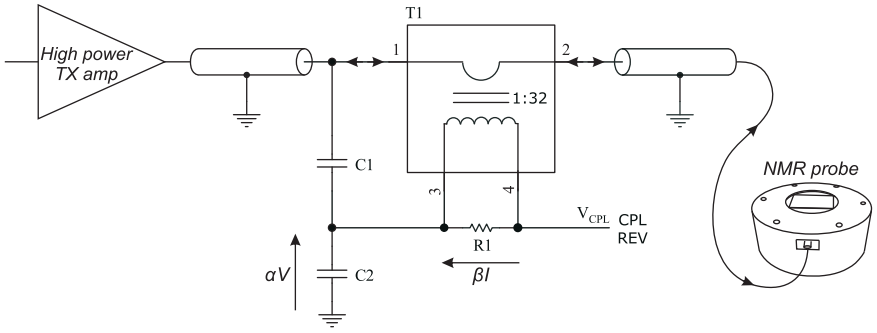

Figure 3.7: The directional coupler circuit consisting of C1, C2, R1 and T1 is built into the PAD standard version. A sample of the reflected power is routed to the CPL REV port. αV and βI indicate the voltages across C1 and R1 respectively.

The directional coupler is always part of the PAD circuit but in normal mode its CPL REV output is ignored. In wobble mode the TX amplifier sends a series of low power RF pulses to the NMR probe. The pulses have $\sim$30μs duration and 1ms separation, and the lower and upper frequencies within the pulses are specified by the experimenter. The B_1 circuit is tuned and matched at only one frequency, so all other frequencies reflect some incident power back toward the TX amplifier as indicated by the arrows in the mainline in Fig. 3.7. A small sample of the reflected power arrives at the CPL REV port.

The directional coupler circuit calculates reflected power by measuring the transmission line voltage V and current I at a single location. Voltage V is a superposition of incident (forward) and reflected (reverse) traveling waves V_F and V_R, and current I is the sum of the incident and reflected currents I_F and I_R. The directional coupler circuit in Fig. 3.7 measures only the reverse traveling waves – although it is relatively simple to modify the circuit to measure power flow in both directions. The following analysis of the directional coupler circuit shown in Fig. 3.7 shows how reflected power is calculated (Hagen (1996) [66]).

Voltage V on the mainline consists of forward and reverse traveling components:

$$V = V_\mathrm{F}\, e^{-jkx} + V_\mathrm{R}\, e^{jkx} \tag{3.2}$$

and similarly for mainline current I:

$$IZ_0 = V_{\mathrm{F}}\, e^{-jkx} - V_{\mathrm{R}}\, e^{jkx} \tag{3.3}$$

which can be solved for V_{F} and V_{R} as follows:

$$V_{\mathrm{F}} = (V + IZ_0)\frac{e^{jkx}}{2} \tag{3.4}$$

$$V_{\mathrm{R}} = (V - IZ_0)\frac{e^{-jkx}}{2}. \tag{3.5}$$

The phase component of the traveling waves $e^{j\omega t}$ is ignored for simplicity. To measure V_{R} the directional coupler circuit needs to compute Eqn. 3.5 from the mainline voltage V and current I. The mainline voltage and current are not measured directly; instead a small voltage sample is measured using the capacitive voltage divider and a small current sample is measured through the transformer. The sampled current is converted to a voltage across resistor R1. Assuming the voltage across C2 is αV and across R1 is βI as shown in Fig. 3.7, the voltage V_{CPL} at the CPL REV port is:

$$V_{\mathrm{CPL}} = \alpha V - \beta I. \tag{3.6}$$

In the case of $\beta/\alpha = Z_0$, Eqn. 3.6 becomes:

$$\begin{aligned} V_{\mathrm{CPL}} &= \alpha(V - IZ_0) \\ &= \alpha([V_{\mathrm{F}}\, e^{-jkx} + V_{\mathrm{R}}\, e^{jkx}] - [V_{\mathrm{F}}\, e^{-jkx} - V_{\mathrm{R}}\, e^{jkx}]) \\ &= (2\alpha e^{jkx})V_{\mathrm{R}} + 0V_{\mathrm{F}}. \end{aligned} \tag{3.7}$$

For $\beta/\alpha = Z_0$, the forward traveling waves cancel leaving only the reverse traveling waves in the computation. Capacitor, resistor and transformer values necessary for nulling forward traveling waves are calculated by setting $V_{\mathrm{CPL}} = 0$. Eqn. 3.6 then simplifies to:

$$\alpha V = \beta I. \tag{3.8}$$

Voltage βI is equal to the current through resistor R1 multiplied by its resistance. The resistor current is a fraction of the mainline current by the primary-to-secondary turns ratio, therefore voltage βI is:

$$\beta I = \left(I \times \frac{N_{\mathrm{P}}}{N_{\mathrm{S}}}\right) \times R1. \tag{3.9}$$

The transformer has a single primary turn and thirty-two secondary turns. This was the maximum number of turns of 0.315mm core-diameter copper wire (RS 357-722) that could fit around a small ferrite core (Amidon FT37-43). Using the turns ratio, Eqns. 3.8 and 3.9 simplify to:

$$\alpha V = \frac{I}{32} \times \mathrm{R1} \tag{3.10}$$

and since $V/I = Z_0$ for forward or reverse traveling waves:

$$Z_0 = \frac{\mathrm{R1}}{32 \times \alpha}. \tag{3.11}$$

If the capacitive voltage divider ratio α is 1/32, R1 = Z_0 which is the 50Ω characteristic impedance. 51Ω was a suitable available value for R1. Suitable capacitor values can be calculated:

$$\frac{1}{32} = \frac{\mathrm{C1}}{\mathrm{C1} + \mathrm{C2}} \approx \frac{30\mathrm{pF}}{30\mathrm{pF} + 1\mathrm{nF}}. \tag{3.12}$$

Additional PCB component footprints were placed in parallel to C2 in case additional trimming was necessary. Capacitor C1 is rated for the full mainline voltage (ATC [33]).

Inserting the directional coupler into the mainline has the effect of adding a small resistance and capacitance to the signal path. The resistance R1 viewed from the mainline is modified by the square of the transformer turns ratio so that 51Ω appears as a tiny series resistance:

$$51\Omega \times \left(\frac{1}{32}\right)^2 \approx 50\mathrm{m}\Omega, \tag{3.13}$$

and the two series capacitors load the mainline with a tiny capacitance:

$$\frac{1}{\mathrm{C1}} + \frac{1}{\mathrm{C2}} = \frac{1}{30\mathrm{pF}} + \frac{1}{1\mathrm{nF}} \approx 29\mathrm{pF}. \tag{3.14}$$

The transformer secondary wires must be soldered to the PCB with the correct polarity for the directional coupler to measure reflected power. The wires are twisted as shown in the photographs to minimize magnetic coupling. A typical wobble signal detected at the directional coupler CPL REV port and displayed in Prospa is shown in Fig. 3.16 on page 98.

3.7 Pre-amplification

The pre-amp is a very important part of the spectrometer as it provides the first stage amplification for the raw NMR signal from the NMR sample/probe. In

addition to providing gain, the pre-amplifier must also provide fast recovery from TX amplifier RF pulses that appear at the pre-amp input. In the absence of fast recovery the pre-amplifier will not be ready to amplify the spin-echo signal from the sample. It is very important that the pre-amp adds as little noise as possible to the NMR signal.

The pre-amp that was used on the two PAD boards was a commercial Miteq AU-1583 fast recovery NMR amplifier module (Miteq [110]) with specified minimum power gain of 36dB, operating frequency range from 0.2MHz up to 400MHz, and noise figure of 1.2dB. The pre-amp was shown previously, mounted on the two different PAD modules in Figs. 3.1 and 3.3. The Miteq online catalog lists twelve fast recovery NMR pre-amp modules (2010) but only two are suitable for the Mole's low operating frequency. The other ten pre-amp modules do not operate at frequencies below 10MHz.

After pre-amplification, further amplifier stages are provided by two cascaded Analog Devices AD8369 integrated circuits located on the low power RX amplifier module. The gains of the two AD8369 amplifiers are digitally controlled via Prospa macros using the Rx Gain (dB) setting shown in Fig 2.4 on page 32. The combined voltage gains of the AD8369 amplifiers can be set between –10dB and +70dB. For all experiments in this thesis, their voltage gain was set to +40dB.

Future PAD designs should consider pre-amplifiers with lower noise figures. The Miteq AU-1583 has a noise figure of 1.2dB. Adams claimed an average noise figure for his five pre-amp modules of 0.9dB (Adams (2005) [12]). Advanced Receiver Research (AR^2) claim their entire range of GaAsFET NMR pre-amps have noise figures of 0.5dB (AR^2 [126]). The AR^2 devices have lower gains than the Miteq pre-amp (26dB versus 36dB) but this can be countered by increasing the spectrometers low power RX amplifier gain with the added benefit of reduced noise figure in the receiver amplifier (AD8369 data sheet [45]).

3.8 Pi attenuators

Pi and Tee attenuators are small networks often made from resistors and connected in π or T arrangements. They are also knows as PADs and should not be confused with the Pre-Amp Duplexer.

Attenuators provide a simple method for limiting RF power transfer around a circuit while also maintaining or transforming impedances. Pi attenuator networks as shown in Fig. 3.8 were used in the PAD designs to limit the power levels entering the RF switch IC inputs and to limit wobble power passing through the directional coupler circuit on the PAD relay version.

By carefully choosing resistor values, the attenuator can reduce power transfer, and be made to have 50Ω impedance in both directions when the source and load

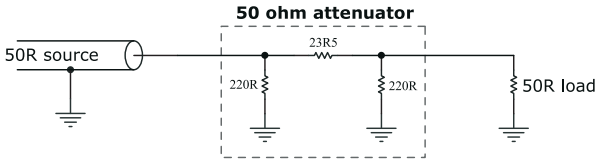

Figure 3.8: A 50Ω 4dB π attenuator.

are also 50Ω. The attenuation provided by the 50Ω attenuator shown in Fig. 3.8 is 4dB; this reduces the power to the load to 40% of the incident power:

$$10log_{10}\left(\frac{40}{100}\right) = -4\text{dB}. \tag{3.15}$$

In cases where the attenuator circuit is not required the 23.5Ω resistor is replaced with a 0Ω resistor and the 220Ω resistors are omitted.

3.9 Power supplies

The PAD modules receive +24V DC from the spectrometer backplane. This voltage is regulated down to +15V using U1 (On Semiconductor, MC78M15 [135]) and to +2.5V using U2 (National Semiconductor, LP2992 [134]) as shown in Fig. 3.9.

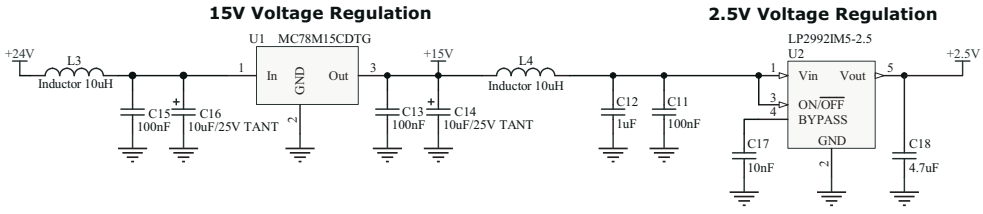

Figure 3.9: Two linear voltage regulators in series, used to reduce the +24VDC supply to +15V, and then to +2.5V. The voltage rails are AC-decoupled from each other using radio frequency inductors.

The 15V power supply is required to power the Miteq pre-amp module, and the two +12V relays on the PAD relay version. The pre-amp requires a nominal 45mA and the relays have coil resistances of 720Ω. The +2.5V power supply has a

quiescent current of 100μA and a load of about 3mA. The total current requirement I at +15V is therefore:

$$I = 45\text{mA} + \left(2 \times \frac{15\text{V}}{720\Omega}\right) + 3\text{mA} \approx 90\text{mA}. \tag{3.16}$$

Power dissipation in the +15V regulator is:

$$\text{P} = (24 - 15)\text{V} \times 90\text{mA} = 0.81\text{W} \tag{3.17}$$

which is slightly below the allowable 1W maximum power dissipation for DPAK devices without heat-sinking. Maintaining a low operating temperature is beneficial for device reliability so the circuit board was designed with a large copper area for soldering the regulator to, thereby achieving both good heat-sinking and mechanical anchoring. To minimize transient coupling through the power rails, several capacitors and inductors were connected to the regulators as shown in Fig. 3.9. These decouple the power rails from each other; C16 is required for 78M15 stability.

The two relays are switched on only in wobble mode, therefore the +15V standing load is about 0.4W for both PAD designs. If a future battery powered spectrometer was to use this PAD design, the effects of de-powering and re-powering the pre-amp during experiments should be researched as this would further reduce power consumption. The Miteq data sheet makes no mention of de-powering and re-powering the amplifier. Power consumption could also reduced by changing from single-sided stable relays (Omron G6Z-1F-A) to double-winding latching relays (Omron G6ZK-1F-A [114]), however this would require additional electronics to pulse the set and reset relay coils.

3.10 Relay and RF switch control

Fig. 3.10 shows the electronic circuit used to set the PAD operating mode. Optocoupler U4 was used to control the relays and optocoupler U5 was used to control the RF switch changeover contact position. For the PAD standard version only optocoupler U5 was required. The operating mode was determined by a control signal on the Kea backplane. For normal mode the control signal voltage is around 0V (logic “0”) and for wobble mode the voltage is around +3.1V (logic “1”).

The control line from the backplane enters the PAD module and is immediately electrically isolated by the optocoupler(s) to minimize the noise entering the PAD (Fairchild, 4N35 [43]).

When the control line is set to logic “0” there is no optocoupler light emitting diode (LED) current and the phototransistor(s) are switched off. In this state the

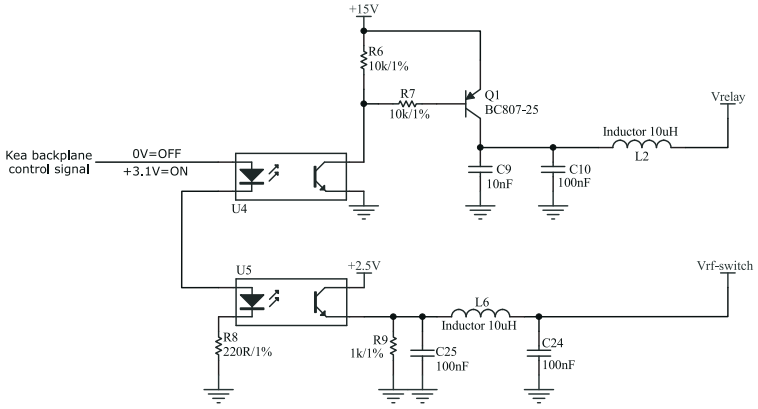

Figure 3.10: The opto-isolated circuit for controlling the relays and RF switch.

voltage $V_{\text{rf-switch}}$ shown in Fig. 3.10 is pulled low through resistor R9 causing the RF switch to route signals from the pre-amp to the receiver amplifier. For the PAD relay version the high-side transistor Q1 would also be off, thereby ensuring no power is delivered via V_{relay} to the relay coils.

Toggling the control line level from logic "0" to logic "1" causes the optocoupler LED(s) to turn on. Optocoupler LED current needs to be sufficient to drive the phototransistor and attached circuit while not being overdriven. The 4N35 optocouplers used on the PAD have a specified current transfer ratio (CTR) of 100% minimum at 25°C, therefore every 1mA through the LED allows at least 1mA to pass through the phototransistor.

To determine the required optocoupler LED current, the optocoupler load needed to be calculated. Referring to Fig. 3.10, the relay load attached to V_{relay} is $2 \times (15\text{V}/720\Omega) = 42\text{mA}$. The BC807 PNP transistor supplying the relays is specified as having a minimum DC current gain of around 100 at 25°C and 100mA collector current I_{C}. To cope with $\sim 50\text{mA}$ relay load, the base current needs to be 0.5mA, thus the required base resistance is:

$$R_{\text{B}} = \frac{15\text{V} - V_{\text{BE}} - V_{\text{CE}}}{I_{\text{B}}} = \frac{(15 - 0.7 - 0.1)\text{V}}{0.5\text{mA}} \approx 28,400\Omega \tag{3.18}$$

where V_{BE} is the voltage dropped across the transistor Q1 base-emitter junction, V_{CEO} is the voltage dropped between the optocoupler collector-emitter, and I_{B} is the transistor's base current. Using a standard 10kΩ resistor to drive the transistor base harder is satisfactory and well within the transistor specifications. Resistor R6 ensured the transistor would turn off; using the same value as R7 minimizes the number of different components and is a suitable value. The optocoupler transistor

therefore needs to sink approximately:

$$I_{\text{CEO}} \approx \frac{15\text{V}}{5\text{k}\Omega} = 3\text{mA}. \tag{3.19}$$

The optocoupler LEDs are required to pass the same current. A 3mA current through the optocoupler diode results in a forward voltage drop V_{F} of $\sim$ 1.1V. The logic "1" control line voltage on the backplane provides 3.1V due to a 3.3V regulator and 74LVT245 octal transceiver on the DSP module. For the two LEDs in series on the PAD relay version the required series resistance is therefore:

$$R = \frac{V_{\text{F}}}{I_{\text{F}}} = \frac{(3.1 - 1.1 - 1.1)\text{V}}{3\text{mA}} \approx 300\Omega. \tag{3.20}$$

The optocoupler should be given some current overhead for worst case conditions, therefore 220Ω is satisfactory. A similar calculation can be made for the single optocoupler circuit on the PAD standard version design.

The RF switch is controlled by $\text{V}_{\text{rf-switch}}$ in Fig 3.10. The RF switch power supply comes from the +2.5V regulator; with this supply voltage the RF switch input logic levels are specified as $V_{\text{INH}} = 1.7\text{V}$ minimum for logic high and $V_{\text{INL}} = 0.7\text{V}$ maximum for logic low. The optocoupler driving the RF switch CTRL line has a V_{CEO} voltage drop of about 200mV due to resistor R9, therefore $V_{\text{INH}} = (2.5 - 0.2)\text{V}$, which is well within specification.

3.11 RF switch biasing

The RF switches discussed in §3.3 and §3.4 are Analog Devices ADG918 8-pin surface-mount integrated circuits (Analog Devices [47]). The ADG918 is similar to a SPDT switch with pins for common, normally open and normally closed. The Analog Devices data sheet denotes the pins RFC, RF1 and RF2 as shown in Fig. 3.11. The position of the switch changeover contact is controlled by the optocoupler circuit $V_{\text{rf-switch}}$. A logic "0" from the optocoupler connects RF2 and RFC while isolating RF1, and a logic "1" connects RF1 and RFC while isolating RF2. The isolated port is terminated internally with 50Ω.

From this description, the ADG918 would appear to be a simple switch component that routes signals depending upon the state of its logic input. This is indeed true when signals at the switch inputs remain within specified bounds. However, when signals stray outside the boundaries the switch becomes less than ideal.

An example encountered in this project was signals at the off channel input affecting signals passing through the switch's on channel. According to a footnote in the ADG918 data sheet, the absolute maximum voltage between RF1 or RF2 and ground in their respective off states is between -0.5V and $V_{\text{DD}} - 0.5\text{V}$, where

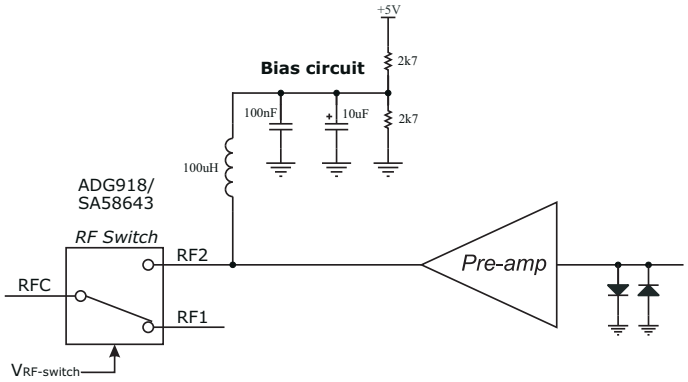

Figure 3.11: The RF switch circuit used for both PAD designs, shown in wobble mode. Modifications to the PAD standard version included changing the ADG918 to a SA58643 and addition of the bias circuit as discussed in the text.

$V_{\mathrm{DD}} = 2.5\mathrm{V}$. This defines a voltage window of $-0.5\mathrm{V}$ minimum to $+2.0\mathrm{V}$ maximum. When testing the PAD standard version in wobble mode it was found that the lower limit was being exceeded, resulting in loss of channel isolation and distortion of wobble signals at the RF switch output.

The loss of channel isolation was tested separately by attaching a signal generator to the off-channel RF2 while sending wobble pulses through the switch from RF1 to RFC. The signal generator frequency was set to 3.25MHz and the AC amplitude to $400\mathrm{mV_{p\text{-}p}}$. No obvious distortion of the wobble pulses was observed even with +6V DC offset on the signal generator, but below a DC offset of $-300\mathrm{mV}$ the wobble pulses became distorted.

The reason the lower window threshold was being exceeded on the PAD standard version in wobble mode was that the $\lambda/4$ line and shorted LL4448 diodes cannot fully block the wobble signal from reaching the pre-amp. The pre-amp boosted the signal and delivered it to RF2, where it was measured at voltages between $-1.3\mathrm{V}$ and $+0.9\mathrm{V}$ (into the internal RF switch 50Ω resistor).

One means of ensuring signals did not exceed the minimum window value at RF2 was to diode clamp them either side of ground using fast back-to-back LL4448 diodes. The LL4448 forward voltage however is marginal in terms of the $-0.5\mathrm{V}$ lower window limit.

An alternative solution was to add a DC bias to the AC coupled pre-amp output to shift the signal within the window, but this would have been poor design practice as the signal magnitude was close to the window limits and the necessary DC bias was outside the recommended upper limit of 0.5V. This upper limit is due to CMOS switch insertion losses that increase exponentially with increasing bias

voltage (Analog Devices [46, 48]). In addition, as the signal frequency decreases below 50MHz, the ADG918 1dB compression point decreases dramatically from around 16dBm to 12dBm. This is due to two factors: The first is that the parasitic diodes in the NMOS transistors becomes forward biased. They have longer to turn on for lower frequency signals and therefore cause greater signal attenuation. The second reason is that at lower frequencies, the shunt transistors in the off state partially turn on thereby passing some of the signal power to ground. The issues are discussed in the Analog Devices references.

A third solution was to reduce the signal amplitude at RF2 by fitting the attenuator components, but this would have led to the undesirable consequence of also reducing FID and spin-echo signals.

The fourth solution was to find an RF switch with better power handling capability. The Philips SA630D and NXP SA58643 (NXP [119]) SPDT switches were alternatives with higher supply voltage and power ratings. Both devices appeared to have identical specifications, differing only in pinout and package. The SA630D/SA58643 supply voltage V_{DD} was +5V compared to +2.5V for the ADG918, and the absolute maximum power rating for the three switch inputs and outputs was 20dBm ($6.3V_{p\text{-}p}$) compared to 18dBm ($5.1V_{p\text{-}p}$). The 1dB compression point near Mole frequencies is 18dBm for the SA58643 compared to 12dBm for the ADG918. The older SA630D was available in both through-hole and SO8 surface mount packages; the newer SA58643 was available in the tiny TSSOP8, which was the same component footprint as the ADG918. It was decided to use the NXP device rather than the Philips device as it was cheaper, and the PCB footprint and pinout were closer to the existing ADG918.

Testing the NXP device using a function generator revealed similar behavior to the ADG918. Reducing the off-channel input voltage below −500mV affected the on-channel signal, but no side effects were observed when increasing the offset to +7V. Unfortunately there was no information regarding DC biasing in the NXP data sheet, and no application note. A DC bias level of around +2.5V was therefore applied as shown in Fig. 3.11, and used successfully for the remainder of this project. The 100μH inductance is capable of passing 10mA and presents an impedance of around 2kΩ at Mole frequencies, thus isolating the DC bias capacitors from RF signals.

The NXP device was carefully soldered above the circuit board as shown in Fig. 3.12 because of slightly different pinouts. The bias circuit consists of two leaded resistors, two capacitors, and one inductor as shown. The LP2992 voltage regulator was changed from a +2.5V to a +5V version to power the new RF switch.

The bias circuit worked well but needs refining in future revisions. If the SA58643 switch behaves like the ADG918 the bias level should be reduced to reduce signal compression. The bias components should be surface mounted to

minimize parasitic inductance and capacitance. The 100μH inductor (Radio Spares 182-6695) has a specified self resonant frequency of 12MHz, which must be kept distant from the operating frequency. RF switch inputs should be also be diode clamped for input protection as transient voltages at the pre-amp input may appear at the pre-amp output.

The PAD relay version did not experience the problems described above for the PAD standard version because signals arrive at either RF1 via the directional coupler or at RF2 via the pre-amp. The arrangement of relay contacts does not allow both signals to be present at the RF switch simultaneously, thus the off-channel voltage window can never be exceeded. The problems also did not occur in the PAD standard version in normal mode. This is because the off-channel RF switch port receives only reflected power signals, and these are insignificant under normal matched conditions, and temporally separated from the FID or spin-echo signals.

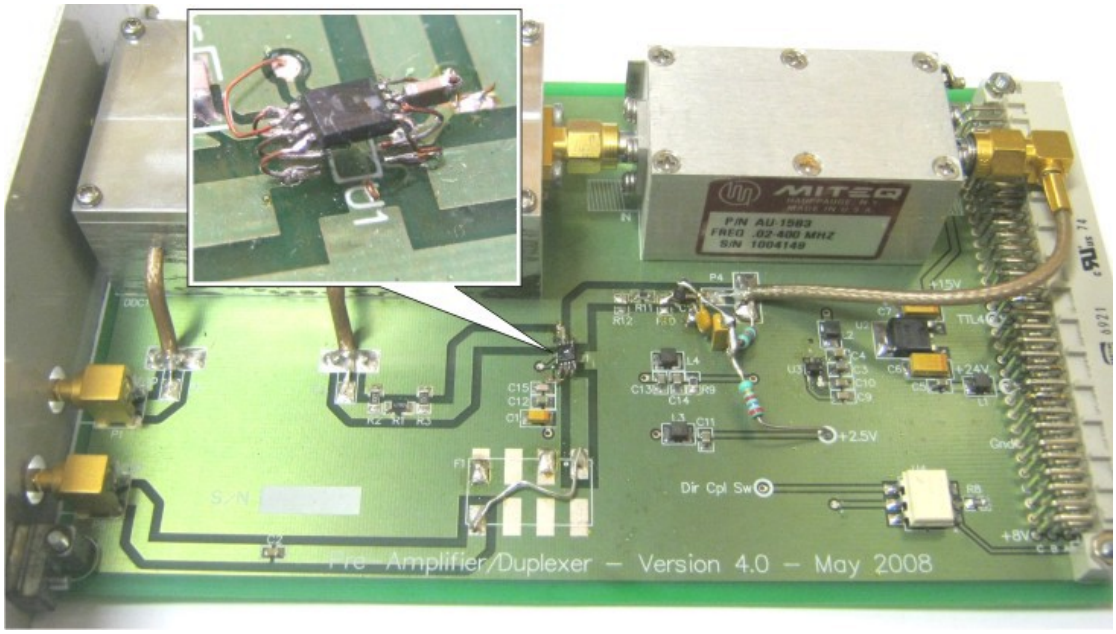

Figure 3.12: Pre-amp duplexer module version 4.0 showing replacement RF switch and biasing components.

3.12 Printed circuit board design

The two (plus one) PAD printed circuit boards were designed using a computer aided design (CAD) schematic capture and PCB layout package (Altium [14]). The electrical drawings were entered into the schematic program, then the PCB program was used to lay out the circuit boards using physically realistic components and copper traces. Full printed circuit board layouts are shown in Appendix A beginning on page 213.

The following steps were taken when designing each PAD module: The electrical circuits were designed on paper and entered into the schematic capture program. All unavailable schematic and PCB component definitions were designed in the Altium libraries. PCB component footprints and hole sizes were carefully checked to ensure they accurately represented the physical components. Placement of the PCB backplane and RF connectors was carefully calculated to fit the existing backplane connector and front panel RF connector holes. PCB microstrip traces were dimensioned for 50Ω impedance. PCB trace routing was carefully considered to minimize crosstalk.

When designing high frequency circuits, it is important to match impedances and to separate PCB traces to reduce coupling. The Mole frequency is toward the low end of the radio frequency spectrum so good high-speed design practices may not be essential, but it was wise to implement them for at least two reasons: First, because the contrary could lead to unknown outcomes, necessitating changes to the design. Second, following good design principles increases the likelihood that the PAD will operate reliably in possible higher frequency applications.

Designing 50Ω traces (strip-lines) on double sided 1.6mm FR4 fibre glass circuit board requires careful dimensioning of trace widths and separations. The traces should be 2.74mm wide, have 1.58mm separation to the surrounding same-layer ground plane, and have a solid copper ground plane directly beneath the trace on the opposite PCB layer (Carr (2001) [28]). Whenever a 50Ω PCB trace changes direction by ninety degrees within the same layer, a carefully dimensioned chamfer needs to be added to maintain the impedance (Harper (2005) [68]); these practices can be seen on the PCB layouts. In addition, manufacturers specify how their components should attach to PCB traces in order to match component impedances to the PCB traces. For example, Mini-Circuits couplers and Omron RF relays specify PCB layout requirements necessary for impedance matching, and include orientation and width of PCB traces and vias. These design rules were followed for both PAD PCB designs. The PCBs were designed with maximal copper ground planes on the top and bottom layers to maximize shielding.

3.13 EMI shielding and the milled box

When designing the PAD modules, shielding against EMI was an important design consideration for several reasons. First, the Mole probe B_1 coil was known to have low sensitivity and signal-to-noise. Second, the sensitive pre-amp input was susceptible to noise pickup through electric and magnetic coupling, especially through the $\lambda/4$ line inductance. Third, the NMR lab environment was very noisy as discussed in Chapter 2. Reducing noise pickup between external sources and the pre-amp input was accomplished using two methods.

The first method was to shield against capacitive coupling by placing a conductive shield around the sensitive circuitry, and connecting it to a common potential (Rich (1982-3) [127,128]). The effects of poor capacitive shielding had been observed previously when the lid of the milled box on the PAD standard version was not screwed down tightly. Even slightly loosened screws were found to result in a very large increase in noise.

The second method was to magnetically shield the sensitive circuitry. This was more difficult since magnetic fields pass through many materials such as aluminium. Mu-metal can constrain magnetic fields but is only suitable for frequencies up to around 1kHz. At high frequencies, copper, aluminium or steel are useful depending upon frequency. Steel provides the best attenuation but is magnetic. Copper is expensive. Aluminium is light-weight, non-magnetic, and reasonably priced (Rich (1982-3) [127, 128]).

On the PAD relay version, the commercial directional coupler already had some shielding. The minimum requirement was thus to shield the $\lambda/4$ line inductor. This was accomplished using tin-strip as shown previously in Fig. 3.1. Shielding of the PAD standard version $\lambda/4$ lumped element and directional coupler circuitry was accomplished using a milled aluminium box as shown in Fig. 3.13. This was designed with SolidWorks [139] and commercially milled in Palmerston North (Absolute Tooling Solutions [140]). The physical size of the milled box was limited by the other components on the module. The walls and lid were made as thick as the design parameters would allow to maximize magnetic shielding effectiveness.

The PCB designed to fit inside the milled box was double sided, with rounded corners to fit the milling, and rectangular cutouts to fit the large $\lambda/4$ inductor and directional coupler as shown in Fig. 3.3. The inductor was wound on a former and then lacquered to ensure it would not change shape after soldered in place. Extra $\lambda/4$ capacitor pads were placed on the circuit board to allow for resonant circuit adjustment. The routed slot was designed to fit an inductor suitable for operation at 3.2MHz. For a higher frequency design the inductor would be physically smaller. Lower frequency designs would require the number of turns on the inductor to be increased so the wire diameter would need to be reduced.

Sourcing an SMA connector with a sufficiently long shaft to pass through the

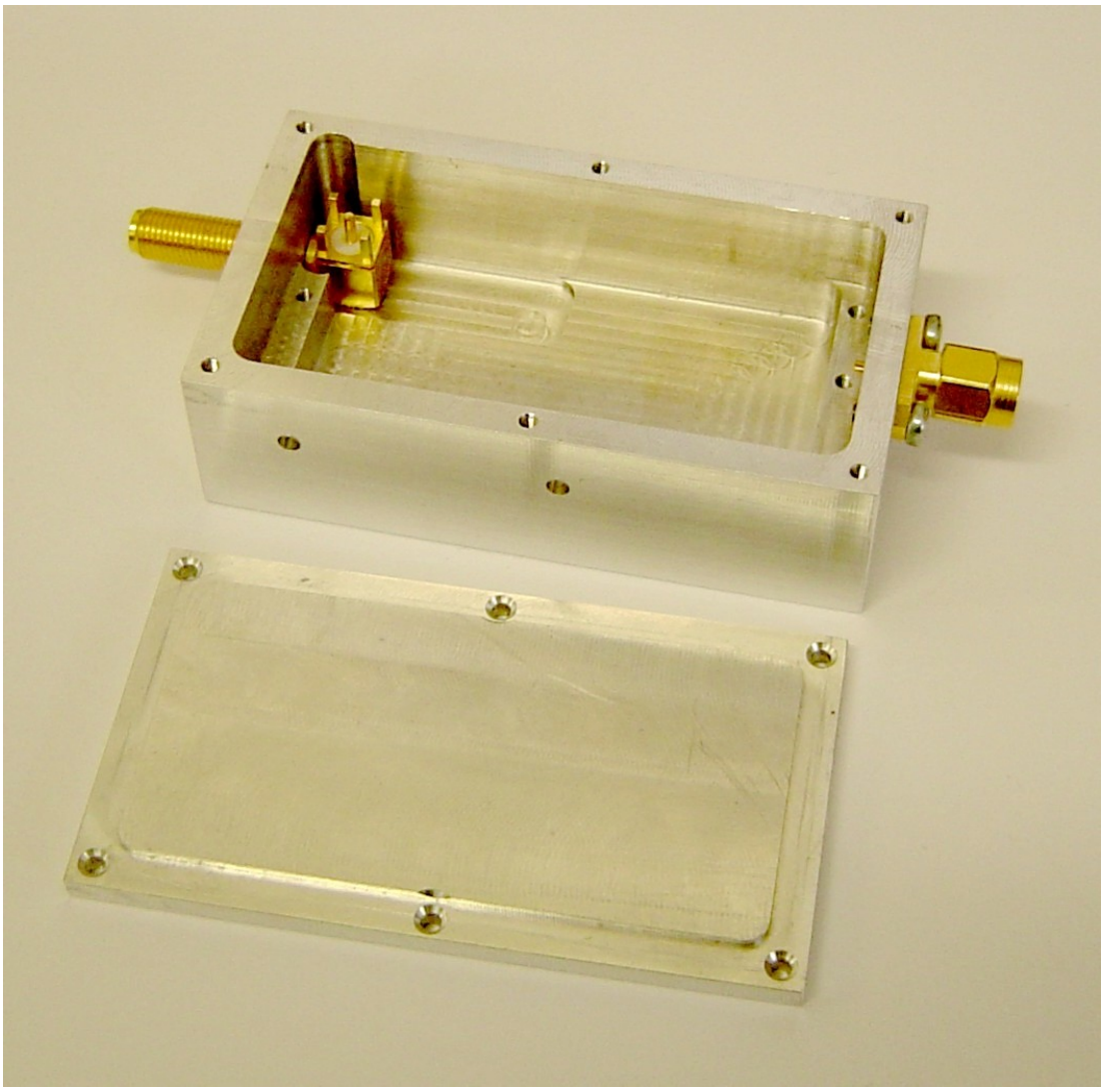

Figure 3.13: Milled box housing for PAD standard version duplexer and directional coupler components.

aluminium box and reach through the Kea front panel was difficult. Only one right angled SMA was found to be available. This needed to be fitted into the milled box as shown in Fig. 3.13 prior to soldering to the PCB. Unfortunately this made future PCB removal very difficult. To fit the SMA into the metal box required milling into one corner, and a small channel to be milled into the base of the box.

Two side holes were drilled through the milled box, and RG-316 cabling for the TX amp and reflected power signals were fitted as shown in Fig. 3.3. The holes were designed to be a tight fit for the cable; the cable's outer insulation was removed and the shield pushed through the hole. The conductors were then separated into three parts and soldered to the PCB. The center conductor was attached to 50Ω PCB traces at each end.

3.14 Performance

The performances of the two PAD modules were measured in terms of how well they fulfilled the three design requirements specified in §3.2.

3.14.1 Signal routing

Signal routing between the TX amplifier, NMR probe and RX amplifier worked well for both modules. The reliability of signal routing on the PAD relay version relies upon the relays as discussed in §3.3.1. The PAD relay design was found to have poorer signal-to-noise than the PAD standard version and was therefore not used extensively during the remainder of the project. The reliability of the relays therefore remains an open question. The PAD standard version was used for thousands of experiments with no signs of performance degradation.

3.14.2 Signal amplification and noise measurements

Signal and noise amplification for the two modules was tested and compared using two Prospa macros: MonitorNoise and Echo. The former was used to measure noise at the NMR probe port and the latter was used to measure spin-echo signals.

All signal and noise experiments were completed in the NMR lab at the same location as almost all other experiments in this thesis. Identical apparatus was used for all experiments and no equipment was moved or adjusted during the experiments. Each PAD module was screwed firmly into the spectrometer using the four front panel screws. The signal bandwidth (488.28kHz) was identical for all experiments and no digital filtering was used.

Three sets of noise experiments were generated for each PAD module using three different probe-port loads. The first load consisted of two 100Ω leaded resistors

connected in parallel and attached directly to the PAD SMA connector. The loop area formed by the resistor body and leads was minimized to reduce pickup. The second load was a shielded 50Ω BNC terminator and was connected to the BNC connector inside the Mole box. The third load was the tuned and matched Mole probe located inside the closed environmental chamber.

Each noise experiment set consisted of thirty-two noise measurements taken around one second apart. The measurements were recorded in the time domain and Fourier transformed by Prospa to show the frequency distribution. Results that were typical of the experiments are shown in Figs. 3.14 and 3.15. The MonitorNoise macro calculates the RMS time domain noise; this was used to calculate an average RMS noise for the three pairs of experiments.

The results consistently showed lower noise levels for the PAD standard version compared to the PAD relay version. When connected to the Mole probe, the RMS noise floor was almost one-third lower. For all three loads the PAD relay version was influenced by severe noise transients of unknown origin in the frequency domain of 2-5 times the amplitude of the noise floor and generally separated by around 95kHz across the 488kHz spectral width. The same periodic transients appeared in the PAD standard version only with the 50Ω load attached directly to the PAD module, suggesting the noise source was coupling to the exposed resistors and not to the Mole probe or PAD standard version circuitry.

Since the PAD standard version was not picking up large transients when terminated to the environmental chamber or Mole probe, this suggests the PAD relay version was picking up noise within the module itself, and possibly through the $\lambda/4$ inductance. The orientation, location and size of the $\lambda/4$ inductances on both modules is almost identical so the difference parameter is the milled aluminium box versus tin shielding.

Additional research is required to determine the exact sources of the noise entering into the PAD relay version. Questions to be answered include: Why is the noise floor significantly lower in the PAD standard version? Is the milled box providing significantly better shielding than the tin? Are the different RF switches and/or relays affecting the noise level? Is noise being coupled to exposed PCB traces? Can noise be reduced by placing PCB traces between two ground planes? Do the two pre-amp modules have different noise factors, even thought they are the same model?

There is a possibility the observed transients were not present during all the experiments. The PAD standard version may have perchance avoided a noise source during its thirty-two experiments, however this is unlikely as the experiments have been repeated at other times with similar results.

To measure the signal amplification of the two designs, a spin-echo experiment with 500μs echotime and 40μs pulse width was performed on each PAD using

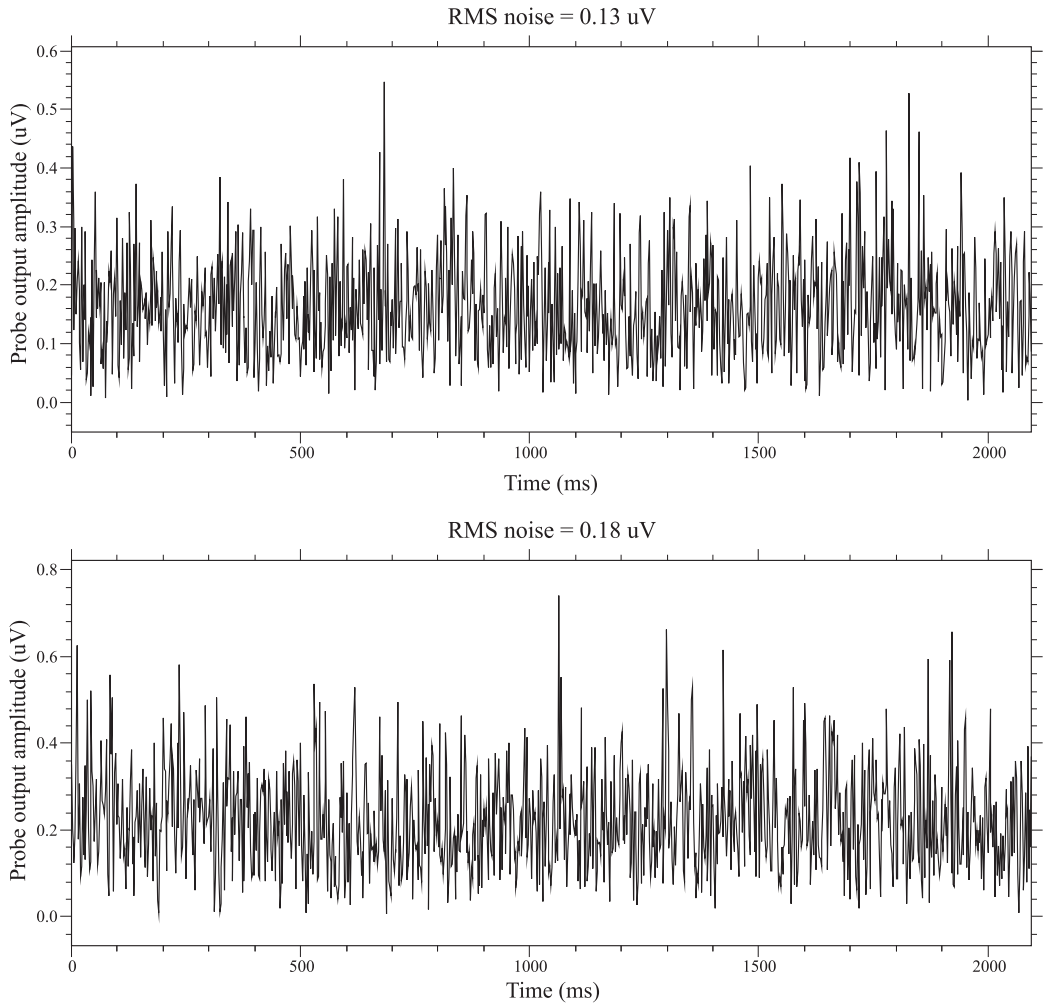

Figure 3.14: Comparing time-domain noise between the two PAD modules, measured using Prospa's MonitorNoise macro. The upper graph is from the PAD standard version; the lower graph is from the PAD relay version. The RMS noise levels are shown above each graph. In each instance, the load was the NMR Mole located inside the closed environmental chamber.

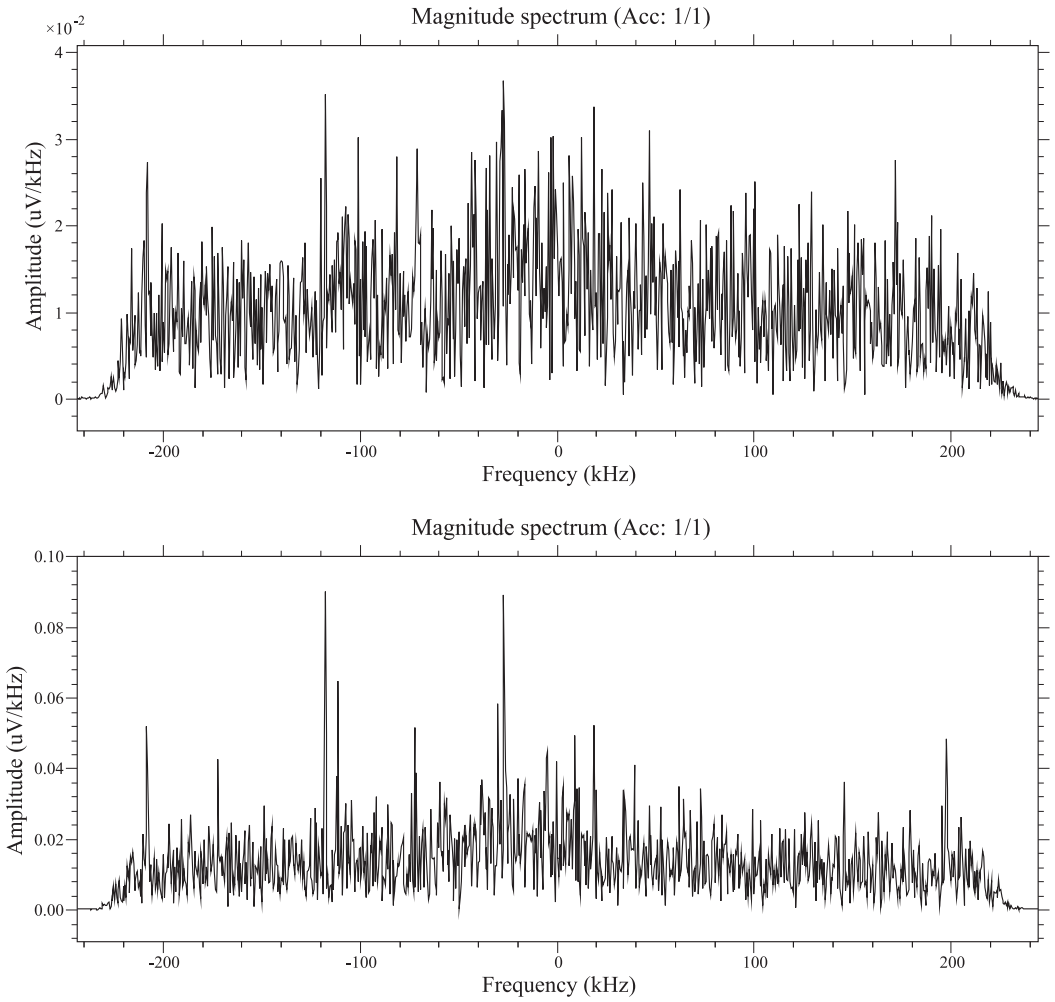

Figure 3.15: Comparing frequency-domain noise between the two PAD modules, measured using Prospa's MonitorNoise macro. The upper graph is from the PAD standard version and shows broadband noise that is reasonably consistent across the entire spectrum. The lower graph is from the PAD relay version and shows the presence of large transients. In each instance, the load was the NMR Mole located inside its metal box.

a 10mL canola oil sample. To reduce noise on the echo signal each experiment consisted of sixteen scans with 4-cycle phase cycling. The amplitude of the spin-echo signals was identical for both the PAD modules within the bounds of uncertainty, suggesting the signal gain of the two pre-amplifiers was similar as expected. The measured spin-echo peak amplitudes for the two modules was $(1.30\pm0.05)\mu$V. The average measured RMS noise levels for the PAD standard and relay versions were 0.130μV and 0.180μV respectively. The signal-to-noise ratio (SNR) is therefore $1.30/0.130 = 10$ for the PAD standard version and $1.30/0.180 = 7.2$ for the PAD relay version with a nominal uncertainty in each case. It should be noted that the signal and noise levels above are probably not the actual voltages since Prospa scales the voltages according to approximate amplifier gains. This however is irrelevant when taking ratios.

3.14.3 Wobble

Wobble functionality worked flawlessly on both PAD designs. The relays on the PAD relay version make an audible click when swapping between modes, which could become irritating to the experimenter. The width of the wobble trough is a lot narrower on the PAD relay version as shown in Fig. 3.16. The reason for this has not been investigated as it did not affect tuning and matching operation. The depth of the trough can be made very close to zero when tuning and matching the Mole, indicating a good impedance match between them. Both PAD modules showed wobble minima at the same frequency.

3.15 Future improvements

It is evident from the discussion above that the PAD modules function well in terms of signal routing and wobble functionality. The PAD relay version needs to have its RF relays extensively tested to determine whether they remain reliable under short intense RF pulses. The biggest area for improvement is certainly noise levels and transient shielding. Milled aluminium boxes are expensive but the best noise and transient shielding solution would appear to be fitting the entire PAD electronics inside a thick-walled aluminium box. The Massey lab environment as described above is an especially rich source of EMI. Filtering also needs to be investigated at the pre-amp output using the unfitted Mini-Circuits SCLF-4.7 low-pass filter component (Mini-Circuits [107]). Prospa's digital filtering should also be investigated.

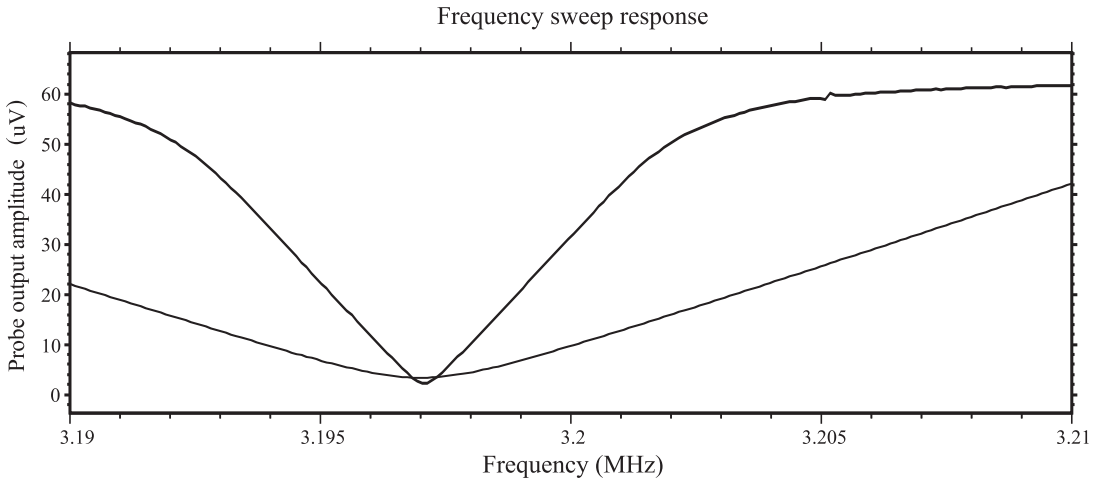

Figure 3.16: Wobble signals for the two PAD designs using identical Mole tuning and matching. The upper trace with the narrower trough is from the PAD relay version.

CHAPTER 4

Studying pectin solutions

The aim of this chapter is to build and study biopolymer systems that mimic similar systems found in nature. The mimic systems are made from pectin biomolecules dissolved in water, and are studied using the low-field NMR apparatus developed in the previous chapters. Understanding the NMR relaxation measurements from these systems may provide an important stepping stone toward understanding measurements from real-world systems such as kiwifruit.

The chapter begins with a brief description of pectin molecules, and their place in nature. Experiments on the pectin solutions, consisting of titration and T_2 relaxation measurements are then discussed, along with a collection of remarkable results that are interpreted within the remainder of the chapter.

Interpretation of the experimental T_2 results from the pectin solutions is accomplished using a mathematical model, and leads to an understanding of the molecular level dynamics of pectin molecules within a water solvent.

The titration results proved to be quite unexpected, and appear to suggest the generally accepted interpretation of pectin titration data is partially incorrect.

Finally, a mathematical model is used to show the similarities and differences between the pectin model and experimental results. Reasons for the differences are suggested.

4.1 Pectins

Pectins are biomacromolecular polysaccharides consisting mainly of long chains of galacturonic acid (GalA) monomers. They have been studied for many decades and their properties utilized in cooking for many centuries (Vincent and Williams (2008) [153]). Pectins are considered to be among the most complex molecules in

nature with structure that is very challenging to analyze (Fraeye et al. (2010) [57], Ralet et al. (2009) [122]).

Pectins are present in many fruits as shown in Table 4.1 and form an essential part of the framework of plant cell walls, contributing to both the adhesion between cells and to the mechanical strength of the cell wall. The main sources of commercial pectins are citrus peel and apple pomace (Papadopoulos (2008) [115]).

Pectin molecular conformations and behaviors in solution vary significantly depending upon temperature, pH, and degree of methyl-esterification as will be discussed in due course (Capel et al. (2006) [27], Fraeye et al. (2010) [57], Gilsenan et al. (2000) [60], Dobies et al. (2006) [50]).

In this chapter we use the low-field NMR apparatus to study pectic solutions made from dried pectin powders dissolved in water. These simple systems can be considered as model systems, simplified versions of more complex natural systems found in nature. Understanding the NMR transverse relaxation measurements from simpler systems may be a first step toward understanding measurements from more complex systems such as fruits.

The GalA and pectin experiments discussed in this chapter consist of pH titration measurements coupled with NMR T_2 relaxation measurements. The NMR results turn out to be especially intriguing, but an understanding of the underlying molecular behavior is only gained through coupling the relaxation and titration measurements together within the context of a mathematical model. By the end of the chapter the macro-level NMR measurements will be understood in terms of micro-level molecular dynamics.

4.2 Preparing galacturonic acid and pectin solutions

All GalA and pectin solutions were prepared in 30ml glass vials then placed inside the Perspex vial holder on the Mole probe as shown in §2.14 on page 56. At the beginning of the experiments it was discovered that adding fresh Milli-Q water with neutral pH into a new vial resulted in the water becoming slightly acidic. This was presumably due to contaminants from the manufacturing process remaining on the inner glass surface. It was found that triple rinsing the glass vials in Milli-Q water consistently removed the contamination source. This involved squirting Milli-Q water into the vial, then screwing the lid on and shaking vigorously for ten seconds, then emptying and repeating. Every vial used in these experiments was thereafter subjected to this process. Furthermore, when a new tray of vials was received a similar contaminating effect was observed – except in this instance the contaminant caused the water pH in the vials to become more basic.

Table 4.1: Examples of pectin sources and their weight fractions.

Source	Weight (%)
Apple[a]	0.5-1.0
Apple pomace[c]	10-15
Apricot[a]	0.5-1.4
Blackcurrent[c]	
Citrus (dry matter)[c]	20-30
Cocoa[c]	
Coffee[c]	
Grapefruit[c]	
Guava[c]	
Kiwifruit[b]	0.3-1.1
Lemon[a]	0.8-3.0
Lime[c]	
Mango[c]	
Onion[c]	
Orange[a]	0.4-2.4
Papaya[c]	
Plum[a]	0.6-1.0
Potato[c]	
Strawberry[a]	0.3-0.6
Sugar beet[c]	

[a] From Beckett (1995) [18].
[b] From Hasey (1994) [69].
[c] From Papadopoulos (2008) [115].

Three GalA solutions were prepared using dried GalA powder (Sigma-Aldrich [13]) and Milli-Q water. The concentrations of the three solutions were 1.37, 3.0, and 20 wt% where wt% is the ratio of the solute weight to the combined solute-solvent weight. At the two lower concentrations the GalA powder dissolved easily upon stirring. By contrast the higher concentration solution required mild heating in the form of running hot tap water over the vial surface for a few seconds. Each solution was thereafter stirred rapidly for one minute. At 3.0 wt% concentration it was evident the viscosity had increased compared to water. A schematic representation of a hydrated GalA monomer is shown in Fig. 4.1.

Six pectin solutions were also prepared using dried pectin powder and Milli-Q water. The first was a 1.5 wt% apple solution made from powder derived from apple pomace. According to the supplier (Fluka Bio-Chemika [20]) the molecular

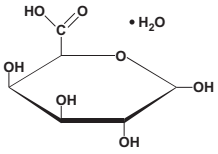

Figure 4.1: Hydrated galacturonic acid monomer, $C_6H_{10}O_7 \cdot H_2O$. Five hydrogen atoms attached to the ring carbon atoms are not shown.

weight M_r of the apple pectin macromolecules is between 30 and 100kDa. Since M_r for each sugar residue is around 200Da, each molecule consists of ∼150–500 GalA residues. The apple pectin is specified as 70–75% methyl-esterified, classifying it as high methoxy (HM) because the degree of methyl-esterification is greater than fifty percent (Strom et al. (2007) [147]).

The remaining five pectin solutions were prepared using dried LM12 pectin powder derived from citrus peel, and Milli-Q water. The concentrations were 0.5, 1.0, 1.5, 2.0, and 2.5 wt%. The molecular weight M_r of the LM12 pectin macromolecules is around 120kDa which means each LM12 molecule consists of ∼600 GalA residues. LM12 is 35–40% methyl-esterified, therefore it is classified as low methoxy (LM) because the DM is less than fifty percent (Strom et al. (2007) [147]).

The apple and LM12 pectin solutions were carefully prepared using the steps shown in Appendix B. Preparing the solutions was not difficult, however failure to follow the given steps carefully was likely to result in poor quality and/or non-repeatable solutions. A schematic representation of a small section of pectin molecule is shown in Fig. 4.2.

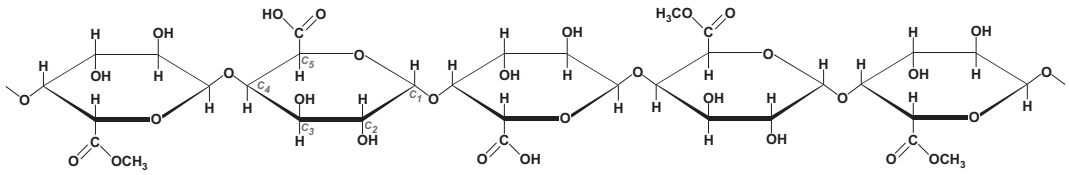

Figure 4.2: A small section of a pectin molecule showing both methylated and de-methylated GalA residues. The second monomer from the left displays carbon atom numbering. Hydroxyl groups are attached to C_2 and C_3 and a carboxyl group is attached to C_5.

4.3 Performing experiments on the solutions

A temperature controlled environment for making the samples was constructed from a magnetic stirrer/heater unit (IKA [86]), a thermocouple probe, and a crystallization dish. The glass vial containing 10mL of sample was placed inside the crystallization dish and the dish was filled with water to a height that just exceeded the height of the sample. The temperature of the water was set to $(25 \pm 0.1)^{\circ}$C and stirred with a magnetic flea to minimize local heating. An additional magnetic flea was placed inside the glass vials to stir each GalA and pectin solution during each titration.

A glass electrode pH probe paired to a pH meter (Mettler Toledo [150]) was used to measure each solution's pH. The pH apparatus was calibrated prior to performing experiments using pH 4 and 7 buffer solutions. Upon completion of the calibration, the probe tip was rinsed to remove any residual buffer solution. It was then lowered into the glass vial until the tip of the probe was immersed in the solution. During this time, the solution was being stirred rapidly so care was required to ensure the pH probe tip was not damaged.

To perform each titration, tiny quantities of 1M sodium hydroxide were added into the solution. The quantities were accurately measured using pipettes (Eppendorf [55]). Rapid stirring of the sample at all times during addition of the titrant ensured pectin de-polymerization due to high localized pH was minimized (Rolin et al. (1998) [131]). Occasionally a 0.1M titrant was used to provide finer control and 1M or 0.1M hydrochloric acid was used to lower the pH if required. It was especially easy to overshoot the desired pH value as neutral pH was approached in either direction. In order to reduce dilution effects, a higher molarity 6M titrant was tested with LM12 2.5 wt% solution. This resulted in the formation of small sheet-like entities within the sample, therefore titrants above 1M were never subsequently used with any pectin solutions unless specifically mentioned.

Upon reaching the desired pH the sample was removed from the water bath and quickly placed on the NMR Mole probe within the Mole's environmental chamber. This was also set to 25°C so that the sample would experience a constant temperature in both environments. The pH probe was first raised out of the sample on its stand, and the magnetic flea removed from the sample vial using a strong NdFeB magnet. A lid was quickly screwed on to the vial which was dried using a paper towel before gently being placed on the Mole probe. An NMR wobble experiment was quickly run to check the tuning of the B_1 coil followed by a CPMG experiment consisting of sixteen scans to measure the transverse relaxation time of the solution. The time required to perform the wobble and CPMG experiments was about three minutes. The sample was then quickly placed back in the water bath in preparation for the next titration.

All of the low-field T_2 relaxation measurements in this chapter were performed

at 25°C at a proton Larmor frequency of 3.197MHz. This frequency was found to remain stable over many months during which many experiments were performed. The stability of the proton Larmor frequency is attributable to the temperature regulation of the probe's environmental chamber as described on page 42. An example CPMG relaxation graph showing echo sum, T_2 relaxation decay curve, Prospa mono-exponential data fit and recycle time are shown in Fig. 4.3.

4.4 Titration and relaxation results

4.4.1 Galacturonic acid

Fig. 4.4 shows experimental titration data for three GalA solutions. The left and center titration datasets are 1.37 and 3.0 wt% solutions respectively, and were titrated against 1M NaOH. More titrant was required to adjust the pH as GalA concentration increased. The right-most titration dataset is 20 wt% solution, and was titrated against 6M NaOH. 1M NaOH was initially used, but a large quantity of titrant was required to substantially adjust the pH thereby significantly reducing the GalA concentration. The displayed pH range is divided into three zones for reasons that will become apparent in due course.

Fig. 4.5 shows experimental T_2 relaxation data for the three GalA concentrations as a function of pH. Each transverse relaxation data point in Fig. 4.5 is a 1:1 mapping from a titration data point in Fig. 4.4. As with the GalA titration graph, the displayed pH range is divided into three pH zones. The three GalA solutions show little deviation in their transverse relaxation times over almost the entire experimental pH range. The behavior of the two lower concentration GalA solutions is almost identical, and they share a similar transverse relaxation time to neutral Milli-Q water as indicated on the graph. By contrast, the 20 wt% solution T_2 relaxation times were reduced by about one-third compared to the lower concentration solutions.

The largest deviation in the T_2 relaxation times for all three GalA solutions was at very high pH. The T_2 time for the 3.0 wt% solution increased significantly, and went beyond the solvent transverse relaxation time. The reason for this was unknown and was not pursued. The high concentration GalA solution, by contrast, showed a decrease in T_2 relaxation time at very high pH. In addition, a color change from green/yellow to deep maroon/red was observed over a period of about 12 hours following the NMR measurements. Interestingly, the significant color change was not accompanied by significant change in T_2 time.

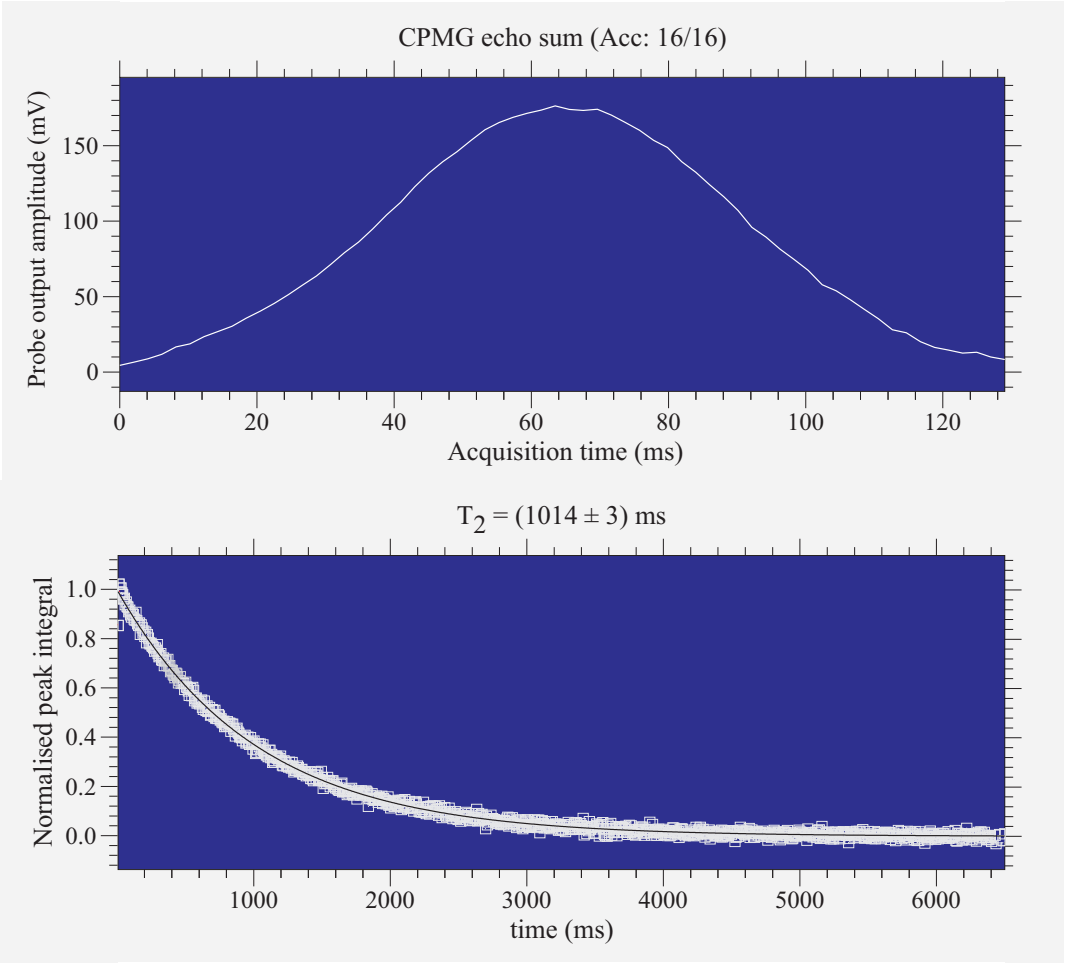

Figure 4.3: Results from a 16-scan CPMG sequence using a 1.5 wt% apple pectin solution near its starting pH. The upper graph shows the CPMG echo sum taken over 16 scans using standard 4-cycle phase cycling. The time between scans was ten seconds, allowing the bulk magnetization vector to return to at least 98% of it maximum value. The lower graph shows the normalized peak integral spin echoes formed by the CPMG refocussing pulses. The decaying integral amplitudes provide the T_2 relaxation fingerprint for the sample. The echoes are fitted as shown using Prospa's mono-exponential fit algorithm which also produces the relaxation time and uncertainty value. Each data point in the lower graph's relaxation result makes a small contribution to the echo sum in the upper graph.

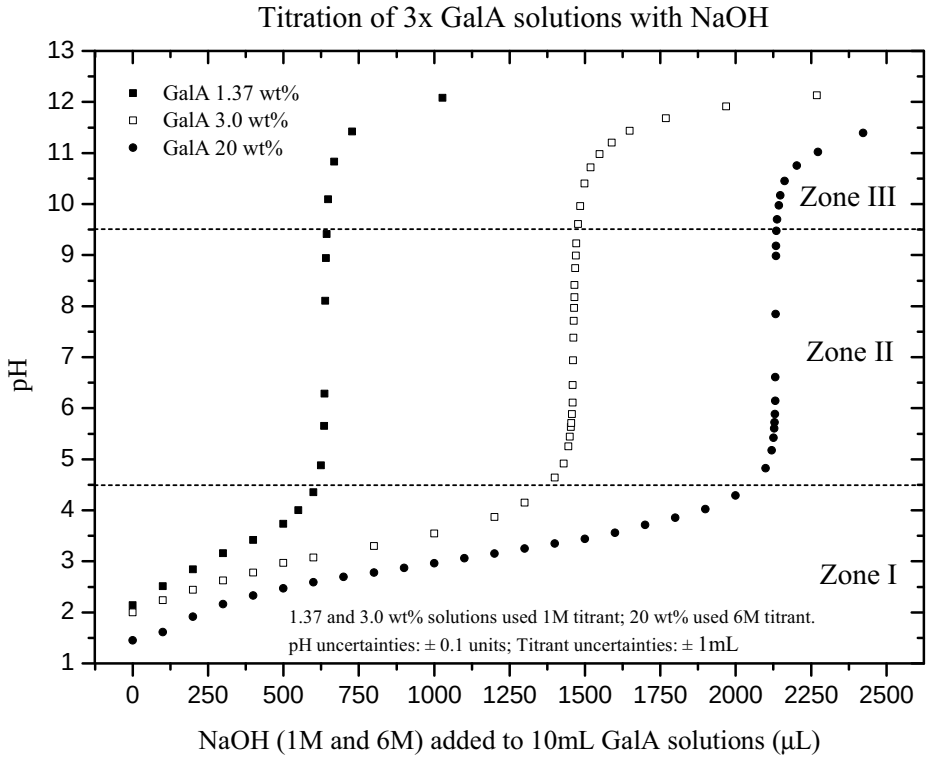

Figure 4.4: pH titration data for three GalA solution concentrations. The two horizontal lines divide the pH range into three zones for reasons discussed in due course.

4.4.2 Apple (HM) pectin

Fig. 4.6 shows experimental titration data for a 1.5 wt% apple pectin solution. As with the GalA solutions, minute additions of titrant in zone II caused large changes in pH, while similar additions in the other two zones caused only small changes in pH.

Fig. 4.7 shows experimental T_2 relaxation data for the apple pectin as a function of pH. Each transverse relaxation data point in Fig. 4.7 is a 1:1 mapping from a titration data point in Fig. 4.6. The titration data for the GalA solutions and apple pectin solution appear similar. By contrast, the transverse relaxation data appear distinctly different. The GalA transverse relaxation data showed little variation over the entire pH range. The apple pectin relaxation data varied both dramatically and systematically with pH. Beginning at very low pH, the T_2 time

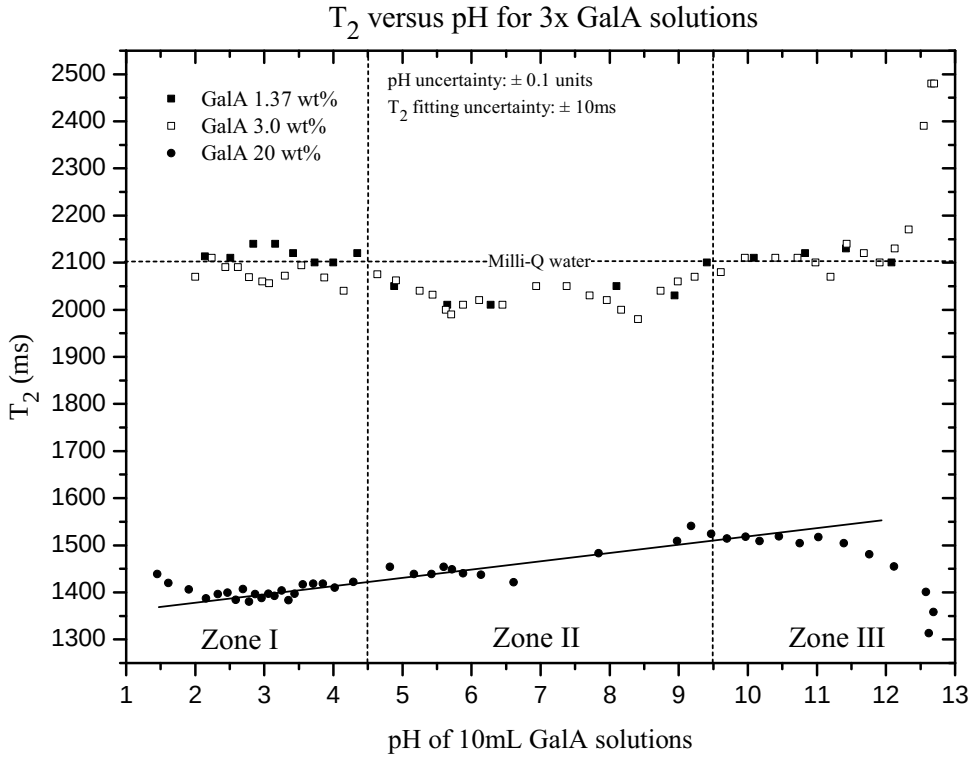

Figure 4.5: [

T_2-versus-pH for three galacturonic solution concentrations]T_2-versus-pH for three galacturonic solution concentrations. The horizontal dashed line indicates the T_2 relaxation time of Milli-Q water at ∼pH 7. The solid line suggests a general T_2-versus-pH trend for 20 wt% GalA. Both lines act as visual aids to emphasize the change occurring in the transverse relaxation times over the full pH range. The two vertical lines correspond to the two horizontal lines shown in Fig. 4.4. The time between consecutive measurements going from lowest to highest pH was around 4 minutes for all three datasets.

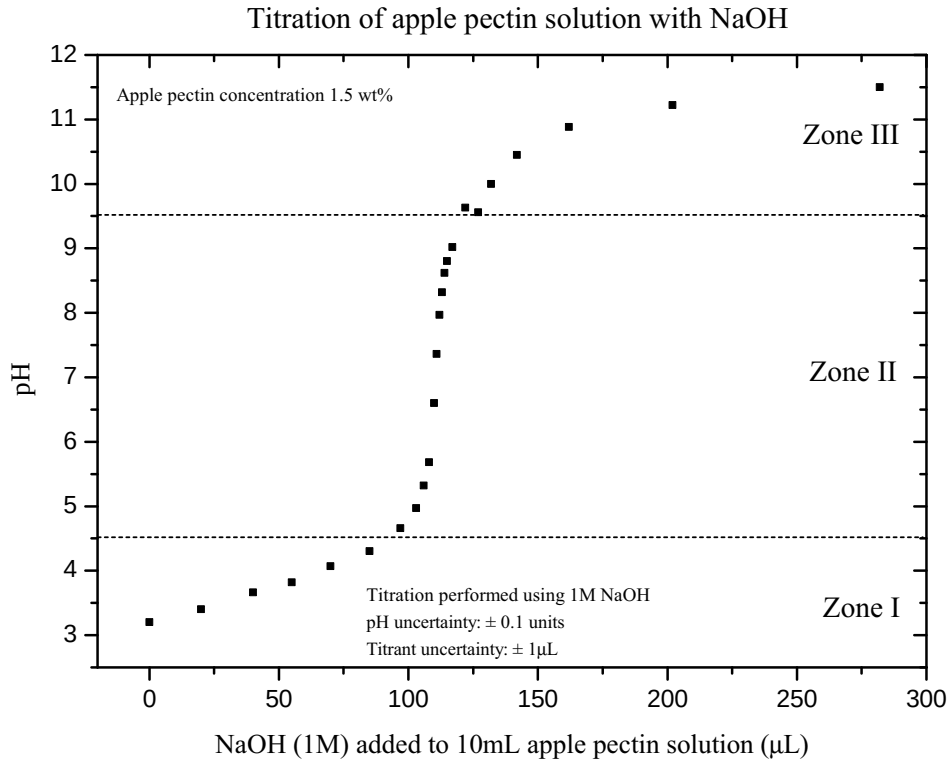

Figure 4.6: pH titration data for apple pectin solution. Measured data points below the starting pH are not shown. The two horizontal lines divide the pH range into three zones for reasons discussed in due course.

initially increased to a maximum, then dramatically fell as the zone I-II boundary was approached. Within zone II the relaxation time increased to a maximum at neutral pH before falling to a minimum as the zone II-III boundary was approached. Finally, in zone III the relaxation time increased again before finally appearing to plateau around pH 12.5.

It should be noted that the starting pH of the apple pectin solution was 3.2. The seven lowest-pH data points in Fig. 4.7 are all below the starting pH. The transverse relaxation times for these points were measured using a second identical pectin solution, and titrated to lower pH using 1M HCl. To reach the two lowest pH values, 500μL and then 1,000μL of 1M titrant was required. At no time did gelling or noticeable color change occur as the pH was lowered.

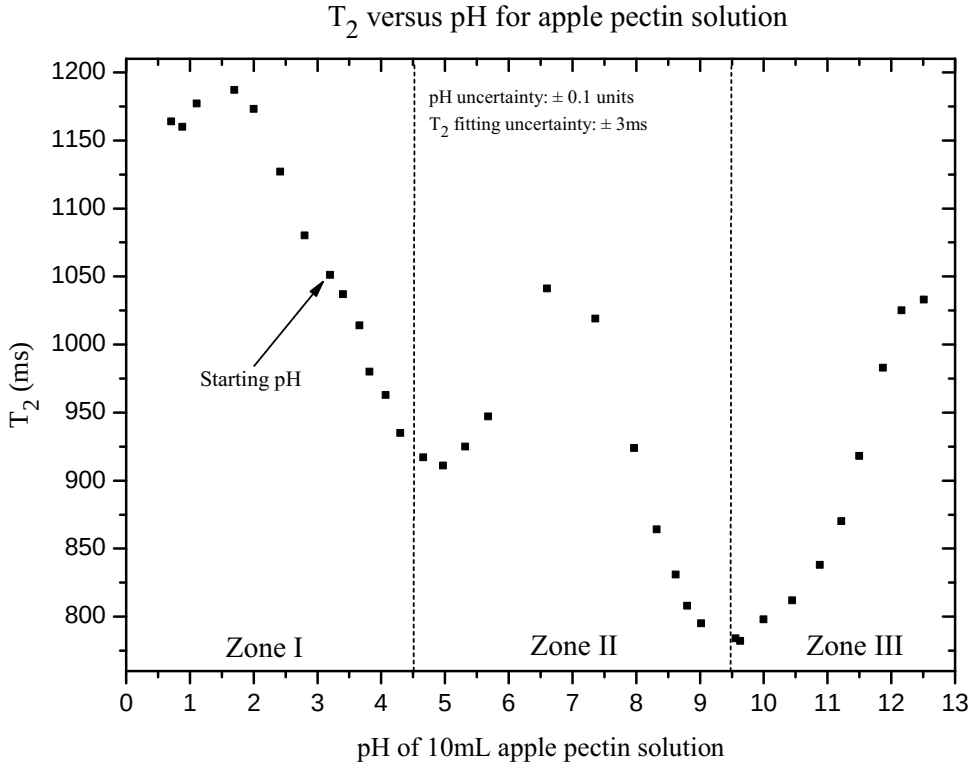

Figure 4.7: T_2-versus-pH for apple pectin 1.5 wt% concentration. A distinct color change occurs at around pH 7.6. An identical apple pectin solution left overnight at high pH and 25°C resulted in a solid light-fawn colored gel the next morning. The two vertical lines correspond to the two horizontal lines shown in Fig. 4.6. The time between consecutive measurements going from lowest to highest pH was around 8 minutes.

4.4.3 LM12 pectin

Fig. 4.8 shows experimental titration data for five LM12 pectin solutions. As with the GalA and apple pectin solutions, minute additions of titrant in zone II caused large changes in pH, while similar additions in the other two zones caused only minor changes in pH.

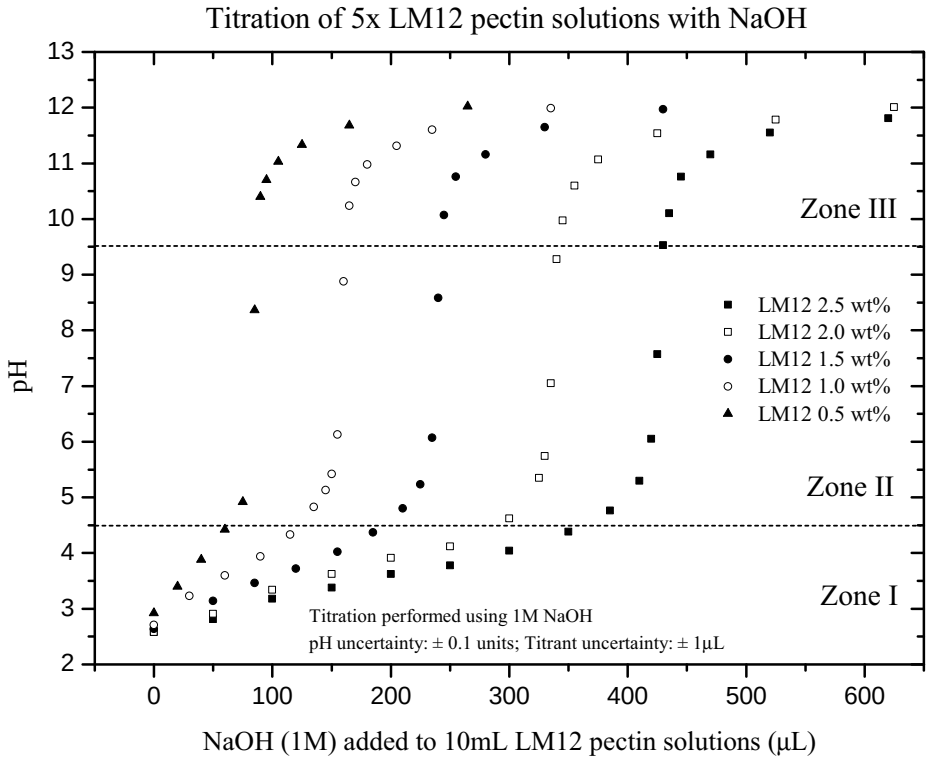

Figure 4.8: pH titration data for five LM12 pectin solutions. The two horizontal lines divide the pH range into three zones for reasons discussed in due course.

Fig. 4.9 shows measured T_2 relaxation times for the five LM12 solutions as a function of pH. Each transverse relaxation data point in Fig. 4.9 is a 1:1 mapping from a titration data point in Fig. 4.8. As can be seen in Fig. 4.8, the starting pH values for all five LM12 solutions are very similar. By contrast, the T_2 relaxation times at starting pH differ considerably. For the highest concentration solution T_2 is close to 550ms, while for the lowest concentration T_2 exceeds this value by a factor of about three. The T_2 relaxation time of the water solvent used in these

solutions was measured separately at 25°C on the utilized low-field NMR apparatus and found to be around 2,100ms. The least concentrated pectin solution at its starting pH was observed to begin at about 80% of the water value and increased to over 90% as the pH approached 12.

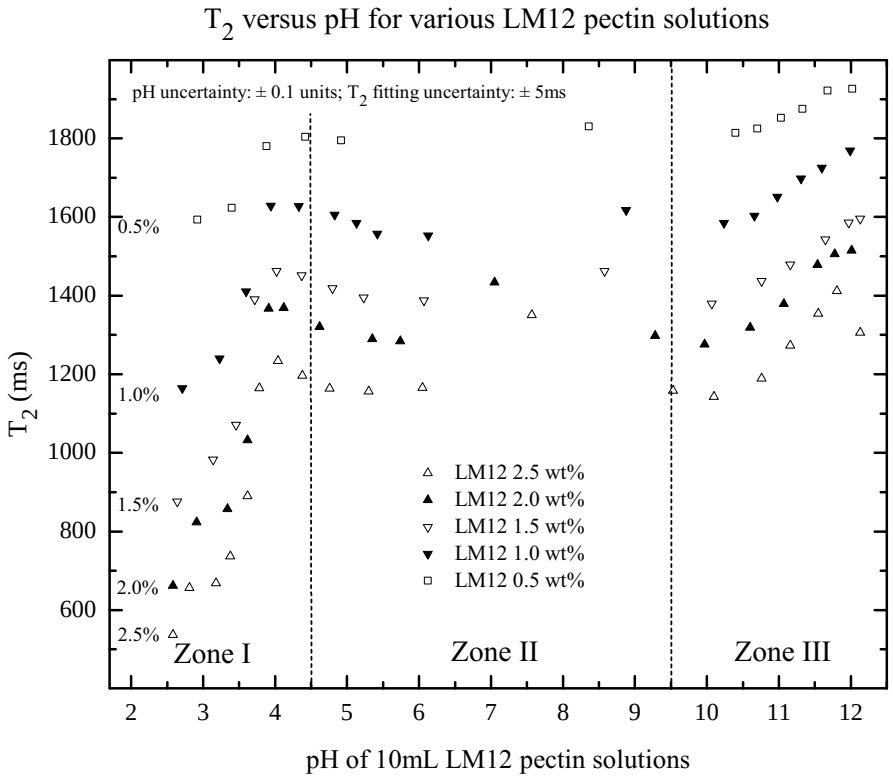

Figure 4.9: T_2-versus-pH for five LM12 pectin concentrations. The two vertical lines correspond to the two horizontal lines shown in Fig. 4.8. The time between consecutive measurements going from lowest to highest pH was around 8 minutes for all five datasets.

Inspection of the results in Fig. 4.9 reveal a measured T_2 value that is highly dependent upon pH, especially at increased pectin concentrations. In zone I, even a small change in pH results in a dramatic change in T_2; for more dilute solutions the effect is less emphatic. As the zone I-II boundary is approached, the spread of T_2 values across the different concentrations is compressed. For each concentration T_2 appears to reach a local maximum around pH 4 before decreasing slightly.

Zone II displays a different characteristic. For each LM12 dataset the values at the zone I-II and zone II-III boundaries are similar, while around neutral pH the two highest concentration datasets show an increased T_2 similar to the apple pectin. The lower concentration datasets have insufficient data points to confirm or deny a local maximum around neutral pH.

Near the zone II-III boundary there appears to be a local T_2 minimum for all concentrations. As the pH is further increased, all T_2 times increase in a linear manner with the higher concentration solutions increasing more rapidly. All T_2 values trend toward the water relaxation time, but only the most dilute solution gets to within ten percent of the water value. The final data point for the 2.5 wt% concentration solution shows a decreased T_2, perhaps behaving similarly to the apple solution.

In comparing the LM12 solution's transverse relaxation results to the GalA and apple pectin results, it is obvious that the three systems exhibit significant differences. The transverse relaxation times for the GalA solutions did not show much pH dependence, while the apple and LM12 pectins showed a striking pH dependence. The LM12 and apple results appeared to follow a similar pattern over the full pH range.

4.4.4 Water

Experimental data in previous sections revealed transverse relaxation behaviors for GalA, apple pectin, and LM12 pectin solutions as the pH was systematically adjusted. It was unknown how the water solvent, from which the majority of the NMR signal was originating, was contributing to the pH dependent relaxation results. It was necessary therefore to measure water T_2 relaxation as a function of pH using NaOH and HCl in like manner to the previous experiments.

The results of these experiments were quite unexpected, and Chapter 5 beginning on page 173 is dedicated to further investigation of water behavior as a function of pH. For now it is sufficient to state that water T_2 relaxation results did reveal a pH dependence but unlike the pectin results the water T_2 relaxation times found a minimum around neutral pH and increased as the pH deviated from neutral.

4.5 Pectin stability and reversibility

It is well known that the chemical stability of pectin molecules in solution changes with pH and temperature. Pectin molecules find their greatest stability at low temperature and within a pH zone of 3.5 ± 1 although authors differ slightly on this value (Spiridon and Popa (2005) [144], Belitz et al. (2009) [19], Shi et al. (2002) [136], Steinbüchel and Rhee (2005) [145], Rolin et al. (1998) [131], Voragen

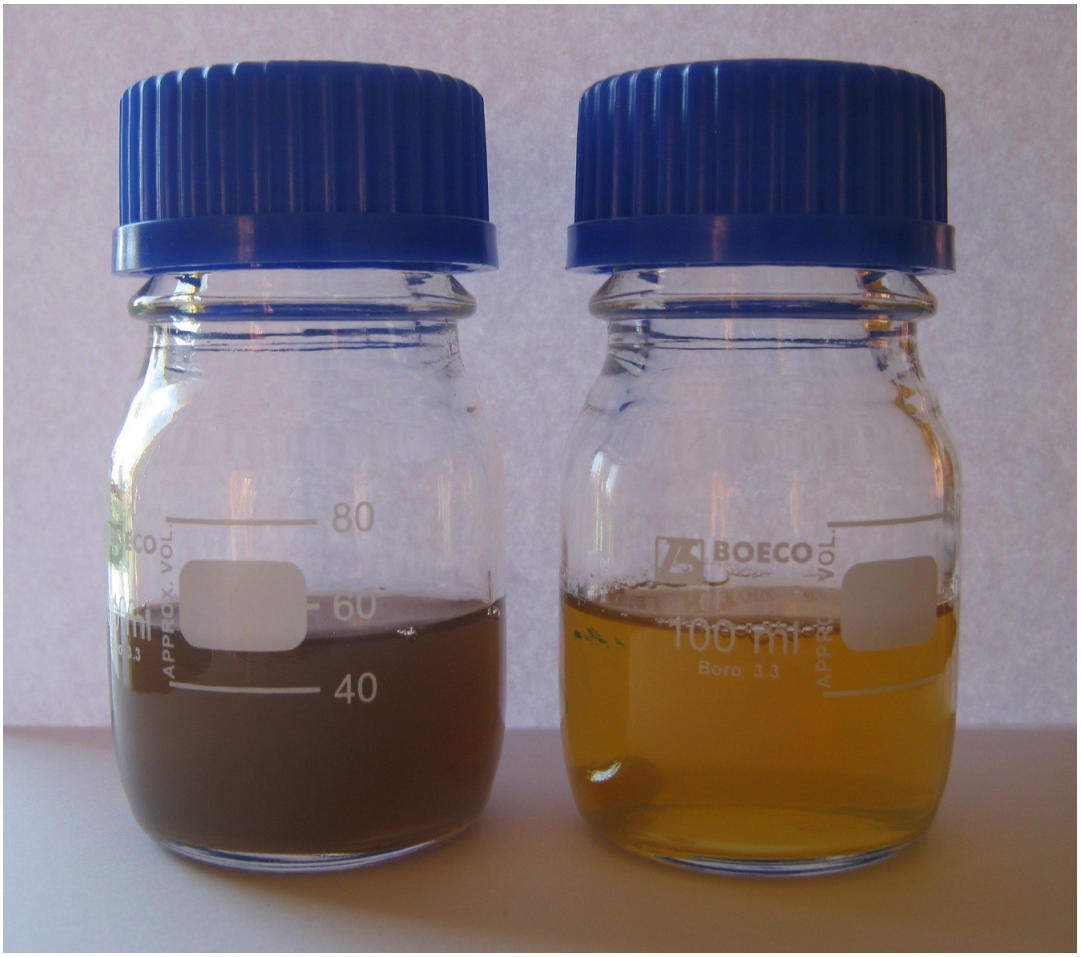

Figure 4.10: From left to right: 50mL apple and LM12 pectin 2.5 wt% solutions, in Schott bottles post titration. These solutions were made near the completion of this chapter.

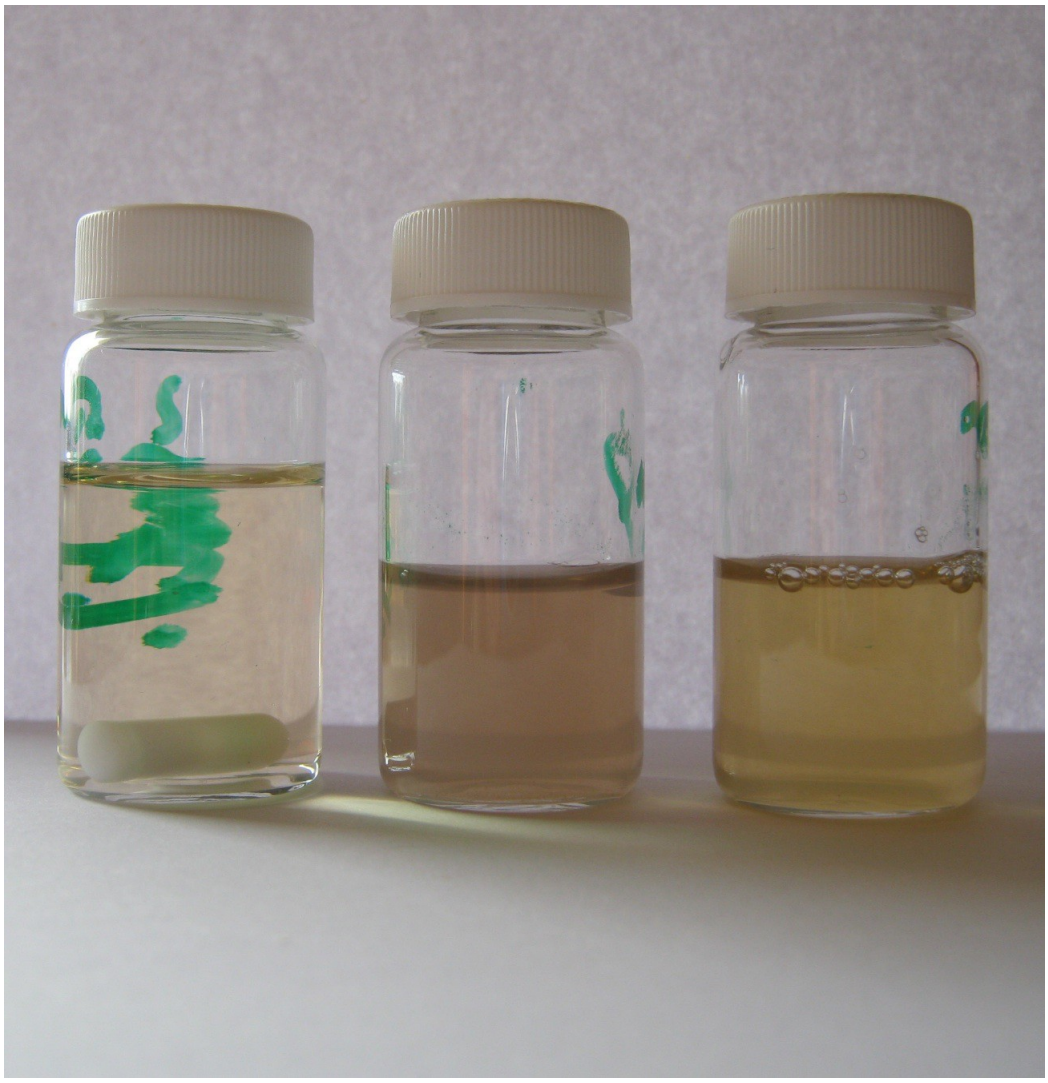

Figure 4.11: From left to right: 10mL galacturonic acid 10 wt%, and 10mL apple and LM12 pectin 2.5 wt% solutions, in glass vials post titration. These solutions were made near the completion of this chapter.

et al. (1995) [154]). Pectin stability is especially important in this thesis because transverse relaxation measurements are sensitive to polymer chain size and mobility. Pectins are often deliberately destabilized (selective degradation) to break the macromolecules into more manageable oligosaccharides (Voragen et al. (2009) [155]).

Lowering a pectin solution's pH below its stable zone can lead to acid hydrolysis in which methoxyl groups, acetyl groups and neutral side chains dissociate from the main polymer chain. Neutral sugar side chains attached to the pectic backbone provide linkages to cellulose fibrils in the cell wall. Acid hydrolysis can be used to split the side chains, allowing pectin extraction (Endress et al. (2006) [54]). At higher temperatures degradation rates accelerate and cleavage of glycosidic bonds along the pectic backbone progressively increases (Shi et al. (2002) [136]). Glycosidic linkages between adjoining galacturonic acid residues are very acid resistant compared to linkages between neutral sugars and uronic acid (Steinbüchel and Rhee (2005) [145]).

Raising a pectin solution's pH above its stable zone can also lead to molecular degradation. Pectin may be stable at room temperature between pH 5 and 6, but if temperature is raised or pH is raised to neutral or alkaline, degradation can occur via two non-enzymatic mechanisms (Steinbüchel and Rhee (2005) [145], Sila et al. (2009) [137]). The first is the saponification of ester groups in which a hydroxyl anion attacks the ester's carbonyl group resulting in the formation of a carboxyl group and the release of methanol. The second mechanism operating in parallel with the first is β-elimination. This mechanism induces the base-catalyzed cleavage of glycosidic bonds between residues with the appearance of a double bond between C_4 and C_5 as illustrated in Fig. 4.12 (Shi et al. (2002) [136], Tomasik (2004) [151]). This mechanism operates at neutral or even weakly acidic pH in the presence of mild heating. HM pectins are especially susceptible to β-elimination as cleavage only takes place at a glycosidic linkage next to an esterified galacturonic acid (Steinbüchel and Rhee (2005) [145], Shi et al. (2002) [136], Rolin et al. (1998) [131]). This is because the hydrogen atom on C_5 is more acidic in the presence of an esterified carboxyl group than a free carboxyl group (Belitz et al. (2009) [19]). LM pectins show better stability under such circumstances since by definition they have fewer methyl-ester groups (Shi et al. (2002) [136]). Increasing the pH further accelerates saponification of ester groups, causing the two mechanisms to work against each other because β-elimination requires the presence of methyl-esters. A summary of pectin behavior at various pH values is shown in Table 4.2.

If cleavage of pectin molecules occurs, a corresponding increase in T_2 would be expected due to shorter rotational and diffusional correlation times of the smaller molecules, depending upon the degree to which the chains were modified. As seen previously in Figures 4.7 and 4.9, both HM and LM pectins did exhibit increased T_2 with pH in zone III suggesting the pectin molecules may have experienced

Table 4.2: Pectin molecular behavior at different pH values.

pH	Behavior
Below stable zone	Acid hydrolysis of esters and glycosidic linkages
Above stable zone	Hydrolysis of esters and β-elimination

fragmentation. Further, since GalA is monomeric, no chain cleavage is possible, and no increase in T_2 would be expected at high pH as observed in Fig. 4.5.

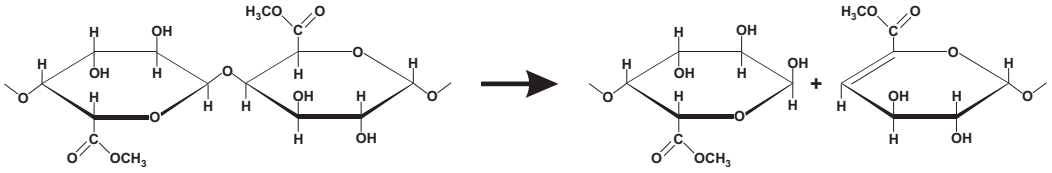

Figure 4.12: Beta-elimination reaction in pectin molecules (Shi et al. (2002) [136]).

To test for chain cleavage in the apple and LM12 pectins, the pectin chains needed to have their T_2 times measured while adjusting the solvent pH over the full pH range. If the chains experienced cleavage at high pH, lowering the pH would not be expected to repair the broken chains. Thus it would be predicted that T_2 would return increasingly higher values upon chain cleavage, or similar values if chain cleavage was absent. This could be tested experimentally by repeating the pH traversals several times over the pH range. If stasis of T_2 was observed then the pectin would be considered pH-reversible. On the other hand, if the value of T_2 increased and remained at the increased value, the pectin would be considered pH-irreversible.

4.5.1 Apple pectin reversibility

Due to the labor-intensive nature of obtaining many titration–T_2 measurements, it was sensible to take strategic spot-measurements of the apple pectin at predetermined pH values. Local minimum and maximum values were the best places to measure, as the rate of change of T_2 with pH at these locations would be minimal. From visual inspection of Fig. 4.7, pH values of 3.5, 5, 6.5, 9.5 and 11.5 were chosen. It was found that pH 11.5 was difficult to attain due to a barrier around pH 10.5 in which the pH could not be raised significantly using small quantities of titrant. Adding excess titrant would have diluted the pectin solution concentration, thereby making it more water-like and increasing T_2. Therefore, the upper measurement

point was lowered to pH 11.1. Fig. 4.13 shows seventeen apple pectin T_2 relaxation spot measurements recorded in the numerical order shown on the graph as the pH range was traversed four times. The earlier apple pectin T_2 relaxation data is superimposed for comparison. The apple pectin used for the spot-measurements was freshly made, thus did not contain salts from previous experiments.

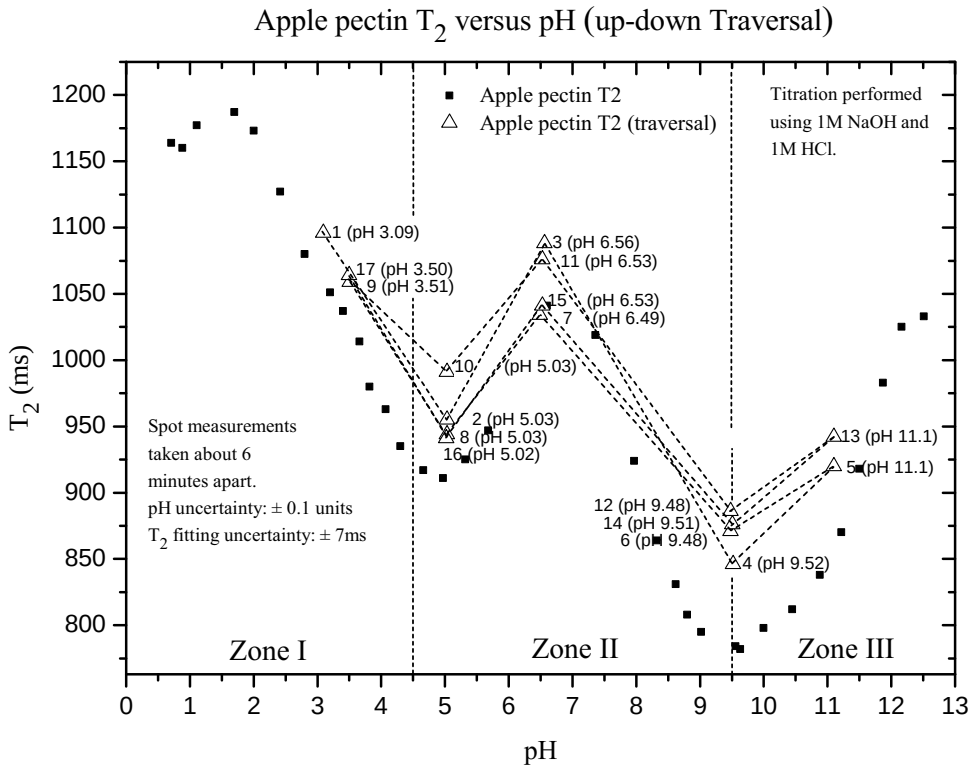

Figure 4.13: Changes in HM 1.5 wt% apple pectin T_2 as the pH range is traversed four times. The filled data points are the earlier apple pectin results. The unfilled data points are the spot-check measurements. The pH uncertainties at the two high pH values may be as high as -1 unit due to chemical changes in the pectin as shown in Fig. 4.14. The time between spot-check experiments was about six minutes. pH was measured prior to T_2 in each instance. Data point 1 is the starting pH of the pectin solution.

It is unknown why the spot measurements all had slightly longer T_2 times than the earlier T_2 data. One explanation was that the solution concentration was measured incorrectly. If the spot-measurement solution was slightly more

dilute than the earlier solution, all T_2 measurements would be slightly longer. A great deal of care was taken in all sample preparation in this project, so a concentration error seems unlikely, however the cause remains unknown. Whatever the source, the minor differences between the spot measurement T_2 times suggest pectic degradation was not a cause of significant T_2 relaxation time variation with pH. If significant chain cleavage was happening, a trend toward longer T_2 times would be expected. The maximum variation in transverse relaxation times between spot-measurements at the same pH was about $\pm$30ms which is about $\pm$3% of the T_2 relaxation times.

Some molecular changes did happen in the apple pectin between pH 9.5 and 11.1. This is supported by Fig. 4.14 which clearly shows the pH of the apple pectin changing during the experimental cycle of pH setting and T_2 measurement. In the absence of changes to the pectin, the data points would all lie on the equality line as shown for GalA. The deviation from the unity line is evidence of a temporally decreasing pH. This is due to protons being added to the solvent, presumably as a result of demethylation of methyl-esters as previously discussed.

Renard and Thibault also observed changes in HM pectins at high pH. They studied the demethylation of commercial 73% DM citrus pectin at pH 8.25 and 11.25 and found that at the lower pH less than twenty percent of the pectin's methyl-esters were saponified after twenty-four hours. At the higher pH value however, half of the methyl-esters were saponified within one hour. The data in Fig. 4.14 supports this general behavior, showing a larger decrease in pH when the pH is higher.

The seemingly anomalous apple pectin data point just beyond the zone II-III boundary in Fig. 4.14 corresponds to an unusually long twenty-five minute period in which the pectin solution remained untouched, lending further credence to Renard and Thibault's observations.

4.5.2 LM12 pectin reversibility

The LM12 T_2 relaxation times shown in Fig. 4.9 exhibit two extremes. At low pH T_2 is relatively short, at high pH T_2 is relatively long, and at increased concentration the extremes are more pronounced. Given the topography of the T_2-versus-pH data, it was sensible to test for chain cleavage using T_2 spot measurements at the extremes of the pH range. These were performed using an LM12 1.5 wt% solution and traversing the pH between pH 2.7 and 11.5 as shown in Fig. 4.15. The earlier LM12 T_2 relaxation data at the same concentration is superimposed for comparison.

Ten pH traversals were completed in the numerical order shown on the graph. The data points were measured approximately nine minutes apart. Five full traversals were required before any significant deviation from the original T_2 measurements was observed. During each excursion through pH 7-8 a dramatic

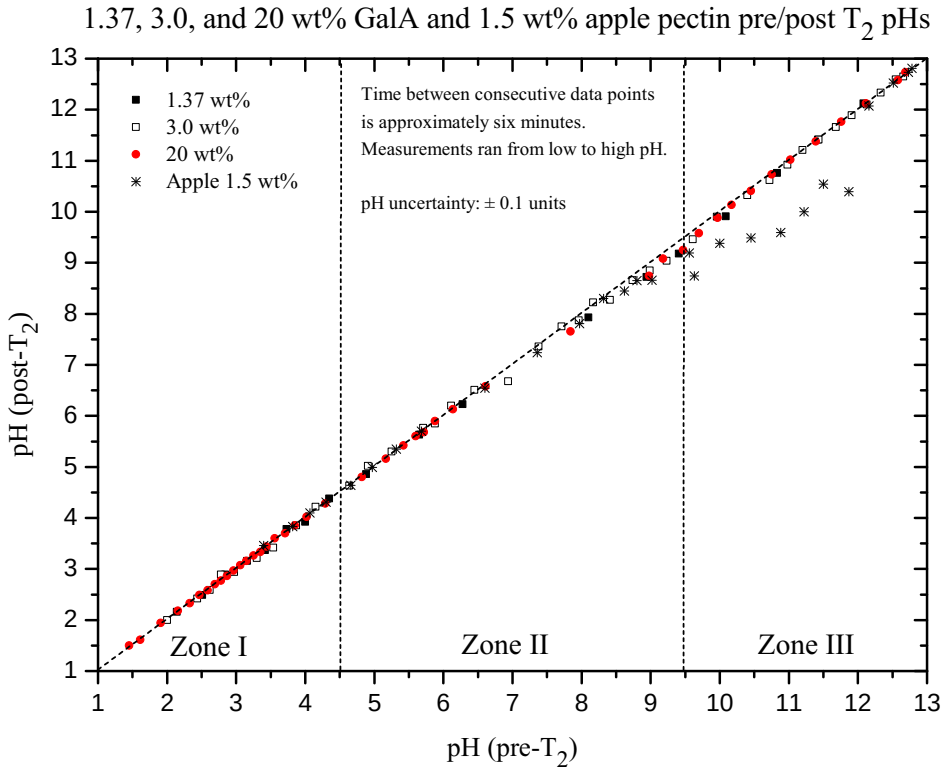

Figure 4.14: pH (pre-T_2 measurement) versus pH (post-T_2 measurement) for GalA and apple pectin solutions. Deviations from the equality line are evident for apple pectin in zone III.

reversible color change (whitish⟷yellowish) was observed. Data points 1 and 2 in Fig. 4.15 are almost identical to earlier measurements performed on an identical pectin sample. Points 2, 4, and 6 share almost identical high-pH T_2 times. Points 1, 3, and 5 show a slight upward T_2 trend, perhaps indicating minor sample dilution or changes in the pectin structure. The apple pectin by contrast did not reveal drift during its four traversals. Data point 7 and beyond show a dramatic downward trend in T_2 times at both low and high pH. At step 9 the pectin solution formed a gel containing tiny visible bubbles, indicating chemical changes had probably happened to the pectin molecules. Raising the pH to 11.52 at step 10 appeared to remove the bubbles and return the viscosity and sample color to the previous non-gelled state. Data points 7 and 8 with slightly fallen T_2 times can perhaps be

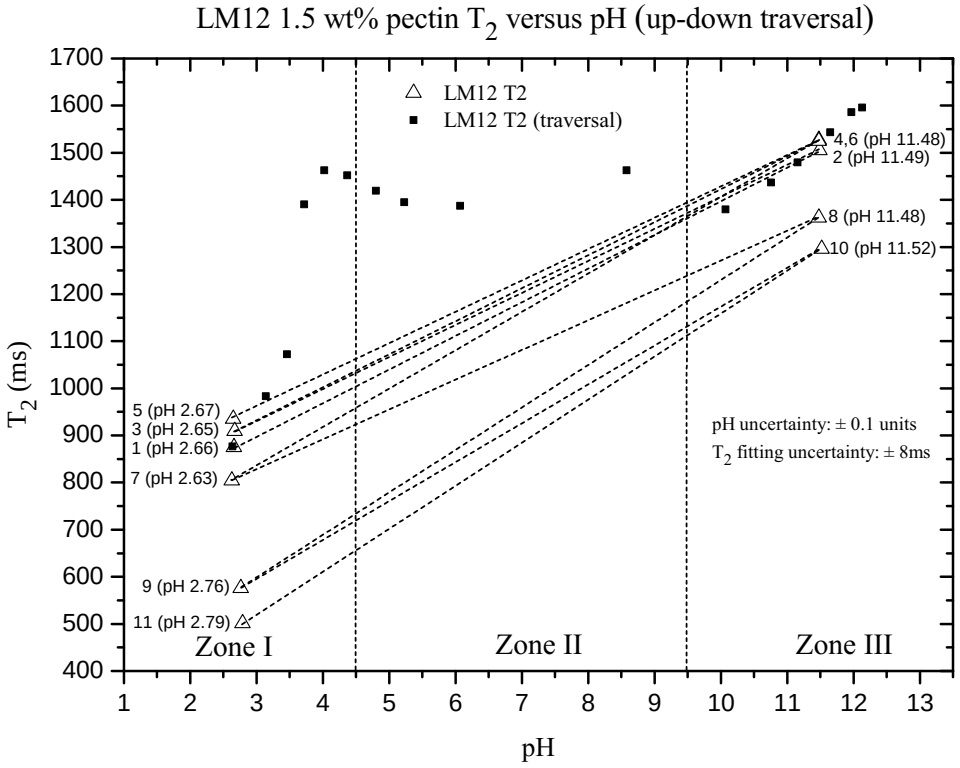

Figure 4.15: Changes in LM12 1.5 wt% pectin T_2 as the pH range is traversed ten times. The filled data points are the earlier LM12 1.5 wt% results. The unfilled data points are the spot-check measurements. pH was measured prior to T_2 in each instance. The time between spot-check experiments was about nine minutes. Data point 1 shows the starting pH of the pectin solution.

explained in terms of early stage gelling with subsequent data points indicating additional pectic modification. After the final experiment about 30% more water was present in the sample than at the beginning. This was expected to increase T_2 but instead was apparently usurped by a more dominant degradation process.

Finally, in §4.5.1 it was shown how the pH of apple pectin can change over time due to demethylation. Evidence of this phenomenon was given in Fig. 4.14 where the pH was observed to decrease by around one unit within a few minutes. LM12 pH change was measured at high and low pH during the traversal experiments. The observed change was -0.06 to -0.17 units at high pH and by -0.03 to $+0.06$ units at low pH. Evidently the LM pectin was barely affected by demethylation changes at high pH compared to the HM pectin. The final traversal measurement at high pH was an exception, dropping 0.28 pH units.

4.6 Interpreting the relaxation data

Before interpreting the GalA and pectin relaxation data, it is useful to review the measurements from the various solutions on a composite graph as shown in Fig. 4.16.

The GalA T_2-versus-pH data show relatively minor pH dependence compared to the pectins irrespective of the solution concentration. The behaviors of the two dilute GalA solutions could be argued to be a mixture of the water and the pectin relaxation results. For example, in zones I and III the GalA T_2 relaxation times are essentially identical to the water results. On the outskirts of zone II T_2 appears to decrease slightly, mimicking the water relaxation pattern shown in Fig. 5.1 on page 175. Around neutral pH however T_2 increases again slightly in like manner to the pectins. These results are perhaps not unexpected given the dilute GalA solutions are a mixture of water and the monomers that combine to form most of each pectin molecule. The concentrated GalA solution reveals a T_2 that is reduced by about one third (2,100ms down to 1,400ms) and reveals neither pectin nor water behavior around neutral pH.

In contrast to GalA, apple pectin T_2 varies gently and systematically over the pH range. Local minima are found near the two zone boundaries, a local maximum appears at neutral pH, and at the pH extremes T_2 increases then plateaus. The average T_2 relaxation time is around half the water relaxation time, thus the presence of dilute pectin is significantly enhancing relaxation of water protons.

The five LM12 solution concentrations shared a similar T_2-versus-pH behavior as seen previously. The 2.5 wt% LM12 shown in Fig. 4.16 reveals a local minimum near the zone I-II boundary and a more obvious local minimum near the zone II-III boundary. Around neutral pH a local maximum is observed. Due to lack of data points this is not strongly confirmed, especially for the lower concentration

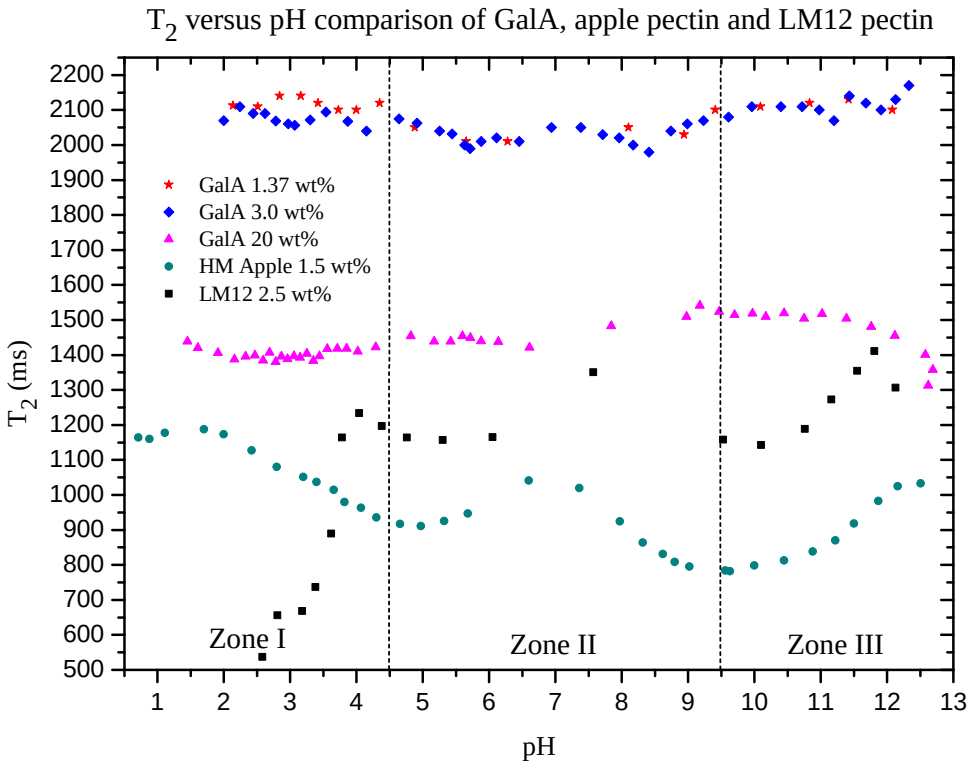

Figure 4.16: T_2-versus-pH composite graph for GalA 1.37, 3.0, and 20 wt%, apple pectin 1.5 wt%, and LM12 2.5 wt%. The four lower concentration LM12 solutions are omitted for clarity and because they follow a similar pattern to the 2.5 wt% solution.

solutions. Between pH 4 and 11.5 the shape of the LM12 T_2-versus-pH data is similar to the apple pectin. Overall, T_2 relaxation is lower for apple than for LM12 pectin even though the apple concentration is about half that of the LM12. Two other differences exist between the LM12 and apple solutions. First, below pH 4 their T_2 behaviors diverge significantly with reducing pH. The LM12 T_2 dramatically plummets while apple T_2 slowly increases. Second, above pH 11.5, LM12 T_2 decreases while apple T_2 reaches a local maximum.

4.6.1 Correlation times or proton exchange?

It is evident that the T_2-versus-pH measurements in Fig. 4.16 differ significantly for different arrangements of the same basic building blocks. It is also evident that relaxation is influenced by solution pH and solute concentration. Since almost the entire NMR signal originates from water protons, it is necessary to understand how the sugar molecules cause the water protons to relax.

The first step toward the interpretation is to recount the basis of the T_2 relaxation phenomena as explained in §1.5.3 on page 20. In essence, T_2 relaxation is caused by loss of phase coherence between ^{1}H proton magnetic moments (spins) over the spin ensemble. The natural or equilibrium state of the spin system is the absence of any phase coherences. In order to raise the spin system to a non-equilibrium state suitable for making T_2 relaxation measurements, a carefully tailored RF pulse sequence is applied to the spin system. If all protons in the ensemble were to subsequently experience identical magnetic environments, there would be no loss of phase coherence between spins, and relaxation would not occur.

For a pure Milli-Q water sample on the Mole probe, the transverse relaxation time is relatively long. This is because every water molecule is surrounded only by other rapidly moving water molecules, all behaving in similar manner. Each ^{1}H proton therefore experiences essentially the same motionally averaged dipole-dipole interaction with the surrounding spins, resulting in slow loss of phase coherence (Martin et al. (1980) [106]). The introduction of an alien species into the Milli-Q water sample can dramatically enhance T_2 relaxation by upsetting motional averaging and causing rapid loss of phase coherence. An extreme example is the presence of a minute quantity of a paramagnetic species such as O_2 (Keeler (2005) [90]) or Cu^{2+}. Unpaired O_2 electrons possess considerably larger magnetic moments than protons, thus their de-phasing influence is severe. For the water and sugar solutions used in this project, paramagnetic relaxation is not important – however there are two other important transverse relaxation pathways that need to be considered.

The first transverse relaxation pathway is hydration water correlation time lengthening. In this relaxation pathway, water molecules residing in the solvation shell of the solute have their rotational and translational correlation times lengthened. At room temperature, water molecules reorientate through 1 radian every 1–2ps (Atkins (1998) [16]), but within hydration layers around ions, sugars, and polysaccharides, the rotational and translational behavior may be slowed, thereby affecting correlation times and T_2 relaxation rates. Hills et al. cite other researchers in suggesting that hydration shell water has its rotational correlation time lengthened three-fold around sucrose, and ten-fold around lysozyme. Similarly, diffusion coefficients for water molecules within ten angstroms of the surface of bovine serum albumin have been shown to decrease translational correlation times

by a factor of five to ten (Hills et al. (1990) [71]).

It is reasonable that slowing water translational and rotational dynamics will enhance T_2 relaxation due to increasing correlation times between spins. The important question however is whether a five-fold or ten-fold slowing of the water dynamics in the hydration layer is sufficient to account for the observed relaxation in the GalA and pectin solutions.

In a series of papers *ca.* 1990, Hills and co-workers published results from dispersion experiments for a number of samples, including methanol (CD_3OH)–water mixtures, and glucose ($C_6H_{12}O_6$), lysozyme, and polysaccharide solutions (Hills et al. (1989-1992) [70–73, 75–77]). In these papers, they argued that lengthening of correlation times, even by an order of magnitude, was insufficient to account for the observed dramatic increase in proton relaxation rates in these samples. By contrast, others have more recently argued that lengthened correlation times are sufficient to account for observed relaxation (Dobies et al. (2008) [49]). This claim will be discussed in due course.

The second transverse relaxation pathway to be considered is ^{1}H proton chemical exchange. This pathway describes the actions of labile protons as they jump between the water solvent and ^{1}H hosts on a solute such as carboxyl or hydroxyl groups on GalA molecules. By exchanging sites, it is argued that protons experience differing magnetic environments, leading to loss of phase coherence. If two sites have identical magnetic environments, the Larmor frequency of the protons at both sites will be unchanged, although one publication does suggest the act of jumping induces relaxation (Gottwald et al. (2005) [63]). This claim is assumed insignificant in this thesis.

In their series of papers Hills and co-workers suggest the proton chemical exchange relaxation pathway is the dominant T_2 relaxation pathway in the systems they studied. However, they do not suggest the correlation time relaxation pathway makes no contribution to overall transverse relaxation. Instead, proton exchange is asserted to be the major pathway for a diverse range of dilute systems, such as those being studied in this thesis. Hills et al. also conclude that in dilute polysaccharide systems there is no division of water into "bound" and "free" domains, and that bound water has no significant part to play in proton relaxation phenomena. They note that it is not clear whether this is the case for more concentrated solutions (Hills et al. (1991) [70]). This comment is pertinent in light of the high concentration GalA results shown earlier.

4.6.2 Dobies et al's. interpretation

Given the conclusions of Hills et al. *ca.* 1990 regarding the insufficiency of the correlation model, it is interesting to note that the model was still being used in 2008. For example, a paper in *Applied Magnetic Resonance* presents a study

of acid-induced gelation in low-methoxy pectin (Dobies et al. (2008) [49]). In a nutshell, the paper argues that water molecules have their freedom restricted by pectin molecules, and the degree of restriction depends upon solution pH. It is worth examining the arguments presented in this paper, firstly because they seem to contradict Hills' correlation time comments, and secondly to determine whether the Dobies et al. model should be considered when interpreting this work.

Dobies et al. began with three identical ∼3 wt% LM pectin solutions and adjusted their pH values to 2.6, 3, and 5. The solutions were then subjected to four experimental techniques: NMR T_1 dispersion, NMR T_2 relaxation, NMR diffusion and rheology. The results from the rheology are not relevant to this discussion, so are ignored.

The proton T_1 NMR dispersion (NMRD) measurements were carried out between 0.01MHz and 9MHz and clearly showed the presence of dispersion, especially at reduced frequency and reduced pH. Attempting to fit the data mathematically using $J(\omega)$ showed that a single τ_c was insufficient, thus a model-free analysis was used. This provided a good fit to the data using three superimposed Lorentzian terms. From these three terms, three parameters were extracted: the average correlation time $\langle\tau_c\rangle$, the overall proton-proton dipolar coupling in the system β, and the fraction of the water proton spin-lattice relaxation rate that remains in the extreme-motional narrowing region up to the highest sampled frequency – which is also the high-field plateau of the dispersion profiles α. The value of τ_c for the water molecules changed from 0.16μs at pH 5 to 0.43μs at pH 2.6 which the authors used as evidence that the average water correlation time was lengthened by decreasing the pH. The value for β changed from $1.264 \times 10^7 s^{-2}$ at pH 5 to $3.065 \times 10^7 s^{-2}$ at pH 2.6. This was used to argue for an increase in the population of water molecules that are trapped between the pectin chains in the gelled state. The value for α increases from 0.578s to 0.841s to 0.713s for pH 5, 3, and 2.6. The authors argue that this may reflect the presence of aggregation processes of pectin chains in the gel sample (pH 2.6).

The T_2 NMR data recorded by Dobies et al. was measured at a proton frequency of 400MHz using a CPMG pulse sequence with a $90° - 180°$ pulse spacing of 1ms. The authors argue that at pH 5 the sample exhibited bi-exponential decay, although it is difficult to discern this from the published graph. The other two samples are essentially mono-exponential, although they show the pH 2.6 sample as having two contributors to the final NMR signal, one contributing 98% and the other 2%. Most importantly, they argue that their data shows T_2 decreasing from 450ms at pH 5 to 130ms at pH 2.6, a factor of about three, and use this as evidence for decreased mobility of water protons in acidic conditions where the LM pectin has gelled. Thus, the main reason for the decrease in T_2 is an increase in the stiffness of the biopolymer chains caused by junction zone formation, leading to reduced

mobility of water protons.

The diffusion data recorded by Dobies et al. used diffusion times between 20ms and 600ms. Their data showed the translational mobility of water molecules is not significantly reduced in the presence of pectin chains. For pH 5 and pH 3, the water mobility is reduced by about 20% compared to bulk water. For pH 2.6, there is less reduction in translational water mobility compared to the higher pH solutions. From this result, Dobies et al. conclude that aggregation processes probably form free spaces which allow the water to have greater freedom of movement.

From these experimental results, their conclusion is essentially that reducing the pH of LM pectin from 5 to 2.6 causes a slowdown in the dynamics of water molecules, and substantial modification to the structure of the system being studied.

There is no reason to doubt the reliability of the experimental data gathered by Dobies et al. There are however several reasons to question whether the interpretation of their results is compelling.

First, the diffusion data from Dobies et al. shows that water molecules are only slightly restricted by the pectin at all three pH values. Whether the pectin molecules form aggregates around pH 2.6 or not therefore seems a moot point since the overall change in water diffusion is so minor. It seems unreasonable therefore to correlate large changes in transverse relaxation time to minor changes in water diffusivity.

Second, the transverse relaxation argument put forth by Dobies et al. relies upon T_2 relaxation data being bi-exponential (or greater) because bi-exponential (or greater) relaxation data can be deconstructed into multiple decaying exponentials with distinct time constants and weighting. Of their three datasets, one is claimed to be mono-exponential and the other two bi-exponential. The amplitude weighting of one bi-exponential set (pH 2.6) was 2% and 98% with time constant ratio of around 3:1. The amplitude weighting of the second bi-exponential set (pH 5.0) was 23% and 77% with time constant ratio of around 2:1. In the first case the amplitude ratio is large and in the second case the time constant ratio is small. If these values are physically realistic, then accurate extraction of them from relaxation data would have been very difficult even with a signal-to-noise ratio of 100:1 (Clayden and Hesler (1991) [38]). In summary, it seems unlikely that their T_2 data provides a satisfactory experimental basis for hydration water correlation time lengthening.

Third, the NMRD data from Dobies et al. certainly shows dispersion behavior, but dispersion data such as this has also been successfully fitted many times using a proton chemical exchange model (Hills (1990) [74], Fabri et al. (2005) [56]).

It is interesting that Dobies et al. stress the importance of the proton chemical exchange mechanism for aqueous carbohydrate systems, and cite six papers by Hills and co-workers (1989–1992), yet fail to interpret their results in terms of Hills' chemical exchange model.

Finally, Chávez and Halle explain the results of their work on water proton relaxation and tissue, deliberately making no appeal to hydration layer water mobility (Chávez and Halle (2006) [36]):

> The proton species mediating the relaxation enhancement (relative to bulk water) was long thought to be hydration water at the surfaces of biopolymers. However, it is now clear that water molecules in the hydration layer are only marginally less mobile than bulk water. Water at biopolymer surfaces therefore cannot be responsible for the water-^{1}H dispersion observed with gels and tissue. The focus has now shifted to internal water molecules and labile biopolymer protons as the intermediary proton species, but opinions differ about the relative importance of the two. Whereas internal water protons exchange with bulk water protons through molecular exchange coupled to conformational fluctuations in the biomolecule, labile biopolymer protons exchange by an acid or base catalyzed process that involves covalent bond disruption. The two species can thus be distinguished on the basis of the strong pH dependence of the labile-proton exchange rate. Here we use this approach to show that the main dispersion is dominated by internal water molecules for agarose, and by labile biopolymer protons for gelatin.

4.7 Interpretation using the proton exchange model

Hills et al. made at least two important contributions to NMR studies of exchanging systems (Williams et al. (2000) [156]; Zhang et al. (2002) [163]). The first contribution showed that proton exchange plays a major role in determining the transverse relaxation behavior of biopolymer sols and gels as discussed in the previous section. The second contribution showed that data from real-world systems is amenable to analysis within the framework of a two-site exchange model (Carver and Richards (1972) [29]).

4.7.1 Defining the Carver-Richards model

The Carver-Richards (C-R) model for two-site exchange is cast in terms of eight parameters. These are listed below with a brief description alongside:

$\delta\omega$ – chemical shift difference between proton solvent and solute sites

k – proton exchange rate between solvent and solute sites

τ – CPMG 180° pulse spacing

P_a – fraction of exchangeable solvent protons

P_b – fraction of exchangeable solute protons; $P_a + P_b = 1$

T_2 – experimentally measured proton T_2 relaxation time

T_{2a} – intrinsic proton T_2 relaxation time of the solvent

T_{2b} – intrinsic proton T_2 relaxation time when resident on the solute

The chemical shift at a proton site is defined as $\omega = \gamma(1 - \sigma)B_0$ where ω is the frequency in radians per second, and σ is the site-specific shielding constant. For low-field NMR the strength of the B_0 field is very weak therefore the chemical shift difference $\delta\omega$ between solvent and solute sites can be safely ignored.

The exchange rate k is the average rate at which protons are jumping between the two sites. k is measured in reciprocal seconds (s^{-1}) and typically ranges from a few hundred up to a few tens of thousands of reciprocal seconds depending upon the pH of the system (Hills (1990) [74], Liepinsh and Otting (1996) [94]).

The τ spacing used for low-field NMR measurements in this chapter was set at 500μs. Considerably longer pulse spacings can be used on homogeneous magnets and values up to 10ms are often used in dispersion experiments.

The fraction of proton exchangeables P_a and P_b are calculated from the molarities of the solvent and solute. For low concentration aqueous GalA and pectin solutions, the number of proton exchangeables on the solute P_b is considerably less than the number of water proton exchangeables P_a. Even for high concentration 20 wt% GalA solutions at starting pH, P_b protons only account for about five percent of total exchangeables protons.

T_2 is the experimentally measured relaxation time of the pectin or GalA solution. T_{2a} is the experimentally measured relaxation time of the Milli-Q water solvent alone, and is assumed for the sake of simplicity to remain constant at its measured value of 2,100ms (at pH 7). In reality the value of T_{2a} is not constant, but appears to be affected by pH as discussed in Chapter 5, and may be reduced slightly in the presence of solute molecules. From the results of Hills et al. this effect is assumed to be insignificant for dilute solutions. They showed that T_{2a} for exchanging aqueous protein systems (bovine serum albumin) at a massive 67 wt% concentration would drop from 2,100ms to 1,300ms, and that proton exchange would still be the dominant relaxation process (Hills et al. (1991) [70]). The only relevant non-dilute solution studied in this thesis was 20 wt% GalA and the C-R model does not provide assistance to these results as discussed in due course. The remaining T_2 parameter is T_{2b}. This parameter is of particular interest because it contains information about the solute molecule's environment and dynamic behavior.

The complex C-R expression (not shown) can be simplified given the following experimental considerations. For low applied fields ($\delta\omega/2\pi \ll T_{2b}^{-1}, k$), short τ, and dilute solutions ($P_b \ll P_a$), the general expression is (Williams et al. (2000) [156]):

$$\frac{1}{T_2} = \frac{1}{T_{2a}} + \frac{P_b}{(T_{2b} + k^{-1})} \tag{4.1}$$

which simplifies further depending upon the relationship between the k and T_{2b}. When $k \gg T_{2b}^{-1}$ Eqn. 4.1 becomes:

$$\frac{1}{T_2} = \frac{1}{T_{2a}} + \frac{P_b}{T_{2b}} \tag{4.2}$$

and conversely when $k \ll T_{2b}^{-1}$:

$$\frac{1}{T_2} = \frac{1}{T_{2a}} + P_b k. \tag{4.3}$$

These expressions provide the mathematical connection between experimental data and low-level molecular behavior, thereby providing a means of extracting dynamical molecular information about the minority solute through its interaction with the majority solvent. If the low-field NMR apparatus was capable of measuring the minority solute protons directly then measuring T_{2b} would be simple and the C-R model would be unnecessary. Since this is not possible, solute information must instead be accessed indirectly using the solvent protons. This is possible because the protons exchange between the solute and solvent. The water protons act as spies, sending their protons on missions to the GalA and pectin molecules, infiltrating the sugar rings to steal T_{2b} information, then smuggling it back to the water. Interrogating water protons thus provides indirect information on the activities of the solute molecules. Of course, the downside to using a model in this way is that data revealed via the C-R model is abstracted from real molecular behavior to the degree that the model is accurate.

4.7.2 Determining P_b experimentally

The simplified C-R equation 4.1 contains five parameters. Relaxation times T_2 and T_{2a} are obtained experimentally, and molecular dynamical parameters k and T_{2b} are obtained through the C-R model. The fifth parameter P_b can be obtained using two different methods. The first method is experimental and uses the titration data from §4.4. The second method is theoretical and calculates P_b as a function of pH using known carboxyl and hydroxyl pK_a values. It will be shown in due course that reconciling the results from these two different methods was difficult, but also provided some interesting additional information on the solute properties.

For a solution containing solvent and solute, the definition of P_b is:

$$P_b = \frac{\text{num. of solute exchangeables}}{\text{num. of solute exchangeables} + \text{solvent exchangeables}}. \tag{4.4}$$

The number of water exchangeables is easy to calculate: it is twice the number of water molecules in the solvent since there are two protons per water molecule. The number of solute exchangeables is more difficult to calculate and is determined from known molecular composition. For GalA monomers there are five exchangeables per monomer: one from each of four hydroxyl groups, and one from the carboxyl group. For apple pectin there are two hydroxyl exchangeables per GalA monomer, and using the apple DM from page 102, about one additional carboxyl exchangeable per four GalA monomers. For LM12 pectin there are two hydroxyl exchangeables per GalA monomer, and using the LM12 DM from page 102, about two additional carboxyl exchangeables per three GalA monomers.

Concentrations of carboxyl and hydroxyl exchangeables are represented in the form [HA] where H is the acid, A is its conjugate base, and the square brackets represent concentration. In their separate states all water protons and all GalA/pectin carboxyl and hydroxyl protons are considered exchangeable, so the fully protonated concentration in each instance is represented as $[\text{HA}]_{max}$. Upon dissolving GalA or pectin in water, a small percentage of exchangeable protons depart the solute for the solvent resulting in a lowered pH and a decrease in the number of solute exchangeables from $[\text{HA}]_{max}$ to [HA]. Using this terminology, Eqn 4.4 is reformulated as:

$$P_b = \frac{[\text{HA}]}{[\text{HA}] + (2 \times [\text{H}_2\text{O}])} \tag{4.5}$$

where [HA] is the concentration of remaining exchangeables on the solute. This concentration is calculated by subtracting the concentration of excess protons in the solvent from the fully protonated solute concentration:

$$[\text{HA}] = [\text{HA}]_{max} - [\text{H}^+]. \tag{4.6}$$

The hydrogen ion (or ^{1}H proton) concentration is calculated from the measured solution pH:

$$[\text{H}^+] = 10^{-\text{pH}}. \tag{4.7}$$

The concentration of solute exchangeables [HA] in Eqn. 4.6 provides information at the starting pH of the solution, subsequent to dissolving the solute and prior to addition of any acid of base titrant. The addition of NaOH adds one Na^+ and one OH^- into the solution for each NaOH molecule added. Whenever an OH^- from the titrant meets an H^+ in the solvent, H_2O is formed, therefore knowing

the concentration and quantity of added titrant and by measuring the pH upon addition of the titrant leads to knowledge of [HA] at any pH:

$$[\mathrm{HA}] = [\mathrm{HA}]_{max} - [\mathrm{H}^+] - [\mathrm{OH}^-]. \tag{4.8}$$

Applying these formulae and the titration results from §4.4 for GalA, apple pectin, and LM12 pectin allowed P_b values to be calculated across the experimental pH range as shown in Figs. 4.17 and 4.18. These figures also show P_b information obtained using the pK_a method that will be discussed in due course.

It is evident from the two plots that P_b behavior is distinct within each of the three zones. For GalA and pectin solutions, P_b is observed to change similarly in zones I and III while remaining essentially static within zone II. This behavior is due to the pK_a values of the carboxyl and hydroxyl groups. The reduction of P_b in zone I is due to de-protonating of carboxyl groups, and the reduction of P_b in zone III is due to the de-protonating of hydroxyl groups. The P_b changes within zone II are minimal as the pH is at least one unit away from the pK_a values.

4.7.3 Determining P_b theoretically

In the previous section it was explained how P_b was calculated from experimental titration data at each titration step. In this section P_b is calculated using carboxyl and hydroxyl acid logarithmic dissociation constants pK_a. These values are around 3-4 and 11-12 respectively (Sila et al. (2009) [137], Williams et al. (2003) [157], Zhong et al. (1998) [164], Williams et al. (2000) [156], Gilsenan et al. (2000) [60]). pK_a expresses the affinity an atom or molecule has for its protons. The higher pK_a of hydroxyl groups means they have greater desire to protect their protons than carboxyl groups, and vice-versa.

pK_a and pH are mathematically related through the Henderson-Hasselbalch equation (Chang [34, p.647]):

$$\mathrm{pH} = \mathrm{p}K_a + log\frac{[\mathrm{A}^-]}{[\mathrm{HA}]}. \tag{4.9}$$

According to this equation, when fifty percent of the HA groups are de-protonated, $[\mathrm{A}^-]$ and [HA] are equal, the logarithm returns zero, and pH and pK_a are identical. Shifting the pH ± 1 unit either side of the pK_a results in ninety percent of the groups being (de)protonated. Likewise a shift of two pH units results in ninety-nine percent (de)protonation. This is an over-simplification as the pK_a of pectins is known in certain circumstances to change with degree of dissociation (Ralet et al. (2003) [121]), and often not all exchangeables are in fact exchangeable for various reasons that will be discussed in due course.

The acid concentration [HA] and its conjugate base concentration [A^-] are related to the exchangeable concentration $[HA]_{max}$ as discussed in the previous section:

$$[HA]_{max} = [HA] + [A^-]. \tag{4.10}$$

Rearranging Eq. 4.9 for [A^-] and substituting into Eq. 4.10 gives:

$$[HA] = \frac{[HA]_{max}}{10^{(pH-pK_a)} + 1}. \tag{4.11}$$

In this general form, Eqn. 4.11 enables evaluation of the solute acid concentration from the fully protonated concentration, the pH, and the pK_a. The total COOH and OH concentrations for the pectins or GalA can then calculated together as follows:

$$[COOH] + [OH] = \frac{[COOH]_{max}}{10^{(pH-pK_a^c)} + 1} + \frac{[OH]_{max}}{10^{(pH-pK_a^h)} + 1} \tag{4.12}$$

where the c and h superscripts indicate carboxyl and hydroxyl. Eqn. 4.12 describes the total concentration of carboxyl and hydroxyl protonated groups for any chosen pH. P_b can now be calculated for any value of pH as follows:

$$P_b = \frac{\left(\frac{[COOH]_{max}}{10^{(pH-pK_a^c)} + 1} + \frac{[OH]_{max}}{10^{(pH-pK_a^h)} + 1}\right)}{\left(\frac{[COOH]_{max}}{10^{(pH-pK_a^c)} + 1} + \frac{[OH]_{max}}{10^{(pH-pK_a^h)} + 1}\right) + (2 \times [H_2O])}. \tag{4.13}$$

4.7.4 Comparing experimental and theoretical P_b

Sections §4.7.2 and §4.7.3 explained how P_b was determined for GalA and pectin solutions using experimental and theoretical methods. The experimental results for the three GalA and six pectin solutions are shown in Figs. 4.17 and 4.18 respectively. The theoretical P_b results for 20 wt% GalA, apple, and LM12 2.5 wt% solutions are also shown.

It is evident from the superimposed datasets that experimental and theoretical P_b for 20 wt% GalA were very similar across the full pH range. The two lower concentration GalA solutions also showed strong experimental and theoretical similarity. Within zone II the experimental P_b values were about 2% higher than the theoretical values for 1.37 wt%, and about 1% higher for 3.0 wt%.

The experimental P_b values for the apple and LM12 pectins in Fig. 4.18 varied with type and concentration as expected. Surprisingly, the experimental and theoretical results, in contrast to the GalA datasets, differed significantly. Considerable

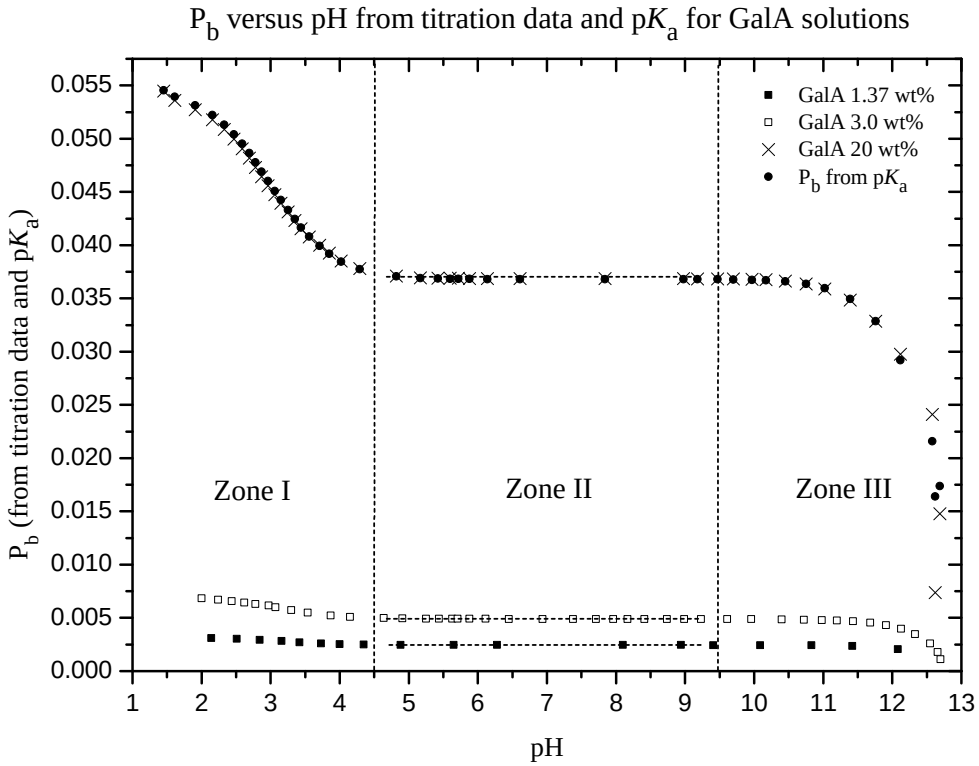

Figure 4.17: Experimentally measured P_b-versus-pH for three galacturonic acid solution concentrations, and calculated P_b-versus-pH for GalA 20 wt% using the pK_a method (lower concentration calculated values omitted for clarity). When normalized, the three datasets share a similar shape. The theoretical pK_a values used to fit the experimental data are shown in Table 4.3 on page 139. The dashed horizontal lines are a visual aid. No coefficients were used to adjust the theoretical COOH or OH values.

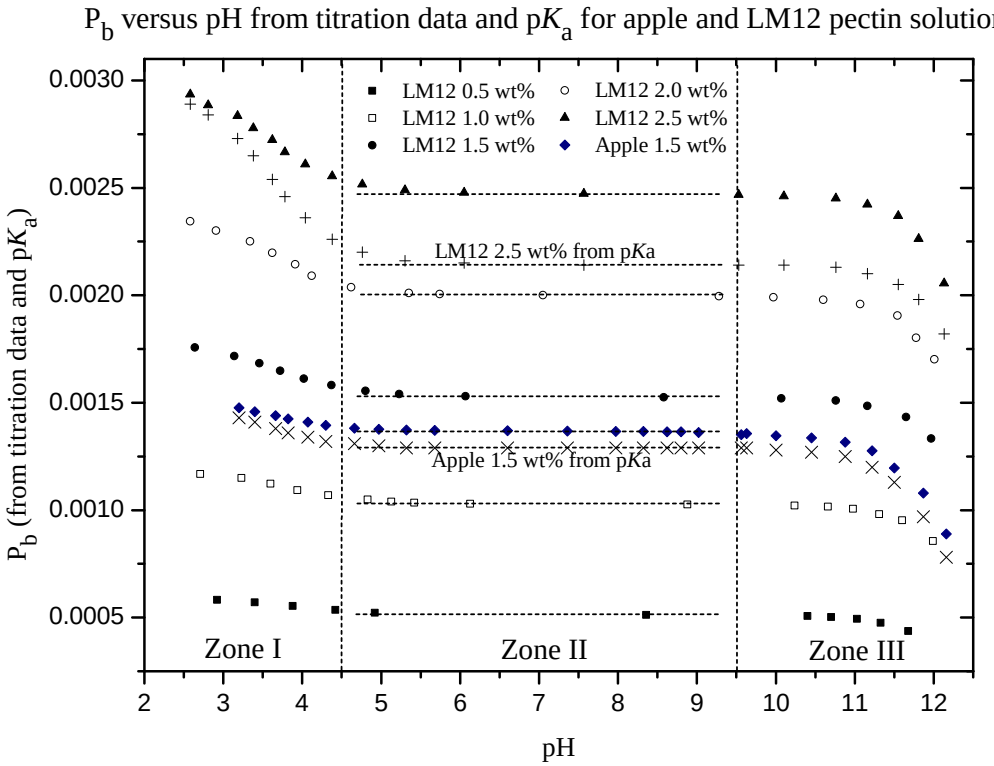

Figure 4.18: Experimentally measured P_b-versus-pH for apple and LM12 pectin solutions, and calculated P_b-versus-pH for apple and LM12 2.5 wt% solutions using the pK_a method. The theoretical pK_a values used for the experimental data are shown in Table 4.3 on page 139. The dashed horizontal lines are a visual aid. No coefficients were used to adjust the theoretical COOH or OH values.

time was spent checking calculations and pondering the reasons for these differences. The same titrant was used for the GalA and pectins, and all experimental preparations were likewise identical. Further, the differences were present in both pectin types suggesting the problem was probably not related to pectin purity or manufacturer error. Instead, the problem appeared to be lower than expected experimental P_b values, suggesting far fewer carboxyl protons were being liberated from the pectin chains than would be expected according to theory. The large discrepancy between experimental and theoretical results did not appear in the GalA solutions.

Fig. 4.19 illustrates the experimentally measured degree of carboxyl protonation for all GalA and pectin solutions from their starting pH values up to around neutral pH. It is assumed that no hydroxyl de-protonation has taken place due to the high pK_a of the hydroxyl groups. Evidently the degree of pectin carboxyl de-protonation reaches only about 50% with apple pectin being slightly higher. By contrast, the GalA solutions reach 90–100% carboxyl de-protonation with the high concentration solution being closest to fully de-protonated as previously discussed.

Fig. 4.20 shows the experimentally measured degrees of protonation for both carboxyl and hydroxyl groups over the full pH range. At neutral pH GalA protonation is around 80% due to almost all carboxyl protons being removed while the four hydroxyl groups remain intact. For the pectins with DM values discussed previously and the experimentally measured maximum degree of de-protonation of around 50%, then approximately 93% and 88% total (COOH+OH) protonation is expected as shown on the graph.

In zone III of Fig. 4.20 the hydroxyl groups begin de-protonating. It is unclear whether the de-protonation was entirely due to hydroxyls or whether there was also a carboxyl contribution. De-protonation of the GalA and LM12 molecules began around pH 10, and the apple pectin began between pH 8 and 9. The lower pH values for the apple pectin may have been due to saponification as discussed previously in §4.5.1 as this would have caused an increase in COOH groups, followed by de-protonation, thus reducing the pH. As the pH is further increased to 11–12 and beyond, de-protonation happens rapidly and it is difficult to quantify the de-protonation without large uncertainties.

4.7.5 Reconciling experimental and theoretical P_b

In order to reconcile the theoretical and experimental P_b values, coefficients were added to $[\text{COOH}]_{max}$ and $[\text{OH}]_{max}$ in the mathematical model described in equation 4.13. The coefficients represent the effective fraction of COOH and OH groups on the GalA and pectin molecules involved in proton donation. Determining the coefficients began with plotting the experimental and theoretical datasets on a common graph, then adjusting the coefficients until the model data matched the

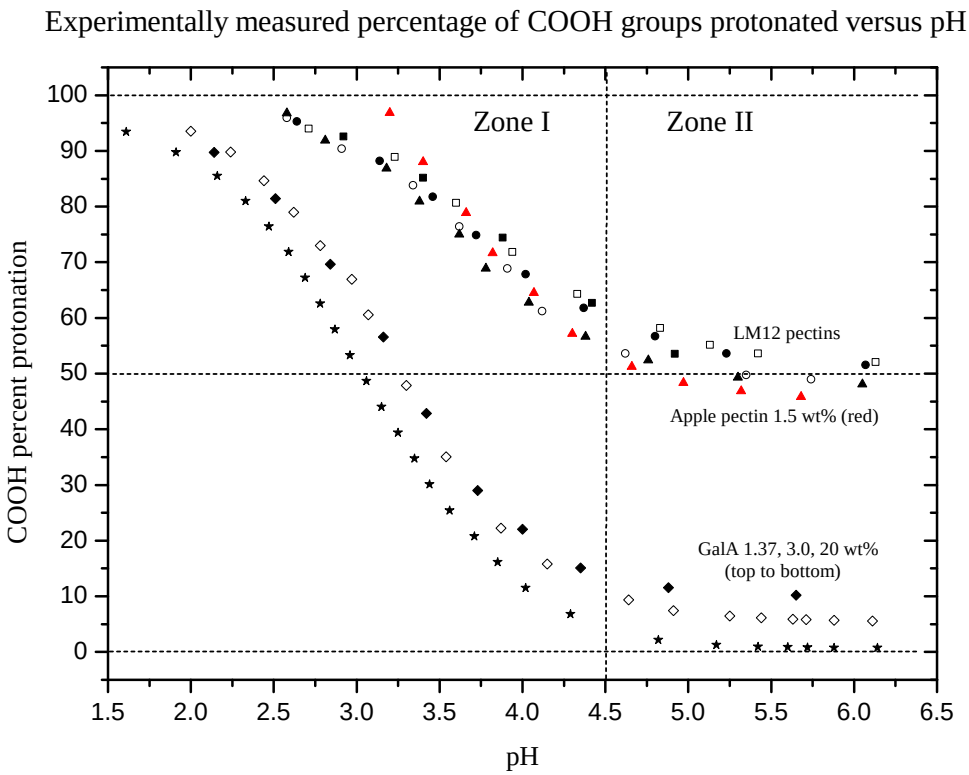

Figure 4.19: Percentage of protonated carboxyl groups for GalA, apple pectin, and LM12 pectin versus pH in zones I and II. At starting pH the GalA carboxyls are ∼93-97% protonated, apple pectin ∼97% protonated, and LM12 pectins ∼92-97% protonated. In zone II where pH is at least two units above pK_a the pectin carboxyls only reach ∼50% protonation. By contrast the GalA carboxyls are almost fully de-protonated. The dashed horizontal lines are a visual aid.

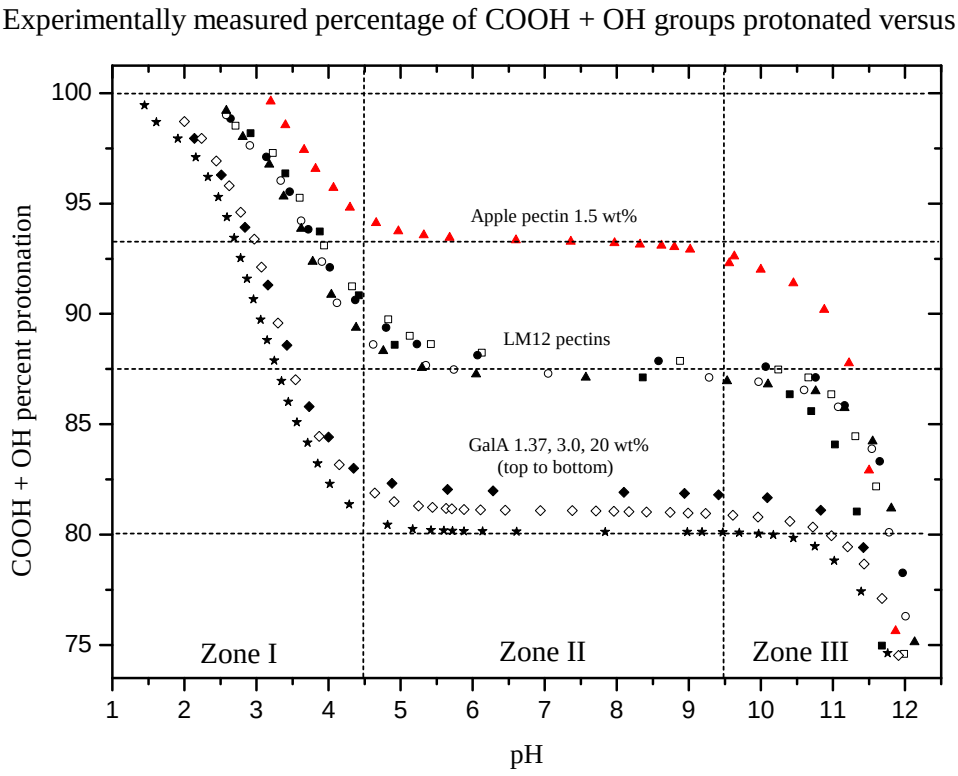

Figure 4.20: Percentage of protonated carboxyl plus hydroxyl groups for GalA, apple pectin, and LM12 pectin versus pH across all three zones. At neutral pH the GalA sugar rings remain 80-82% protonated, apple pectin 93% protonated, and LM12 pectins 87-88% protonated. The dashed horizontal lines are a visual aid.

experimental data as closely as possible. In addition, the two pK_a values were adjusted to complete the fitting. The resulting datasets for the pectins are shown in Fig. 4.21. The coefficients and pK_a values are shown in Table 4.3.

During fitting of each dataset, the OH pK_a and coefficient adjustments were nicely separable, and could be adjusted to accurately fit the theoretical data to the experimental data. Fitting of the COOH coefficients and pK_a values was more difficult as both parameters operated upon the same low-pH data points. The apple fit proved most elusive, requiring a COOH coefficient significantly different from the measured value (0.73 versus 0.56). Reducing this coefficient to around 0.56 led to a slightly worse fit and raised the pK_a to around 3.8, similar to the LM pectins.

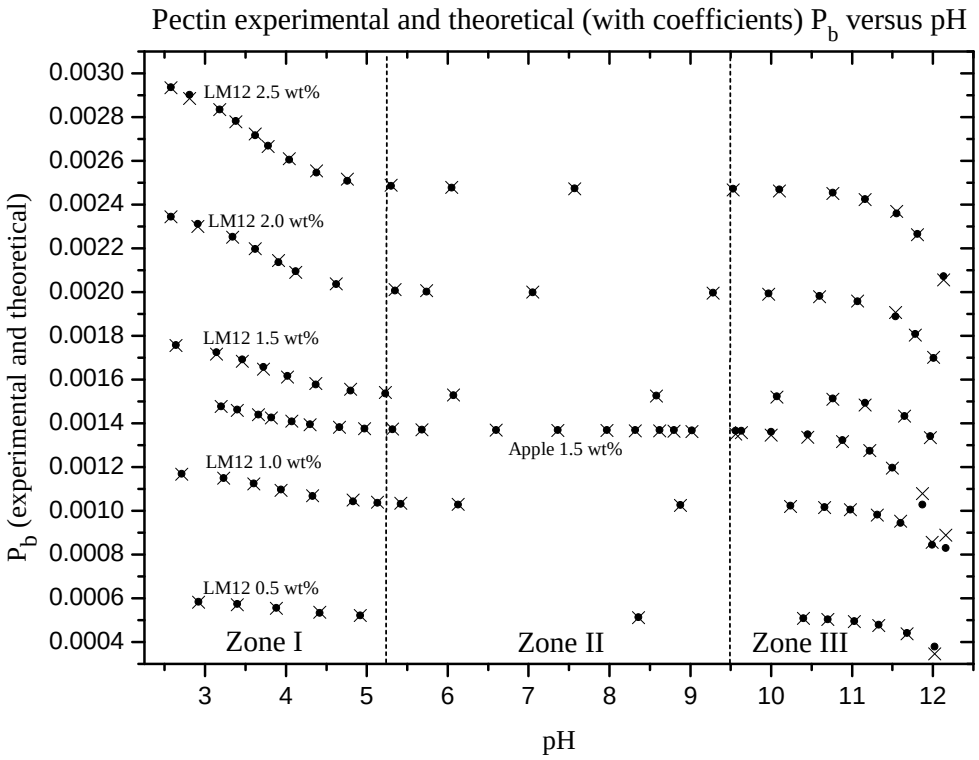

Figure 4.21: The modeled and experimental P_b values were reconciled by adjusting the carboxyl and hydroxyl coefficients and pK_a values as shown in Table 4.3. The experimental and model data values are represented by "•" and "×" respectively.

Table 4.3: Carboxyl and hydroxyl coefficients and pK_a values for GalA and pectin. These values reconciled the experimental and theoretical data as shown in Fig. 4.21. Uncertainties were calculated by adjusting the model parameters to fit the model data to the experimental data.

Sample	Conc. (wt%)	Carboxyl coeff.	Hydroxyl coeff.	Carboxyl pK_a	Hydroxyl pK_a
GalA	1.37	0.87±0.03	1.02±0.01	3.2±0.1	12.9±0.2
GalA	3.0	0.93±0.03	1.01±0.01	3.3±0.1	13.0±0.2
GalA	20	0.96±0.03	1.00±0.01	3.1±0.1	12.9±0.2
Apple pectin	1.5	0.73±0.03	1.06±0.01	3.6±0.1	12.4±0.2
LM12 pectin	0.5	0.50±0.03	1.15±0.01	4.0±0.1	12.5±0.2
LM12 pectin	1.0	0.46±0.03	1.17±0.01	3.9±0.1	12.7±0.2
LM12 pectin	1.5	0.46±0.03	1.16±0.01	3.8±0.1	12.9±0.2
LM12 pectin	2.0	0.52±0.03	1.16±0.01	3.7±0.1	12.9±0.2
LM12 pectin	2.5	0.54±0.03	1.15±0.01	3.6±0.1	13.0±0.2

As expected, the GalA coefficients required minimal adjustment, especially at the highest concentration. The modeled carboxyl pK_a values were at the low end of the published range discussed on page 131, and the hydroxyl pK_a values were around one pH unit above the published range.

The apple pectin hydroxyl coefficient required almost no adjustment. The carboxyl pK_a value was near the middle of the published pH range and the hydroxyl value was about half a unit above the published range.

The LM12 pectin carboxyl coefficients all required values around 0.5, agreeing with the experimental results, showing around 50% de-protonation at neutral pH. The hydroxyl coefficients needed minor adjustment above unity. The carboxyl coefficients indicated that only about half the carboxyl groups were ionized irrespective of concentration. The LM12 carboxyl pK_a values were inside the published range and trended monotonically downward with increasing pectin concentration suggesting a concentration dependence. A similar trend was not observed for the GalA solutions. The hydroxyl pK_a values showed a similar trend in the upward direction beginning about half a pH unit above the published range.

In summary, the coefficients and pK_a values extracted from the modeled data provide useful information regarding the degree of de-protonation experienced by both the GalA and the pectins. The modeled GalA de-protonation required minimal coefficient adjustment. By contrast, the apple and LM12 pectins required significant adjustments, especially to the carboxyl coefficients for reasons that are

discussed further in due course. The GalA carboxyl pK_a values were lower than the pectin values suggesting the pectins hold their carboxyl protons more firmly, especially at lower concentrations. LM12 hydroxyl coefficients around 1.16 suggests the number of hydroxyl groups is greater than expected. This may be due to the assumption used in the model that only 90% of the LM12 monomers contained hydroxyl groups. This assumption ignores any contribution from other sugars present in pectins (Ridley et al. (2001) [129]). The small variations within the modeled pK_a values and their differences with the published values suggest the carboxyl and hydroxyl pK_a values are species dependent.

4.7.6 Understanding experimental P_b

In §4.7.4 it was observed that experimental and theoretical P_b values were almost identical for the GalA solutions but were significantly different for the pectin solutions. The observation that molecular differences lead to reduced P_b finds sympathy with Hills et al. who suggest P_b is reduced by conformational changes that alter the accessibility of exchangeable biopolymer protons to chemical exchange (Hills et al., (1990, 1996) [70, 74]). The evidence provided by Hills et al. originates from dispersion measurements performed on laminaran which is a low molecular weight (DP $<$ 300) molecule consisting of unbranched glucose units in β-1,3 conformation. For the dispersion measurements to fit the theoretical model, the number of exchangeables P_b needed to be reduced to 70%. These authors also cite an experiment by Nardin and Vincendon in which polydisperse laminaran was dissolved in D_2O. After two hours ∼70% of the hydroxyl protons had exchanged. The other ∼30% were presumed to be inaccessible due to longer Laminaran chains ($>$ 49 glucose units) forming rigid helical structures. While Hills' interpretation could apply to pectins within zone I whereupon minimal electrostatic repulsion between chains exists, thus allowing entanglement, it seems unlikely that steric hindrance would limit accessibility to exchangeables in zone II and zone III where the chains exist in an extended conformation.

Further, Hills et al. quoting Nardin and Vincendon describe the exchange percentage for schleroglucan in solution (Hills et al., (1990) [70]). Schleroglucan consists of a linear chain of β-1,3 linked glucose units with a single pendant β-1,6 linked glucose on every third unit along the backbone. In the solid state schleroglucan adopts a triple helical structure with the pendant units pointing radially outward from the helix. In solution schleroglucan forms a thick gel, suggested to result from a high percentage of triple helical structures. Schleroglucan was found by Nardin and Vincendon to have exchanged only ∼18% of its OH groups for OD groups after four cycles of dissolving in D_2O, heating to 90°C for two hours, then freeze drying (Nardin and Vincendon, (1989) [111]). This was attributed to a rigid and packed helical structure and an ordered hydration water

shell around the triple helix core. Hills et al. noted this as surprising because the pendants alone were expected to provide 33% of the exchangeables, suggesting helix association or a tight hydration sheath as the cause. The latter seems unlikely at the elevated temperatures, and it is difficult to see how helical association or a hydration sheath could be applied to extended pectin chains in dilute solution.

The explanations for reduced P_b given by Hills et al. and by Nardin and Vincendon are somewhat satisfying. However, there are several reasons why these explanations for reduced P_b should not apply to dilute pectin solutions. First, while LM pectins are known to form hydrogen bonded gels at low pH due to minimal electrostatic repulsion between chains, at pH 7 pectin chains are extended and charged with no hint of gel formation (Gilsenan et al. (2000) [60]). Repulsive intra- and inter-molecular forces causing extended chain conformations seem unlikely to support steric hindrance. Second, it seems unlikely ordered hydration water shells around pectin molecules would permanently restrict access to one half of the pectin carboxyl exchangeables. Third, de-protonation of the five LM12 solutions is almost identical in spite of dramatic concentration variations and remains essentially constant within zone II. This suggests the P_b limiting mechanism was not inter-molecular but rather intra-molecular, and the remaining carboxyl protons were very firmly attached to the group since even basic conditions were unable to dislodge them.

Hypothesizing that P_b is not restricted by chain entanglement or hydration water but rather by an intra-molecular phenomena necessitates another explanation. One possibility is the existence of a physical boundary to the ionic charge density along the molecular chains. At starting pH the ionic charge density is low as only a few percent of pectin carboxyl protons are donated to the solvent. Raising pH increases the percentage of proton donors which in turn increases the charge density and the pK_a. The pK_a is thus a function of pH, and is known to differ depending upon pectin structure (Ralet et al. [121]). (This was ignored in the modeling in §4.7.4.)

Gerald Manning addressed the subject of ionic charge density in a series of papers beginning in 1979 under the banners of polyelectrolyte theory and counterion condensation (CC) (Manning (1979-1996) [101–104], Ray and Manning (2000) [123]). Manning's CC theory has been considered controversial and in competition with Poisson-Boltzmann theory for theoretically predicting the distributions of small, mobile ions around polymers, colloids, biomembranes, and biomolecules in solution (Stigter (1995) [146]). Around DNA, counterions are believed to form a cloud around the charge density of the nucleic acid. They are not bound to specific sites, and maintain their inner sphere hydration water as they move up and down the phosphate backbone. The effect of the counterion condensation is to reduce the effective charge on the nucleic acid, which in turn has a profound effect upon

solution properties, binding interactions, and stability of nucleic acids (Blackburn (2006) [22]).

Manning's theory attempts to describe distributions of counterions around highly charged polyelectrolytes in terms of the linear charge density parameter:

$$\xi = l_B/b \tag{4.14}$$

where l_B ($= e^2/4\pi\epsilon_0\epsilon kT$) is the Bjerrum length of ~7Å in water solvent at 25°C and b is the average charge spacing along the contour of the polymer (Stigter (1995) [146]). The Bjerrum length is the distance between two elementary charges when the electric potential energy is comparable to the thermal energy. When the value of ξ is less than unity for monovalent counterions (1/2 for divalent, 1/3 for trivalent...), the average charge spacing is greater that the Bjerrum length, and there is no layer of counterions. When ξ is greater than the Bjerrum length a condensed layer is present containing the number of counterions required to lower the net charge density of the complex polymer with its condensed layer to the critical value (Manning (1996) [104]).

The repeat unit length of polygalacturonan from which pectins are largely constructed is ~0.435nm (Rinaudo (2009) [130]). For LM12 with DM around 40% the value of $\xi = (l_B/b)(1 - \mathrm{DM}/100) = 0.98$ which essentially equals the critical value. To reach this value however all LM12 carboxyls need to be de-protonated. The experimental results showing only ~50% de-protonation therefore either suggests an inadequacy in this model or a pectin structure with a smaller repeat unit length between carboxyl groups. For apple pectin with DM around 70% the critical value $\xi = 0.49$. According to Manning no counterion layer should exist, suggesting the model is inadequate to explain what is inhibiting the donation of carboxyl protons. Chain entanglement, crossovers or other interactions seem improbable since the LM12 P_b results are almost identical for all concentrations. The fact that P_b was observed to decrease near the hydroxyl pK_a suggests that Manning's limit had not been reached. If the limit had been reached, the protons would have remained fixed to the pectin molecules. De-protonation of pectins remains as an area requiring future research.

4.7.7 Extracting $T_{2b} + k^{-1}$ for galacturonic acid and pectins

In §4.7.1 the simplified C-R equation was shown to contain five parameters. Subsequently three of those parameters were obtained experimentally (T_2, T_{2a}, and P_b). Rearranging the simplified C-R equation for the remaining unknowns results in

Eqn. 4.15:

$$T_{2b} + k^{-1} = \frac{P_b}{\left[\frac{1}{T_2} - \frac{1}{T_{2a}}\right]}. \tag{4.15}$$

Assuming the C-R model provides a realistic picture of the underlying molecular reality, then the information contained in $T_{2b} + k^{-1}$ is specific to the molecular dynamics of the GalA and pectin solutions across the measured pH range.

4.7.7.1 Galacturonic acid molecular level data

Applying Eqn 4.15 to the three experimental GalA datasets shown in Figs. 4.5 and 4.17 revealed the $(T_{2b} + k^{-1})$-versus-pH information shown in Fig. 4.22. It was not possible to use the equation to extract useful information from the 1.37 and 3.0 wt% datasets due to T_2 and T_{2a} values being very similar, resulting in the denominator of Eqn. 4.15 hovering around zero. In this condition the denominator acts to amplify noisy data resulting in $T_{2b} + k^{-1}$ ranging between approximately ±2,000ms. By contrast, the 20 wt% GalA T_2 data was distant from T_{2a} and could not be extracted.

4.7.7.2 Apple and LM12 molecular level data

Applying Eqn 4.15 to the pectin datasets shown in Figs. 4.7, 4.9 and 4.18 revealed the $(T_{2b} + k^{-1})$-versus-pH information shown in Fig. 4.23. Unlike the dilute GalA solutions, the pectin T_2 and T_{2a} times were distant from one-another thus allowing sensible data to be extracted.

These results share few similarities with the 20 wt% GalA results. The behavior of the LM12 data across the three zones is generally opposite to the GalA behavior, and the extracted values for $T_{2b} + k^{-1}$ are significantly shorter than the GalA values.

4.7.8 Interpreting T_2–versus–pH for GalA solutions

Fig. 4.5 on page 107 shows the experimentally measured T_2-versus-pH data for three different GalA solutions. Contained within the data is molecular level information about the solutions and the solvent-solute interactions.

Accessing the molecular information requires interpretation of the T_2 data which in turn requires an understanding of the relaxation mechanisms. Two mechanisms were discussed for exchanging solvent-solute systems on page 123. They were the correlation time and proton chemical exchange mechanisms. As pointed out by Hills, one of the major difficulties in interpreting water proton relaxation times

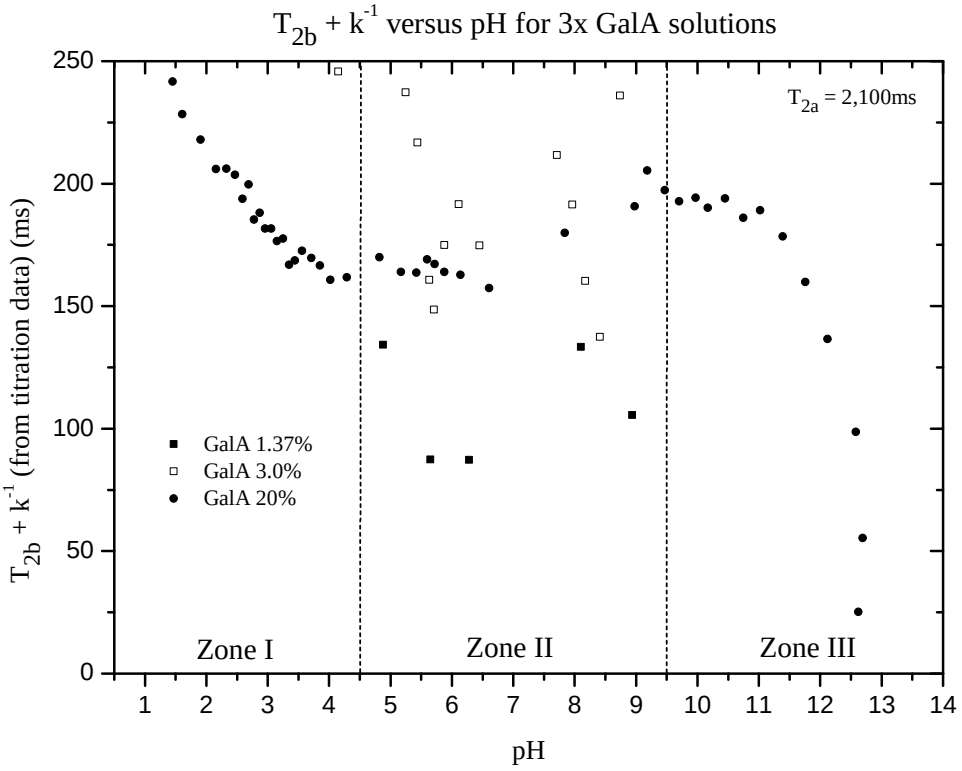

Figure 4.22: $(T_{2b} + k^{-1})$-versus-pH for the three GalA solutions. The ordinate axis is defined to fit the 20 wt% data and therefore clips much of the 1.37 and 3.0 wt% data.

in solutions is knowing to what extent these two mechanisms contribute to the relaxation (Hills (1996) [74]).

For the pectin solutions it is assumed the C-R proton chemical exchange model accurately represents underlying molecular behavior. For GalA solutions the chemical exchange model is also likely to apply, however at high solute concentration the effects of lengthening correlation times may also play a significant role.

The dilute GalA solutions could not be interpreted using the C-R model due to similarity of T_2 and T_{2a} values. It can be seen from Eqn. 4.15 that such a condition leads toward a zero denominator, resulting in physically unrealistic values of $T_{2b} + k^{-1}$. Some of these values are shown for the dilute solutions in Fig. 4.22 while other lie well outside the confines of the graph. In contrast to the dilute solutions, the concentrated solution T_2 and T_{2a} values did allow meaningful $T_{2b}+k^{-1}$

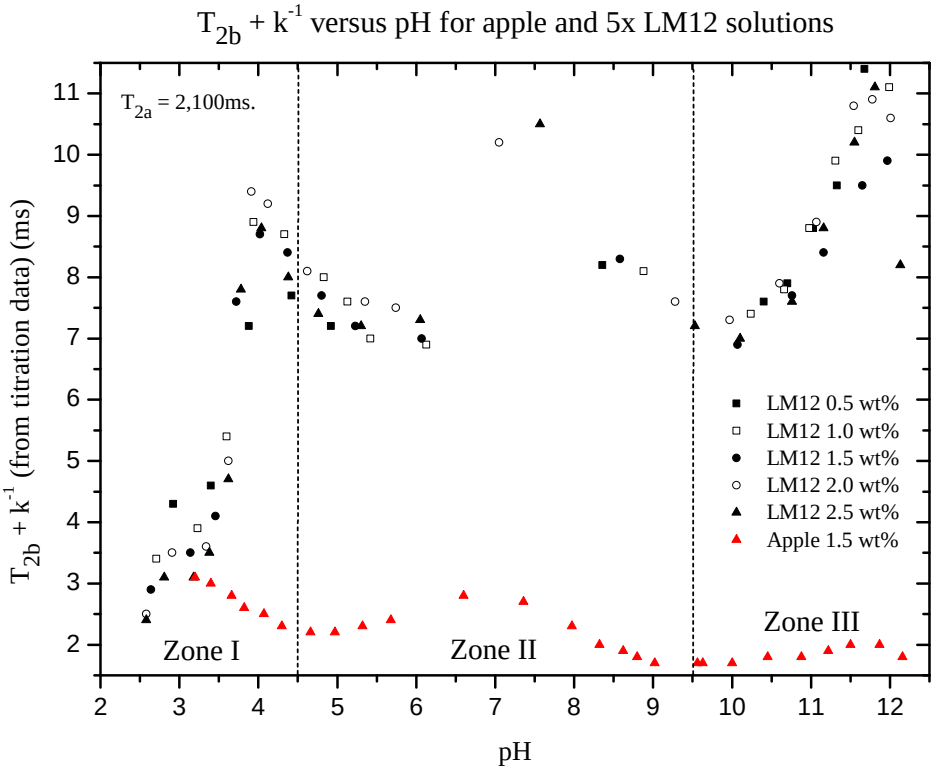

Figure 4.23: $T_{2b} + k^{-1}$ for apple and LM12 pectin solutions. The LM12 results are similar irrespective of solution concentration. All apple pectin $T_{2b} + k^{-1}$ times are significantly shorter than LM12 values at the same pH except below around pH 3.5.

data to be extracted as shown.

The extracted data from the concentrated solution shows that as the pH was increased, $T_{2b} + k^{-1}$ decreased within zone I, increased slightly in zone II, and decreased again within zone III. According to the figure, values for T_{2b} were generally between 150–250ms, which are physically realistic values. Fabri et al. studied many similar sugars using dispersion measurements obtained using a Bruker 80MHz electromagnet-based NMR apparatus and generally found T_{2b} times to vary between 100-300ms depending upon sugar type and concentration. Larger sugars and higher concentrations tended to have shorter T_{2b} times (Fabri et al. (2005) [56]).

If these numbers were correct then k^{-1} could be safely ignored for reasons to be discussed in due course, leaving the high concentration result in Fig. 4.22 purely in

terms of T_{2b}-versus-pH.

To accept the changing T_{2b} in Fig. 4.22 as physically realistic, an underlying chemical mechanism is required to explain the changes. It will be seen later that pectin T_{2b} values vary significantly with changes in polymer conformation. This cannot be applied to simple monomers however, therefore another mechanism is necessary.

Fig. 4.17 showed how P_b changed with pH across the three zones. This provides an insight into the chemical changes happening to the GalA molecules. As P_b decreased in zone I, the carboxyl groups changed from almost fully protonated to almost fully de-protonated. This reduced the fraction of exchangeable carboxyl protons as shown in Fig. 4.19 and the total fraction of exchangeable protons as shown in Fig. 4.20. Reducing exchangeables would be expected to increase T_2 in zone I and further increase T_2 in zone III. Within zone II P_b was static and should likewise be reflected in T_2 within zone II.

The T_2 predictions due to P_b could be loosely observed to fit Fig. 4.5. There is an overall trend toward higher T_2 with increased pH if the pH extremes are ignored, however zone II does not appear to show the predicted stasis compared to zones I and III. Perhaps additional chemical changes were happening, resulting in T_{2b} mimicing P_b across all three zones, or perhaps correlation time lengthening was actually the cause of relaxation.

Correlation time lengthening would be expected to have minor effect upon dilute GalA solutions since the GalA-to-water molar ratios were around 1:700 and 1:350 for the two solutions. At these ratios the vast majority of water molecules at any particular time would be unaffected by the GalA molecules. By contrast, correlation time lengthening could have a strong effect upon T_2 for the 20 wt% solution since the molar ratio was around 1:45. At this ratio most GalA molecules would be motionally restricted and most water molecules would be within a hydration layer. Depending upon the molecular correlation times, this mechanism seems a viable alternative to proton chemical exchange. As with the dilute solutions, this did not change the mono-exponential nature of any relaxation decays, indicating no compartmentalizing of water protons.

The dispersion measurements mentioned earlier revealed proton exchange, so there is excellent reason to believe this relaxation pathway is active in the GalA solutions. However the fact that Fabri et al. were unable to find a clear pattern between the C-R parameters and different sugar chemistries may suggest chemical exchange was not the only pathway. In that case the GalA T_{2b} values deemed physically realistic may in fact need revision.

It may be argued that concentrated solutions reduce T_{2a} due to restricted water movement. While this is a possibility, Hills suggests from the solutions he studied that there is only a slight shortening of T_{2a} (Hills (1996) [74]).

4.7.9 Interpreting T_2–versus–pH for the pectins

Figs. 4.7 and 4.9 on pages 109 and 111 show the experimentally measured T_2-versus-pH data for the apple and LM12 pectin solutions. The goal of this section is to interpret these results in terms of molecular behavior. The apple and LM12 results were clearly different: the apple pectin data varied gently with pH within a small range of T_2 values (800-1,200ms) while the LM12 data varied abruptly over a wide range of T_2 values (500-1,900ms). It will be argued in due course that these arose largely due to changes in the number of exchangeable protons and conformational rearrangements of the pectic molecules.

4.7.9.1 The utility of zones

At the beginning of this chapter titration and T_2 measurements were plotted against pH for GalA and pectin solutions. The spanned pH range was then divided in three zones: I, II and III. In the first and third zones the pH was observed to change slowly with relatively large additions of titrant, while in the middle zone the pH changed rapidly with minute additions of titrant.

In the first and third zones the dilute GalA and Milli-Q water samples showed minimal T_2 variation while in the middle zone T_2 was found to decrease slightly. By contrast, the pectin measurements did not easily separate into three zones although it could be argued the behavior pattern in each zone was unique.

Upon examination of P_b for the GalA and pectin solutions, the three zones showed more utility. In zone II P_b showed stasis while in zones I and III significant changes were revealed. This was due to the pK_a values of the carboxyl and hydroxyl groups respectively.

While P_b changed only in the outer zones, T_2 for the pectins also changed in zone II as shown in Figs. 4.7 and 4.9. This indicated that another pH-dependent phenomena was active in the pectin solutions in addition to protonation and de-protonation. The manifestation of this mechanism was seen clearly in the apple pectin T_2 results due to the abundance of data points around neutral pH.

4.7.9.2 Interpreting zone I

Many studies utilizing a variety of techniques have focussed upon pectin under the acidic conditions found in zone I. This is sensible as dissolved pectin is naturally acidic, and is chemically stable around its starting pH as discussed in §4.4.2 and §4.4.3 (Sila et al. (2009) [137]). In addition, within this limited pH range, pectic molecular behavior changes dramatically, therefore providing conditions for obtaining a rich variety of experimental data.

The chemical conformations of macromolecular pectin molecules are known to change with pH. This is due in part to charged groups along the length of

the polymer as expressed in the fraction of exchangeable protons P_b. At starting pH pectin molecules are almost fully protonated, having lost only a few percent of their carboxyl protons to the solvent. At increased pH additional carboxyl protons abandon the polymer, leading to increased electrostatic repulsion within and between the pectin chains. Changing conformations affect relaxation times due to proton spin relaxation being largely determined by dipole-dipole interactions. The effect of these interactions is proportional to the inverse-sixth power of the distance between the protons and is therefore sensitive to local motions (Callaghan (1991) [26]).

An examination of the HM and LM pectin T_2 data in Fig. 4.16 reveals significant differences between the two pectin types over the full pH range. The T_2-versus-pH patterns may appear at first glance to be uncorrelated. Upon close inspection however, significant T_2-versus-pH similarities also exist between the two pectin types. For example, in zone II both the apple and LM12 pectins exhibit similar maxima around neutral pH and decrease as each zone boundary is approached. In zone III both pectin types show T_2 increasing with pH, with perhaps a sudden decrease at the highest pH similar to the concentrated GalA solution. In zone I however significant behavioral differences appear between the two pectin types: the apple pectin T_2 increases with reducing pH while LM12 shows a similar initial increase followed by a sudden and rapid decrease.

Starting slightly inside zone II at around pH 5 and moving toward lower pH, the apple and LM12 pectins share a similar T_2-versus-pH shape until reaching pH 4. At this point the apple data continues to increase gently while the LM12 changes direction abruptly and T_2 plummets. This change cannot be attributed to exchange rate k for reasons to be discussed in due course. As the pH is lowered, the number of biopolymer exchangeables P_b increases, which should lead to a gentle decrease in T_2 according to the C-R equation. However the opposite is observed for apple pectin, and the change observed for LM12 pectins, while moving in the predicted direction, is much more abrupt than expected as will be seen in due course. The results from the C-R equation in which $T_{2b} + k^{-1}$ data was extracted is shown in Fig. 4.23 and shows how T_{2b} changes within zone I. Assuming the C-R model provides a realistic picture of the underlying molecular reality, then the problem is how to relate T_{2b} to the molecular level changes in the pectins. In the following, results from other pectin researchers using several different techniques are discussed.

Molecular modeling A suitable place to start is with a molecular modeling study of three dimensional pectin structures (Pérez et al. (2000) [117]). According to this theoretical study, four different low energy helical conformations are possible in the backbone of methyl-esterified α-(1→4) galacturonan which forms the majority

of all pectin molecules. The four conformations are: three-fold left-handed, and two-fold, three-fold, and four-fold right-handed, where an n-fold helical conformation refers to the number of subunits required to provide a full helical rotation. Examples of two-fold and three-fold pectin conformations are shown in Fig. 4.24. According to the modeling results, the energy differences between the different conformations were sufficiently small that conformational changes could be driven by neighboring ions, the solvent, other macromolecules, and presumably protonation or de-protonation of charged carboxyl groups along the pectic backbone.

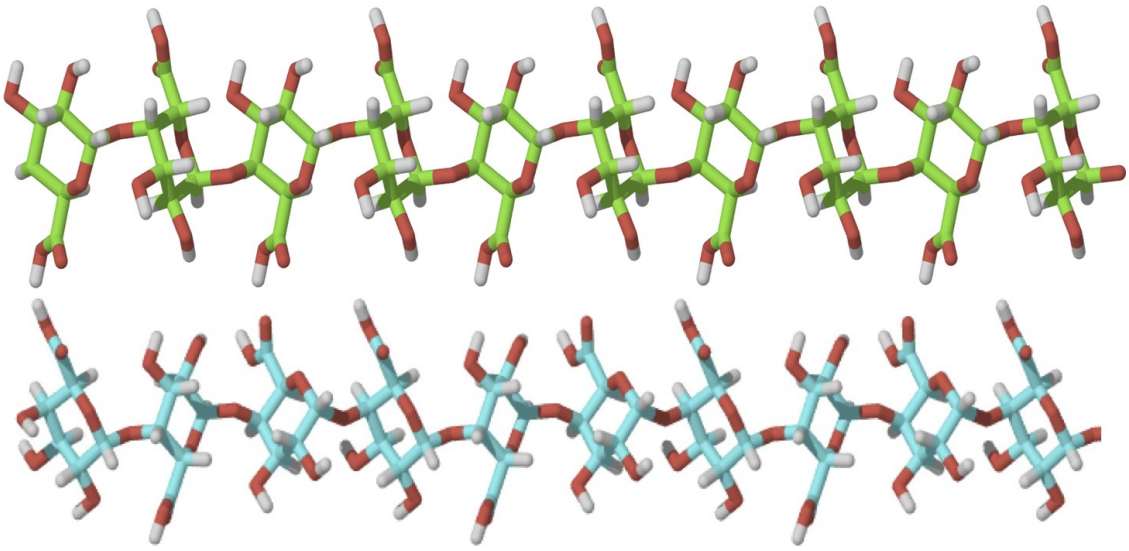

Figure 4.24: Small sections of a pectin molecule. The upper and lower images shows the pectin in two-fold and three-fold helical conformations respectively. Images courtesy of Erich Schuster.

Rheology Other researchers performed concurrent rheological, optical rotation and DSC experiments on LM 31.1 pectins (Gilsenan et al. (2000) [60]). The rheological experiments were performed on 3.0 wt% pectin at 5°C to obtain storage (G′) and loss (G″) moduli. At pH 4.0, G″ > G′ indicated predominantly liquid-like behavior. At pH 3.0 the results indicated cross-linking just sufficient to give a continuous network. At pH 2.0, G′ ≫ G″ indicating gel-like behavior which became more pronounced at pH 1.6.

Further rheological experiments were performed using the same pH values with temperature as the independent variable. Interestingly, around pH 2.5-3.5 there was virtually no thermal hysteresis in either G′ or G″. At pH 1.6 there was some

thermal hysteresis, while at pH 4.0 there was massive thermal hysteresis. The absence of thermal hysteresis between pH 2.5-3.5 was suggested as evidence against the formation of large aggregated networks within this pH range. Instead, it was suggested that three-fold helices form dimers, or perhaps somewhat larger assemblies such as trimers or tetramers. Below approximately pH 2.5 thermal hysteresis is attributed to extensive aggregation as electrostatic repulsion is suppressed. Above approximately pH 3.5 thermal hysteresis is attributed to slow formation of intermolecular hydrogen bonds by protonated carboxyl groups.

Optical rotation Alongside the rheology measurements, optical rotation measurements were also performed using the same pectin but at 0.4 wt% and at pH values of 2.0, 3.0, 3.5 and 7.0. According to the authors optical rotation is well established as a sensitive index of changes in polysaccharide chain conformation. At pH 2.0 and 7.0 the specific rotation $[\alpha]$ changed linearly with temperature over a 10-80°C range indicating no conformational changes. At pH 3.0 and 3.5 $[\alpha]$ did not change linearly with temperature, indicating a conformational transition over the same temperature range as the gelation and melting process observed using rheology. Also in line with the rheological studies was the observation of no hysteresis between cooling and heating over this small range of pH values.

Differential scanning calorimetry In addition to the rheology and optical rotation experiments, differential scanning calorimetry (DSC) experiments were performed using the same pectin but at 3.0 wt% and at pH values between pH 1.6 and 4.0. The most striking feature of the results was a sharp maximum in transition enthalpy at around pH 3. According to the authors, this suggests that pectin converts from a compact hydrogen bonded conformation in the protonated form to a more extended structure in the ionized state.

Light scattering Finally, light scattering was used to study LM pectins in aqueous solution (Sawayama et al. (1988) [132]). The results from five different pectins indicated that lowering the pH from around 4 to 2 led to molecular aggregation with the degree of aggregation highly dependent upon the pectin type.

With the results of these experiments in mind, the next task was to understand the T_{2b}-versus-pH NMR results shown in Fig. 4.23 on page 145. At very low pH, the apple and LM12 pectins at similar concentration shared similar T_{2b} times. The relaxation times for the apple pectin did not change significantly from this value across all three zones, however the LM12 pectin T_{2b} times increased enormously within zone I. At low pH the LM12 pectin chains likely adopted a three-fold conformation and aggregated with radius of gyration (the mean squared distance

of each point on the object from it center of gravity) increasing further as the pH was lowered (Jones [89], Sawayama et al. (1988) [132]). In this state, T_2 relaxation of protons on the pectin would be significantly enhanced, evidenced by the short T_{2b} times. Since the T_2 relaxation is mediated by exchanging water and biopolymer protons, this indicated that many pectin protons remained accessible to the solvent in the aggregated state. However, it was unknown whether a majority or minority of carboxyl protons remain exchangeable, or whether exchange was restricted as suggested for schleroglucan pendant units discussed on page 140.

If the pectin was loosely aggregated, solvent molecules would be free to move through the aggregation. On the other hand, if the pectin was tightly aggregated, water would likely become trapped within the pectin, leading to bound and bulk water compartments. This would be difficult to detect using the low-field NMR apparatus if the bound water fraction was small or the T_2 relaxation exceedingly fast. Loss of mono-exponential relaxation however was never observed experimentally for any of the pectin solutions. More information about aggregation may be accessible using other measurement techniques such as diffusion or the other techniques mentioned earlier.

Increasing solution pH causes electrostatic repulsion between pectin chains to increase. If carboxyl protons were being blocked by pectic aggregation, then increasing pH would be expected to increasingly free more exchangeables, thus making them accessible and placing downward pressure upon T_{2b}. This was not observed, suggesting the exchangeables were either always accessible, or their increased freedom at higher pH was being masked by the effects of increased chain separation.

As the pH was further increased, the pectic network experienced greater electrostatic repulsion and chains continued to spatially separate, leading to further T_{2b} increases. From Gilsenan's rheological results, the pectin network moved from an aggregated state to a cross-linked continuous network. At the same time P_b decreased rapidly thereby encouraging T_{2b} toward longer times. Unfortunately Gilsenan et al. used temperature rather than pH as an independent variable therefore it is difficult to determine the pH at which the helices changed from three-fold to two-fold. The conformational transition using optical rotation measurements happened at both pH 3.0 and pH 3.5 but was also driven by temperature.

The apple pectin T_{2b} over the same low pH range decreased from around 3ms to 2.5ms. In light of the preceding arguments and the different direction of LM12 T_2-versus-pH changes, there is no reason to suggest that apple pectin formed aggregates. Fig. 4.7 shows the effect of forcing the apple pectin below its starting pH: T_2 continues to increase until around pH 1.5 then starts to decrease. From these results it appears that apple pectin molecular structure prefers not to aggregate even at very low pH. This may be due to electrostatic repulsion from the large

fraction of exposed methyl protons.

The LM12 pectin used in these experiments had a slightly higher degree of methyl-esterification than the LM pectin used by Gilsenan et al. and therefore had fewer carboxyl groups per unit length. The resulting electrostatic repulsion would thus be lower for LM12 at the same pH, and the transition from three-fold to two-fold helical would be expected to happen at higher pH. The conformational transition observed by Gilsenan et al. using optical rotation appeared at pH 3.0 and pH 3.5. The abrupt LM12 T_{2b} change observed at pH 4 seems likely to be the same transition. An interesting set of experiments to test this hypothesis would involve making LM pectin solutions of differing DMs and observing how their T_2 times change across this small pH range.

As the pH was increased from 4-5, LM12 T_{2b} was observed to decrease from 9ms to 7ms. By contrast, in zone I, increasing the pH was observed to increase LM12 T_{2b}. Further, from pH 4-5, P_b decreased and thus reduced the number of biopolymer exchangeables. According to the C-R model, decreasing P_b should lead to a T_2 increase, however the opposite was observed. The increasing exchange rate k from pH 4 to 5 should also increase T_{2b}; yet again the opposite was observed. A likely explanation of the T_{2b} behavior between pH 4-5 is hydrogen bonding. Gilsenan et al. referenced an earlier paper by Walkinshaw and Arnott (1981) suggesting from X-ray data that carboxyl groups of pectic acid are involved in three types of hydrogen bonding. These were: (i) to O(2) (oxygen atom located on carbon position 2 – see Fig. 4.2) on an adjacent residue along the same chain, (ii) to O(3) on a neighboring (antiparallel) helix, and (iii) to a neighboring antiparallel chain carboxyl group. If hydrogen bonding was operating, it could be reducing the fraction of exchangeables P_b by locking up labile protons so they are unable to exchange with the solvent. The hydrogen bonding hypothesis appears to fit the experimental data, and receives additional support from Gilsenan et al. who suggested tentatively that hydrogen bonds progressively form over time around this pH thus shifting the equilibrium between ionized and protonated carboxyl groups toward higher pH values. They observed drift from around pH 4 to 4.5 to be rapid while drift from around pH 7 to 8.1 required over 24 hours. Both of these observations support a reduction in hydrogen bonding as the pH is increased from around 4 to 8.

Assuming the hydrogen bonding hypothesis corresponds to chemical reality, it may now be possible to explain the behavior of the apple pectin T_{2b} at low pH as follows. Between pH 4-5 the apple and LM12 pectin relaxation data behave in like manner suggesting similar molecular behaviors. Around pH 4 the LM12 data showed a sharp transition due to a change in helical conformation. The apple pectin did not change conformation but instead experienced increased hydrogen bonding. As the pH continued to reduce, electrostatic repulsion weakened allowing greater

numbers of hydrogen bonds to form. If the apple pectin chains were forming dimers or larger formations as the pH was reduced, this would be expected to increasingly slow the motions of the macromolecules thus reducing T_{2b}. The contrary however is observed in the apple T_{2b} measurements, suggesting the effect of inter-molecular bonding upon T_{2b} was minimal. The dipole-dipole interactions defining the value of T_{2b} must therefore be intra-molecular. This claim will be repeated for LM12 for different reasons in due course.

At around pH 2 the electrostatic repulsion between apple pectin chains due to de-protonated carboxyl groups was essentially absent and T_2 began to decrease, perhaps due to inter-molecular interactions or to intra-molecular changes. It would be interesting to repeat the non-NMR experiments on the HM apple pectin at this pH, and also the NMR experiments with different HM pectins.

As noted earlier, the raw T_{2b} times for apple pectin were significantly shorter than for LM12 except at very low pH. This was due to different molecular structures and different environments experienced by exchanging protons on the two different pectins.

Many other experiments could be performed in order to shed addition light on pectin zone I behavior. For example, the apple pectin could be examined at various concentrations in like manner to the LM12 pectins. A pectin with DM midway between apple and LM12, for example DM 55%, would disclose additional information on the importance of the methyl-to-carboxyl ratio, and how this affects conformation and hydrogen bonding within zone I. Using pectin DM as a parameter, it should be possible to determine the DM threshold at which helical conformational changes happen. It would also be interesting to compare random and blocky pectins, and perhaps very weak pectin gels and pectin solutions using divalent cation quantities as an adjustable parameter.

The final comment for this section is that raising then lowering the pH of LM12 pectin solution does not return the solution to its original state. To illustrate this, two identical 1.5 wt% LM12 pectin solutions were prepared in glass vials. Symbols were marked on paper and placed behind the glass vials. The symbols could not be read due to the solution's high turbidity. However, raising one solution's pH from 2.5 to 4.5 reduced the turbidity and allowed the symbols to be clearly read, in clear contrast to the unmodified solution. Returning the solution pH to its natural value, and even lowering the pH to 1.3 did not restore the solution to its original state. Presumably the initial turbid state was due to light scattering off dissolved particulates that, after being extended, were unable to return to their earlier states due to chain mixing and entanglement. Future low-field NMR research could focus upon pectins in these states in order to probe the conditions and threshold at which irreversible entanglement appears.

4.7.9.3 Interpreting zone II

During the interpretation of zone I it was argued that T_2-versus-pH varied due to P_b and T_{2b}. Within zone II these parameters have minimal effect upon T_2.

As observed in Fig. 4.18 on page 134 P_b remains essentially unchanged in zone II for all pectin samples. T_{2b} was observed in zone I to change considerably due to conformational changes but in zone II the pectin chains are already fully extended thus only minimal conformational changes are possible. Hydrogen bonding affected T_2 up to around pH 5 and even at neutral pH at a greatly reduced rate but seems unable to explain the $T_{2b} + k^{-1}$ variations centered around pH 7.

To understand the changes in zone II it is necessary to introduce acid-base catalyzed proton exchange. This chemical reaction involves covalent bond disruption and results in the rate of proton exchange between water and biopolymer increasing under off-neutral conditions (Chávez and Halle (2006) [36]). Importantly, the acid-base catalyzed exchange rate is parametrized by k within the C-R model.

Acid-base catalyzed proton exchange has been discussed in the literature. Hills and Williams et al. measured exchange rates in methanol-water mixtures (Hills, (1996) [74], Williams et al., (1998) [160]). Others have performed in-depth studies on molecules such as agarose, gelatin, and proteins to determine the presence and effects of exchange (Chávez and Halle (2006) [36]) and have used the exchange phenomenon to improve magnetic resonance image contrast (Liepinsh and Otting (1996) [94]).

The standard model for describing the acid-base catalyzed exchange rate is:

$$k = k_1[\mathrm{H_3O^+}] + \frac{k_2 K_w}{[\mathrm{H_3O^+}]} \tag{4.16}$$

where k is the proton exchange rate, k_1 and k_2 are the acid and base rate constants respectively and K_w is the dissociation constant of water ($= 1 \times 10^{-14}$M) (Fabri et al. (2005) [56]). To fit the model data to the experimental data it was found that an additional neutral cyclic exchange term $k_3[\mathrm{H_2O}]$ was required as shown in Eqn. 4.17 where $[\mathrm{H_2O}]$ is 55.6M. Without the additional term the experimentally measured exchange rate was too slow between pH values of around 5.5 and 8.5 (Hills (1996) [74], Williams et al. (1998) [160], Fabri et al. (2005) [56]).

$$k = k_1[\mathrm{H_3O^+}] + \frac{k_2 K_w}{[\mathrm{H_3O^+}]} + k_3[\mathrm{H_2O}]. \tag{4.17}$$

For methanol-water mixtures Hills and Williams et al. showed the exchange rate k to be around $600\mathrm{s}^{-1}$ at neutral pH, and well in excess of $12{,}000\mathrm{s}^{-1}$ at the zone boundaries. The reciprocals of these values have the same units as T_{2b} and are around 1.7ms and 83μs respectively. Assuming similar exchange behavior for the pectin samples, the acid-base catalyzed mechanism only contributes meaningfully to the NMR signal within zone II when k^{-1} is within an order of magnitude of

T_{2b}. An examination of Eqn. 4.1 shows that reducing k increases T_2 and increasing k decreases T_2 which is consistent with the experimental pectin data shown in Fig. 4.23.

Assuming the changes in T_2 within zone II are due solely to acid-base catalyzed proton exchange, an approximate estimate of k at neutral pH is possible from Fig. 4.23 by calculating the difference between the T_{2b} values in the absence of exchange at the zone boundaries and $T_{2b} + k^{-1}$ peak amplitude at neutral pH. For apple pectin the boundary values differ considerably, perhaps due to a small overlap of T_{2b} and k at the zone I-II boundary. By measuring the peak value and subtracting the average of the two boundary values, the exchange rate k is estimated to be $(1,170 \pm 320)\text{s}^{-1}$ where the uncertainty is due to boundary value differences. For the LM12 pectins the manifestations of T_{2b} and k are clearly demarcated thus there is no confusion at the boundaries, however there are just a few data points at neutral pH. The exchange rate k for LM12 is calculated to be $(290 \pm 30)\text{s}^{-1}$ and given the likeness of the LM12 pectin samples and similarity of T_{2b} values can reasonably be assumed the same for all concentrations. There would be less ambiguity if there were more data points around neutral pH.

In comparison to these approximate pectin exchange rates, Hills and Williams et al. found k for methanol-water mixtures to be 600-700s^{-1} at neutral pH (Hills (1996) [74], Williams et al. (1998) [160]). The exchange rate differences between the pectins were not investigated, and provide an avenue for further research. Quantitative exchange rates values for the pectins are estimated again in due course using another technique.

4.7.9.4 Interpreting zone III

In contrast to zones I and II, the study of pectin solutions within zone III appears to have been largely ignored in the literature. This is understandable for reasons stated earlier concerning the pH range within which pectins are chemically stable. Due to the lack of research, the following observations and interpretations are standalone and seek future experiments using other scientific techniques.

The first observation is that increasing the pectin solution pH caused additional protons to be removed from the pectin molecules. This was evidenced by the change in P_b beginning near the zone II-III boundary. It is unknown however whether protons being removed in zone III were from carboxyl or hydroxyl groups as around fifty percent of the carboxyl groups appeared to remain protonated near the boundary. If the protons being removed were from carboxyl groups, then it was not obvious why this did not happen within zone II. The de-protonation began as shown in Fig. 4.18 on page 134 at around two pH units below the pK_a value for hydroxyls.

The second observation was that as a result of P_b changing inside zone III, the experimentally measured T_2 also began increasing as predicted by the C-R equation. This was presumed due to fewer exchangeables being available to reduce the solvent T_2 although other factors must have contributed to the relaxation reduction as evidenced by the model data to be discussed in due course. One possibility is that at very high pH, increased numbers of charged groups may have increased electrostatic intra- and inter-molecular repulsion thus reducing the effects of dipolar interactions.

The third observation was that very high negative charge density along the pectin chains would attract positively charged entities such as water molecules and Na^+ ions, possibly forming solvation shells around the biopolymer. If water was forming large solvation shells and experiencing lengthened correlation times, then there was no obvious manifestation of this within the mono-exponential T_2 relaxation data. Within zone III there are approximately the same number of Na^+ ions in the solution as there are de-protonated biopolymer sites, and around one Na^+ ion for every 1,000 water molecules, depending upon pectin concentration. The behavior of the Na^+ ions around the biopolymer is unknown and requires further investigation.

Fourth, the zone III behavior patterns for apple and LM12 T_2 data shown in the composite Fig. 4.16 on page 122 were very similar. This was true also for the T_{2b} data shown in Fig. 4.23 on page 145. This suggests similar molecular changes were happening to both pectin types.

Fifth, as observed in zone II, the zone III 1.5 wt% apple pectin T_2 times shown in Fig. 4.16 were slightly shorter than the 2.5 wt% LM12 times. At the same time the T_{2b} differences shown in Fig. 4.23 changed enormously although the respective changes were by similar percentages. The fact that 1.5 wt% apple pectin and 2.5 wt% LM12 pectin have similar T_2 times and vastly different T_{2b} times shows that at high pH the apple pectin environment provides a much more efficient relaxation environment than the LM pectins.

Sixth, as observed in zones I and II, T_{2b} for LM12 does not appear to be affected by concentration suggesting once again that intra-molecular interactions are the source of transverse relaxation. This seems sensible especially in zone III in light of the strong inter-molecular electrostatic shield surrounding the rigid extended pectin molecules.

4.8 Modeling the pectin solutions

Previously T_2-versus-pH data was measured experimentally and $T_{2b} + k^{-1}$ information was extracted with the aid of a simplified Carver-Richards model. In this

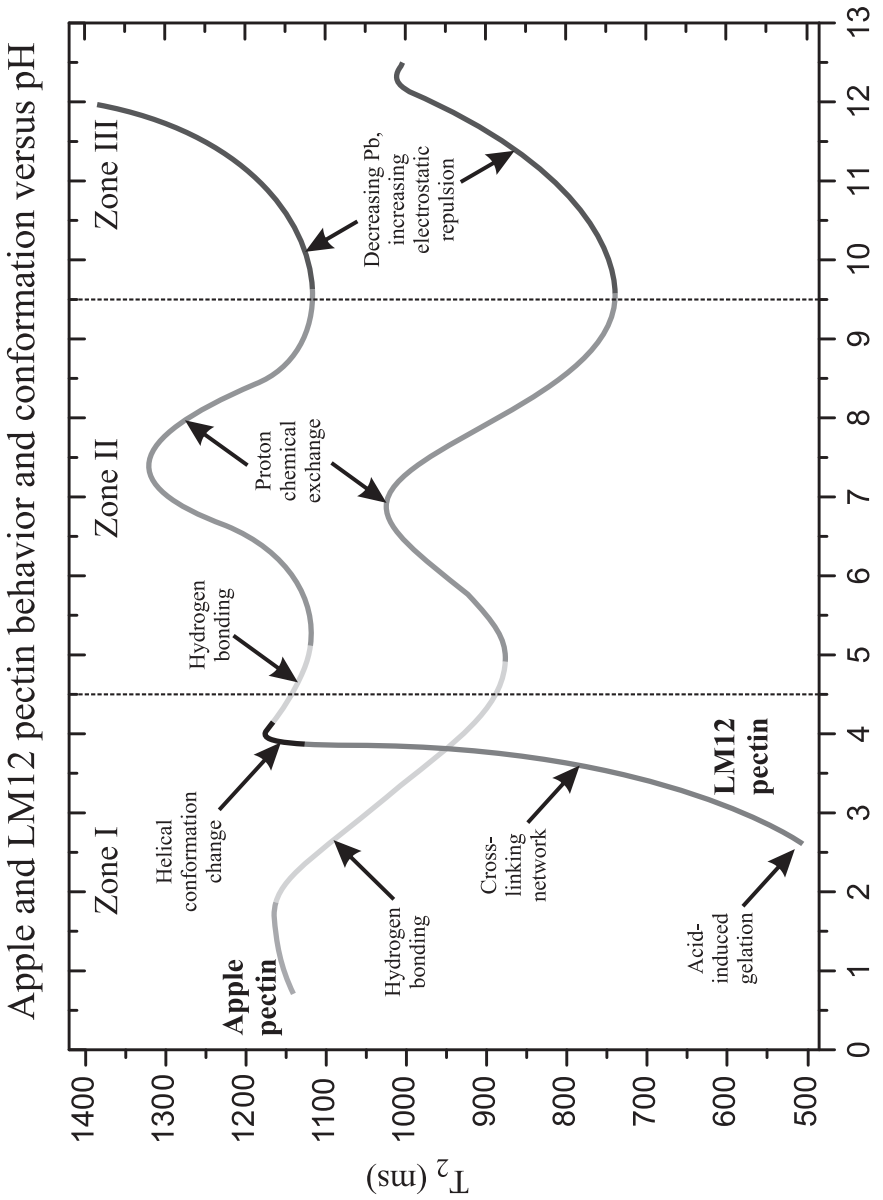

Figure 4.25: Apple and LM12 1.5 wt% pectin behavior and conformational changes as the pH is varied.

section the simplified Carver-Richards model and experimental values for P_b were used to model the experimental data.

To produce data from the C-R model, each of the parameters in Eqn. 4.1 on page 129 needed to be defined over the full pH range. T_{2a} was the simplest parameter to define; it was assumed to be constant irrespective of pH or concentration. The reasonableness of this assumption was discussed in §4.7.1 on page 127 and in Chapter 5.

Calculating P_b was more complicated for two reasons. The first reason was because experimental P_b was defined discretely over the pH range and therefore needed to be modeled using piecewise continuous functions before arbitrary values could be determined. The second reason was because calculating P_b required knowledge of concentrations of carboxyl and hydroxyl groups as illustrated in Eqn. 4.13 on page 132. For every pH increase the pectins became more dilute therefore the quantity of titrant added to each solution also needed to be modeled. P_b was modeled using OriginLab to fit functions to the experimental quantities, then the fitted data was used to calculate arbitrary titrant quantities and concentrations.

The first stage in the modeling began with simplified parameters. First, k^{-1} was ignored by setting k to a large value, and second, T_{2b} was set at a constant value across the pH range for each pectin type. The T_{2b} values were determined by fitting the simplified model data to the experimental data in order to provide the best fit within zone II. The pectin results for the first stage modeling are represented by the "+" symbol in Figs. 4.26 to 4.31 along with the experimental data. A pair of horizontal lines are shown either side of the model data in zone II indicate where the model data would sit for slightly larger and smaller values of T_{2b}.

The second stage in the modeling was to add the exchange rate k using Eqn. 4.16 on page 154. In each instance this resulted in the formation of a peak centered around neutral pH as displayed using the "×" symbol in the figures. For apple pectin the two rate constants k_1 and k_2 were initially adjusted so the experimental and modeled peak amplitudes were identical however this resulted in the modeled peak being too narrow. Widening the modeled data resulted in the peak amplitude well exceeding the measured amplitude (∼1,500ms versus ∼1,050ms). To solve this problem required the addition of the neutral exchange term shown in Eqn. 4.17. This enabled the modeled peak amplitude and width to be uniquely defined and well fitted as shown.

Fitting the LM12 data was more precarious as there were few data points near the center of zone II. All five model datasets share common values for T_{2a}, T_{2b}, k_1, k_2 and k_3 and the fitted model data was constrained by fitting across all solution concentrations. In contrast to the apple pectin, the LM12 modeled data amplitudes were similar to the measured data without requiring the neutral exchange term. The amplitude of the exchange rate peaks resulting from setting all five values to $k_3 = 0$

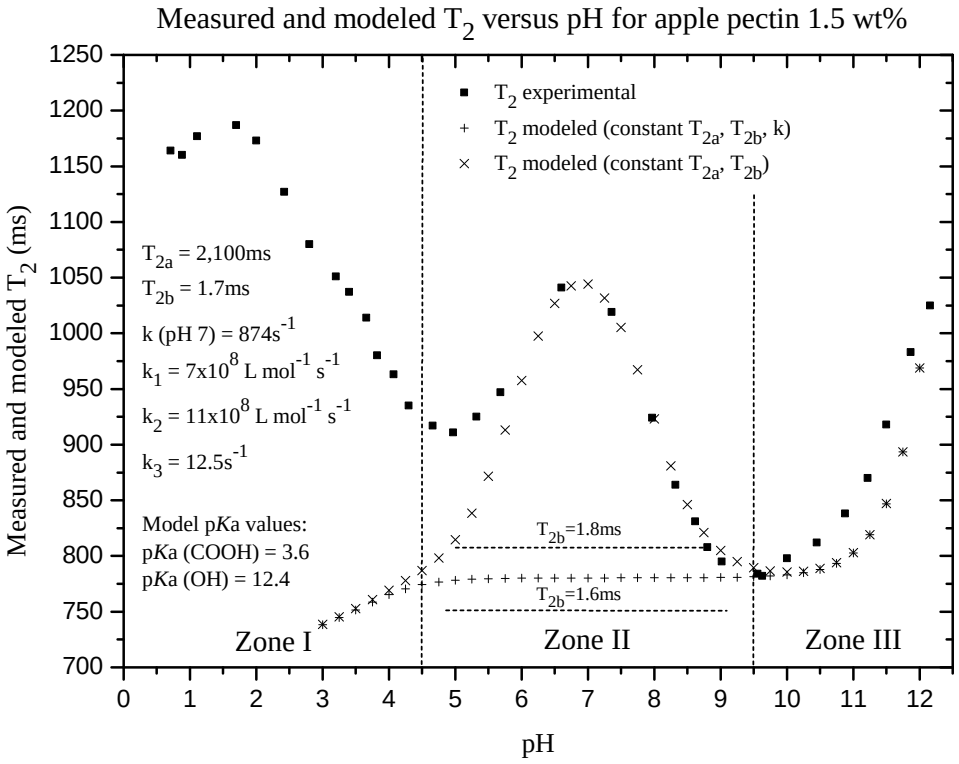

Figure 4.26: Comparing experimental and modeled apple pectin 1.5 wt% data. The "+" model uses constant T_{2a}, T_{2b}, and k. The "×" model includes acid-base catalyzed proton exchange rate k. The dashed horizontal lines indicate the effects of adjusting T_{2b} by ± 0.2ms.

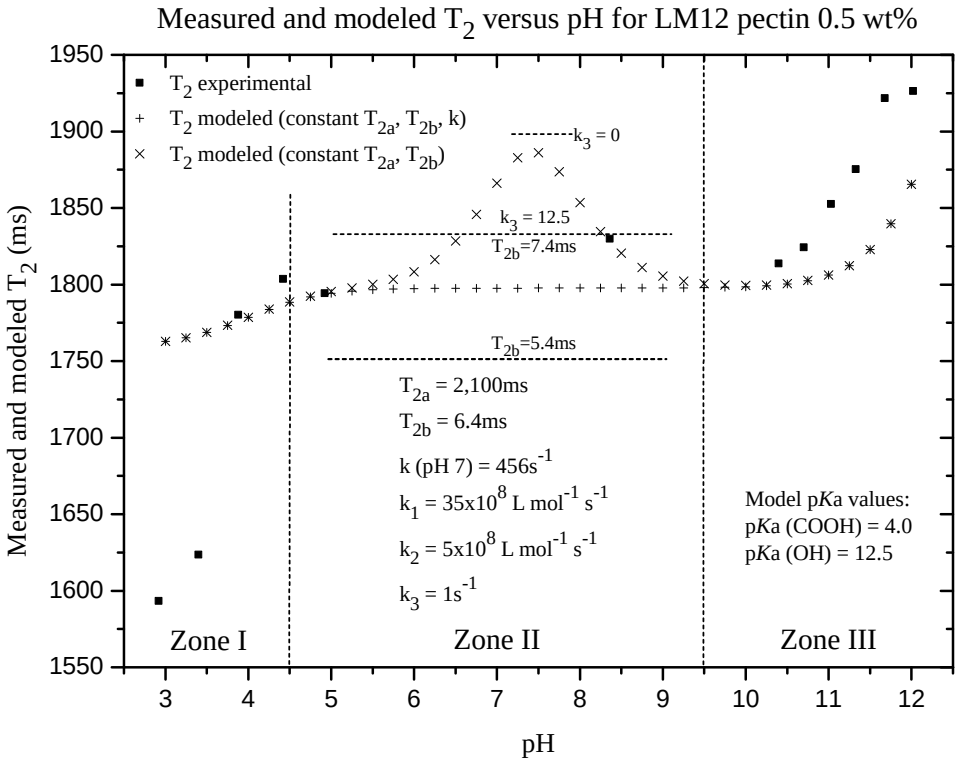

Figure 4.27: Comparing experimental and modeled LM12 pectin 0.5 wt% data. The "+" model uses constant T_{2a}, T_{2b}, and k. The "×" model includes acid-base catalyzed proton exchange rate k. The dashed horizontal lines indicate the effects of adjusting T_{2b} by ±1.0ms. The k_3 (shared) horizontal line indicates the peak amplitude in the absence of neutral exchange.

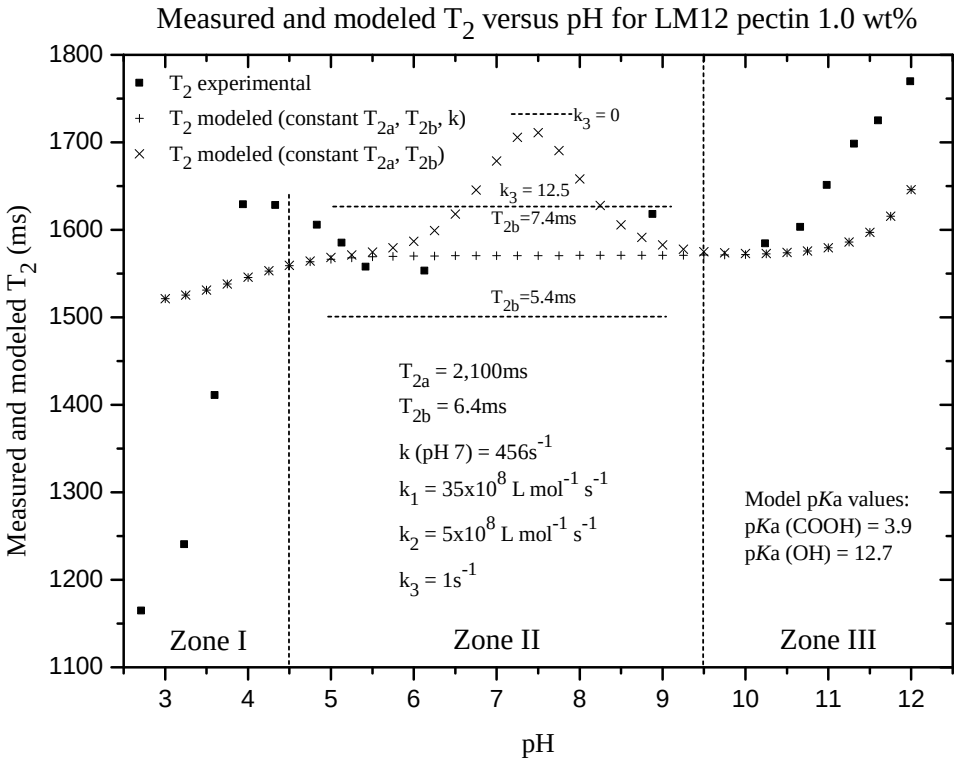

Figure 4.28: Comparing experimental and modeled apple pectin 1.0 wt% data. The "+" model uses constant T_{2a}, T_{2b}, and k. The "×" model includes acid-base catalyzed proton exchange rate k. The dashed horizontal lines indicate the effects of adjusting T_{2b} by ±0.2ms. The k_3 (shared) horizontal line indicates the peak amplitude in the absence of neutral exchange.

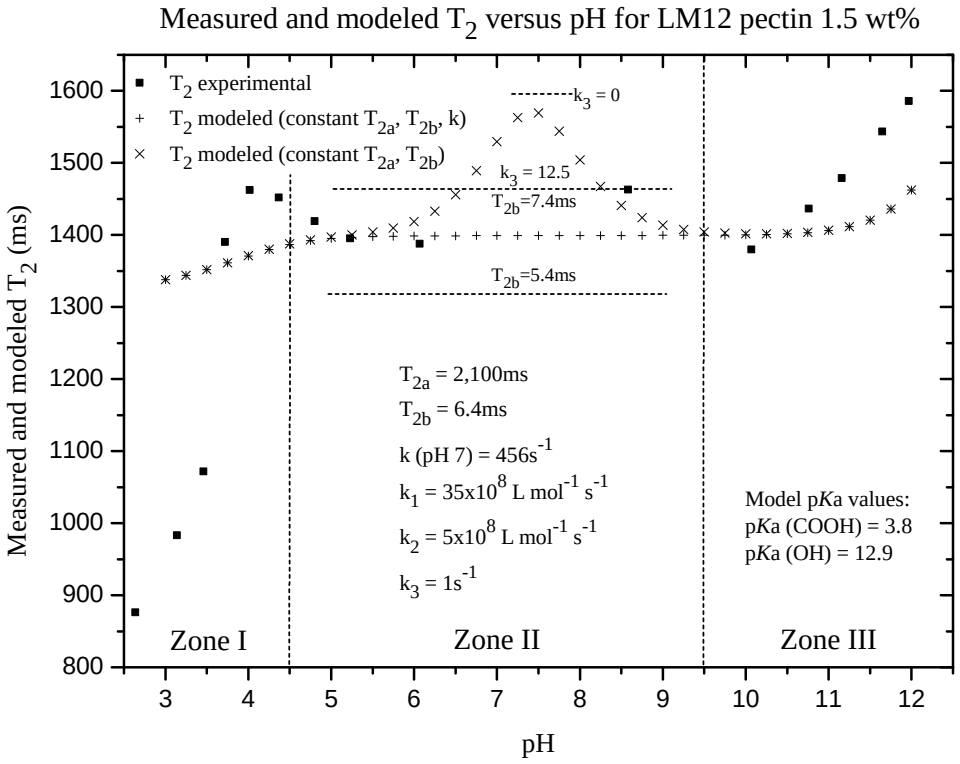

Figure 4.29: Comparing experimental and modeled apple pectin 1.5 wt% data. The "+" model uses constant T_{2a}, T_{2b}, and k. The "×" model includes acid-base catalyzed proton exchange rate k. The dashed horizontal lines indicate the effects of adjusting T_{2b} by ±0.2ms. The k_3 (shared) horizontal line indicates the peak amplitude in the absence of neutral exchange.

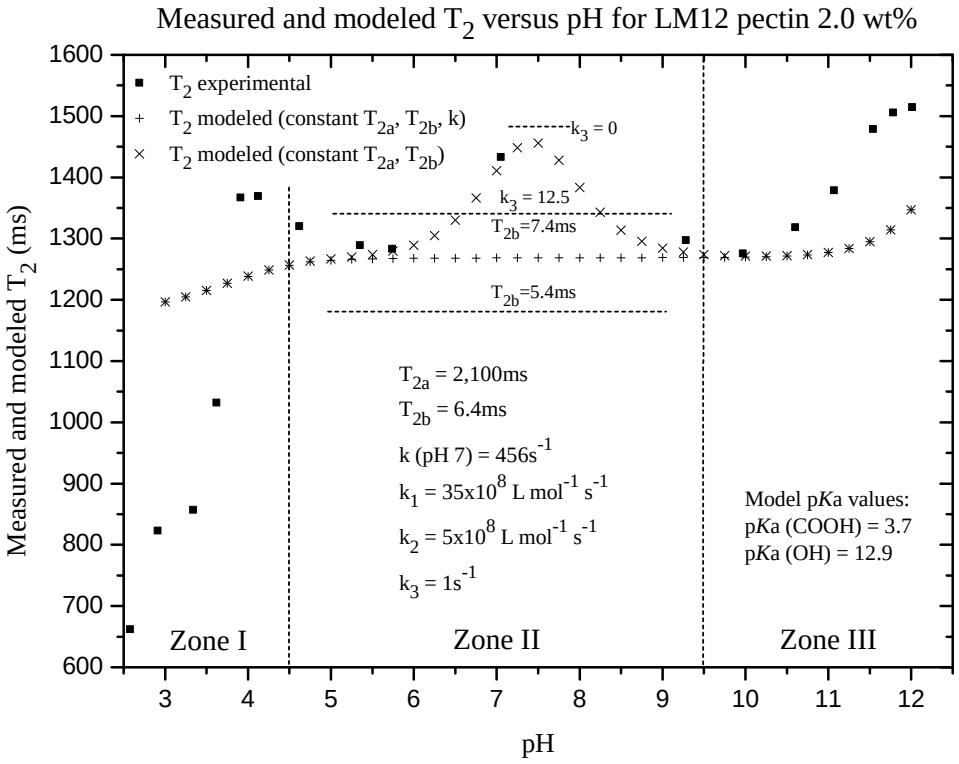

Figure 4.30: Comparing experimental and modeled apple pectin 2.0 wt% data. The "+" model uses constant T_{2a}, T_{2b}, and k. The "×" model includes acid-base catalyzed proton exchange rate k. The dashed horizontal lines indicate the effects of adjusting T_{2b} by ±0.2ms. The k_3 (shared) horizontal line indicates the peak amplitude in the absence of neutral exchange.

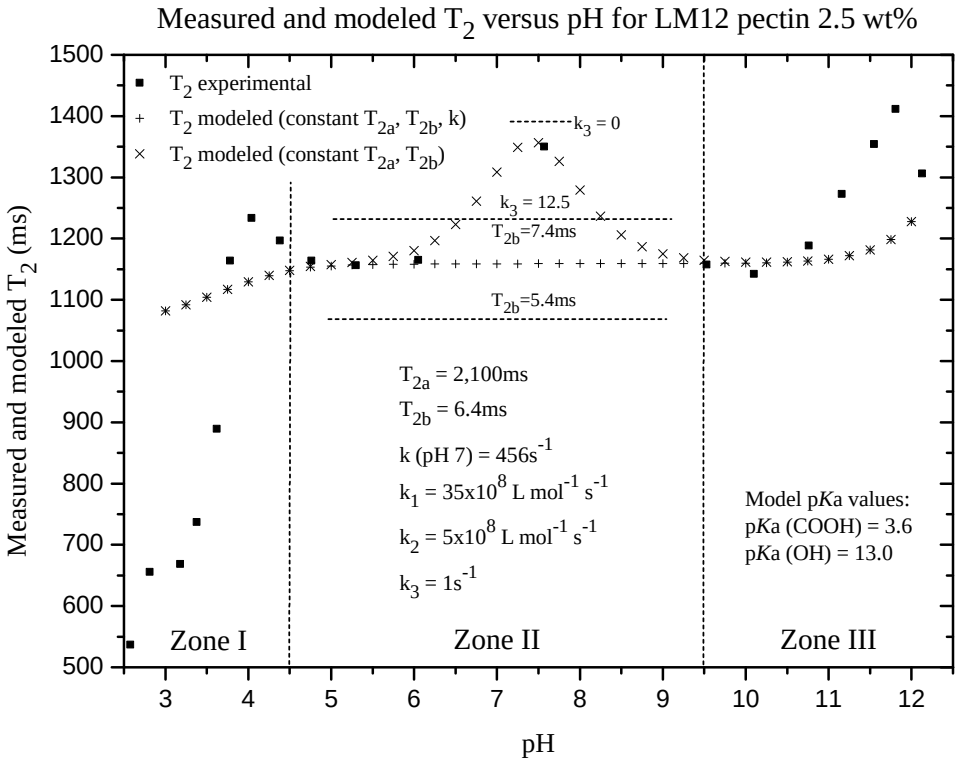

Figure 4.31: Comparing experimental and modeled apple pectin 2.5 wt% data. The "+" model uses constant T_{2a}, T_{2b}, and k. The "×" model includes acid-base catalyzed proton exchange rate k. The dashed horizontal lines indicate the effects of adjusting T_{2b} by ±0.2ms. The k_3 (shared) horizontal line indicates the peak amplitude in the absence of neutral exchange.

(no neutral exchange) and $k_3 = 12.5$ (apple neutral exchange value) are shown in the LM12 figures. The lack of zone II data points makes it difficult to draw firm conclusions regarding the width of the exchange peak or to definitively compare the apple and LM12 rates. The rate constants k_1 and k_2 used in the models were well within an order of magnitude of published values (Hills (1996) [74]). By contrast, the values of k_3 for apple and LM12 were significantly lower than Hills' values of $500s^{-1}$. This may be due to Hills' use of P_b in his exchange rate formulation which differs from the equations used by Fabri et al. and Liepinsh and Otting (Liepinsh and Otting (1996) [94]).

The modeled exchange rates k at neutral pH for the apple and LM12 solutions were around $875s^{-1}$ and $450s^{-1}$ respectively, and were comparable with the estimates given on page 155. For comparison, the exchange rates for methanol-water mixtures were around 550-$600s^{-1}$ (Hills (1996) [74], Williams et al. (1998) [160]).

Overall, the model results for the six pectin solutions were similar to the experimental data. The most simple model using a constant T_{2b} and ignoring k showed similarity to the experimental data but was obviously insufficient. Adding the exchange term improved the model data significantly within zone II leaving T_{2b} as the parameter necessary to fit the model to the remaining data in zones I and III. Below approximately pH 5 the model and experimental T_2 data for all pectins began separating due to hydrogen bonding discussed previously. This effect needs to be investigated and integrated into the mathematical definition of P_b. Likewise, in zone I the effects of conformational change upon T_{2b} were not factored into the model. This also requires additional research and integration into the model.

The model and experimental data in zone III also require reconciling. All six pectin solutions revealed similar T_2 differences between the measured and modeled data as pH was increased. This was more dramatic for the LM12 pectins than for the apple pectin.

Previously it was argued that pectin macromolecules at high pH were extended and rigid, and raising the pH further could not force further conformational extensions. To explain the deviation between model and experiment therefore required another mechanism that was both reversible and would prematurely increase T_{2b}.

When pectin molecules are mechanically stretched, the individual monomers are known to go through two conformational changes (Williams et al. (2007) [159]). Initially they exist in low energy 'chair' conformation. Stretching causes 'clicks' whereupon monomers are changed from the low energy 'chair' state to the higher energy 'boat' conformation, then finally to the higher energy 'chair' conformation. The force required to click a monomer from the low energy state to the boat conformation is of the order of a few hundred pico-Newtons. The equivalent force generated by coulomb repulsion between two charges at the monomer spacing

mentioned in §4.7.6 is significantly less than the force required to cause clicks, however multiple charges on each residue along the polyelectrolyte rapidly increases the force. For example, assuming a water permittivity $\epsilon_r = 80$ and charge spacing of 0.435nm, the force between two like charges is around 15pN and increases to around 140pN for two groups of three like charges.

The force between charges changes in proportion to the reciprocal of the permittivity. If water was replaced by empty space, the coulomb force between the charges would dramatically increase setting the force between two like charges to over 1,000pN. The hypothesis that clicks happen at high pH could be verified by further research using techniques such as computer modeling, AFM, or perhaps high-resolution NMR or Raman spectroscopy.

Assuming clicks were operating in zone III then at least two predictions could be made. First, if clicks extend the separation between exchangeable proton sites and the sources of intra-molecular T_{2b} relaxation, then T_{2b} and therefore T_2 should increase prematurely as compared to the model. This is observed.

Second, if clicks are related to charge density then the two pectin types may reasonably be expected to behave differently. Apple pectin has fewer exchangeable protons than LM12, and additional methyl groups. Without building a physical model or using computer modeling it is difficult to know how these differences would affect T_{2b} or the clicks. De-protonation leads to negative charges on the polymer whereas the methyl groups have exposed positive charges. The larger charge imbalance on the LM pectin may make it more susceptible to clicks thus leading to greater deviation between model and experimental data as observed in the graphs. It should be noted however that the pK_a values extracted through the fitting of each pectin's P_b were also slightly different for each model. If the apple hydroxyl pK_a was increased by half of one pH unit giving it the same values as the 1.5 wt% LM12, the apple model data in zone III would be pushed by the same amount toward the right making it more similar to the LM12 results.

It should be remembered that apple pectin exhibited chemical instability between pH 9 and 12 as shown in Fig. 4.14 on page 119. The time period between the experimental adjustment of the pH to the measurement of T_2 allowed the pH to drop slightly. This would have skewed the apple measurements and reduced the differences between the measured and modeled apple results within zone III.

Also shown in Fig. 4.14 is the apple pectin change at pH values above 12. The pH does not appear to change over the measurement time indicating the changes observed between pH 9 and 12 were no longer happening. This may have been due to the apple pectin click conformation at very high pH altering the pectin sufficiently to inhibit degradation by the means described in §4.5. This could also be experimentally tested.

4.9 Conclusion

In this chapter low-field NMR T_2-versus-pH relaxation measurements were performed upon samples consisting of galacturonic acid powder dissolved in water. Three samples had concentrations 1.37, 3.0 and 20 wt% and each was measured over a pH range from approximately 2 to 12. The results showed that T_2 remained relatively constant with pH irrespective of concentration. The two low concentrations gave T_2 results that were essentially identical with each other and with Milli-Q water, and dropped slightly around neutral pH. The high concentration GalA T_2 times were reduced by around one-third compared to the dilute solutions.

Low-field NMR T_2-versus-pH relaxation measurements were also performed upon samples consisting of HM and LM pectin powder dissolved in water. The HM apple pectin sample concentration was 1.5 wt% and the five LM12 concentrations were 0.5, 1.0, 1.5, 2.0 and 2.5 wt%. In contrast to the GalA results, the pectin T_2 results varied significantly with pH. The apple pectin data showed gentle changes while the LM12 data varied abruptly in zone I and more gently in the other two zones. The apple and LM12 results differed dramatically in zone I but showed similarities in zones II and III. At 1.5 wt% concentration the range of LM12 T_2 values was significantly greater than the T_2 range for the apple pectin solution. As pectins consist mainly of joined GalA residues, it was hoped each would shed light upon the results of the other. Instead the results were found to be significantly different, showing that T_2 is highly sensitive to molecular structure.

Initial struggles to understand the experimental data also led to T_2-versus-pH experiments on water. This resulted in data that appeared slightly anomalous within zone II and that could have been treated as equipment or experimental artifacts. Pursuing the anomoly however proved rewarding and showed that relatively simple experiments may at times reveal mysterious phenomena, even within substances as simple and ubiquitous as water. The resulting water study was sufficiently interesting to be assigned a small stand-alone chapter simply entitled "Water". The results from this study provide avenues for future research.

In nature dissolved pectins sit comfortably around pH 3-4, thus the T_2-versus-pH experiments raised each solution's pH well outside their comfort zone. Some pectins are known to experience depolymerization at elevated pH values thus reversibility experiments were performed on each pectin type to determine whether the pectin molecules were experiencing irreversible damage. This was important because chain depolymerization could have influenced the integrity of the T_2-versus-pH measurements. Minor chemical instability was observed for the high-methoxy pectin between pH 9-12. Irreversible chemical changes were observed for both high- and low-methoxy pectins following several full traversals of the pH range.

Understanding the T_2-versus-pH relaxation data for all samples proved to be very difficult for a variety of reasons. The literature contains varying interpretations

and misinterpretations of the specific causes of T_2 relaxation in pectins. This is largely caused by disagreement over the influence of water mobility and proton chemical exchange in transverse relaxation. These difficulties were discussed at length in the context of the galacturonic acid solutions and especially at higher concentrations.

After determining that the pectin solutions should be interpreted using a proton exchange model, a simplified version of the Carver-Richards two-site exchange model was introduced and the relevant parameters discussed. Significant difficulties arose with understanding the parameter P_b which was measured experimentally and calculated from theory. The results were sensible for galacturonic acid solutions but could not be reconciled for the pectin solutions. Manning counterion condensation was introduced as a solution however upon further examination also appeared to fail in providing a satisfactory explanation.

After establishing P_b-versus-pH values for the experimentally measured data, the simplified Carver-Richards equation was used to back out $T_{2b} + k^{-1}$ values for each solution. These results finally provided molecular level data containing information on the dynamics of the dissolved molecules and water solvent. Interpreting these results proved to be very difficult and certainly requires further research. Assistance from the scientific literature provided important information on pectin molecular behavior from a variety of experimental and computer modeling techniques. This information was used in the discussion on interpreting $T_{2b} + k^{-1}$ across two of the three pH zones and appeared to provide a consistent interpretation. The hypotheses formulated to explain the NMR data require further testing using other techniques and careful re-testing using low-field NMR. These remain as areas for future research.

T_2-versus-pH model data was calculated for the pectin solutions based upon the simplified Carver-Richards equation and experimental P_b values. The simplest model ignored the proton exchange rate k and defined T_{2b} as a constant. The improved model added k and the effects of acid-base catalysis in order to fit the experimental data within zone II. The model datasets differed significantly from the experimental data in zones I and III for both pectin types thereby emphasizing the complex contribution T_{2b} made within these zones.

Finally, this work was uncovered numerous areas for future pectin research using low-field NMR. The issues surrounding Manning condensation, polymer charge density, and P_b need to be solved. Conformational changes in zone I need to be better understood; low-field NMR is especially well suited to the numerous low-pH experimental possibilities. Hydrogen bonding within zone-I and at the low end of zone II remains to be tested and compared for HM and LM pectins. Relaxation times for LM12 around pH 2.5-3 need careful re-measuring to determine whether a T_{2b} concentration dependence exists and how this depends

upon aggregation. Modeling pK_a as a function of pH is necessary to improve the mathematical model. Building a physically realistic ball-and-stick pectin model could assist with understanding which helical transformations and conformational changes are realistic. Modeling of charge densities and forces between charges in zone III would provide additional information on whether clicks are possible at high pH. This could then provide a model that is relatively simple and testable using low-field NMR. Other pectin permutations with higher and lower degrees of methyl-esterification, varying concentrations, and galacturonic acid dimers, trimers, oligomers provide many experimental possibilities. Blocky and random pectins could be compared using pH as the independent variable to determine how carboxylic acid and methyl group distributions change the pectic behavior. Adjusting solution pH using different anions and cations provides another easily adjustable experimental parameter. Adding divalent cations to pectin solutions introduces additional inter-molecular relationships. This leads to the possibility of studying and controlling physically realistic pectin gel model systems by altering pH levels.

4.10 Postscript

The titration measurements shown earlier in this chapter appeared to indicate that galacturonic acid monomers lost around 100% of their carboxyl protons as solution pH was raised to about 7. By contrast, apple and LM12 pectin molecules were observed to lose about 50% of their carboxyl protons at the same pH. A discussion ensued regarding Manning counterion condensation, and whether chain charge densities would inhibit removal of protons if a particular charge density was reached.

An interesting experiment to further test these observations involved performing a similar titration on a small quantity of tri-galacturonic acid. If charge density was stopping de-protonation, then perhaps only two of the three carboxyl protons on the trimer would be removed. This would result in around 67% of the carboxyls being de-protonated at pH 7.

A week prior to submitting this thesis, a tiny 25mg sample of tri-galacturonic acid arrived in the lab. It was dissolved in 250uL of Milli-Q water as shown in Fig. 4.32 and a titration performed using high quality Agilent 1M NaOH titrant. During the titration, the magnetic flea shown in the figure stirred the solution, and the pH was monitored using a small pH probe inserted into the eppendorf tube.

At pH 7 the results showed that 69% of the carboxyl protons had been removed. A small quantity of the trimer was then measured using capillary electrophoresis (CE) from which it appeared that the trimer solution was at least 99% trimer, with

Figure 4.32: 250μL tri-galacturonic acid solution and magnetic stirrer, post titration.

perhaps very small quantities of monomer and dimer present. The CE sample was taken from the trimer solution after sitting at around pH 11 for about 24 hours.

Previous CE experiments using the same trimer but performed several years earlier showed de-protonation of all three carboxyl groups at pH 7. This contradicts the titration measurements described above, with the only obvious experimental differences being the presence of Na^+ ions in the titration experiments, and the CE's buffer solution and high voltage presence. This issue remains unresolved.

A sample of di-galacturonic acid is due to arrive in New Zealand within a few weeks, so similar titration and CE experiments can be performed. A prediction of 50% de-protonation at pH 7 seems sensible.

CHAPTER 5

Water

The aim of this chapter is to briefly examine several T_2 relaxation experiments that were performed on water. These experiments formed part of the pectin experiments and were necessary for determining whether the water solvent in which dried pectin powder was dissolved was contributing to the pH-dependent T_2 relaxation results. The experiments involved measuring the T_2 of water as a function of pH using the Mole probe and then repeating the measurements on a Bruker high-field NMR system. The results did not assist in the interpretation of the pectin data, however they were found to be fascinating in and of themselves and may assist in shedding light on the mysterious behavior of ubiquitous water.

5.1 Studying water

Studying water may appear too trivial and simplistic for a PhD thesis, but in fact the molecular behavior of water is not well understood and the study of water is a fascinating and controversial area of contemporary research, as will be discussed in due course. It is hoped that the study of water T_2 relaxation in this chapter may contribute to a better understanding of water molecular behavior and shed additional light on its many mysteries and anomalies (Science Daily (2009) [10], Chaplin (2011) [35]).

It became necessary to study water T_2 relaxation as a function of pH during the pectin experiments. Pectin T_2 relaxation times had been observed to depend strongly upon pH and any contribution to the relaxation times by the majority water solvent needed to be investigated. Adjusting the water pH by adding NaOH or HCl was expected to either leave the water T_2 relaxation times unchanged or perhaps enhance T_2 relaxation slightly due to solvation effects and increased

correlation times around the Na^+ or Cl^- ions. This is certainly not what was observed.

5.1.1 Water T_2-vs-pH using the Mole probe

Experimentally measuring water T_2 as a function of pH appeared to require a trivial set of experiments. First, fresh Milli-Q water would be added to a glass vial and its pH adjusted as required. The water T_2 would then be measured. The pH would be adjusted to the next measurement value and the measurements repeated until the attainable pH range was covered.

In reality, adjusting the water pH turned out to be far from trivial for two reasons. First, water absorbs carbon dioxide from the air causing the pH to drift downward when beginning around neutral pH. For example, water in a glass container exposed to the air was observed to decrease in pH from around pH 7 to 5.5 within a few minutes. Second, adjusting the pH of water, especially within two to three units either side of neutral pH proved very difficult due to the minute quantities of acid or base titrant required. Nevertheless, the experiments were performed, returning the results shown in Fig. 5.1.

It should be noted from the numbering of the data points in Fig. 5.1 that the pH began at around 5.5 and was increased monotonically to 12.5, then returned to pH 5.5 and decreased monotonically to pH 1. A better method would have been to randomize the order of the measurements in order to eliminate the effects of increasing Na^+ and Cl^- ion concentration and other possible accumulative effects. An improved ordering was used for the high-field measurements in Fig. 5.3.

The T_2 relaxation time for fresh Milli-Q water with pH around 7 had been measured many times on the Mole and the (2,100±25)ms result shown in Fig. 5.1 was expected. However the increase in T_2 as the pH deviated from neutral upon addition of titrants was unexpected. Two possible explanations for the increased T_2 were initially considered. First, the presence of additional ions were causing the tuning of the Mole probe B_1 coil to change. This hypothesis was nullified however when wobble experiments showed the tuning was unaffected even when adding relatively large quantities of 6M HCl and 6M NaOH to the water sample. The second possibility was the meta-structure of the water was being altered by the presence of the ions thereby leading to relaxation changes. It was not obvious how this hypothesis could be tested using NMR.

5.1.2 Water T_2-vs-NaOH using the Mole probe

The addition of another substance to water is generally found to enhance the relaxation rate. This is in contrast to the results shown in Fig. 5.1 therefore it was reasonable to test whether adding comparatively large quantities of the same NaOH

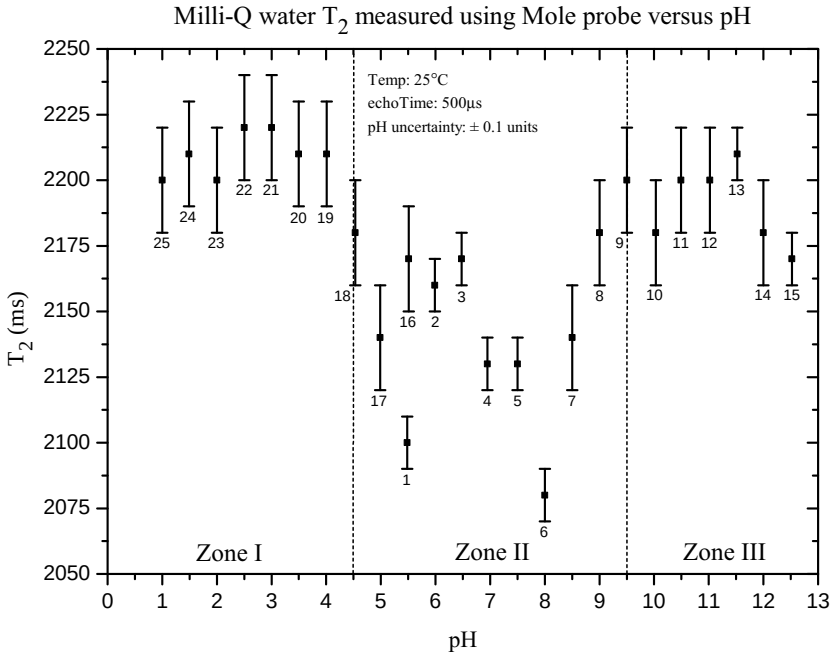

Figure 5.1: Change in water T_2 relaxation times measured on the Mole as minute quantities of NaOH and HCl were added to the water sample. The quantities of salts added to the water in order to adjust the pH were not measured. Measurements began around pH 5.5. The numbers "1" through "25" show the order in which the experiments were performed.

titrant to the water would follow this pattern. The experiment involved gradually adding 1M NaOH to a 10mL water sample while measuring T_2. The results are shown in Fig. 5.2. After addition of 1.2mL of 1M NaOH titrant the hydroxide ion concentration $[OH^-]$ within the water sample had increased to 0.107M. By comparison, the quantity of 1M NaOH required to raise the 10mL water sample from pH 7 to 12 in Fig. 5.1 would have been only ∼0.01mL. It was evident from Figs. 5.1 and 5.2 that the results were fundamentally different. At the pH extremes in Fig. 5.1, it may be the larger quantities of titrant present caused enhanced relaxation, however this remains to be tested.

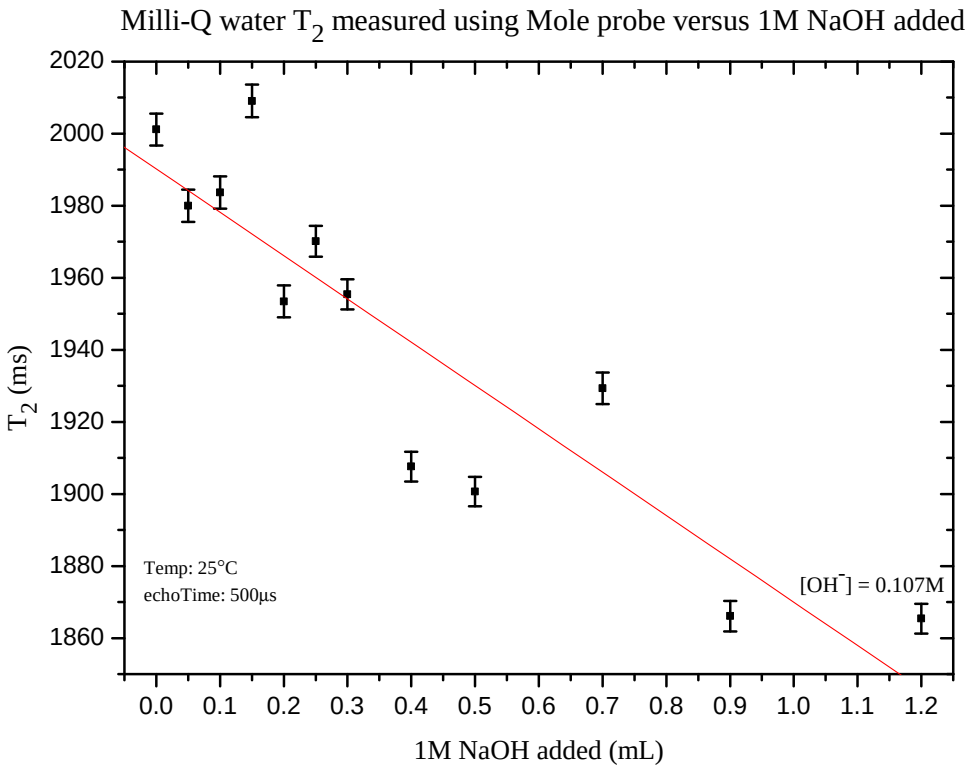

Figure 5.2: Change in water T_2 relaxation times as large quantities of Na^+ ions were added to the water sample. T_2 uncertainties are due to Prospa's fitting algorithm. The linear fit could have been improved by replacing it with a decaying mono-exponential but this is of little importance to the discussion.

5.1.3 Water T_2-vs-pH using the Bruker 400MHz

To determine whether the changes in T_2 with pH were peculiar to the low-field apparatus, it was sensible to repeat the experiments using a high-field NMR system. To achieve this, twenty-three 5mm NMR tubes were thoroughly cleaned and then dried in a heating chamber. One at a time the dried NMR tubes were then triple rinsed (except numbers one and two which were mistakenly single rinsed) using their own pH-adjusted sample. Sample was squirted into the tube, then shaken to expel before finally being re-filled to 560μL. Each was capped ready for insertion into the Bruker 400MHz magnet. For each experiment, several minutes were waited for the sample temperature stabilize to 25°C inside the magnet. The B_0 field was carefully shimmed then T_2 was measured using a CPMG experiment. The results from the twenty-three experiments are shown in Fig. 5.3. The ordering of the experiments as indicated in the figure was not randomized in terms of the pH, however the ordering was sufficiently non-sequential that it was unlikely to produce the T_2-versus-pH relationship shown. In addition, the results follow a similar pattern to those obtained previously using the low-field apparatus.

Experiments 1 and 22, and 2 and 23, had similar pH values but were measured at the start and finish of the experimental sequence. As the experiments progressed the concentration of Na^+ and Cl^- ions in each sample increased as they were drawn from a common source. The two pairs of T_2 times show a small difference, indicating that changing ion concentrations do not significantly effect T_2 at high field strength.

It should be noted that generating these results required significant effort for several reasons. First, there was a steep learning curve required to operate the Bruker software and hardware. Second, the method of measuring CPMG data with the Bruker macro and pulse program was cumbersome compared to the single-shot technique used by Prospa. The Bruker T_2 CPMG begins with a $(\pi/2)$ pulse followed by a series of (π) pulses then by acquisition of the FID. The FID is subsequently Fourier transformed and the peak amplitude or integral is used to determine just one data point in the relaxation curve. Water was found to have a T_1 of almost four seconds and thus a repetition time of almost twenty seconds. Taking phase cycling into account, the length of a simple experiment measuring less than ten T_2 relaxation points could easily exceed ten minutes. Re-writing the CPMG pulse program was considered however time constraints and lack of available technical information regarding the spectrometer made that unfeasible. Bruker were contacted but had no alternative CPMG pulse programs available for Topspin (Bruker TopSpin [21]).

In these twenty-three experiments only seven relaxation data points were recorded per experiment. In each instance, an exponential fit was applied to the T_2 relaxation data. The time-axis data points were initially linearly spaced. This

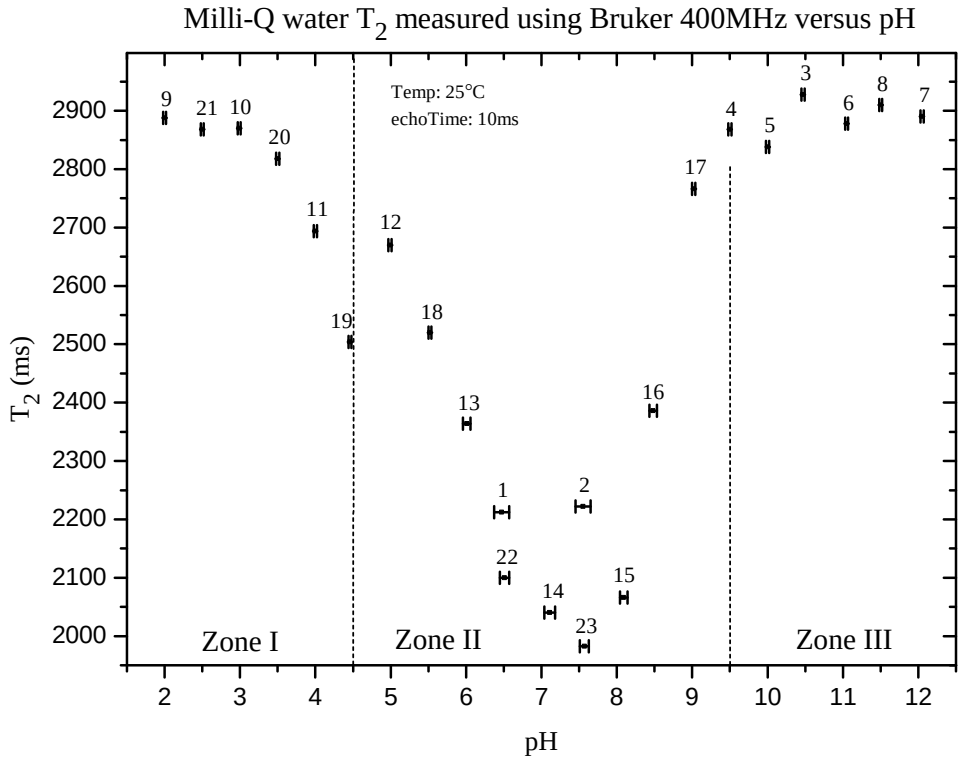

Figure 5.3: Change in water T_2 relaxation times measured on Bruker 400MHz as minute quantities of NaOH and HCl were added to the water sample. The quantities of salts added to the water in order to adjust the pH were not measured. Measurements began around pH 6.5. The numbers "1" through "23" show the order in which the experiments were performed. Uncertainties in pH were estimated from observed stability of the measurements within the source container.

proved unsuitable for fitting as there were insufficient data points at the beginning of the decay therefore spacings were re-calculated using a logarithmic base. These numbers were then used to calculate a "vclist" list of values specifying the number of (π) pulses necessary prior to recording the FID, and were entered into Bruker's Topspin macro.

To double-check these results a further experiment using fresh Milli-Q water from a different water purifier was pipetted into a triple washed NMR tube. The tube was sealed with Parafilm to limit atmospheric CO_2 accessing the water sample and changing the pH away from neutral. No NaOH or HCl was added to the sample. After reaching the same stable 25°C temperature, the magnet was carefully shimmed and T_2 was remeasured at 500μs and 10,000μs spacing. The results were 2,880ms and 2,110ms respectively, indicating that T_2 is pulse spacing dependent even in the absence of salt ions.

It should be noted that twice during pipetting the twenty-three samples, additional water totaling around 30mL was added to the 50mL Schott bottle containing the source sample. This had the unfortunate side-effect of diluting the ionic strength of the sample and could be argued to have affected the NMR results. In the context of other measurements however, this would appear to be unlikely.

5.1.4 Changing the pulse spacing on the 400MHz

One of the differences between low- and high-field measurements described above was the pulse spacing between (π) refocussing pulses. The Mole probe used 500μs spacing and measured the full relaxation response in one sequence. By contrast the Bruker CPMG (π) pulses were separated by around 10ms. Unlike the Mole probe the well-shimmed Bruker magnet was able to use long pulse spacing because diffusive effects were minimal. It remained desirable however to repeat the Bruker measurements with a shorter 500μs pulse spacing in case this parameter was somehow contributing to the T_2-versus-pH dependence. This required a large number of CPMG refocussing pulses to be applied to the probe. Since it was unknown whether the probe was capable of handling the power necessary, the probe-head was dismantled and the coil and capacitor temperatures observed in the presence of increasingly large number of RF pulses. No significant component heating was observed.

Upon measuring T_2 using short 500μs pulse spacing on ten samples over a range of ten pH values between 2 and 12, it was found that T_2 remained almost constant over the entire range. A linear fit to the ten data points suggested a gradual T_2 increase with pH from around 2,500ms up to 2,600ms.

5.1.5 Summary so far

At this point the water experiments appeared to be showing a distinct T_2-versus-pH behavior. This was evidenced at low-field with short pulse spacing, and at high-field with long pulse spacing. At short pulse spacing on the high field magnet the pH dependence disappeared. Long pulse spacing measurements on the Mole probe were not feasible due to diffusion although a slightly longer pulse spacing such as 1,000μs may have been possible. At high field, the presence of many ions due to the process of making the water sample acidic, then basic, then acidic, then basic, then neutral, as shown in Fig. 5.3, appeared to have minimal effect upon T_2. This suggested the T_2-versus-pH dependence did not depend upon ion concentration, at least for low ion concentrations.

To confirm this, an additional experiment was performed at high field using a single fresh Milli-Q water sample with no ions added. It was found to have vastly different T_2 times at two different pulse spacings around neutral pH. This result was similar to previous T_2 results using ions. Adding large quantities of NaOH produced a different effect than adding minute quantities. Heavily doping water with NaOH on the low-field magnet reduced T_2 according to ion concentration.

5.1.6 Hypotheses

From these results several hypotheses could be formed. First, the calculations used to extract the T_2 times from the Bruker relaxation data were wrong, but this was refuted by the other measurements that used the same calculations, and by the low-field results. Second, diffusion was the cause of the large reduction in T_2. This could explain why the reduction in T_2 was only present at long pulse spacing. However this did not explain the pH dependence. Third, the water mobility was being hindered by the presence of ions in the solution thus increasing or decreasing relaxation, however this seems unlikely given that raising the pH from 7 to 12 using NaOH required only one Na^+ ion per 55,000 water molecules. Fourth, reduced T_2 times at neutral pH could be due to paramagnetic oxygen dissolved in the water, while adding ions nullifies the presence of O_2. Further, at short pulse spacing the de-phasing caused by the O_2 molecules could be reversed thus maintaining a long T_2 time. Nullifying O_2 with ions seems unlikely however as unpaired electrons on O_2 may bond to oppositely charged Na^+ but not to like-charged Cl^-. The presence of paramagnetic O_2 could be investigated further by comparing the water T_1 and T_2 relaxation times. Fifth, there were pH dependent convection currents within the sample due to temperature gradients along the length of the NMR tube. Like diffusion, perhaps de-phasing due to convection could be minimized using short echo times.

5.1.7 Measuring T_1, diffusion, and convection

To test these hypotheses additional T_1 and diffusion experiments were formulated. First, in the extreme narrowing limit, correlation times τ_C would be very short and T_1 and T_2 were expected to have similar time constants. A shortened T_2 would suggest a lengthened water correlation time, diffusive attenuation, or paramagnetic O_2. Second, measuring T_2 at 500μs and 10,000μs for acetone and comparing with water would indicate whether diffusion (or convection) were causing severe relaxation enhancement. Acetone has a diffusion coefficient almost exactly twice that of water.

5.1.7.1 T_1

To measure water T_1, the same ten samples used in §5.1.4 to measure T_2 at 500μs echo spacing were used again. The T_1 relaxation trend with pH was found to be similar to the T_2 trend. The T_1 relaxation times increased slightly from around 3,250ms to 3,300ms as pH was increased from pH 2 and pH 12. By comparison, at the same pH, the T_2 times were around 79% of the T_1 times. An acetone sample was likewise measured for T_1 and T_2 using the same experimental parameters. The pH of the acetone was unmeasured so the two measurements are only assumed to have been performed around neutral pH. The T_2 time was about 93% of the T_1 time. These results suggest the presence of paramagnetic species such as O_2. A similar case could also be made for acetone which can also contain dissolved O_2.

5.1.7.2 Diffusion

If diffusion was the cause of the dramatic T_2-versus-pH dependence, acetone would be expected to respond even more dramatically. T_2 was therefore measured using 500μs and 10,000μs spacing and found to have 5,850ms and 5,610ms T_2 times respectively. Compared to the twenty percent drop between T_1 and T_2 for water, the drop for acetone was only four percent. This suggests that diffusion is not the cause of the water T_2-versus-pH dependency. Again, the pH of the acetone was not measured so this result remains uncertain.

5.1.7.3 Convection

One further experiment was performed on a water sample to test for the presence of convection within the sample. To test this experimentally a 3mm NMR tube was filled to a height of only 4mm with Milli-Q water. Shimming was very difficult as the sample did not fill the required volume inside the magnet. Using 500μs and 10,000μs spacing the water was found to have 2,930ms and 1,890ms T_2

times respectively. These values were consistent with previous measurements thus eliminating convection.

5.1.8 Older water measurements

A literature search was performed in order to find similar experiments. After significant searching, only two papers were found to have been published within the last fifty-four years. These were written by the same authors and detailed experiments similar to those studied in this chapter (Glick and Tewari (1966) [61,62]). These researchers had measured water T_1 and T_2 as functions of pH using a Varian high resolution spectrometer at fixed frequencies of 4.3MHz and 60MHz. The T_1 measurements used the adiabatic fast-passage method and the T_2 measurements the adiabatic half-passage method of Solomon. The water samples were pH adjusted using HCl and NaOH, and the T_2 measurements were performed using both unbuffered and phosphate buffered water. Each set of measurements produced the same results. Importantly, the water samples used by Glick and Tewari were vacuum-freezed to purge them of oxygen.

Glick and Tewari found T_1 to be pH-independent at both experimental frequencies. Between pH 5 and pH 9 Glick and Tewari found T_2 to decrease from around 3,600ms at 4.3MHz and 3,300ms at 60MHz to around 2,500ms at pH 7. These results are very similar to the T_2 measurements using the 400MHz Bruker apparatus with 10ms pulse spacing.

Glick and Tewari interpret the frequency dependence of T_2 in terms of a chemical shift δ where the shift is ascribed to the difference in resonance frequency between that of a hydrogen bonded proton and one without this specific interaction. They rejected the idea that δ was associated with re-orientation of hydrogen bonded water molecules suggesting instead that water molecules transfer between framework and interstitial sites. They also argue that water molecules rather than protons are transferred between sites. This would appear to be in contradiction with more recent ideas of proton mobility and the Grotthuss mechanism (Tuckerman et al. (2002) [152]). Using X-ray results from another group they suggest that the ratio of framework water P_A to interstitial water P_B is 0.8 to 0.2 at room temperature.

The similarity between the water results gathered during this thesis and measurements taken over fifty years ago is significant, especially since the earlier data was measured prior to the advent of pulsed NMR. In addition Glick and Tewari's interpretation of water as being in two states is very interesting in light of the pectin measurements, and contemporary studies of water.

5.1.9 Recent water measurements

There is currently significant interest in studying water. Isolated water molecules are well understood from experiments and quantum mechanical calculations, but large numbers of water molecules grouped together are not well understood (Skinner (2010) [138]). In the following the behavior of water molecules around large, small, and other water molecules is considered.

Water molecules are believed by some scientists to play a fundamental role in protein folding (Kim et al. in *Science Daily* (2008) [7]). Significant differences in water behavior surrounding folded proteins and around unfolded or slightly mutated proteins support the hypothesis that water and proteins are not independent of each other (Ebbinghaus et al. in *Science Daily* (2008) [9]). It is postulated that the properties of water may be changed in the presence of proteins in order to perform particular tasks in different parts of our cells (Kim et al. in *Science Daily* (2008) [8]). In addition, water around proteins is believed to be highly ordered compared to water several solvation layers away from the protein. Some researchers have likened water molecules around proteins to minuet dancers, in contrast to distant water molecules behaving like disco dancers (Kim et al. in *Science Daily* (2007) [6], Heyden in *Science Daily* (2010) [11]). This information was gained using terahertz absorption spectroscopy in which absorption of very short bursts of radiation passing through the sample are monitored. Terahertz radiation lies between the radio and optical wavelengths, and interacts differently in ordered water near the protein than in disordered water.

Water molecules in the presence of ions are variously believed to be either unaffected or dramatically perturbed (Mancinelli et al. (2007) [100]). According to several experimental techniques the short range effect of monovalent ions perturbs only the first water solvation shell (Skinner (2010) [138], Tielrooij et al. (2010) [149]). For certain ions however perturbations beyond the first solvation shell have been observed, and for specific combinations of cations and anions dynamic hydration effects extend well beyond the first structural solvation shell (Tielrooij et al. (2010) [149]). According to Tielrooij et al. there are eighteen hydrating water molecules per $MgSO_4$ molecule. According to their paper, water can be separated into two types: water molecules surrounding the ions in which the orientational dynamics are slowed down, and the remaining water molecules in which the orientational dynamics are similar to those of bulk water. Another study using simulations suggests that the structure and dynamics of water well beyond the first hydrations shells are significantly affected by the presence of the ions (Paschek and Ludwig (2011) [116]).

The behavior of water molecules in water is also mysterious and the subject of intense debate. Ice is known to have a tetrahedral structure and liquid water is assumed to be similar but less structured since heat creates disorder and breaks

bonds. According to recent X-ray experiments two distinct and spatially separated structures exist in liquid water irrespective of temperature (From *Science Daily* (2009) [10]). One region contains tetrahedral structures of about one-hundred molecules surrounded by disordered regions and exists at temperatures from ambient up to almost boiling point. As the temperature increases, fewer tetrahedral clumps exist but there are always some and their size remains similar.

5.1.10 Conclusions

The experimental observations made on water during this thesis, and work contributed from other research groups, indicates the study of water is far from finished. Numerous techniques are currently being used to investigate water structure and dynamics. As far as this author is aware however, there are no recent contributions to the study of water from the NMR community or attempts at perturbing water structure using a pH parameter.

From the information presented in this chapter a number of conclusions can be drawn:

First, recent X-ray studies on pure water suggest that water molecules within bulk water form transient ordered and disordered regions.

Second, other recent studies and the cited NMR study from the 1960s suggest that water forms orderly structures around ions, or at least around some ions. There is however disagreement over the size of these structures. Some authors suggest a single solvation layer which others suggest many layers. In all cases however there seems to be agreement on the existence of both ordered and disordered regions.

Third, the NMR results at long pulse spacing behaved very similarly to the 1960s results using deoxygenated water. From this it is reasonable to assume that paramagnetic O_2 did not significantly affect the high-field NMR results in this thesis.

Fourth, at long pulse spacing the non-neutral pH condition of water due to minute quantities of ions diminishes the effectiveness of the T_2 relaxation mechanism. If T_2 is understood in terms of spectral densities, then the $J(0)$ term is being reduced by the presence of the tiny ion imbalance. The problem with this however is that addition of many ions was observed to increase $J(0)$ and reduce T_2. There appears to be something special about tiny ion quantities or their effect upon pH.

Fifth, if T_2-versus-pH was framed in terms of a Carver-Richards two-site exchange model, then the number of proton exchangeables P_b at neutral pH increased by the ordering of the water molecules leading to reduced T_2. This could be tested by measuring T_2 at different temperatures since according to X-ray results, increasing the water temperature reduces the number of tetrahedrally structured water molecules which may in turn reduce the number of exchangeables.

Sixth, it appears that T_2 depends strongly upon CPMG (π) pulse spacing thus a non-constant water dispersion should be observed. This was indeed found to be the case although the results are not shown in this thesis. This may to be in contradiction with dispersion results in which water T_2 appears to remain constant irrespective of pulse spacing (Williams et al. (1997) [160], Williams and Halstead (1997) [158]), although it is difficult to determine if this is true from the published figures.

Seventh, T_2 appears to depend upon pH rather than the actual quantities of Na^+ and Cl^- ions in the water solution. It is reasonable to assume that these ions do not form NaCl in solution. The measured T_2 at neutral pH may suggest the presence of both ions in equal quantities destroys any water structure. It is unclear however how the ions behave when slightly more of one or other are added.

To further this work, these experiments need to be repeated with great care utilizing the parameters of temperature and (π) pulse spacing. Deoxygenated water should be used. Different ions should be used to control the pH. Buffers should certainly be investigated for providing better control of the pH as used by Glick and Tewari. Adding additional molecules for buffering does of course have the side-effect of altering the system which is undesirable. The T_2 maxima seen in zones I and III would be expected to decrease as further titrant was added, and could be tested at low and high fields. Other relaxation mechanisms need to be investigated.

As to the utility of these results to the interpretation of the pectin measurements, it would appear that, at most, the water pH dependence manifested itself only in the dilute GalA experiments.

.

CHAPTER 6

Other experiments

The aim of this chapter is to examine three different experiments that were performed between the completion of the NMR apparatus and the beginning of the pectin experiments. At this time a potential list of samples for studying with the Mole probe was compiled. The list included diary products, fruits, body fat content, meat tenderness, mimic systems for breast tissue, and water/oil emulsions. In addition, an interesting and potentially useful collection of pulse sequences for generating temporally separate coherences had recently been published by Hürlimann et al. Diffusion measurements were also of interest, especially in light of the central magnet incident and B_0 gradients discussed in §2.16. In the following we examine flow measurements based upon a Hürlimann pulse sequence, diffusion measurements, and finally T_2 relaxation experiments performed on kiwifruit. All of these experiments require additional time and experimentation and provide interesting areas for future research.

6.1 Flow experiments

Between 1999 and 2007 a fascinating series of papers were published detailing unusual pulse sequences for use in grossly inhomogeneous B_0 magnetic fields (Hürlimann et al. (1999-2007) [80–85, 142, 143]). Their experimental research was performed using the stray field of a superconducting magnet (∼1.7MHz proton frequency).

When B_1 RF pulses are applied across a sample within a grossly inhomogeneous B_0 field, the pulses become slice-selective and nutation angles vary significantly across the sample (Hürlimann (2007) [83]) as discussed in §1.4.2.2. In this context multiple coherences are formed. For a CPMG sequence the number of coherences is

of the order 3^N where N is the number of (π) refocussing pulses. The total nuclear magnetization may be decomposed into different coherence pathways, however the major contributors to the detected CPMG NMR signal are within the direct (Hahn) echo and stimulated echo pathways (Song (2002) [141]). Generally the different echoes are indistinguishable as they temporally overlap, appearing as a single echo. For non-standard nutation angles coupled with carefully timed RF pulses however, the direct and stimulated echoes may be temporally separated.

In 2006 Hürlimann published a paper detailing how T_1, T_2 and diffusion information can be extracted from the CPMG echo shape generated by an unusual pulse sequence. One example extracted T_1 information from a sample using a series of carefully timed 127° B_1 RF pulses. Of special interest however was a T_2–diffusion (T_2-D) sequence that caused temporal separation of the direct echo and stimulated echo coherences, resulting in a triplet of time-domain echoes. The central echo peak resulted from the direct echo and the two symmetric satellite peaks from the stimulated echo. Particularly interesting was the differing sensitivities of the two coherence pathways to diffusion and flow. According to Hürlimann the direct echo coherence pathway is, to first order, unaffected by flow, whereas the stimulated echo pathway is sensitive to the mean squared displacement of the spins with respect to the applied magnetic field (Hürlimann (2007) [83]).

To determine whether the Mole probe could be used to measure flow using the techniques described by Hürlimann et al., a macro and pulse program capable of executing the following pulse sequence from Hürlimann's paper were programmed into Prospa:

$$\left(\frac{\pi}{2}\right)_x - \left[\frac{t_{E1}}{2} - \frac{t_{180}}{\pi}\right] - (\theta)_y - [t_{E1} + \tau] - (\theta)_y - \left[\frac{t_{E1} + t_E}{2} + \tau\right] - [\text{echoes}]_n \quad (6.1)$$

where t_{E1}, $(\theta)_y$, and τ are experimental parameters, t_{E} is the echo time between the string of n $(\pi)_y$ refocussing pulses, and $[\text{echoes}]_n$ are a series of $(\pi)_y$ refocussing pulses separated by t_{E} as also used in a CPMG pulse sequence. To test the sequence a large bottle of water was placed on the Mole probe and the macro executed. The τ parameter adjusts the time between the echoes and was adjusted to fit the triplet within the time domain sampling window. The θ parameter adjusts the relative peak heights and was adjusted until the peaks were the same height under zero flow conditions. These values were 100μs and 112° respectively. The water bottle was then shaken and placed back on the Mole probe and the sequence re-run. The result was an almost fully formed center peak and the gradual emergence and restoration of the satellite peaks.

Using this experimental observation, an experiment to measure flow was designed. A glass flow tube was available as shown in Fig. 6.1, and rubber tubing was sourced and attached. A peristaltic pump with adjustable flow rate was obtained to cycle

Milli-Q water through the glass tube. The sample fluid was water doped with $CuSO_4$ to give it a T_2 time similar to the values used by Hürlimann. Care had to be taken to avoid spillage on the Mole probe and damage to the glass flow tube. A layer of plastic bubble wrap was used to surround the tube before laying it centrally on the B_1 printed circuit board along the x-axis shown in Fig. 1.5 on page 12.

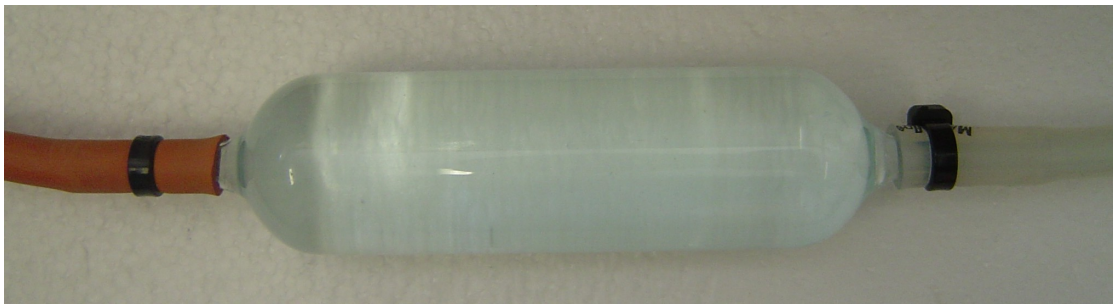

Figure 6.1: Glass flow tube and attached piping. The inside diameter of the body of the glass tube was around 31mm and the inside diameter of the two ends around 4mm. The larger diameter was constant over a length of about 95mm.

The initial attempt at measuring flow failed due to the pulsating nature of the peristaltic pump therefore a gravity fed solution was instead designed. This involved securing a 4L glass vessel near the lab ceiling and using the peristaltic pump to recharge the vessel from a large beaker on the lab floor. A valve was fitted in the pipe line to control the flow rate and the rate was measured using a stopwatch and volume markings on the beaker. Measurements of peak triplets were recorded at flow rates of between 0mL per minute and 286mL per minute using 512 averaged scans. The results are shown in Fig. 6.2. Each pair of stimulated echo amplitudes was then averaged and divided by the direct echo amplitude. A graph plotting the amplitude ratio against flow rate is shown in Fig. 6.3.

The data points in the figure could be interpreted as increasing exponentially with flow rate as shown by the fitted curve. This would indicate that the direct and stimulated echoes change smoothly with increasing flow. The data could also be interpreted using piecewise linear fits between 0 and 125mL and between 125 and 225mL per minute as shown in the figure. This could indicate a discontinuity in the flow behavior. Improving the experimental configuration and measurement techniques should provide additional clarity.

The dimensionless Reynolds number R_e describes the flow type of a fluid through

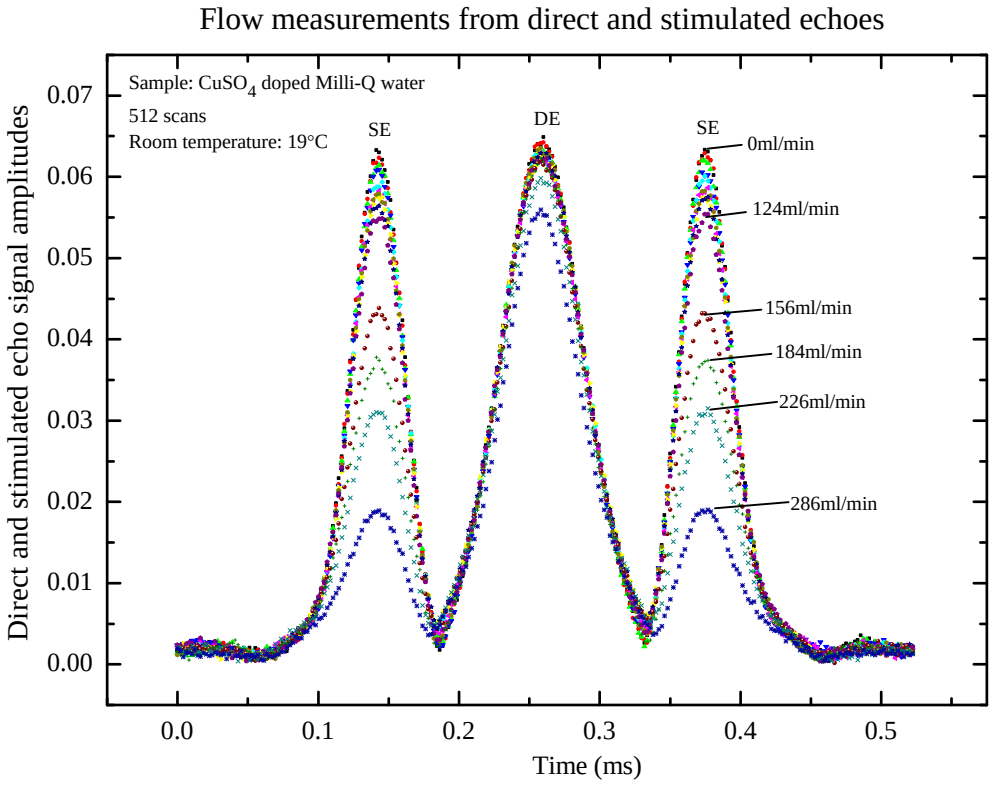

Figure 6.2: The direct echo and stimulated echo peaks. The central direct echo (DE) peak is largely unaffected by increased flow while the stimulated echo (SE) peaks are significantly attenuated.

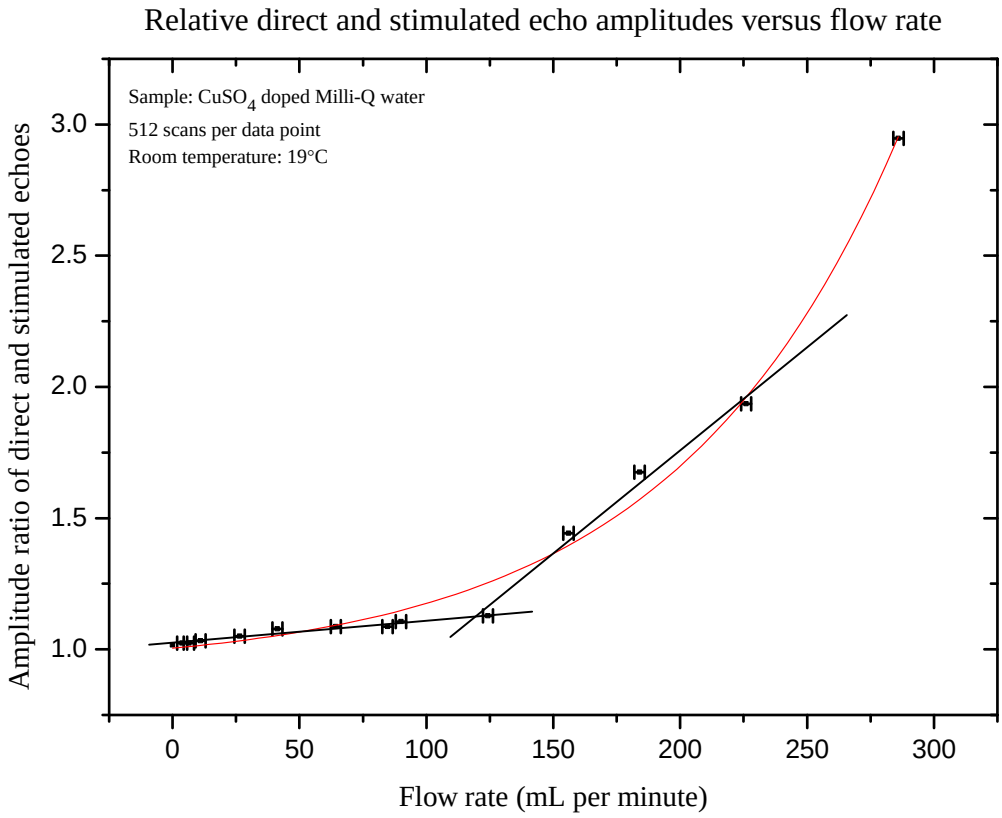

Figure 6.3: Flow rate measured using a T_2–diffusion pulse sequence developed by Hürlimann et al. The ordinate axis shows the amplitude ratio of the central peak to the averaged satellite peaks. The amplitude-flow relationship may be exponential as indicated by the curved fit line, but at slower flow rates the fit appears to be linear. Uncertainties were caused by inaccuracies in the measurement apparatus.

a pipe and is calculated using:

$$R_e = \frac{v\rho D}{\eta} \tag{6.2}$$

where v is the flow velocity of the fluid, ρ is the density, D is the flow tube diameter, and η is the fluid viscosity. For a smooth straight uniform pipe a value of R_e less than 2,000 indicates laminar flow, and a value greater than 3,000 indicates turbulent flow (Isaacs (2000) [87]. At the maximum measured flow rate of 286mL per minute R_e is around 200 through the wide section of the flow tube and around 1,500 at each end. Both of these values by themselves indicate laminar flow, however the effect upon the flow of the changing pipe dimensions is unknown and was not investigated.

This experiment needs to be re-run using improved experimental apparatus and a greater quantity of flow data needs to be recorded. Improved experimental apparatus was constructed but remained untested due to time constraints. Experiments using flow tubes with various inlet, outlet and center diameters could also be used to test for minor flow instabilities and eddies. The experiment could also be repeated using other samples such as oils and molten cheese.

6.2 Diffusion experiments

A basic requirement for measuring diffusion using NMR is that B_0 must vary spatially within the sample. This leads to proton spin precession rates that vary within the sample and increased de-phasing rates across the spin ensemble. Unlike NMR magnets especially designed for measuring diffusion, the Mole probe in its standard configuration has neither a constant linear gradient or pulsed field gradient functionality. A constant linear gradient, at least along the z-axis, appears to be easily generated as discussed in §2.16 by adjusting the height of the central magnet however this remains to be tested experimentally. A gradient set consisting of etched PCB coils was manufactured for the Mole probe (personal correspondence [5]) but as far as the author is aware the design was not successfully implemented.

While the Mole probe in its pseudo-homogeneous configuration does not have gradients in the normal sense, its sensitive volume does consists of gradients surrounded by outer regions of greater inhomogeneity (Manz et al. (2006) [105]). The gradient within the sensitive volume is a maximum of around $0.2\text{T}\cdot\text{m}^{-1}$; by contrast, a superconducting magnet gradient set may produce gradients between $0.1\text{T}\cdot\text{m}^{-1}$ and $1\text{T}\cdot\text{m}^{-1}$. To limit diffusive effects when using the Mole, CPMG refocussing pulse echo times must be limited to a maximum of around 500μs for a water sample. This is due to the diffusion term within the mathematical

description of relaxation and diffusion in a CPMG experiment (Fukushima and Roeder (1981) [59]):

$$M(t,\tau) = M_0\, e^{-t/T_2}\, e^{-\gamma^2 D G^2 \tau^2 t/3} \tag{6.3}$$

where $M(t,\tau)$ is the magnitude of the measured magnetization, M_0 is the magnitude of the equilibrium magnetization, t is the elapsed time since the first (π) pulse, γ is the magnetogyric ratio of the spins, D is the diffusion coefficient in $\mathrm{m^2{\cdot}s^{-1}}$, G is the magnetic field gradient in $\mathrm{T{\cdot}m^{-1}}$, and τ is the echo time between CPMG refocussing pulses. In the absence of a gradient, the diffusion term is unity and the general T_2 equation ensues.

A useful observation from Eqn. 6.3 is that the relaxation and diffusion exponential terms are multiplied. This means that a sample with mono-exponential T_2 relaxation in a constant gradient field G will remain mono-exponential irrespective of the magnitude of the gradient, thus always avoiding ill-posed fitting requirements. Unfortunately the Mole probe does not have a constant gradient, as evidenced experimentally by loss of mono-exponential T_2 relaxation behavior of water at longer echo times. At $\tau \approx 500\mu$s water relaxation is essentially mono-exponential, but a faster decaying component appears at $\tau \approx 1000\mu$s and likewise for $CuSO_4$ doped Milli-Q water, acetone, ethanol, formamide, and n-pentane. Glycerol and vaseline oil by contrast were found to exhibit no obvious change in T_2 relaxation even with echo times of 8,000μs.

It should be noted that even if relaxation data is bi-exponential at long echo spacing, it may still be possible to extract additional information by using the mono-exponential data gained at short echo spacing and applying it to the bi-exponential result. This would not be possible to achieve if the sample was intrinsically bi-exponential.

The observed multi-exponential behavior at longer pulse spacings was presumed to be mostly due to fast decaying signals from the outer regions of the homogeneous volume and slower components from the bulk pseudo-homogeneous region. To test this hypothesis a plastic vial was partitioned by gluing a small plastic cylinder centrally to the inner base of the vial, then each volume was filled in turn with water and the T_2 time and amplitude measured using a 500μs echo time. The volume of water added to the inner and outer volumes was 3.5mL and the samples filled the volume to heights of 10mm and 11.5mm respectively. Water in the inner cavity had T_2 relaxation time (2,303±2)ms and amplitude 30 units. Water in the outer cavity had T_2 relaxation time (1,005±4)ms and amplitude 5 units. Evidently the outer volume was experiencing significantly greater diffusion, and the contribution to the overall NMR signal was minor. The reduced contribution was probably due in part to the larger distance between the outer sample and B_1 field source, and in part to non-orthogonal tip angles discussed in §1.4.2 on page 14.

Diffusion can be measured on the Mole using at least two different pulse sequences. The first is the standard CPMG pulse sequence in which the τ parameter is varied as described mathematically in Eqn. 6.3. The second involves a two-stage pulse sequence in which the first section encodes for diffusion and the second section measures the remaining nuclear magnetization using a string of (π) refocussing pulses in like manner to a CPMG sequence. This pulse sequence is similar to the two dimensional T_2-D sequence mentioned earlier (Hürlimann and Venkataramanan (2002) [85]). One advantage of this technique is that a mono-exponential T_2 will not become multi-exponential even for long encoding times due to the short pulse spacing between (π) refocussing pulses. Another advantage is that measuring samples with long T_2 time constants such as water need not require ten to fifteen seconds of sampling time. Only a few tens of milli-seconds of sampling is necessary to determine the relative amplitudes of the magnetization remaining immediately after the diffusion encoding.

A macro and pulse program for measuring diffusion using this technique were developed and used to measure several samples with a spread of diffusion coefficients. The transverse magnetization remaining at the end of each encoding sequence was measured by summing a fixed number of spin-echoes. Increasing the length of the diffusion encoding period increases the magnetization attenuation thus decreasing the detected NMR signal. The normalized results from these experiments are shown in Fig. 6.4.

Prior to normalizing, the raw magnetization amplitudes from the three water samples following the 1ms encoding time varied slightly; the amplitudes of the un-doped water and 1mM doped water were around five percent above and below the 0.1mM doped water respectively. By contrast, the T_2 times ranged from 2,173ms to 1,372ms to 474ms for the three paramagnetic doping levels. Normalizing the three water datasets as shown in Fig. 6.4 resulted in the datasets lying almost directly over the top of each other as expected.

The amplitude of the acetone signal at 1ms encoding time was about two-thirds of the un-doped water amplitude, while the *n*-Pentane and ethanol amplitudes were almost identical to the 1mM doped water amplitude. Each of their self diffusion coefficients however, once normalized, reflected the published coefficients listed in the figure. Ethanol having the lowest diffusion coefficient showed the least decay at increasing encoding times, followed sequentially by the water, acetone then *n*-Pentane.

Plotting the data from Fig. 6.4 on a semi-log graph (not shown) linearizes the diffusion datasets for encoding times between 10ms and 40ms. Linear fitting the six datasets between these encoding times provides slopes of -40.1 for Abs. ethanol, -49.6 for water, -49.7 for 0.1mM doped water, -50.4 for 1mM doped water, -59.3 for acetone, and -66.5 for n-pentane. The variations in slope between 10ms and

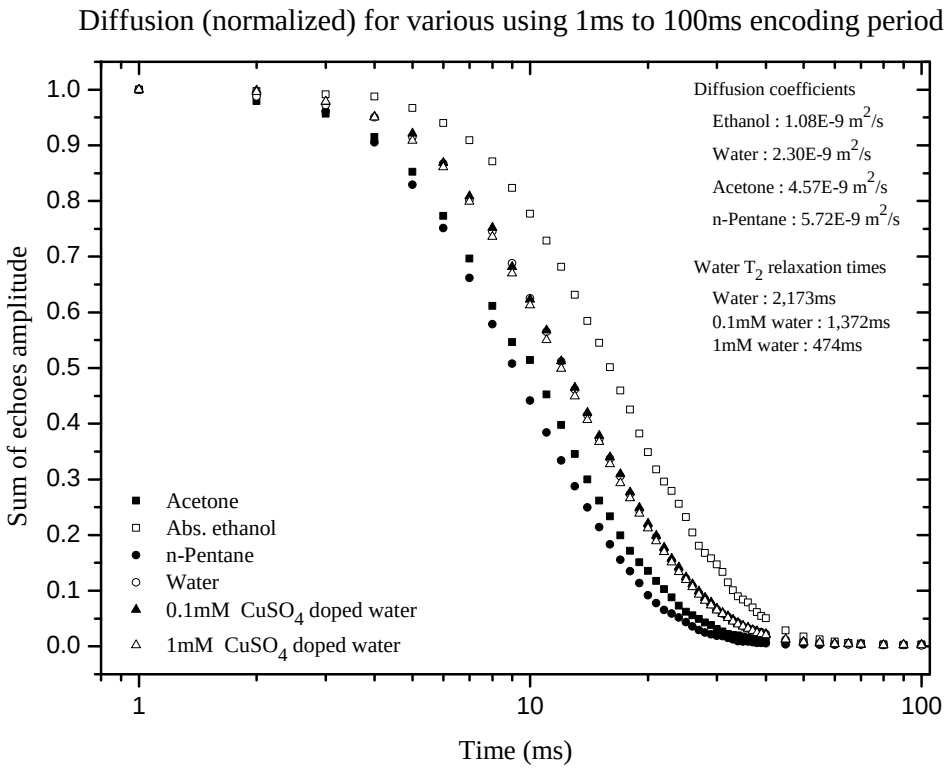

Figure 6.4: Diffusion measurements for substances with a spread of diffusion coefficients. The pulse sequence used an initial encoding period as shown along the abscissa followed by a string of (π) pulses to measure the remaining magnetization. Published self-diffusion coefficients are also shown (Bruker (2011) [24], Casieri et al. (2003) [31]).

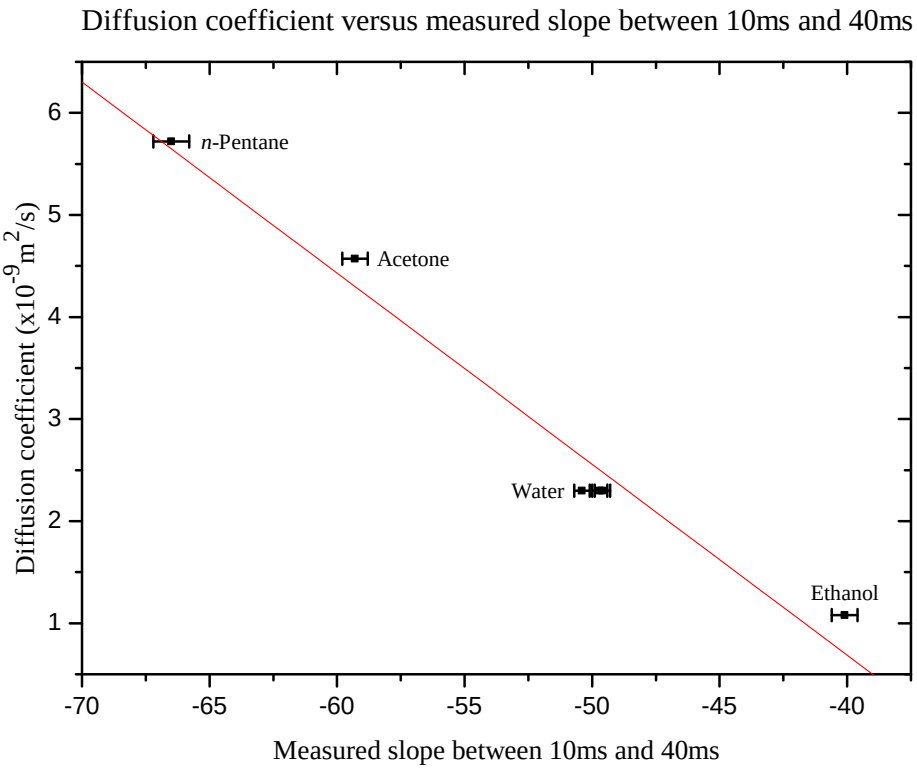

Figure 6.5: Self-diffusion coefficients (from Bruker (2011) [24] and Casieri et al. (2003) [31]) plotted against the slope of the (non-normalized) data from Fig. 6.4 between 10ms and 40ms as described in the text. Uncertainties in slopes are from the linear fits. Uncertainties in the diffusion coefficients are unknown. The linear best fit line is shown.

40ms can also be intuited directly from Fig. 6.4. The result of plotting these six slopes against the provided diffusion coefficients is shown in Fig. 6.5. These results suggest diffusion coefficients could be measured using the Mole probe by measuring just two data points, one using 10ms encoding time and the other 40ms. Only a few echoes are required to do the diffusion encoding and a few tens or hundreds of echoes to measure the two magnetization values. These results need to be repeated using samples having diffusion coefficients which have been independently measured. The samples used in these experiments were obtained from various labs and their quality was unknown.

6.3 Kiwifruit experiments

Kiwifruit are an important part of New Zealand's agriculture industry. Kiwifruit are harvested within a small seasonal window then often packaged and cool-stored in preparation for delivery to local and overseas markets. Determining the best time to harvest the fruit is important for maximizing economic returns and minimizing waste. The kiwifruit industry would like to have a technology available to easily and non-destructively measure fruit ripeness. At present a variety of cumbersome and labor intensive techniques are used such as dehydration, dry matter measurement, and Brix measurement – all of which require destruction of the sample.

Due to the interest of a Massey University colleague, T_2 relaxation experiments were performed on a firm (under-ripe) and a soft (over-ripe) Hayward variety green kiwifruit to determine if the NMR measurements could be correlated with the bulk properties of the fruit. Each fruit was subject to twelve T_2 CPMG experiments with varying echo times between 350μs and 5,000μs. Each measurement consisted of 128 scans in order to improve the signal-to-noise ratio for multi-exponential fitting, which is very susceptible to minor variations in data and noise (Clayden and Hesler (1991) [38]). Curve fitting the data in OriginLab revealed at least tri-exponential relaxation for both fruit and surprisingly the extracted amplitude and time values for the different fruit were found to be almost identical. This was surprising because the two kiwifruit appeared to be at distinctly different ripening stages.

The best way to compare the firm and soft kiwifruit datasets was to graph them against each other. Due to serendipitous separation of the three extracted times and amplitudes, the three datasets fitted nicely on two graphs as shown in Figs. 6.6 and 6.7.

The data shown in the two figures was taken from tri-exponential relaxation decay data. As mentioned, it is very difficult to obtain reliable information from higher-order exponential decays. By assuming the extracted tri-exponential

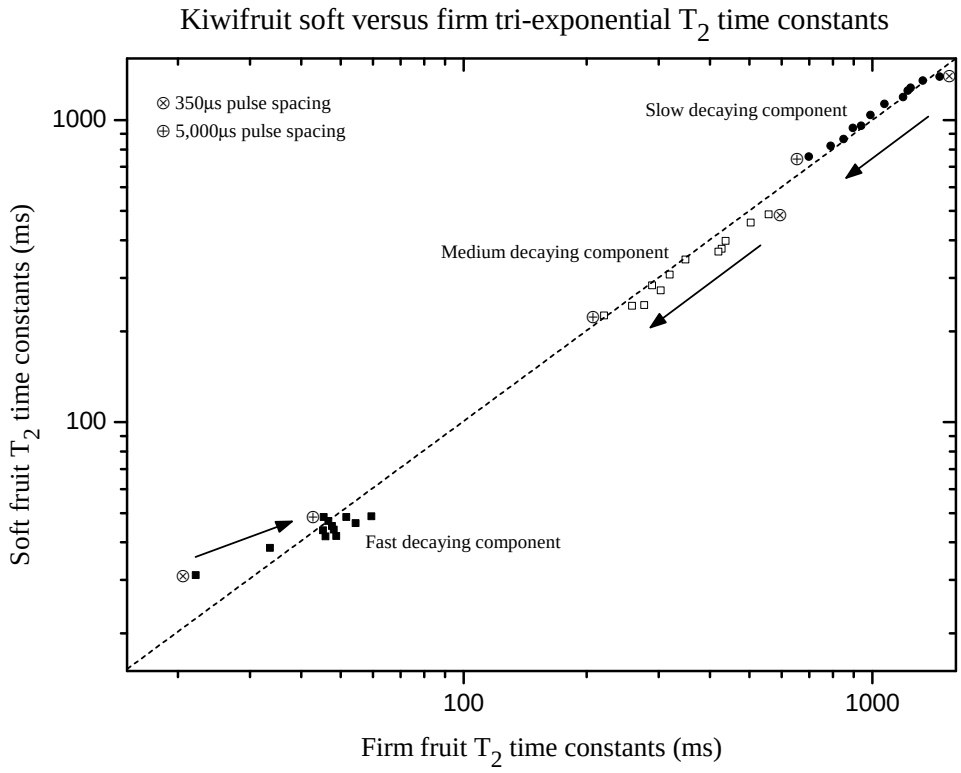

Figure 6.6: Comparative tri-exponential relaxation time components for firm versus soft kiwifruit. Data lying on the equality line have identical values in both firm and soft fruit. The arrows indicate the T_2 relaxation time trend as echo spacings were increased.

relaxation data described above did in fact represent the underlying physical reality, the following observations were made.

First, three distinct behavioral regions existed within both the ripe and un-ripe kiwifruit as represented by the three relaxation and amplitude groupings shown in Figs. 6.6 and 6.7. The three time constants were between 20ms and 60ms (fast component), 220ms and 550ms (medium component), and 650ms and 1,500ms (slow component). The three amplitude components were between 1 and 4.5 units (fast component), 5 and 7.5 units (medium component), and 8 and 15 units (slow component).

Second, T_2 relaxation times for the medium and slow decaying components in Fig. 6.6 decreased significantly and systematically with increased echo spacing.

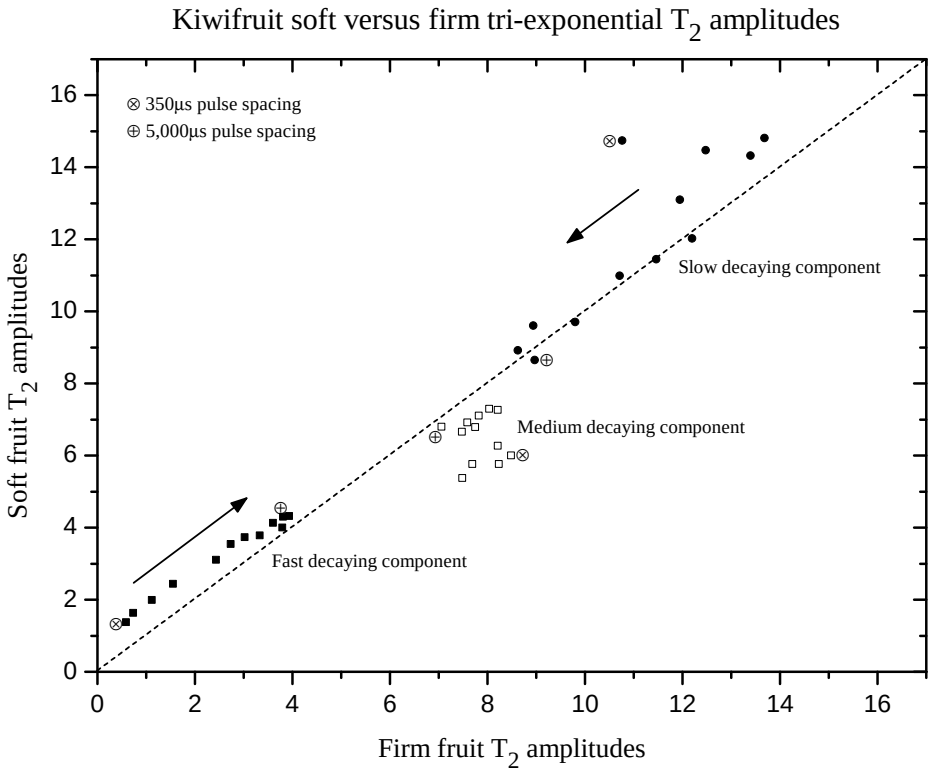

Figure 6.7: Comparative tri-exponential relaxation amplitude components for firm versus soft kiwifruit. Data lying on the equality line have identical values in both firm and soft fruit. The arrows indicate the T_2 relaxation amplitude trend as echo spacings were increased.

This would be expected if diffusion was taking place within the kiwifruit. By contrast the relaxation time of the fast decaying component increased with echo spacing, reaching a maximum at about 1,500ms spacing before dropping slightly and thereafter remaining constant. This may be due to the slower decaying components skewing toward the faster decaying component as the pulse spacing increased. This could be tested by modeling tri-exponential data and including diffusion terms for the slower relaxing components.

Third, calculations of the amplitudes of the three decaying exponentials in Fig. 6.7 at 350μs echo spacing showed the fast decaying component made up only about 5% of the total NMR signal, the medium component 25%, and slow component 60%. With increased echo spacing the amplitude of the slow component decreased in proportion to the total NMR signal, the medium component remained relatively constant, and the fast component increased. At 5,000μs echo spacing the fast component had increased to around 20% of the total NMR signal.

Fourth, the medium and slow decaying T_2 time constant components are almost identical for both fruits and for all echo spacings. This is shown by the soft and firm fruit data lying on the equality line in Fig. 6.6. These time constants therefore appear to provide no information on kiwifruit ripeness; nor do their amplitudes – although there may be a trend away from the equality line in the slow component at short pulse spacing.

Fifth, the most promising component for distinguishing between firm and soft kiwifruit may be in the fast decaying time and amplitude values, especially at short echo spacings. These comparative points deviate from the equality line and appear to do so systematically. The observation that firm kiwifruit have shorter relaxation times than soft kiwifruit was expected. However the larger amplitudes of the fast component in the soft fruit was unexpected. There may be a biochemical reason for this, or a simpler explanation may be that the soft fruit was compressing on the Mole probe surface and thus provided increased NMR signal from the harder regions of the fruit. The fact that similar but opposite change appears in the medium decay component lends weight to this hypothesis. These measurements need to be repeated very carefully, taking into consideration the positioning of the soft and hard kiwifruit within the Mole's active volume.

6.3.1 Katikati experiments

In late May 2009 further experiments were performed on kiwifruit. This time the NMR apparatus was packed into a vehicle and transported to a commercial kiwifruit harvesting and sorting plant in Katakati near Tauranga. Upon arrival the apparatus was configured and left overnight for the Mole temperature to stabilize. Experiments were then performed on both green (Hayward variety) and gold kiwifruit.

The first set of experiments measured the T_2 relaxation times of ten green kiwifruit and ten gold kiwifruit. All kiwifruit were taken from a chiller and kept in polystyrene trays before and after measurement to maintain a constant temperature. Following the T_2 measurements the kiwifruit were tested destructively for Brix, dry matter, and firmness with a penetrometer, then a statistical analysis was performed by a company employee. The only observed correlation appeared between the amplitude of the medium and slow decaying components of the T_2 signal and Brix data, but the validity of the correlations was dubious.

Further experiments were then performed on sixty green kiwifruit taken directly from vines rather than from the coolstore. Because of time constraints and slow NMR data transfers between the DSP and the computer, CPMG echoes were only recorded for approximately the first 200ms of transverse relaxation. This enabled capture of the fast decay component and some of the medium decay component. The slow decay component would have been partially suppressed by the fast 150ms repetition time of the CPMG sequence. While no correlation was found between this T_2 data and the experimental measurements listed earlier, the amplitudes of the relaxation data from the sixty samples varied significantly. This could have been caused by differing sample temperatures, by different sized kiwifruit, or by the regions being measured within the kiwifruit.

To test for temperature dependence, transverse relaxation times were recorded for green and gold kiwifruit at three temperatures. The green kiwifruit were measured at 1.8°C, 9.9°C, and 21.9°C and the gold at 2.1°C, 9.6°C, and 22.2°C. To perform the experiments quickly, only 32 scans at each temperature were possible therefore the signal-to-noise was not as high as for the Massey lab kiwifruit experiments. This was reflected in the tri-exponential fitting data which lacked the clear time and amplitude patterns shown earlier. It was evident from the plots however that the relaxation data amplitude changed with sample temperature. The lowest temp provided the largest signal. The middle temperature amplitude was reduced by about five percent and the highest temperature amplitude by about twenty percent.

The differing sizes of the kiwifruit could also have led to amplitude variations depending upon how many NMR sensitive protons were located inside the sensitive volume. Alternatively different parts of the kiwifruit may have been located inside the sensitive volume. For example, a small kiwifruit may have some of its central core inside the sensitive region while a large kiwifruit may have only the fleshy section in the region.

An additional complication when measuring kiwifruit was determining the part of the fruit being measured. Six large green fruit were separated into five different sections: (i) the skin and layer of flesh close to the skin, (ii) pure flesh, (iii) flesh plus seeds, (iv) seeds, and (v) the core. Various pieces of the kiwifruit from the

same region were arranged to fill the sensitive volume then wrapped in Glad Wrap. The T_2 relaxation results for the different regions within the kiwifruit are shown in Fig. 6.8.

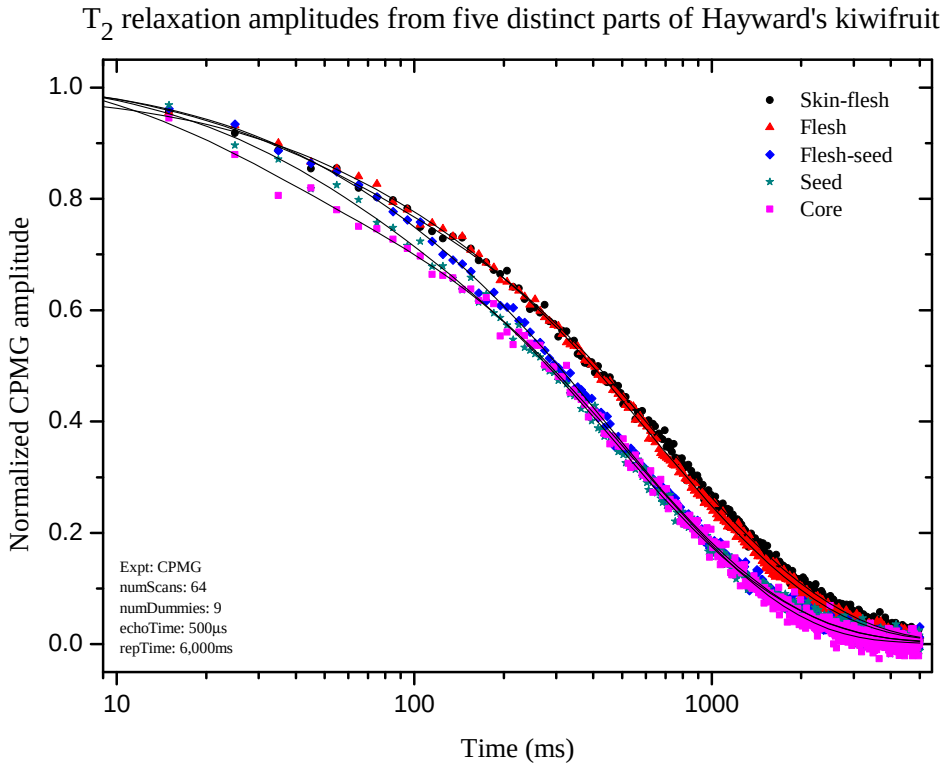

Figure 6.8: Transverse relaxation data from five regions within Haywards kiwifruit. The amplitudes are normalized so the regions can be easily compared. Semi-log plotting emphasizes the fast decaying components. The curve fits are all tri-exponential. Every second data point is omitted for clarity.

The core, as expected, was observed to decay the fastest since it is the hardest piece of the fruit. This was followed by the seed and mushy region surrounding the core. Again this would be expected due to the solid nature of the seeds. The flesh-seed region decayed more slowly followed by the near-identical flesh and skin-flesh regions. The similarity of the flesh and skin-flesh results is useful because the Mole probe can easily be focussed on this volume alone while ignoring the seeds and core. It would be more difficult to achieve measurements of the core alone.

Unfortunately the expedition to Katikati had strict time limitations and a brute-force statistical approach was taken to the measurements. Many fruit were measured with the NMR apparatus then measured destructively and correlations sought between the measurements. Rushed measurements resulted in poor signal-to-noise due to too few scans being recorded. This was further hindered by lack of data transfer speed between the spectrometer DSP and computer. To circumvent the slow data transfer problem the CPMG macro and pulse program were re-written to provide three adjustable sampling periods. The first period sampled every data point, then the second and third introduced an increasing number of dummy echoes. Using this technique a long T_2 could be measured using relatively little data while maintaining sufficient data points during the fast decay period for fitting. The newer DSP module shifted the speed bottleneck to Prospa.

The kiwifruit measurements above have been shown to provide a rich array of data. These experiments require repeating very carefully using multiple samples. A combined understanding of kiwifruit biochemistry, pectin solution relaxation, and experimental NMR measurements, especially during the fast decaying phase, may provide pointers to the internal state of the fruit. This certainly requires additional research before the measurements could be used as a fruit picking tool.

Other relaxation measurements that should be performed on kiwifruit are T_1 and spin-lock ($T_{1\rho}$) measurements. The first of these has taken a back seat in this thesis due to the focus on T_2, but may provide additional information. Spin-lock measurements were also suggested as a further source of information. They were attempted during this project, but unfortunately the Tomco HPA amplifier was unable to perform in the required manner, so spin locking remains as a future possibility.

CHAPTER 7

Conclusion

At the beginning of this PhD project, a rudimentary low-field NMR apparatus was provided, and preliminary NMR measurements were recorded. The measurements were found to be of low quality and insufficiently repeatable. After receiving a replacement NMR probe, and expending significant effort shielding the apparatus against electromagnetic interference, two matters of significant concern remained. These were: continued electromagnetic interference, and probe temperature instability. These problems were effectively solved by placing the NMR probe inside a custom-designed environmental chamber.

Following shielding and temperature stabilizing the probe, a variety of experiments were performed to test system stability, measurement stability, and Prospa's exponential fitting algorithms. Other experiments were also performed to optimize the sample's signal-to-volume ratio, to examine the temperature dependence of the Mole probe, and to determine the effects of misalignment between the B_0 Larmor frequency, and the probe tuning and excitation frequencies. Sample temperature dependence measurements led to the heat death of the Mole's central magnet, and an acoustic ringing saga that was finally solved by shielding the central magnet. Sample heating was investigated in light of small samples, long T_2 times, and large numbers of RF pulses. By the completion of Chapter 2, the apparatus was producing repeatable measurements, in preparation for the following chapters.

The pre-amplifier duplexer module in the Kea spectrometer became unavailable soon after, so a new module design was proposed. This resulted in the development of two new pre-amplifier duplexer modules. These were discussed in detail in terms of their functionality and electronic circuit implementation in Chapter 3. Both designs worked successfully, however one of the designs had better signal-to-noise, and was used successfully for the remainder of the thesis.

The NMR apparatus was thereafter put to work performing T_2 experiments on galacturonic acid and pectin solutions. The T_2 results were a fascinating source of information, especially when coupled with the Carver Richards two-site exchange model. With the aid of published results from other researchers, and molecular level information from the model, the molecular behaviors of two types of pectin molecules at varying pH levels and concentrations were revealed. Accompanying the relaxation measurements were titration measurements. These measurements also proved to be a fascinating source of molecular information. The results of the pectin measurements and their interpretations were discussed in Chapter 4.

As an offshoot from the pectin measurements, T_2-versus-pH experiments were also performed on Milli-Q water. The pH-dependence displayed in the measurements did not appear to be a result of the NMR apparatus, but instead may be due to the inherent properties of bulk water. This was discussed in Chapter 5.

Several other interesting experiments were performed using the low-field apparatus as discussed in Chapter 6. The first set of experiments showed that the Mole probe can be used to measure flow rates using an unusual pulse sequence that generates direct and stimulated echoes. The second set showed two different pulse sequences that can be used to measure diffusion with the Mole probe. The third set of experiments measured kiwifruit tri-exponential T_2 relaxation times. Subtle differences were found to exist between an under-ripe and an over-ripe fruit.

In summary, the experiments performed in this thesis revealed many exciting results. The results of the pectin experiments provided profound insights into the molecular behavior of pectin molecules, and have left many questions open for further research. The titration experiments on mono- and tri-galacturonic acids, and on the pectins, likewise require further research. Experiments are planned on di-galacturonic acid as soon as the chemical arrives in New Zealand. Water behavior is presently being studied by other research groups using various techniques. The source of the T_2 dependence upon pH remains to be determined. Perhaps future NMR studies can contribute to the other techniques that are seeking a deeper scientific understanding of water. Flow and diffusion were successfully measured using the Mole probe, and could have industrial applications. Low-field NMR has been successfully used in the oil industry, and may have applications in New Zealand-specific areas such as meat, dairy, fish, or timber. Fruit ripeness determination may be possible using low-field NMR. As far as the author is aware, kiwifruit research using NMR has so far been unsuccessful in determining ripeness, although recent results from a colleague may suggest otherwise. It may be economically beneficial to New Zealand to study kiwifruit further using low-field relaxation measurements, including spin locking.

Finally, after several years working on low-field NMR in this project, a book has finally been published specifically on this subject (Casanova et al. (2011) [30]).

As I submit my thesis for examination, it has become available from the Massey University library.

CHAPTER 8

Future work

Numerous possibilities exist for future research and development using the low-field NMR apparatus discussed in this thesis. The work can be divided into two categories: continued development work on the experimental apparatus, and continued experimental work. Some future possibilities are discussed below.

8.1 Future apparatus development work

From an experimenters vantage point, low-field NMR systems will always benefit from having more NMR signal and less noise as this leads to better and faster experimental results. To achieve this requires larger magnetic fields, better shielding of the electronics from EMI, lower noise first-stage pre-amplification, and analog or digital noise filtering. All of these suggestions could be implemented using contemporary technology and knowledge.

Temperature compensating the NMR sensor using a combination of improved magnets and auto-tuning would eliminate tuning capacitor failures and the temperature control apparatus. It would also quicken experimental work, although impedance matching, and tuning frequency drift due to the sample salinity, may still need addressing.

Reducing the size of the experimental apparatus would make it more portable and would cause less clutter within the workspace. This is certainly possible, but would require a significant investment in re-engineering the circuit schematics, printed circuit boards, and enclosures.

Repeatedly measuring the relaxation properties of biopolymers as a function of pH during this project was physically and mentally demanding. It required large numbers of very careful experiments, and many repetitive actions. The sample had

to be transported between the magnet and the water bath at every step, and pH probes and magnetic stirrers needed to be inserted and removed. An experimental cell with the following functions would make measurements significantly faster and perhaps even automate much of the process. All of these suggestions could be controlled through Prospa macros.

- ⋆ Titrant injectors for adding controlled quantities of acid and base titrants into the sample.
- ⋆ Sample temperature control for maintaining the temperature of the sample, and for heating and/or cooling the sample.
- ⋆ A stirrer for mixing the titrant into the sample. This could be speed controlled and would need to be non-magnetic.
- ⋆ Integrated pH meter.

8.2 Future experimental work

Many experiments remain to be performed. Experiments are required on pectins with DM values that differ from those of apple and LM12 pectins. Other DM values are available, and it would be fascinating to see how their T_2 times behave across pH range. The LM12 pectin was measured at five different concentrations, and each concentration was found to have almost identical T_{2b}-versus-pH results. Apple pectin and other pectins need to have T_{2b}-versus-pH measured at different concentrations. Different titrants could also be evaluated to see if different anions and cations made any difference to the T_2 or titration measurements.

Titration experiments remain to be performed on di-galacturonic acid. At a cost of around eleven million United States dollars per kilogram, it is unlikely that di-galacturonic acid will be available in sufficient quantities for low-field NMR T_2 measurements.

Pectin oligomers and homo-galacturonans are intermediate in size between galacturonic acid and the pectins used in this thesis. These also need to be investigated using T_2-versus-pH experiments to determine the effect of molecular size upon the results. Pectins are also available in random and blocky forms. Comparing titration measurements between these two pectin types could help to explain the unexpected titration measurements. Blockiness could also affect the T_2-versus-pH behavior within zone I.

Pectin gels having different concentrations and R_{eff}-values (Vincent and Williams (2009) [153]) were formed from pectin solutions using both an enzyme and GDL. The gels formed in the presence of calcium cations, which were used to form

bonds between the chains. By controlling the R_{eff} value, the amount and extent of interchain association can be tuned to control elasticity of the sample. T_2 relaxation times were measured during the gelling process, and appeared to reconcile well with similar results using identical samples measured using SAXS at the Australian synchrotron. The results are not shown in this thesis and require further work.

Kiwifruit require further study. The three separate relaxation components need to be very carefully investigated to determine whether they contain useful ripening information. It may be useful to investigate kiwifruit using temperature as the adjustable experimental parameter as this could be easily varied in a post-harvest environment. Understanding cell-wall biochemistry may further illuminate the T_2 results. Different regions within the fruit (e.g. flesh versus core) could also be studied for ripening indicators. Spin-locking can measure relaxation of slowly moving molecules and may be useful for kiwifruit. Adding cellulose to pectin solutions and gels would bring them closer to real-world systems. T_2 experiments need to be investigated in this context.

There are many other interesting systems that remain to be studied using low-field NMR. The water experiments from this thesis are probably better investigated using high-field NMR as the changes in T_2 are much greater. By contrast, samples such as dairy products contain a rich variety of large molecules such as proteins and fats that co-exist alongside water. These systems are well suited for low-field NMR, and with a combined knowledge of the underlying chemistry could prove both interesting for researchers and beneficial economically.

APPENDIX A

Circuit diagrams

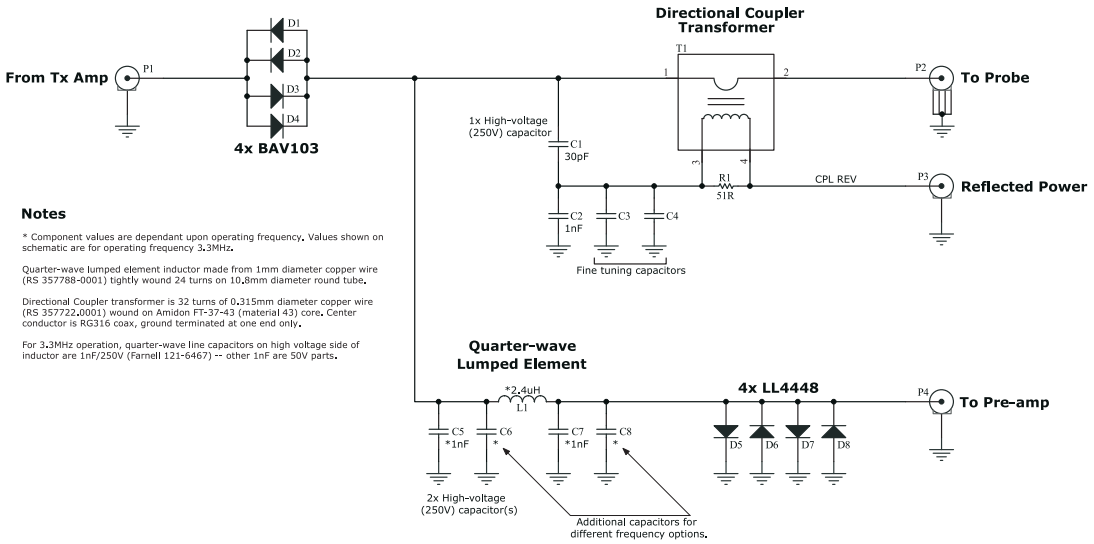

Figure A.1: The pre-amplifier duplexer standard version Duplexer/Directional Coupler Version 1.0 electrical schematic.

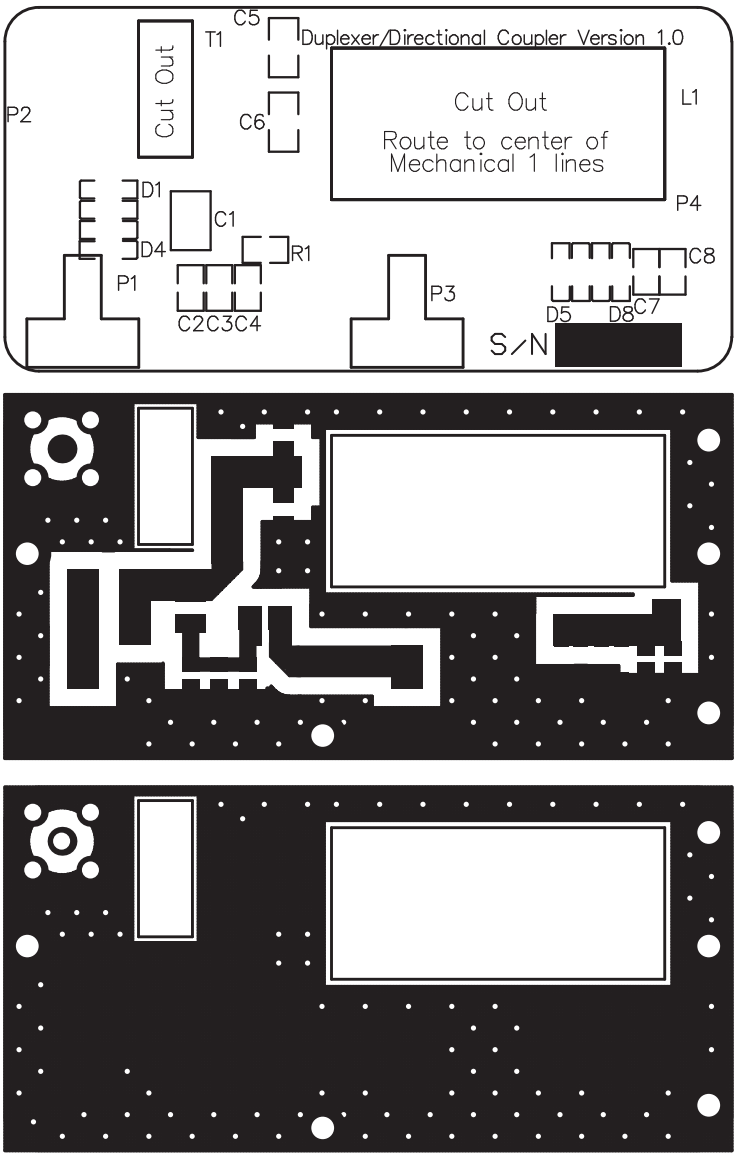

Figure A.2: The pre-amplifier duplexer standard version Duplexer/Directional Coupler Version 1.0 printed circuit board. The upper drawing show the top overlay with component designators. The middle drawing shows the top layer copper tracks and ground plane. The lower drawing shows the bottom layer copper and is almost entirely ground plane. The two rectangular regions are cutouts designed to fit the magnetic components. Mounting holes are shown around the outside of the PCB. The small white dots are copper plated vias that connect the top and bottom copper ground planes together. Having many junction between layers reduces ground plane impedance.

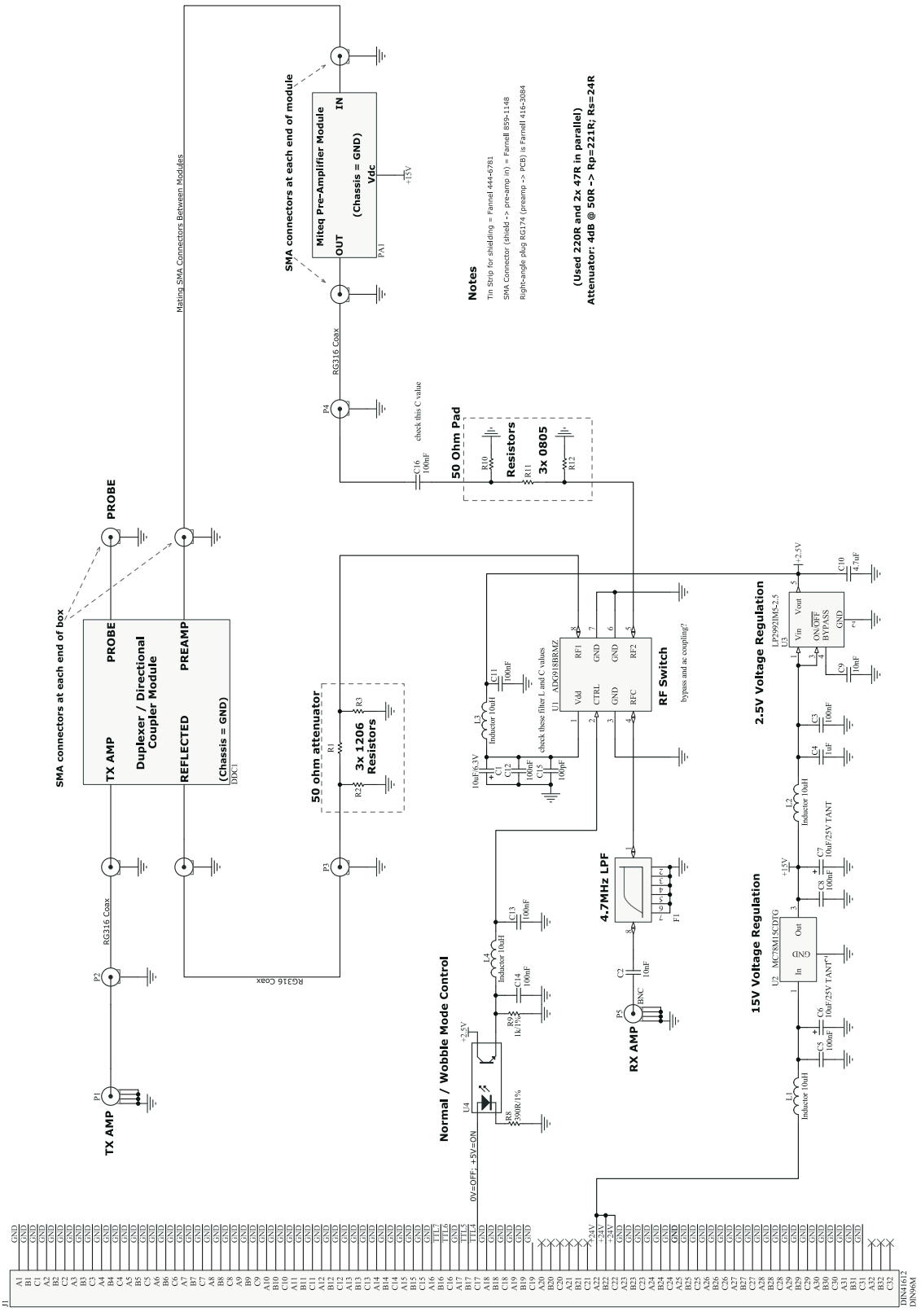

Figure A.3: Pre-amp duplexer standard version electrical schematic.

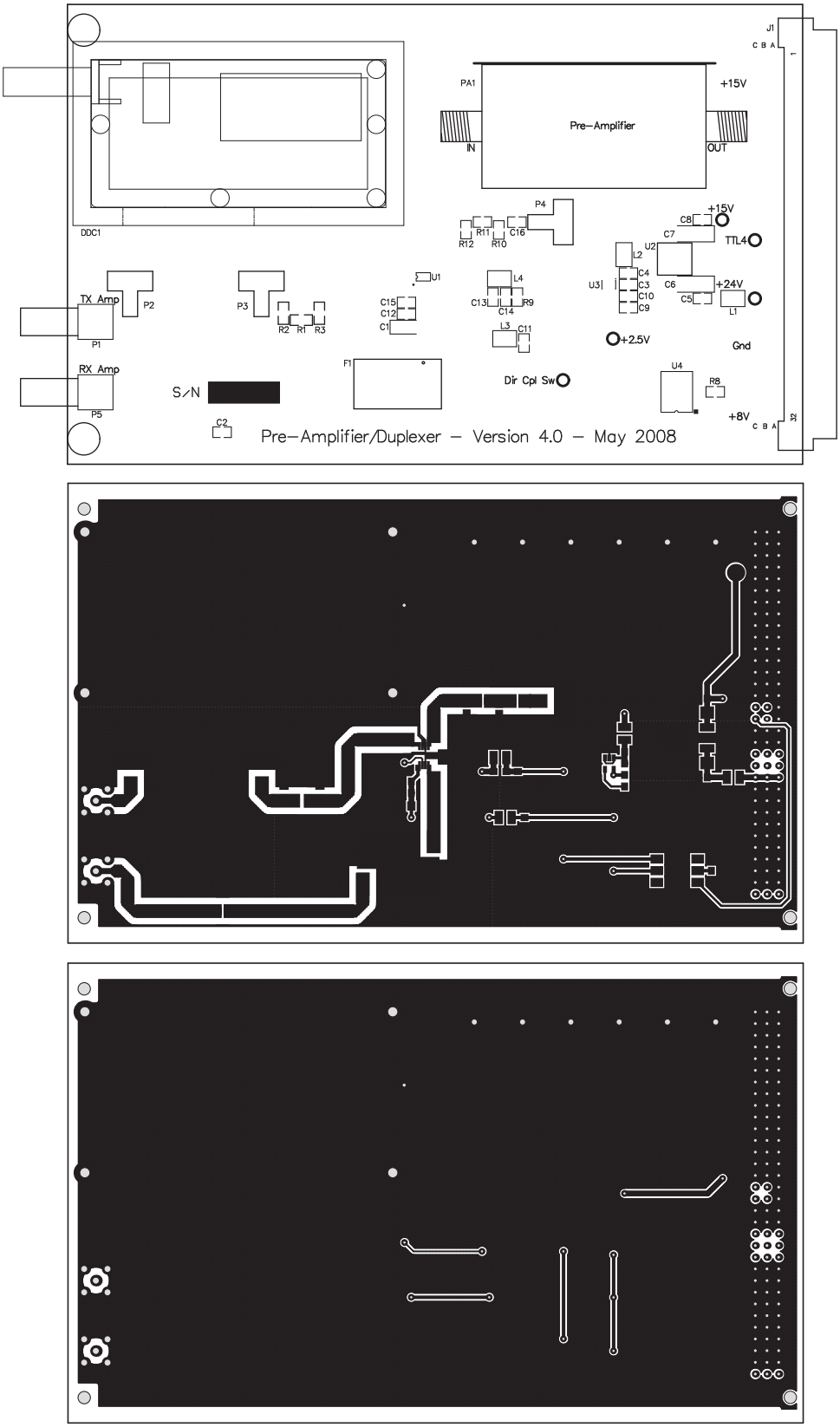

Figure A.4: Pre-amp duplexer standard version PCB showing (in descending order) the top overlay, top layer copper, and bottom layer copper.

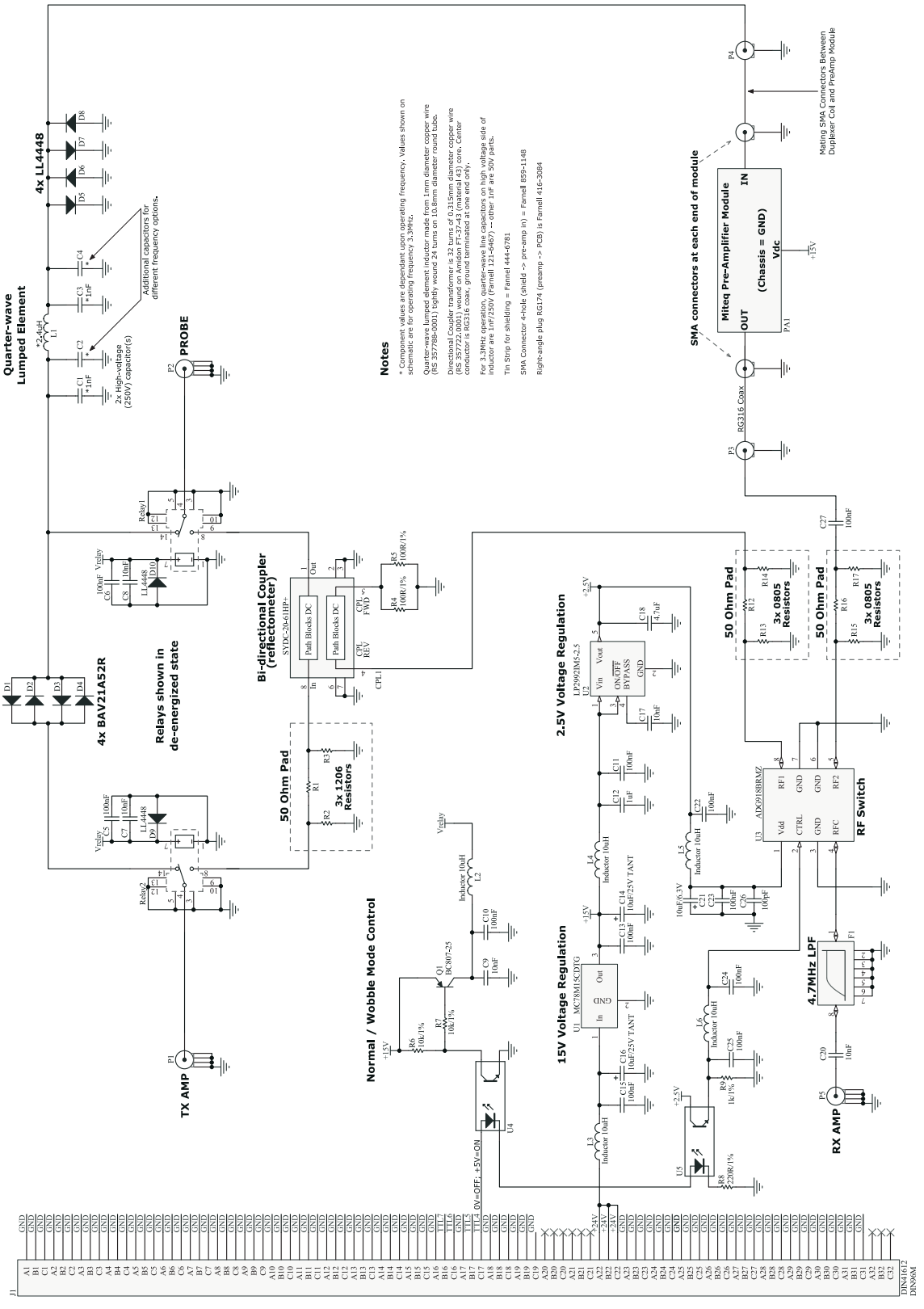

Figure A.5: Pre-amp duplexer relay version electrical schematic.

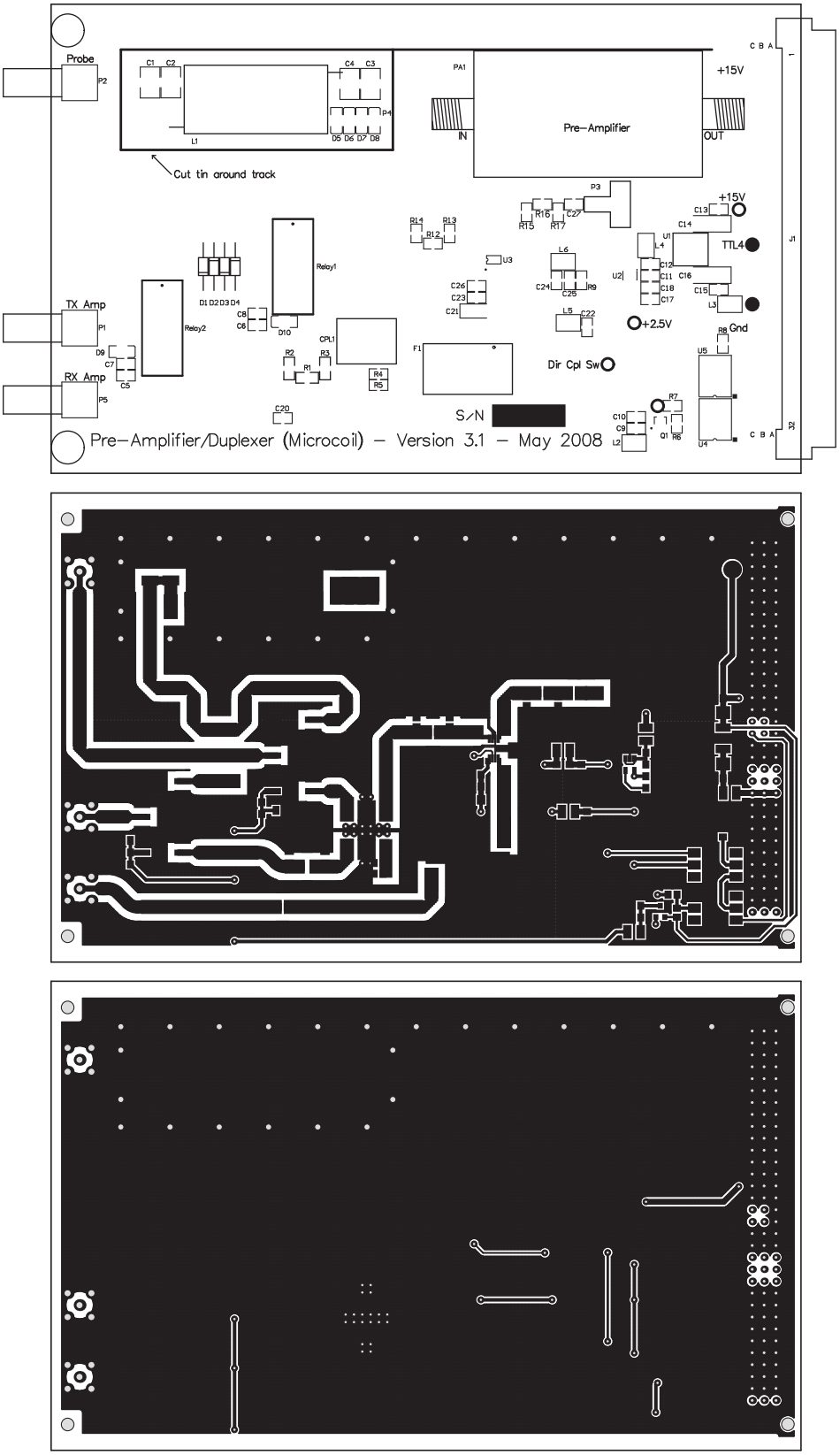

Figure A.6: Pre-amp duplexer relay version PCB showing (in descending order) the top overlay, top layer copper, and bottom layer copper.

APPENDIX B

Making pectin solutions

Pectins solutions are not difficult to make, however if the steps below are not followed then the resulting solution may contain undissolved pectin lumps. In addition, in the interests of experimental repeatability, the solutions should be made using the same method each time. Failure to do so may result in unknown differences that could, in turn, manifest themselves in the relaxation measurements.

1. Before starting to make the solutions, all vials should be thoroughly cleaned as contaminants may remain in the vials after their manufacture. This was observed in the glass vials used during this thesis. It was found that triple rinsing the vials with fresh Milli-Q water and vigorous shaking removed the contaminant(s). The vials should thereafter be left upside down on paper towels to dry.

2. Weighing scale calibration should be checked. This was tested by pipetting a known quantity of water into a tray and weighting it.

3. Spatulas and magnetic fleas should be washed using detergent then thoroughly rinsed in hot water then in fresh Milli-Q water before being dried.

4. Pectins should be measured in a clean plastic measuring tray that has not been left to collect dust.

5. The required quantity of fresh Milli-Q water should be carefully pipetted into the vial. The water should be cold – for example, below room temperature. This encourages the pectin molecules to unfold without coagulation.

6. The magnetic flea should be added directly into the water without touching human skin. The magnetic stirrer speed should be set to maximum in order

to create a water vortex in the center of the vial. If the magnetic flea is too small, it will not be able to maintain a vortex as the solution becomes more viscous.

7. The pectin powder should be added slowly onto the side of the water vortex so that it is dispersed evenly throughout the solvent.

8. If any obvious lumpiness is observed in the solution, or on the sides of the vial, the solution should be shaken vigorously to break up the lumps. Generally a small amount of lumpiness will remain after cold stirring, depending upon the type of pectin and concentration. The lumps should disappear during the heating/stirring process.

9. Once the dried pectin is all dispersed throughout the solvent, place the lid on the vial and place in a water bath. The level of the water should be sufficient to cover the height of the pectin solution in the vial. A small magnetic flea should be placed in the water bath to reduce localized heating of the water.

10. Set the temperature of the water-bath to 60°C and the stirring speed to maximum. Once the temperature has reached 60°C, continue rapid stirring for 20-30 minutes.

11. Turn off the magnetic stirrer and heater element, and allow the sample to return to ambient temperature. The pectin solution should now appear uniform with no lumps in the solution or on the vial walls.

After the pectins have cooled, they can be safely stored in a fridge for several weeks. If they are left at room temperature, bacteria can grow in the sample (this was observed).

A tiny quantity of sodium azide may be added to the solutions to stop bacterial growth. This was not used for any experiments in this thesis, with the exception of pectin gels (not included in thesis). Sodium azide is a hazardous chemical.

APPENDIX C

Software

C.1 T_2 drift test

```
procedure(T2DriftTest)

# Cache macros
   cd("$appdir$\\Macros\\Kea-NMR")
   cachemacro("cpmg.mac","local")
   cd("$appdir$\\Macros\\Kea-Core")
   cachemacro("keaNMR.mac","local")

   guipar = ["saveData = \"true\"",
             "incExpNr = \"yes\"",
             "expNr = 1",
             "expName = \"cpmg\"",
             "dataDirectory = \"C:\\Working Directory\"",
             "alpha = 1e10",
             "x_maximum = 5000",
             "x_minimum = 10",
             "fitType = \"biexp\"",
             "sumEchoes = \"yes\"",
             "timeMag = \"no\"",
             "filterType = \"sinebellsquared\"",
             "filter = \"no\"",
             "acqTime = 0.26214",
             "usePhaseCycle = \"yes\"",
             "accumulate = \"yes\"",
```

```
              "bandwidth = 488.28",
              "nrScans = 128",
              "bandwidthFile = 2.048",
              "nrPnts = 128",
              "rxPhase = -110",
              "rxGain = 40",
              "echoShift = 0",
              "nrDummies = 1",
              "nrEchoes = 2000",
              "echoTime = 500",
              "pulseLength = 26",
              "180Amplitude = -10",
              "90Amplitude = -16",
              "repTime = 30000",
              "b1Freq = 3.222"]

# Run the macro via the backdoor
clear ("cli")

pr("T2 Drift Test Macro\n")
pr("Tests variation in T2 over many hours\n")
pr("-------------------------------------\n\n")
pr("CPMG scans running...\n")

for (Count = 1 to 100)
  pr("About to run CPMG seq. no. $Count$\n")
  cpmg:backdoor(guipar)
  pr("Finished CPMG sequence $Count$\n")
  pr("Pausing for 6 hours...\n")
  pause(21600) # 21600s = 6 hours
next(Count)

endproc()
```

APPENDIX D

Recommended reading

The following is a small sample of the books used during this project. They are listed in order of recommendation.

- ⋆ *Spin Dynamics - Basics of Nuclear Magnetic Resonance* by Malcolm H. Levitt
- ⋆ *Understanding NMR Spectroscopy* by James Keeler
- ⋆ *Experimental Pulse NMR* by E Fukushima and S Roeder
- ⋆ *A Handbook of Nuclear Magnetic Resonance* by Ray Freeman
- ⋆ *Principles of Nuclear Magnetic Resonance Microscopy* by Paul T. Callaghan
- ⋆ *Essential NMR* by Bernhard Blümich
- ⋆ *A Dictionary of Concepts in NMR* by S. W. Homans

APPENDIX E

Equipment list

Table E.1: Partial list of chemicals used for this thesis.

Chemical	Description
Galacturonic acid	Fluka BioChemika 48280 $C_6H_{10}O_7.5H_2O$ $M_r = 212.16$ (hydrated) Assay $\geq 93\%$ Product of Slovakia
HM Apple pectin	Fluka BioChemika 76282 Lot and filling code 1217124 40206009 $H_2O \leq 10\%$; Ash $\sim 6\%$; DE 70-75% $M_r \sim 30,000 - 100,000$; Hygroscopic
LM12	CG, CP Kelco Pectin Commercial sample $M_r \sim 120,000$; DE 35–40%
Tri-galacturonic acid	Sigma T7407-25MG $C_{18}H_{26}O_{19}$ Assay $\geq 90\%$ HPLC Lot number #064K5023V

Table E.2: Partial list of software and hardware used for this thesis.

Software	Description
Altium Designer	Schematic and PCB design
BibDesk	LaTeX bibliography management
CorelDRAW X4	Image editing
Microsoft Excel	Mathematical modeling
OriginLab	Graphing, curve fitting, modeling
Papers	PDF and bibliography management
Prospa	NMR spectrometer and macros
SolidWorks	3D drawings and modeling
TeXShop	LaTeX editor for Mac OS X
Hardware	**Model number**
Gaussmeter	Lakeshore 421
Gaussmeter probe	MNA-1904-VH probe
Magnetic heater/stirrer	IKAMAG
Omron temperature controller	E5CN-Q2MT-500
Omron USB-Serial Conversion cable	E58-CIFQ1
pH meter	Sartorius PP-15
pH probe	Sartorius PY-P11
Temperature logger	EL-USB-1
Tomco RF pulse amplifier	BM0250-AB; 0.25-8MHz; 250W Serial number 1966

Bibliography

[1] Massey University Chemical Stores.

[2] Mike Christie Sheetmetals Ltd, 10 Moa Street, Palmerston North.

[3] Personal correspondence with Mark Hunter.

[4] Sensortech Technology, Auckland.

[5] Work partaken with Mark Hunter at Victoria University.

[6] Dance of water with proteins: Disco becomes a minuet. *Science Daily*, 2007.

[7] Protein folding: One picture per millisecond illuminates the process. *Science Daily*, 2008.

[8] Water is 'designer fluid' that helps proteins change shape. *Science Daily*, 2008.

[9] The way a protein is folded affects the molecular dance of water. *Science Daily*, 2008.

[10] The dance of water: New insight into water's strange bulk properties. *Science Daily*, 2009.

[11] Supercomputer provides new insights into the vibrations of water. *Science Daily*, 2010.

[12] Michael Adams. The Pre-amplifier Unit of LapSpec. *Institute of Macromolecular Chemistry, RWTH-Aachen, Germany.*, 2005.

[13] Sigma Aldrich. *www.sigmaaldrich.com.*

[14] Altium. *www.altium.com.*

[15] ER Andrew and K Jurga. NMR Probe With Short Recovery Time. *Journal of Magnetic Resonance*, 73(2):268–276, 1987.

[16] PW Atkins. *Physical Chemistry.* Oxford University Press, 6th edition, 1998.

[17] Edwin D Becker, Cherie L Fisk, and CL Khetrapal. Encyclopedia of Magnetic Resonance. pages 1–154, Mar 2007.

[18] ST Beckett. *Physico-chemical aspects of food processing.* Blackie Academic and Professional, 1st edition, 1995.

[19] Hans-Dieter Belitz, Werner Grosch, and Peter Schieberle. *Food Chemistry.* Springer, 2009.

[20] Fluka BioChemika. *www.sigmaaldrich.com.*

[21] Bruker BioSpin. *www.bruker-biospin.com.*

[22] G Michael Blackburn. *Nucleic Acids in Chemistry and Biology.* Royal Society of Chemistry, 1st edition, 2006.

[23] Warren B Bruene. The inside picture of directional wattmeters. pages 1–5, Oct 2010.

[24] Bruker. *Almanac.* 2011.

[25] ML Buess and GL Petersen. Acoustic ringing effects in pulsed nuclear magnetic resonance probes. *Review of Scientific Instruments*, 49(8):1151–1155, 2009.

[26] Paul T Callaghan. *Principles of Nuclear Magnetic Resonance Microscopy.* Oxford University Press, 1991.

[27] F Capel, T Nicolai, D Durand, and P Boulenguer. Calcium and acid induced gelation of (amidated) low methoxyl pectin. *Food hydrocolloids*, Jan 2006.

[28] Joseph J Carr. *The Technician's Radio Receiver Handbook: Wireless and Telecommunication.* Newnes, 1st edition, 2001.

[29] JP Carver and RE Richards. A general two-site solution for the chemical exchange produced dependence of T_2 upon the Carr-Purcell pulse separation. *Journal of Magnetic Resonance*, 6(1):89–105, 1972.

[30] F Casanova, J Perlo, and B Blumich. *Single-Sided NMR.* Springer, 2011.

[31] C Casieri, S Bubici, and F De Luca. Self-diffusion coefficient by single-sided NMR. *Journal of Magnetic Resonance*, 162(2):348–355, 2003.

[32] John Cavanagh, Wayne J Fairbrother, Arthur G Palmer III, Nicholas J Skelton, and Mark Rance. *Protein NMR spectroscopy.* Academic Press, 2nd edition, 2006.

[33] American Technical Ceramics. *www.atceramics.com.*

[34] Raymond Chang. *Chemistry.* McGraw-Hill, 6th edition, 1998.

[35] Martin Chaplin. Anomalous properties of water. *London South Bank University*, 2011.

[36] FV Chávez and B Halle. Molecular basis of water proton relaxation in gels and tissue. *Magnetic Resonance in Medicine*, 56(1):73–81, 2006.

[37] Timothy DW Claridge. *High-Resolution NMR Techniques in Organic Chemistry*. Elsevier, 2nd edition, 2004.

[38] NJ Clayden and BD Hesler. Multiexponential analysis of relaxation decays. *Journal of Magnetic Resonance*, 98(2):271–282, 1992.

[39] GR Coates, L Xiao, and MG Prammer. NMR Logging Principles and Applications. pages 1–253, Oct 2000.

[40] CAL Controls. *www.cal-controls.com*.

[41] Fairchild Semiconductor Corporation. BAV103 high voltage, general purpose diode. 1997.

[42] Fairchild Semiconductor Corporation. BAV21 small signal diode. 2001.

[43] Fairchild Semiconductor Corporation. General Purpose 6-Pin Phototransistor Optocouplers. 2005.

[44] Voltronics Corporation. *www.voltronicscorp.com*.

[45] Analog Devices. 45dB Digitally Controlled Variable Gain Amplifier. 2002.

[46] Analog Devices. *Analog Dialogue*, 38(4), 2004.

[47] Analog Devices. ADG918 Wideband CMOS Mux. 2008.

[48] Analog Devices. AN-952 ADG9xx Wideband CMOS Switches: Frequently Asked Questions Application Note. 2008.

[49] M Dobies, M Kempka, S Kuśmia, and S Jurga. Acid-Induced Gelation of Low-Methoxyl Pectins Studied by ^{1}H NMR and Rheological Methods. *Applied Magnetic Resonance*, 34(1):71–84, 2008.

[50] M Dobies, S Kuśmia, and S Jurga. ^{1}H NMR and Rheological Studies of the Calcium Induced Gelation Process in Aqueous Low Methoxyl Pectin Solutions. *Acta Physica Polonica A*, 108:33, Jul 2006.

[51] Norman Dye and Helge Granberg. *Radio Frequency Transistors: Principles and Practical Applications*. Newnes, 2nd edition, 2001.

[52] Robin Dykstra. *The Development of a Spectrometer for Portable NMR Systems*. 2006.

[53] LASCAR Electronics. EasyLog USB Termperature Logger. *www.lascarelectronics.com*.

[54] Hans-Ulrich Endress, Frank Mattes, and Karl Norz. *Handbook of Food Science, Technology, and Engineering*, volume 3. CRC Press, 2006.

[55] Eppendorf. *www.eppendorf.com*.

[56] D Fabri, M Williams, and T Halstead. Water T_2 relaxation in sugar solutions. *Carbohydrate research*, Jan 2005.

[57] I Fraeye, T Duvetter, E Doungla, and A Van Loey. Literature review: Fine-tuning the properties of pectin calcium gels by control of pectin fine structure, gel composition and environmental conditions. *Trends in Food Science*, Jan 2010.

[58] E Fukushima and SBW Roeder. Spurious ringing in pulse NMR. *Journal of Magnetic Resonance*, 33(1):199–203, 1979.

[59] Eiichi Fukushima and Stephen BW Roeder. *Experimental Pulse NMR, A Nuts and Bolts Approach*. Addison-Wesley Publishing Company, Inc., 1981. First paperback printing, September 1993.

[60] P Gilsenan, R Richardson, and E Morris. Thermally reversible acid-induced gelation of low-methoxy pectin. *Carbohydrate Polymers*, Jan 2000.

[61] R Glick and K Tewari. Proton nuclear magnetic relaxation studies on water: The rates of acid and base catalyzed proton exchange. *The Journal of Chemical Physics*, 44(2):546–547, Jan 1966.

[62] RE Glick and KC Tewari. Proton nuclear magnetic resonance investigations of water. *Nature*, 211:739–740, Aug 1966.

[63] A Gottwald, LK Creamer, PL Hubbard, and PT Callaghan. Diffusion, relaxation, and chemical exchange in casein gels: A nuclear magnetic resonance study. *The Journal of Chemical Physics*, 122:034506, 2005.

[64] David J Griffiths. *Introduction to Quantum Mechanics*. Prentice-Hall Inc., 1995.

[65] David J Griffiths. *Introduction to Electrodynamics*. Prentice Hall International, Inc., 1999.

[66] Jon B Hagen. *Radio Frequency Electronics - Circuits and Applications*. Cambridge University Press, 1996.

[67] David Halliday, Robert Resnick, and Jearl Walker. *Fundamentals of Physics*. John Wiley and Sons, Inc., 1997.

[68] Charles A Harper. *Electronic Packaging and Interconnection Handbook*. McGraw-Hill Professional, 4th edition, 2005.

[69] Janine K Hasey. *Kiwifruit Growing and Handling*. ANR Publications, University of California (System). Division of Agriculture and Natural Resources, 1994.

[70] B Hills, C Cano, and P Belton. Proton NMR relaxation studies of aqueous polysaccharide systems. *Macromolecules*, Jan 1991.

[71] B Hills, S Takacs, and P Belton. A new interpretation of proton NMR relaxation time measurements of water in food. *Food Chemistry*, 37:95–111, Jan 1990.

[72] BP Hills. The proton exchange cross-relaxation model of water relaxation in biopolymer systems. *Molecular Physics*, 76:489–508, 1992.

[73] BP Hills. The proton exchange cross-relaxation model of water relaxation in biopolymer systems. *Molecular Physics*, 76:509–523, 1992.

[74] BP Hills. *Signal treatment and signal analysis in NMR*, volume 18. Elsevier, 1996.

[75] BP Hills, SF Takacs, and PS Belton. The effects of proteins on the proton NMR transverse relaxation time of water. *Molecular Physics*, 67:919–937, 1989.

[76] BP Hills, SF Takacs, and PS Belton. The effects of proteins on the proton NMR transverse relaxation times of water. *Molecular Physics*, 67:903–918, 1989.

[77] BP Hills, KM Wright, and PS Belton. Proton NMR studies of chemical and diffusive exchange in carbohydrate systems. *Molecular Physics*, 67:1309–1326, 1989.

[78] SW Homans. *A Dictionary of Concepts in NMR*. Oxford Science Publications, 2002.

[79] Paul Horowitz and Winfield Hill. *The Art of Electronics*. Cambridge University Press, 2nd edition, 1990.

[80] Martin D Hürlimann, Lauren Burcaw, and Yi-Qiao Song. Quantitative characterization of food products by two-dimensional D-T_2 and T_1-T_2 distribution functions in a static gradient. *Journal of Colloid And Interface Science*, 297(1):303–11, May 2006.

[81] MD Hürlimann. Carr-purcell sequences with composite pulses. *Journal of Magnetic Resonance*, 152(1):109–123, 2001.

[82] MD Hürlimann. Diffusion and relaxation effects in general stray field NMR experiments. *Journal of Magnetic Resonance*, 148(2):367–378, 2001.

[83] MD Hürlimann. Encoding of diffusion and T_1 in the CPMG echo shape: Single-shot D and T_1 measurements in grossly inhomogeneous fields. *Journal of Magnetic Resonance*, 184(1):114–129, 2007.

[84] MD Hürlimann and DD Griffin. Spin dynamics of Carr-Purcell-Meiboom-Gill-like sequences in grossly inhomogeneous B_0 and B_1 fields and application to NMR well logging. *Journal of Magnetic Resonance*, 143(1):120–135, 2000.

[85] MD Hürlimann and L Venkataramanan. Quantitative measurement of two-dimensional distribution functions of diffusion and relaxation in grossly inhomogeneous fields. *Journal of Magnetic Resonance*, 157(1):31–42, 2002.

[86] IKA. *www.ika.net*.

[87] Alan Isaacs. *Oxford Dictionary of Physics*. Oxford University Press, 4th edition, 2000.

[88] Jainming Jin. *Electromagnetic Analysis and Design in Magnetic Resonance Imaging*. CRC Press, 1st edition, 1998.

[89] Richard AL Jones. *Soft Condensed Matter*. Oxford University Press, 2006.

[90] James Keeler. *Understanding NMR Spectroscopy*. John Wiley and Sons, Ltd, 2005.

[91] James Keeler. *Understanding NMR Spectroscopy*. John Wiley and Sons, 2nd edition, 2010.

[92] LakeShore. *www.lakeshore.com*.

[93] Malcolm H Levitt. *Spin Dynamics - Basics of Nuclear Magnetic Resonance*. Wiley, 2nd edition, 2008.

[94] E Liepinsh and G Otting. Proton exchange rates from amino acid side chains-implications for image contrast. *Magnetic Resonance in Medicine*, Sep 1995.

[95] Wainhouse Distribution Limited. *www.wainhousedist.co.nz*.

[96] Reinhold Ludwig and Pavel Bretchko. *RF Circuit Design - Theory and Applications*. Prentice Hall, 2000.

[97] Macmill Magnets. *www.macmillmagnet.com*.

[98] Magritek. *www.magritek.com/prospa.html*.

[99] Magritek. *Terranova-MRI*. 2006.

[100] R Mancinelli, A Botti, F Bruni, MA Ricci, and AK Soper. Perturbation of water structure due to monovalent ions in solution. *Phys. Chem. Chem. Phys.*, 9(23):2959, Jan 2007.

[101] G Manning. Counterion binding in polyelectrolyte theory. *Accounts of Chemical Research*, Jan 1979.

[102] G Manning. Limiting laws and counterion condensation in polyelectrolyte solutions. *The Journal of Physical Chemistry*, Jan 1981.

[103] G Manning. Is the counterion condensation point on polyelectrolytes a trigger of structural transition? *The Journal of Chemical Physics*, Jan 1988.

[104] G Manning. The critical onset of counterion condensation: A survey of its experimental and theoretical basis. *Berichte der Bunsengesellschaft für*, Jan 1996.

[105] B Manz, A Coy, R Dykstra, CD Eccles, MW Hunter, BJ Parkinson, and PT Callaghan. A mobile one-sided NMR sensor with a homogeneous magnetic field: the NMR-Mole. *Journal of Magnetic Resonance*, 183(1):25–31, 2006.

[106] ML Martin, JJ Delpuech, and GJ Martin. *Practical NMR Spectroscopy*. Heyden & Sons Ltd, 1980.

[107] Mini-Circuits. SCLF-4.7 Surface Mount Low Pass Filter. (Rev. D).

[108] Mini-Circuits. SYDC-20-61HP+ directional coupler data sheet. (Rev. C).

[109] Mini-Circuits. Directional Couplers Application Note COUP7-2. 1999.

[110] Miteq. *Miteq NMR Amplifiers*. 2010.

[111] Nardin and Vincendon. Isotopic exchange study of the scleroglucan chain in solution. *Macromolecules*, (22):3551–3554, Oct 1989.

[112] John H Nelson. *Nuclear Magnetic Resonance Spectroscopy*. Prentice Hall, 2003.

[113] Omron. *www.omron.com*.

[114] Omron. Surface-Mounting High-Frequency Relay (G6Z) datasheet.

[115] Konstantinos N. Papadopoulos. *Food Chemistry Research Developments*. Nova Publishers, 2008.

[116] Dietmar Paschek and Ralf Ludwig. Specific ion effects on water structure and dynamics beyond the first hydration shell. *Angewandte Chemie International Edition*, Feb 2011.

[117] S Pérez, K Mazeau, and C Hervé du Penhoat. The three-dimensional structures of the pectic polysaccharides. *Plant Physiol. Biochem*, Jan 2000.

[118] Philips. PMLL4448 High-speed Diodes. 2002.

[119] Philips. Philips SA58643 Single-Pole Double-Throw (SPDT) Switch. (Rev. 1), 2006.

[120] EM Purcell. Research in nuclear magnetism. *Nobel lectures, physics*, 1962, 1952.

[121] M Ralet, M Crépeau, and H Buchholt. Polyelectrolyte behaviour and calcium binding properties of sugar beet pectins differing in their degrees of methylation and acetylation. *Biochemical Engineering*, Jan 2003.

[122] M Ralet, P Lerouge, and B Quéméner. Mass spectrometry for pectin structure analysis. *Carbohydrate research*, Jan 2009.

[123] J Ray and G Manning. Formation of loose clusters in polyelectrolyte solutions. *Macromolecules*, Jan 2000.

[124] International Rectifier. IPS521/IPS521S Fully Protected High Side Power Mosfet Switch. *www.irf.com.*

[125] International Rectifier. IR6220 Intelligent High Side Mosfet Power Switch. *www.irf.com.*

[126] Advanced Receiver Research. *www.advancedreceiver.com.*

[127] Alan Rich. Understanding Interference-Type Noise (AN-346). *Analog Dialogue*, 16(3), 1982.

[128] Alan Rich. Shielding and Guarding (AN-347). *Analog Dialogue*, 17(1), 1983.

[129] B Ridley, M O'Neill, and D Mohnen. Pectins: structure, biosynthesis, and oligogalacturonide-related signaling. *Phytochemistry*, Jan 2001.

[130] Marguerite Rinaudo. Polyelectrolyte properties of a plant and animal polysaccharide. *Struct Chem*, 20(2):277–289, Apr 2009.

[131] Claus Rolin, Beinta U Nielsen, and Poul-E Glahn. *Polysaccharides: Structural Diversity And Functional Versatility.* Marcal Dekker, Inc., 1st edition, 1998.

[132] S Sawayama, A Kawabata, H Nakahara, and T Kamata. A light scattering study on the effects of pH on pectin aggregation in aqueous solution. *Food hydrocolloids*, 2(1):31–37, Jul 1988.

[133] National Semiconductor. LM2599 Simple Switcher Power Converter 150kHz 3A Step-Down Voltage Regulator. 2001.

[134] National Semiconductor. DS200294 Datasheet. 2005.

[135] ON Semiconductor. MC78M00/D Datasheet. 2010.

[136] John Shi, G Mazza, and Marc Le Maguer. *Functional Foods: Biochemical and Processing Aspects*, volume 2. CRC Press, 2002.

[137] DN Sila, S Van Buggenhout, T Duvetter, I Fraeye, A De Roeck, A Van Loey, and M Hendrickx. Pectins in Processed Fruits and Vegetables: Part II—Structure–Function Relationships. *Comprehensive Reviews in Food Science and Food Safety*, pages 1–19, Mar 2009.

[138] J Skinner. Following the motions of water molecules in aqueous solutions. *Science*, Jan 2010.

[139] SolidWorks. *www.solidworks.com*.

[140] Absolute Tooling Solutions. *www.atsl.co.nz*.

[141] YQ Song. Categories of coherence pathways for the CPMG sequence. *Journal of Magnetic Resonance*, 157(1):82–91, 2002.

[142] YQ Song, MD Hürlimann, and C Flaum. A method for rapid characterization of diffusion. *Journal of Magnetic Resonance*, 161(2):222–233, 2003.

[143] YQ Song, L Venkataramanan, MD Hürlimann, M Flaum, P Frulla, and C Straley. T_1-T_2 correlation spectra obtained using a fast two-dimensional Laplace inversion. *Journal of Magnetic Resonance*, 154(2):261–268, 2002.

[144] Iuliana Spiridon and Valentin I Popa. *Polysaccharides: Structural Diversity And Functional Versatility*. Marcal Dekker, Inc., 2nd edition, 2005.

[145] Alexander Steinbüchel and Sang Ki Rhee. *Polysaccharides and Polyamides in the Food Industry*, volume 1. Wiley-VCH, 2005.

[146] D Stigter. Evaluation of the counterion condensation theory of polyelectrolytes. pages 1–9, Aug 1995.

[147] Anna Ström, Pascual Ribelles, Leif Lundin, Ian Norton, Edwin R Morris, and Martin AK Williams. Influence of Pectin Fine Structure on the Mechanical Properties of Calcium–Pectin and Acid–Pectin Gels. *Biomacromolecules*, 8(9):2668–2674, Sep 2007.

[148] Tomco Technologies. *250W Pulsed RF Amplifier Module Model BM0250-AB Alpha Operation Manual*. 2004.

[149] KJ Tielrooij, N Garcia-Araez, M Bonn, and HJ Bakker. Cooperativity in ion hydration. *Science*, 328(5981):1006, 2010.

[150] Mettler Toledo. *www.mt.com*.

[151] Piotr Tomasik. *Chemical and Functional Properties of Food Saccharides*. CRC Press, 2004.

[152] M Tuckerman, D Marx, and M Parrinello. The nature and transport mechanism of hydrated hydroxide ions in aqueous solution. *Nature*, Jan 2002.

[153] Romaric R Vincent and Martin AK Williams. Microrheological investigations give insights into the microstructure and functionality of pectin gels. *Carbohydrate research*, 344(14):1863–1871, Nov 2003.

[154] AGJ Voragen, W Pilnik, Jean-Francois Thibault, MAV Axelos, and Catherine MGC Renard. *Food polysaccharides and their applications*. Marcel Dekker, Inc., 1995.

[155] Alphons G. J Voragen, Gerd-Jan Coenen, René P Verhoef, and Henk A Schols. Pectin, a versatile polysaccharide present in plant cell walls. *Struct Chem*, 20(2):263–275, Apr 2009.

[156] M Williams, T Foster, D Martin, and I Norton. A molecular description of the gelation mechanism of konjac mannan. *Biomacromolecules*, Jan 2000.

[157] M Williams, T Foster, and H Scholss. Elucidation of pectin methylester distributions by capillary electrophoresis. *J. Agric. Food Chem*, Jan 2003.

[158] M Williams and TK Halstead. An analytical form describing T_2 dispersions resulting from diffusive exchange. *Molecular Physics*, 93(4):609–613, Oct 1997.

[159] M Williams, A Marshall, P Anjukandi, and R Haverkamp. Investigation of the effects of fine structure on the nanomechanical properties of pectin. *Physical Review E*, 76(2):021927, Aug 2007.

[160] MAK Williams, RD Keenan, and TK Halstead. A nonlinear regression method for the analysis of ^{1}H T_2 dispersion curves including comments on the role of polydispersity. *Magnetic Resonance in Chemistry*, 36(3):163–173, 1998.

[161] Carol Young. *The New Penguin Distionary of Electronics*. Penguin Books, 1979.

[162] Hugh D Young. *University Physics*. Addison Wesley, 8th edition, 1992.

[163] Zhang, K Nishinari, M Williams, and T Foster. A molecular description of the gelation mechanism of curdlan. *International Journal of Biological Macromolecules*, Jan 2002.

[164] HJ Zhong, MAK Williams, DM Goodall, and ME Hansen. Capillary electrophoresis studies of pectins. *Carbohydrate research*, 308(1-2):1–8, 1998.